RUPRECHT-KARLS-UNIVERSITÄT HEIDELBERG

Sebastian Weber

Measurement of Vector Boson plus Jet Production Cross Sections and Dark Matter Interpretation with the ATLAS Detector

Dissertation

HD-KIP 23-20

KIRCHHOFF-INSTITUT FÜR PHYSIK

Measurement of Vector Boson plus Jet Production Cross Sections and Dark Matter Interpretation with the ATLAS Detector

Sebastian Weber

Heidelberg 2022

Dissertation
submitted to the
Combined Faculty of Mathematics, Engineering and Natural Sciences
of Heidelberg University, Germany
for the degree of
Doctor of Natural Science

Put forward by
Sebastian Weber
born in: Heilbronn
Oral examination: 16. January 2023

Measurement of vector boson plus jet production cross sections and Dark Matter Interpretation with the ATLAS detector

First referee: Prof. Dr. Hans-Christian Schultz-Coulon
Second referee: Prof. Dr. Stephanie Hansmann-Menzemer

Zusammenfassung

In dieser Arbeit wird eine Messung der Z-Boson-plus-Jet-, W-Boson-plus-Jet- und Photon-plus-Jet-Produktion in Proton-Proton Kollisionen mit einer Schwerpunktsenergie von $\sqrt{s} = 13\,\text{TeV}$ und einem hohen Transversalimpuls des Bosons vorgestellt. Die Messung wird unter Verwendung von Daten durchgeführt, die mit dem ATLAS Detektor am Large Hadron Collider mit einer integrierten Luminosität von $139\,\text{fb}^{-1}$ aufgenommen wurden. Für Endzustände, bei denen das Z-Boson in ein Neutrinopaar oder ein Paar entgegengesetzt geladener Elektronen oder Myonen zerfällt, das W-Boson in ein Elektron-Neutrino- oder ein Myon-Neutrino-Paar zerfällt und für Endzustände, die mindestens ein Photon enthalten, werden differentielle Wirkungsquerschnitte gemessen. Die Vektorbosonen werden dabei zusammen mit mindestens einem hadronischen Jet ($p_\text{T} \geq 120\,\text{GeV}$) oder in einer Vektor-Boson-Fusionstopologie gemessen. Bei letzterer wird gefordert, dass die hadronischen Jets eine große Rapiditätsdifferenz aufweisen. Die gemessenen Wirkungsquerschnitte werden mit QCD-Vorhersagen nächst-führender Ordnung verglichen, die mit Sherpa bestimmt wurden und stimmen im Rahmen der Unsicherheiten mit diesen überein. Es wird auch eine Messung von Wirkungsquerschnittsverhältnissen vorgestellt, um die korrelierten systematischen Unsicherheiten hervorzuheben. Darüber hinaus werden die gemessenen Wirkungsquerschnitte auf ihre Anpassungsgüte hin untersucht, um die Übereinstimmung mit dem Standardmodell zu quantifizieren. Bei einer kombinierten Anpassung über alle gemessenen Endzustände wird eine gute Übereinstimmung beobachtet. Da keine signifikanten Abweichungen von den Vorhersagen des Standardmodells gefunden wurden, werden die gemessenen Wirkungsquerschnitte im Kontext von Physik jenseits des Standardmodells interpretiert. Für ein Modell, das die Paarproduktion von schwach wechselwirkender Dunkler Materie vorhersagt, werden verbesserte Ausschlussgrenzen bestimmt.

Abstract

A measurement of Z boson plus jet, W boson plus jet and photon plus jet production at high transverse boson momentum in proton-proton collisions at $\sqrt{s} = 13\,\text{TeV}$ is presented. The measurement is performed using data collected with the ATLAS detector at the Large Hadron Collider with an integrated luminosity of $139\,\text{fb}^{-1}$. Differential cross sections are measured for final states with the Z boson decaying to a pair of neutrinos or a pair of oppositely charged electrons or muons, the W boson decaying to an electron-neutrino or a muon-neutrino pair and for final states containing at least one photon. The cross sections are measured both in a monojet-like topology, where the boson recoils against at least one energetic jet ($p_\text{T} \geq 120\,\text{GeV}$) and in a vector boson fusion topology with at least two jets separated in rapidity. The measured cross sections are compared to next-to-leading order QCD predictions from Sherpa and are found to agree within the uncertainties. A measurement of cross section ratios is also presented to highlight the effect of correlated systematic uncertainties. Furthermore the measured cross sections are used in a goodness-of-fit test to quantify the agreement with the Standard Model. Good agreement is observed in a combined fit across all measured final states. As no excess over the Standard model predictions is found, the measured cross sections are interpreted in the context of beyond the Standard Model physics. Improved exclusion limits are set on a model predicting pair production of weakly interacting Dark Matter.

Contents

1. Introduction

The quest to understand the fundamental principles of nature is the driving force behind particle physics. This has not been without its surprises and since the discovery of the electron and the proton - the elementary particles of their time - at the turn of the 20th century both our experimental and theoretical understanding of particle physics has been revolutionized[1].

The current best knowledge on the fundamental particles and interactions that exist in nature is encoded in the Standard Model of particle physics (SM). This very precise theory[2] has been tested and expanded in the past to accommodate new phenomena and explain differences between measurements and prediction.

Now, at the beginning of the 21st century, there are a number of experimental observations that are not explained within the framework of the SM. One of these observations is the presence of a large amount of matter of unknown origin in the universe that interacts at most weakly with ordinary matter and is therefore called Dark Matter (DM). DM makes up 23 % of the energy content in the universe, compared to 4.6 % visible matter and its existence has been corroborated by numerous experiments. There are good reasons to assume that DM has a particle nature, however none of the particles present in the SM have the required properties.

Therefore DM and also other unexplained phenomena, like dark energy or the matter-antimatter asymmetry in the universe, might require new particles or interactions, which are not (yet) part of the SM. This motivates the ever more precise testing of the SM through precise measurements at increasingly high energies and the search for phenomena that go beyond the Standard Model (BSM).

The measurement of vector gauge boson production in association with highly energetic jets in the proton-proton collisions at the Large Hadron Collider (LHC) provides a fundamental test of the SM. These processes allow to access Quantum Chromodynamics (QCD) at high momentum transfer. Also the electroweak (EWK) sector of the SM is tested, especially if the bosons are produced by vector-boson fusion. In this production mode two bosons interact to produce a third and this trilinear coupling allows to access the underlying gauge structure of the EWK theory [2]. Differential cross section measurements of boson plus jet production also feed into the development of Monte Carlo (MC) event generators. The calculations provided by these generators allow to compare the measured data with SM predictions and are therefore a cornerstone of the LHC physics programme [3].

Vector gauge boson plus jet production also plays an important role in the search for phenomena beyond the Standard Model (BSM). Many of the new particles predicted in BSM

[1] Not the least by the discovery that the proton is actually not a fundamental particle, but consists of quarks and gluon, which are, as far as we know today, fundamental.

[2] One of the free parameters of the Standard Model, the fine-structure constant α_S is known to an accuracy for 81 parts per trillion [1].

theories do not interact with the detector material. They can therefore only be detected if they are produced in association with a visible SM object, for example a jet. In this case their signature is very similar to either the Z boson decaying invisibly in association with a jet or another vector gauge boson decay where the visible particles are not detected due to detector limitations. This makes boson plus jet production the main irreducible background for many BSM searches and explains the requirement for a very good modelling of these processes in MC simulation. In addition a precise cross section measurement itself has sensitivity to many models of BSM physics and can be used to constrain them in case no excess over the SM prediction is observed.

In this work differential cross section measurements of six different boson plus jet processes are presented. These processes are $Z \to \nu\nu$ + jets, $Z \to ee$ + jets, $Z \to \mu\mu$ + jets, $W \to e\nu$ + jets, $W \to \mu\nu$ + jets and γ + jets. Each process is measured in two different recoil jet topologies, which enhance the sensitivity to different models for BSM physics. These are called the monojet phase space and the vector-boson fusion (VBF) phase space. The monojet phase space is designed to be very inclusive and to enhance the sensitivity to a broad range of BSM models, especially DM production. The VBF phase space is constructed to enhance the electroweak production mode, where the measured boson is produced by vector-boson fusion. The VBF phase space is especially sensitive to invisible decays of the Higgs boson, which could also couple to DM as predicted in so-called Higgs portal models [4].

In each of the phase spaces the differential cross section is measured as a function of boson p_{T}, since this observable is especially sensitive to models for BSM physics. In addition other observables are measured that probe important kinematic properties of the jet system in the VBF phase space. These are the differential cross section as a function of the invariant dijet mass and the rapidity-ordered azimuthal angle ϕ between the first two leading jets. Rapidity ordering means in this case that the azimuthal angle of the jet at lower η is subtracted from the azimuthal angle of the jet at higher η. This observable probes the CP structure in Higgs boson interactions [5].

The aim of this measurement is to determine the differential cross sections as precisely as possible, with good control over the various background contributions and the systematic uncertainties. These measured cross sections are compared to SM predictions produced with Sherpa [6] to validate their modelling. In addition a combined maximum likelihood fit is performed including all regions to test the agreement with SM taking the correlation of the uncertainties between the different processes into account. Finally the measured cross sections are used to constrain a simplified DM model.

Previous cross section measurements of similar final states include Z boson decays to charged leptons with the ATLAS experiment at centre-of-mass energy of $\sqrt{s} = 13$ TeV and the full Run 2 luminosity of 139 fb^{-1} both in monojet-like [7] and VBF topologies [8], a measurement of the Z boson decay to charged leptons at $\sqrt{s} = 8$ TeV [9] and a ratio measurement of the Z boson decaying to neutrinos and the Z boson decaying to charge leptons at $\sqrt{s} = 13$ TeV with early Run 2 data and an integrated luminosity of 3.2 fb^{-1} [10]. Furthermore decays of W bosons were measured in the electron channel at $\sqrt{s} = 8$ TeV [11] and in the electron and muon channels at $\sqrt{s} = 8$ TeV [12]. For the photon plus jet measurement, results were reported at $\sqrt{s} = 13$ TeV for a VBF-like final state in 36.2 fb^{-1} [13] and for a monojet-like topology in early Run 2 data with 3.2 fb^{-1} [14] and also at $\sqrt{s} = 8$ TeV [15].

Previous searches for BSM physics with the ATLAS experiment at $\sqrt{s} = 13$ TeV and 139 fb^{-1} include a search for the Higgs boson decaying invisibly in a VBF phase-space [16], a search for several models for BSM physics, including DM, in the monojet phase space [17] and a search for a heavy W boson (W') [18].

To the author's knowledge the cross section measurements of the $Z \to \nu\nu$ + jets, $W \to e\nu$ + jets, $W \to \mu\nu$ + jets and γ + jets final states in the monojet and VBF phase spaces presented here, are the first published differential cross section measurements of these final states performed with the ATLAS detector at $\sqrt{s} = 13$ TeV and $L = 139\,\text{fb}^{-1}$.

This thesis is structured as follows. In Chapter 2 the theoretical background is discussed and an introduction to the LHC and the ATLAS detector is given in Chapter 3. The analysis strategy of the measurement is outlined in Chapter 4 and the physics objects that are measured with the detector as well as the event selection for the various regions in the measurement are introduced in Chapter 5. Chapter 6 discusses the simulation of the measured collision events and an overview of the experimental and theoretical systematic uncertainties is given in Chapter 7. A precise estimate of the backgrounds in the measurement is needed and is explained for the fake backgrounds in Chapter 8 and for the backgrounds due to the limited detector acceptance and efficiency in Chapter 9. Chapter 10 discusses the comparison between data, simulation and the background estimates on detector-level. The correction of the data for detector-effects is explained in Chapter 11 and the final cross sections and their to theory predictions are shown in Chapter 12. The compatibility of the measurement with the SM is investigated in Chapter 13 and models for BSM physics is constrained in Chapter 14. A summary of the presented work is given in Chapter 15.

1.1. Author's contribution

The measurement presented here was performed as part of the ATLAS collaboration. It would indeed have been impossible without the numerous dedicated and experienced people working continuously to operate, calibrate and improve the ATLAS detector. The collaboration, together with CERN, also provided many reconstruction and analysis software tools and frameworks employed by the author in this measurement.

As part of the ATLAS collaboration, the author contributed to the operation and calibration of the detector, specifically to the Level-1 Calorimeter Trigger (L1Calo). The author contributed both to the operation of L1Calo at CERN and to the L1Calo algorithm calibration and testing. Some of this work is documented in [19], [20] and [21].

The author was also the lead administrator of the ATLAS Heidelberg high-throughput computing (HTC) cluster. This cluster is used to perform computation and analysis tasks locally and was also key to conducting this measurement in its current form. Major contributions include an upgrade of the computing power by nearly a factor of 20, the introduction of the HTCondor HTC software framework and fully automated installation and configuration.

Furthermore the author contributed to two ATLAS physics analyses. The first analysis is the Monojet search that was published recently [17]. This detector-level search focuses on BSM physics signatures that could be present in events with large missing transverse

energy and jets. The author contributed with the main fake background estimate in the Signal Region and also studied the fake background in one of the control regions of the search. In addition he studied additional background rejection methods and improved the Signal Region selection. A model for long-lived particles was also studied. Some synergies between the work for the Monojet search and the work presented here exists. Especially the techniques discussed in Section 8.1 and Section 8.4.

The second analysis [22] is presented here. The analysis has two complementary approaches. In the first approach only fake backgrounds are subtracted from the data and an unfolding is performed of all processes contributing to a given final state (e.g. all processes contributing to a two electron plus jet final state). In the second approach all backgrounds are estimated and subtracted and the boson plus jet cross sections are measured (e.g. the $Z \to ee$ + jets production cross section is measured). The author contributed to nearly all major parts of the second approach, presented in this thesis, as well as several key elements to the first approach. Main contributions include the development, the testing and the validation of the analysis software framework, especially the bootstrap capability and the capability to efficiently process a large number of data and simulation events for the numerous distributions and systematic uncertainties. Furthermore the author introduced the measurement of the γ + jets process to the analysis and optimised all trigger and selection criteria involved. The author also contributed with the optimisation of many selection criteria to the other boson plus jet final states. In addition the author was responsible for the estimation of the backgrounds due to the limited efficiency and acceptance of the detector as well as the fake background estimates for the $Z \to \nu\nu$ + jets, $W \to e\nu$ + jets and γ + jets final state. The author was also in charge of the unfolding framework, including the implementation using the RooUnfold software package and the required studies and validations. Furthermore the author evaluated and validated the systematic uncertainties on the measurement and was involved in the development and validation of the fitting and limit setting framework. Finally the author served as analysis contact for the analysis within the ATLAS collaboration and as such was responsible for the coordination of the analysis team, but also for the communication and coordination with the ATLAS physics subgroups. The analysis is currently undergoing the final steps of the internal ATLAS review and will be promptly published. A paper draft is currently being written.

2. The Standard Model of Particle Physics and Beyond

The success of the particle physics experiments at the LHC is impossible to imagine without a solid theoretical foundation that motivates measurements and guides searches for BSM physics. The foundation of this theoretical understanding is the SM, which is also tested in this analysis. Therefore a brief introduction to the SM is given in the first sections of this chapter. This introduction is based on [23][24][25][26][27], where more details are given.

The boson plus jet processes that are measured in this analysis, are produced by different production channels in the proton-proton collisions at the LHC. The cross sections with which the different processes are produced depend on the SM interactions of the involved particles. Both the production channels and the production cross sections are discussed in the second section of this chapter.

We know from astrophysical and other observations, that the SM is not complete. An example for potential BSM physics is DM, which accounts for nearly a quarter of the energy content of the universe. Many different experiments have delivered a large amount of evidence for the existence of DM. However, despite large experimental efforts, the nature of DM has not been discovered yet and this is a very active field of research. In the third section of this chapter a brief introduction to DM is given together with an overview of the current efforts to discover its constituents.

2.1. The Standard Model of Particle Physics

The SM is a quantum field theory that is characterised by its invariance under local $U(1)_Y \times SU(2)_L \times SU(3)_C$ gauge transformations. This theory describes all known elementary particles and their interactions. The particle content of the SM is shown in Figure 2.1, together with the particle mass, electrical charge and spin. It is divided into two classes, where particles with half-integer spin are fermions and particles with integer spin are bosons. Bosons with spin 0 are scalar bosons and bosons with spin 1 are vector bosons. Each particle has an anti-particle with opposite electrical charge.

The particles interact via three forces which are mediated by bosons: The electromagnetic force is mediated by the massless photon, the strong force by the massless gluons and the weak force by the massive Z, W^+ and W^- bosons. In addition particles also interact via exchanges of the Higgs boson. The forces have different ranges. The range of the electromagnetic force is not limited, since the photon is massless. The range of the weak force is limited to roughly 10 fm, since the weak bosons are massive. The range of the strong interaction is also limited, even though the gluons are massless. This is due to an aspect of the

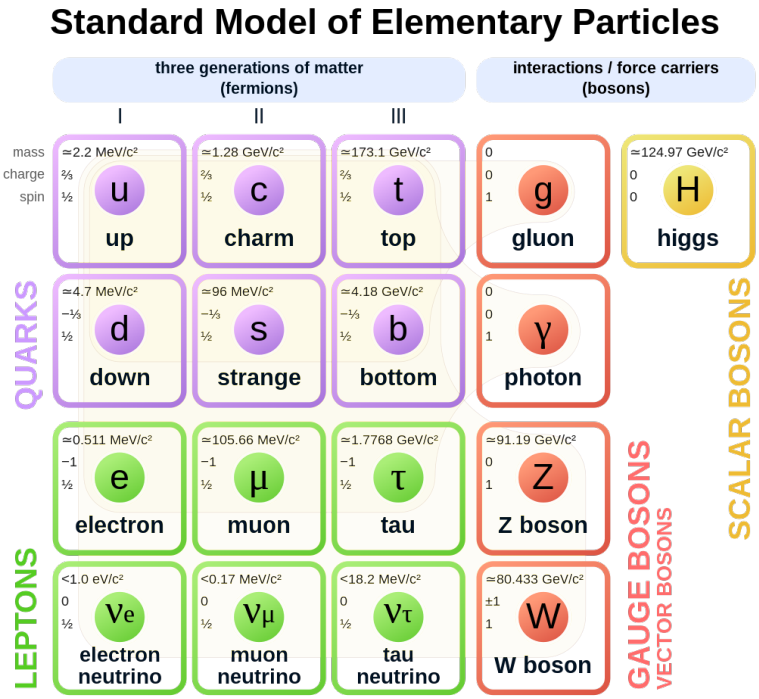

Figure 2.1.: Particle content of the SM, together with mass, electrical charge and spin of each particle. Each quark and lepton has an anti-particle with the same properties, but opposite electrical charge. Adapted from [28].

theory called confinement, which is discussed in more detail below. Gravitational forces are not described by the SM and the unification of the SM with general relativity remains one of the big open questions of theoretical physics. However the strength of gravity is sufficiently weak on the scales of particle physics experiments that it can be neglected.

There are two types of fermions: leptons and quarks. Both interact via the weak interaction and the electromagnetic interaction, if they are electrically charged. Quarks interact also via the strong interaction.

The leptons can be grouped into three families, where the electrically charged leptons electron e, muon μ and tau τ only differ from each other in their masses and lifetimes. A neutral particle, called neutrino ν, is associated to each charged lepton. Neutrinos only interact via the weak interaction. They were long thought to be massless, however the discovery of neutrino oscillations indicates a neutrino mass [29][30].

The six quarks are also grouped into three families, where each family contains one quark with electrical charge $+\frac{2}{3}$ and one with electrical charge $-\frac{1}{3}$ in units of the absolute electron charge. Quarks only appear as bound states in nature. These bound states are referred to as *hadrons*, where systems with a net quark number of three are called *baryons* and those with a net quark number of two are called *mesons*.

The SM is described in the Lagrangian formalism as a quantum field theory that is completely characterized by a Lorentz-invariant Lagrangian density $\mathscr{L}$. The action S used in the

calculation of physical observables, e.g. using the path integral formalism, is then given by

$$S = \int \mathscr{L} dt d^3x. \tag{2.1}$$

The calculation of these physical observables is very involved in the general case and perturbative expansions in the coupling constants are typically used in analytic calculations. Single terms in this expansion can be depicted as so-called Feynman diagrams - some examples are shown below.

The construction of the SM is deeply linked to symmetries. The requirement that the Lagrangian density is invariant under a local $U(1)_Y \times SU(2)_L \times SU(3)_C$ gauge transformations leads to the introduction of a gauge field for each generator of the group. These gauge fields are identified with the bosons mediating the fundamental forces after the spontaneous electroweak symmetry breaking discussed in the next section.

Starting from the gauge symmetries, key elements of the electroweak and the strong sector of the theory are discussed in the following and aspects important to this measurement are highlighted.

2.1.1. The Weinberg-Salam Electroweak Theory

The electroweak sector of the SM is constructed by building a Lagrangian density that is invariant under a local $U(1)_Y \times SU(2)_L$ gauge transformation. The quantum numbers associated to these symmetries are the weak hypercharge Y for $U(1)_Y$ and the weak isospin I for $SU(2)_L$. Only particles that carry these quantum numbers take part in the corresponding interactions. While all known fermions carry the weak hypercharge, only left-handed[1] fermions have a weak isospin different from zero. This means that the $SU(2)_L$ symmetry only acts on left-handed (L) fermions. Therefore the left-handed fermions are arranged in $SU(2)$ doublets according to the families in the Lagrangian density and the right-handed fermions enter as singlets.

Four gauge bosons are introduced to ensure gauge invariance, one for each generator of the symmetry. Since $SU(2)_L$ is a non-Abelian group, its generators are non-commuting. This leads to self-interaction terms between the gauge fields in the Lagrangian density.

In addition the Higgs doublet, with two complex scalar fields, is part of the Lagrangian density to allow for the mass generation of the massive gauge bosons. This happens in a process called spontaneous symmetry breaking, where the Higgs acquires a non-zero vacuum expectation value in its potential. This breaks the $SU(2)_L$ symmetry locally. During the symmetry breaking three massless Goldstone bosons appear, which are absorbed by the $SU(2)_L$ gauge bosons. These gauge bosons gain mass in this process and can be identified with the three experimentally confirmed bosons that mediate the weak interaction: The Z, the W^+ and the W^- boson.

There is a $U(1)_Q$ symmetry that is left after the electroweak symmetry breaking $U(1)_Y \times SU(2)_L \rightarrow U(1)_Q$. The massless gauge boson corresponding to this symmetry is then identified with the photon. The fourth degree of freedom of the Higgs doublet corresponds to

[1] Left-handed means that the fields have a negative chirality [26].

a single scalar field, describing a boson with spin 0, which corresponds to the Higgs boson discovered by the ATLAS and CMS experiments at the LHC [31][32].

In this way the electroweak theory unifies the electromagnetic and the weak interaction at energies above the electroweak symmetry breaking scale.

The terms in the Lagrangian density describing the electrons, muons and taus and their neutrinos are identical, apart from their coupling to the Higgs. This means, that especially the coupling to the massive gauge bosons is independent of the lepton flavour. This feature is referred to as *lepton universality*. Furthermore each of these Lagrangian densities is invariant under a global $U(1)$ symmetry. Following Noether's theorem, this leads to lepton number conservation for each lepton flavour. Finally both the charged leptons and the quarks acquire mass by interacting with the Higgs doublet field, where the fermion mass is proportional to the Yukawa coupling of the fermion to the Higgs field.

2.1.2. The Theory of the Strong Interaction

The construction of the strong sector of the SM proceeds in a similar way to the electroweak theory. It is based on a Lagrangian density that is invariant under a local $SU(3)_C$ symmetry. The associated quantum number is called *colour* and the theory of the strong interaction is also called Quantum Chromodynamics (QCD). Only quarks and gluons carry the colour charge. Therefore for each quark type a colour triplet is introduced in the Lagrangian density which contains three spinors each representing a different colour state of the quark type. All other fermions do not interact via the strong interaction and are represented by colour singlets.

A gauge field is introduced for each of the eight generators of $SU(3)$ to enable conservation of the local gauge symmetry. These gauge field are identified with the gluons and since the Higgs is colourless it does not couple to the gluons and they remain massless. However as $SU(3)$ is also a non-Abelian group the gluons are self-interacting.

An important difference between the electroweak theory and QCD is *asymptotic freedom*, which signifies that at large momentum transfer or short distances quarks and gluons can be regarded as quasi-free particles, whereas at low energies they are only found in bound states. To understand asymptotic freedom one has to consider the *running* of the strong coupling constant α_S. This is explained in the following.

Vacuum polarization effects lead to Feynman diagrams, where quark and gluon pairs are spontaneously created from the vacuum. The contributions from these diagrams lead to infinities during the cross section calculation. These infinities can be removed in a process called *renormalisation*, which is also used in the electroweak part of the theory and was one of the pre-requisites to make the SM possible. In the renormalisation process the infinities are removed by absorbing them into a parameter of the theory and adding infinite counter-terms, such that both infinities cancel. In QCD this parameter is the strong coupling constant α_S.

The resulting α_s is shown in Equation 2.2 for a momentum transfer q^2

$$\alpha_S\left(q^2\right) = \frac{\alpha_S\left(\mu_R^2\right)}{1 - 4\pi\alpha_S\left(\mu_R^2\right)\left(\Pi\left(q^2\right) - \Pi\left(\mu_R^2\right)\right)}, \tag{2.2}$$

where $\Pi\left(q^2\right)$ is the infinite term due to the loop corrections and $\Pi\left(\mu_R^2\right)$ is the infinite counterterm at a chosen scale μ_R. This scale is called the renormalisation scale. The difference between the two infinite terms is finite and leads to a finite coupling constant that can be expressed as

$$\alpha_S\left(q^2\right) \approx \frac{\alpha_S\left(\mu^2\right)}{1 + B\alpha_S\left(\mu^2\right)\ln\left(\frac{q^2}{\mu^2}\right)}. \tag{2.3}$$

Here B is a positive constant that depends on the number of colours and quark types in the theory. While the α_S given by Equation 2.3 is finite for a given q^2, it has acquired a q^2-dependence. This especially means that the coupling strength decreases with increasing momentum transfer, leading to the asymptotically free behaviour of quarks and gluons. Perturbative calculations are only possible if the coupling is small, i.e. at high momentum transfers and for large couplings, perturbation theory breaks down. However this regime can be studied numerically in the field of lattice QCD.

Divergences in the cross section calculation also occur due to soft or collinear emissions of gluons. These divergences are called infrared divergences since they involve integrations to very low momenta. They are removed from the cross section calculation in a manner similar to renormalisation. Also in this procedure a scale is introduced, which is called the *factorisation* scale μ_F.

Another important property of QCD is that quarks and gluons are always observed in bound colourless states. This is a non-perturbative feature of the theory, called *confinement* that is analytically not accessible but that has been supported by lattice QCD calculations. To illustrate confinement one can imagine two quarks being pulled apart, with a colour field of gluons between them. As the quarks are separated a very large amount of energy is stored in the field until it is possible to generate a new quark-antiquark pair that forms bound states with the original quarks.

Due to colour confinement quarks or gluons produced at particle colliders do not propagate freely and can only be observed as a jet of colourless particles. In this process additional partons are produced until they have a sufficiently low energy to form bound states. This is called *hadronisation*.

2.1.3. Proton-proton Interactions

The LHC is colliding protons, which consist of two up and one down quark. However, the internal dynamics are more complicated due to QCD effects. The three so-called *valence* quarks (uud) are bound by gluons, leading to a continuous exchange of momentum. Furthermore the gluons are subject to vacuum fluctuations that spontaneously create and destroy quark-antiquark pairs. These spontaneously created quarks are called sea quarks. The entirety of these objects inside the proton is referred to as partons.

When two protons collide it is actually one (or more) parton in each proton that participates in the interaction. This parton will only carry a fraction x of the total proton momentum. The momentum distribution for a given parton type is given by the parton distribution function (PDF) $f_i\left(x\right)$ [33]. These are obtained using measurements at a given factorisation

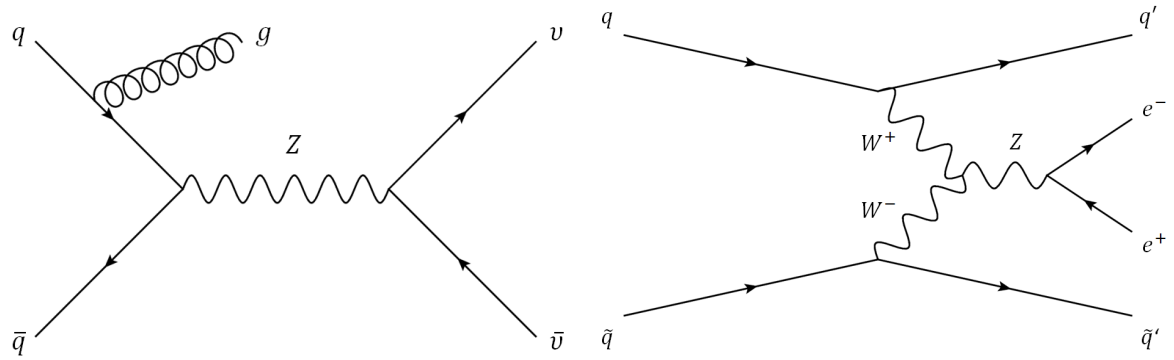

Figure 2.2.: Feynman diagrams depicting the production of a Z boson decaying to neutrinos in the monojet topology (left panel) and the production of a Z boson decaying to an electron-positron pair in the VBF topology (right panel).

scale μ_F, since they are not currently accessible to calculation from first principle. The measured PDF is then evolved to a different momentum scale using the Dokshitzer–Gribov–Lipatov–Altarelli–Parisi (DGLAP) evolution equations.

The hadronic production cross section [24] for a collision process at the LHC is given by

$$\sigma_{tot}\left(\mu_F, \mu_R\right) = \int_0^1 dx_1 \int_0^1 dx_2 \sum_{ij} f_i\left(x_1, \mu_F\right) f_j\left(x_2, \mu_F\right) \hat{\sigma}_{ij}\left(x_1 x_2 s, \alpha_S\left(q^2, \mu_R^2\right), \mu_F, \mu_R\right), \tag{2.4}$$

where i,j are the incoming partons with momentum fractions $x_{i,j}$, μ_R and μ_F are the renormalisation and factorisation scales, s is the squared center-of-mass energy and $\hat{\sigma}_{ij}$ is the partonic interaction cross section.

2.2. Boson plus Jet Production in Proton-proton Collisions

The electroweak gauge bosons can be produced at the LHC- also in association with jets. The production mechanism typically involves the presence of quarks, as these bosons do not couple directly to gluons. The left panel of Figure 2.2 shows one possible production Feynman diagram. A Z boson is produced in a quark-antiquark annihilation and subsequently decays to a neutrino anti-neutrino pair. In addition a gluon is radiated from one of the initial quark lines and forms a jet that recoils against the Z boson. This production channel is commonly called the monojet topology. The radiation of additional jets is also possible, but additional radiation processes are suppressed by additional orders of α_S. Another possible production mechanism is shown in the right panel of Figure 2.2. Here two quarks in the initial state each radiate a vector boson, in this case a W^+ and a W^- boson. These bosons interact and form a new vector boson, in this case a Z boson. This Z boson subsequently decays to an electron-positron pair. This production channel is commonly called the VBF topology. A characteristic of this topology is that no additional hadronic activity is expected in the gap between the two outgoing quarks, since there is no colour connection between them.

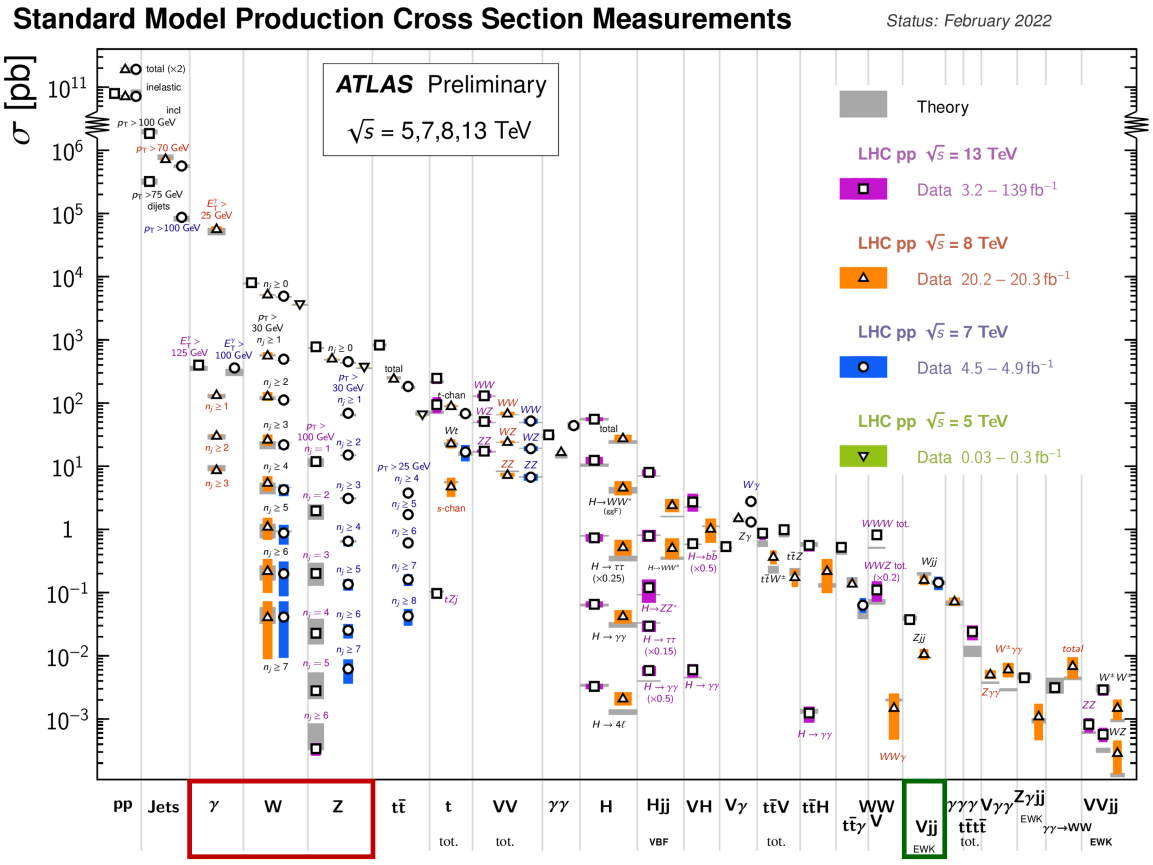

Figure 2.3.: Summary of several Standard Model total and fiducial production cross section measurements. The measurements are corrected for branching fractions, compared to the corresponding theoretical expectations. In some cases, the fiducial selection is different between measurements in the same final state for different centre-of-mass energies √s, resulting in lower cross section values at higher √s. [34].

The boson plus jet processes have different production cross sections. Figure 2.3 shows an overview of different total and fiducial production cross sections measured with the ATLAS detector. The columns that show the production cross section for photons, W and Z bosons are highlighted with a red box. Each column shows the inclusive cross section without any additional jet radiation and the production cross sections, if at least n_j jets are radiated in addition to the produced boson. Due to the additional couplings of α_S that enter for each additional jet, the cross sections decrease for higher n_j. It is also shown that the inclusive cross section is largest for the photon and decreases for the W and Z bosons. Reasons for this include the different coupling strengths of the bosons to the quarks, the different diagrams contributing to their production, as well as the proton PDF.

The cross sections for the VBF production of W and Z bosons are highlighted with a green box in Figure 2.3. The cross section for this production channel is more supressed than for

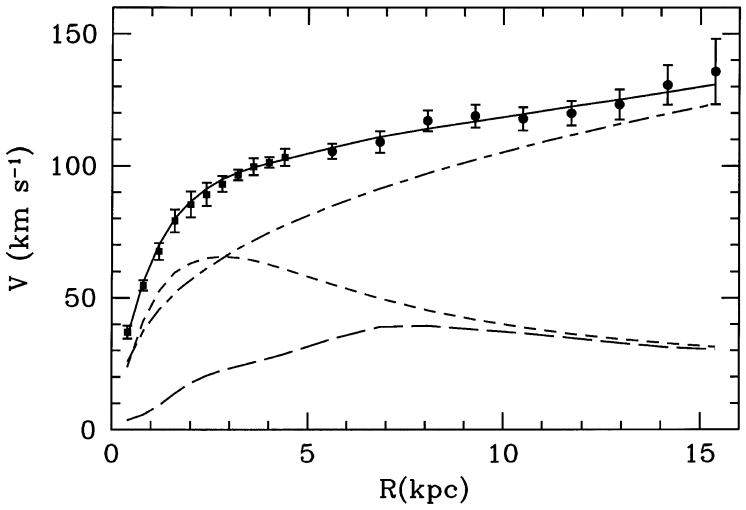

Figure 2.4.: Measured rotational velocity curve of M33 (points) together with a fitted model (continuous line). The templates contributions to the fit are the DM halo contribution (dot-dashed line), the stellar disc (short-dashed line) and the gas contribution (long-dashed line). Adapted from [40].

the monojet topology, among other reasons due to higher orders in the electroweak coupling strength in the production Feynman diagrams.

2.3. Beyond the Standard Model - Dark Matter

The existence of DM is supported by numerous astrophysical observations of different phenomena. These include the rotational velocity curves of stars in galaxies [35][36], the precise measurement of the cosmic microwave background (CMB), weak and strong gravitational lensing [37][38] and the structure formation in the universe [39]. The observations of the rotational velocity curves and the CMB are discussed in more detail in the following.

The distribution of luminous matter in a galaxy can be measured using astronomical observations. For spiral galaxies it is found to be located mostly at the centre of the galaxy. Assuming only the gravitational field of the luminous matter, the radial velocity v of a star at radius r is given by

$$v = \frac{G \cdot M(r)}{\sqrt{r}}, \tag{2.5}$$

where G is the gravitational constant and $M(r)$ is the total mass within a sphere of radius r around the galactic centre. Hence the radial velocity of stars outside the central mass concentration should decrease with r roughly by $\frac{1}{\sqrt{r}}$.

Observations of spiral galaxies however show very different radial velocity distributions. An example is shown in Figure 2.4 for the galaxy M33. Here the measured rotational velocity does not decrease, but increases with r. So from gravitational principles one can infer that

a large amount of additional non-luminous mass must be contained within the galaxy. This non-luminous mass is identified with the DM and its contributions to the rotational velocity curve are shown as the dotted-dashed line. The contributions both from the visible matter in the stellar disc (short dashed line) and from the gas disc (long-dashed line) are also shown. This demonstrates that the galaxy contains a much larger amount of DM than luminous matter.

More evidence for the existence of DM is found in the cosmic microwave background (CMB), a radiation field that dates back to the early universe and the point in time when radiation and matter decoupled. The CMB is almost perfectly isotropic, however small anisotropies have been measured by the COBE [41], WMAP [42] and Planck [43] satellites. The power spectrum of these anisotropies shows a characteristic pattern that can be used to extract and calculate the matter, dark matter and dark energy contributions to the total energy density of the universe [27][44]. The measurements of the CMB are in very good agreement with the Standard Model of Cosmology, the so-called ΛCDM model [44]. This model predicts non-relativistic cold DM (CDM).

A common assumption is that DM has a particle nature. No particle in the SM fulfils all requirements for this hypothetical DM particle. However many BSM physics theories contain particles that can serve as DM candidates. These are often weakly interacting massive particles (WIMPS), which are cold and reproduce the correct DM relic density observed in the universe today [27]. Other well motivated DM candidates exist, especially the axion [45] and axion-like particles [46] and also sterile neutrinos [47], however they are not further discussed in the following.

There are a large number of experiments that aim to detect these hypothetical DM particles. An overview is given in the next section.

2.3.1. Searches for Dark Matter

Searches for DM can be grouped into three categories: Direct detection, indirect detection and production experiments.

Direct detection experiments typically aim to directly measure the recoil of a DM particle from the local DM halo against a nucleus in the detector medium [27]. Experiments that follow the direction detection approach are for example XENONnT [48] and CRESST [49].

Indirect detection experiments search for the annihilation of DM to SM particles, which could occur in astrophysical sources where DM is accumulated. Experiments that pursue the indirect detection approach include the ground-based H.E.S.S telescope [50] and the space-based Fermi-LAT telescope [51].

Finally DM might also be produced at colliders such at the LHC. A typical approach to search for this production are so-called Mono-X topologies. In these topologies the DM is produced in association with a SM particle. The SM particle recoils against the invisible DM and is used to tag the event. In the measurement presented in this thesis, the recoil particles are jets and DM candidates would be visible in the cross section measurement of the $Z \rightarrow \nu\nu$ + jets final state. Other recoil particles that are commonly measured are photons [**Sirunyan_2017**], W/Z [52] and Higgs [53] bosons. Another possibility to search for DM at the LHC are dijet events where the mediator particle that couples the DM to

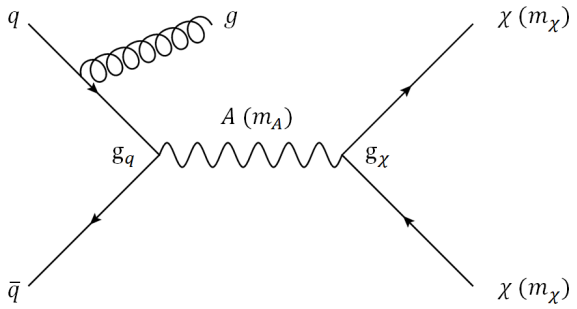

Figure 2.5.: Feynman diagram depicting the production of an axial-vector mediator A with mass m_A decaying to DM particles χ with mass m_χ.

the SM particles is resonantly produced and visible the invariant mass spectrum of the two jets [54][55].

DM searches at colliders usually rely on BSM physics models to interpret the measured data in absence of a discovery. During Run 1 of the LHC effective field theories (EFT) were used for this purpose. These assume a contact interaction between the SM and the DM particles and allow to set limits on the energy scale by which higher dimensional operators are suppressed [56]. However at the higher centre-of-mass energy during Run 2, EFTs suffer from validity problems [57]. For this reason DM searches in Run 2 are typically interpreted in terms of simplified DM models, which are discussed in the following section.

2.3.2. Simplified Dark Matter Models

Simplified DM models provide an extension of the EFTs by resolving the contact interaction into a mediator particle [57]. This mediator particle couples the DM to the SM particles. Typically simplified models are characterised by a few parameter as opposed to complete DM models (e.g. Minimal supersymmetric SM). These complete DM models usually come with a large number of parameters and a rich phenomenology, but are difficult to test with the limited statistical precision currently available. Therefore the simplified model offers a good compromise between the contact interaction of the EFT and the full DM model [56].

In this analysis a simplified DM model is used to interpret the measured cross sections. The model assumes a spin-1 mediator with axial-vector coupling. This model is chosen as an example. Other models involving other coupling types and spin-0/-1/-2 mediators also exist [57].

The right panel of Figure 2.5 shows a Feynman diagram of the axial-vector mediator model. It is characterised by an axial-vector mediator A with mass m_A and DM particles χ with mass m_χ. The DM particles are assumed to be Dirac fermions. The coupling strengths of A to quarks and the DM particles are respectively given by g_q and g_χ, where g_q is assumed to be universal for all quarks. The mediator A is assumed not to couple to leptons [57].

3. The ATLAS Detector at the Large Hadron Collider

Many interesting SM and potential BSM physics processes have very small production cross sections. This means that in order to measure or discover these processes at a particle accelerator, a very large number of collision events must be produced. To be able to produce particles of higher masses, it is also necessary that sufficient energy is present in the centre-of-mass system of the colliding particles. The LHC is the largest and most powerful particle accelerator currently in operation and has achieved records in both areas. How this is achieved is discussed in the first part of this chapter.

In order to analyse the LHC collision data and measure rare processes, it is necessary to identify the final state particles of the collisions and measure their properties with high precision. This is a challenging task in the high rate environment of the LHC, which is dominated by QCD jet production (see Figure 2.3). The ATLAS [58] detector is a general purpose particle detector designed to meet this challenge. It is used to record the physics data analysed in this measurement and is discussed in the second part of this chapter.

3.1. The Large Hadron Collider

The LHC is a circular particle accelerator with a length of 26.7 km, located between 45 m and 170 m below the surface at the European Organization for Nuclear Research (CERN) near Geneva, Switzerland [59]. It mainly accelerates and collides bunches of protons in two beams circulating in opposite direction. The LHC also has a heavy ion collision program with lead-lead, xenon-xenon and proton-lead collisions [60]. The accelerator has been operated at a centre-of-mass energy of $\sqrt{s} = 13$ TeV for the proton-proton collisions from 2015 to 2018 and has exceeded its design luminosity of $\mathscr{L} = 1.0 \times 10^{34}\,\mathrm{cm}^{-2}\mathrm{s}^{-1}$ [59].

The instantaneous luminosity $\mathscr{L}$ determines the event production rates at an accelerator and is connected to the number of collision events N produced in a process with cross section σ that are expected to occur in time T via

$$N = \sigma \int_T \mathscr{L}(t)\, dt. \tag{3.1}$$

$\mathscr{L}$ depends on the particle beams in the accelerator and is proportional to the collision frequency and the number of protons available in each bunch and inversely proportional to the horizontal and vertical beam size. This means smaller beams with a higher number of protons will result in more collisions [26].

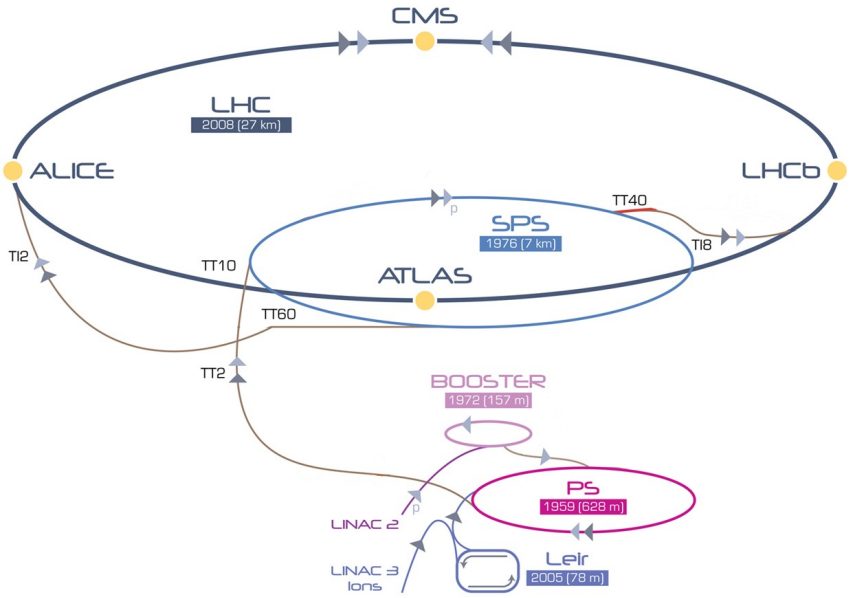

Figure 3.1.: The CERN accelerator complex: The LHC injector chain, the LHC and the main experiments ATLAS, ALICE, CMS and LHCb. Adapted from [61].

The protons that circulate in the LHC are pre-accelerated by various machines. An overview of the CERN accelerator complex is given in Figure 3.1. Protons are first accelerated in a linear accelerator (Linac 2, 50 MeV[1]) and then pass through a chain of circular accelerators to further increase their energy and form the LHC beam structure: the Proton Synchrotron Booster (acceleration to 1.4 GeV), the Proton Synchrotron (acceleration to 25 GeV) and the Super Proton Synchrotron (acceleration to 450 GeV) [59]. The final acceleration up to 6.5 TeV[2] takes place in the LHC.

The two proton beams are structured in up to 2808 bunches[3], each containing around 1×10^{11} protons, with a bunch spacing of 25 ns [59][65]. The collisions for the experiments are produced by crossing the beams at four interactions points (IPs) around the ring, with a so-called bunch crossing typically happening every 25 ns, resulting in a collision frequency of 40 MHz.

The four main experiments are situated at the four IPs. These are the two general purpose detectors ATLAS and CMS [66], the LHCb detector, which is designed to study rare decays of beauty and charm quarks [67] and the ALICE detector which is primarily used to study heavy ion collisions [68]. The ATLAS detector is discussed in the following section.

[1]The Linac 2 was replaced by the Linac 4 in 2020 [62].
[2]The beam energy has been increased to 6.8 TeV in run 3 of the LHC [63].
[3]The maximum number of colliding bunches reached so far is 2544 [64].

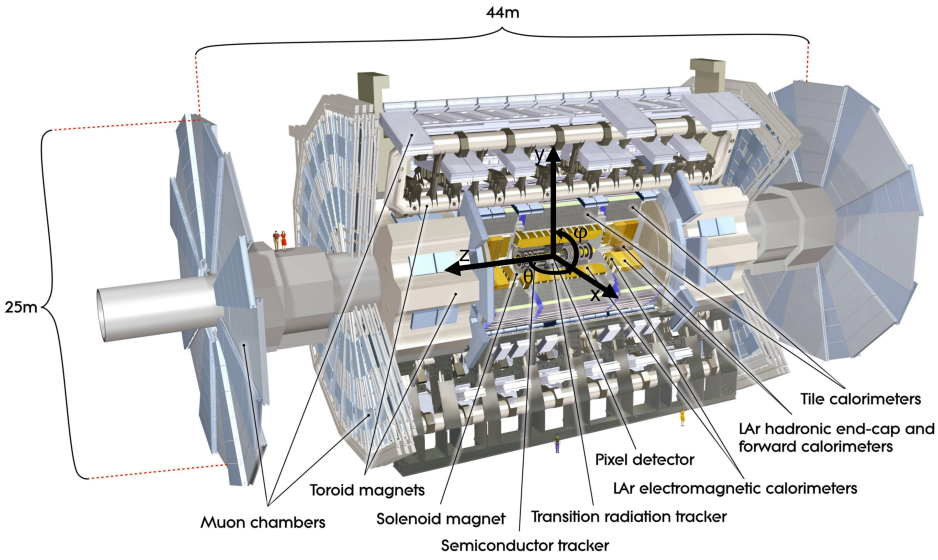

Figure 3.2.: Schematic layout of the ATLAS detector, including the ATLAS coordinate system. The x-axis points towards the center of the LHC, the y-axis points up and the z-axis points along the beamline. Adapted from [58].

3.2. The ATLAS Detector

The ATLAS detector is a highly granular general purpose particle detector. An overview is given in Figure 3.2. ATLAS consists of the inner-detector (ID), which provides tracking information, an electromagnetic and a hadronic sampling calorimeter, which measure particle energy and a dedicated muon spectrometer (MS). The ATLAS magnet system comprises a superconducting central solenoid with a 2 T magnetic field around the ID and an air-core toroid system with a 1 T magnetic field for the MS, to allow for precise momentum measurements of charged particles. A highly efficient trigger system, using custom designed hardware and a large computing cluster, is used to select physics collisions of interest from the very large amount of collision data produced at the LHC every second. A dedicated detector for luminosity measurements is situated in the forward region of the detector [64][58].

In the first part of this section the ATLAS coordinate system is introduced and in the second part a brief overview of the detector components and the trigger system is given, with more general details in [58] and specific details in the references given below. In the third part, the dataset recorded with the ATLAS detector that is analysed in this measurement is discussed.

3.2.1. Coordinate System and Important Variables

The ATLAS coordinate system is shown in Figure 3.2. It is centred on the nominal IP, with the z-axis pointing along the beam direction and the $x-y$ plane orthogonal to the beam direction. The x-axis is pointing towards the centre of the LHC, while the y-axis points upwards. The polar angle θ is measured from the z-axis and the azimuthal angle ϕ is measured around the z-axis [58].

The direction of a collision product in the detector is expressed by the azimuthal angle ϕ and the rapidity y, that is defined as $y = 1/\ln\left[(E + p_z)/(E - p_z)\right]$. The rapidity has the advantage over the polar angle θ that its differences are invariant with respect to Lorentz boosts along the beam axis. This is useful, since the final state particles are typically boosted along the beam axis, as the momentum fraction x is usually not identical for both colliding partons. For final state particles with negligible mass the pseudo-rapidity $\eta = -\ln\tan(\theta/2)$ is used. Distances between physics objects are typically measured in the $\eta - \phi$ plane as $\Delta R = \sqrt{\eta^2 + \phi^2}$ [58].

The final state particles experience no boost in the direction transverse to the beam, since the initial state partons only have momentum in the beam direction. Therefore the net sum of the momenta of all final state particles in the transverse plange $(x - y)$ is zero. This feature makes quantities defined in the transverse plane useful and a subscript T is used to indicate that a quantity is defined in the transverse plane. Examples are the transverse momentum p_T or the transverse energy E_T.

3.2.2. The Inner Detector

The ATLAS inner detector (ID) is the central part of the ATLAS tracking system. It is used to measure the ionisation energy deposits of charged particles passing through the detector material [26]. These energy deposits, or hits, form the basis of the track reconstruction. The track reconstruction is important in the particle identification to distinguish charged and uncharged particles. In addition the particle tracks are used to measure the particle momentum and charge, from the curvature of the particle track due to the Lorentz force which is exerted by the magnetic field of the central solenoid.

The ID consists of the Pixel Detector, the SemiConductor tracker (SCT), the Transition Radiation Tracker (TRT) and the central solenoid [69]. An overview of the inner detector is given in Figure 3.2. The Pixel Detector and the SCT cover the region $|\eta| < 2.5$ and are built of four layers of silicon pixel sensors and four layers of silicon microstrip sensors arranged in stereo pairs. The layers themselves are arranged in barrels around the beamline and the IP, which are closed by endcaps consisting of disks containing the sensors on both sides[4] . The pixels (sensor size: $50\,\mu m^2 \times 400\,\mu m^2$) provide the high space point resolution necessary to cope with the challenging track density close to the IP. Situated at larger radii and covering $|\eta| < 2.5$, the TRT is built of layers of proportional drift tubes. It typically provides most hits to the tracks and is part of the particle identification of electrons using transition radiation [69][58].

The ID is designed to provide a transverse momentum resolution [71] of

$$\frac{\sigma_{p_T}}{p_T} = 0.05\,\% p_T \mathrm{GeV} \oplus 1\,\%. \tag{3.2}$$

The relative resolution gets worse towards higher p_T as the curvature of the particle tracks in the magnetic field becomes more difficult to measure [72].

[4]The fourth and innermost layer of the Pixel Detector, the insertable B-layer, was installed in 2014 and has no additional endcap disks [70].

3.2.3. Calorimetry

The energy of both hadronic and electromagnetic particles is determined in calorimeters. These measure the energy that is deposited in the calorimeter material by the particle showers, which are produced when the incident particles interact with the material. The ATLAS calorimeters provide precise energy and position measurement of electromagnetic objects and hadronic jets. The calorimeters are segmented, which allows to measure the shape of the particle showers, especially for electromagnetic showers. The measured shower shapes are then used in the particle identification, e.g. to distinguish hadronic (wide) from electromagnetic (narrow) showers. ATLAS uses sampling calorimeters, which interleave passive high-Z absorber material to induce shower development and active material to sample the energy deposition of the showers [58]. A schematic layout of the calorimeters is given in Figure 3.2.

The electromagnetic calorimeter (EM calorimeter) surrounds the ID and is optimized to contain and measure the electromagnetic showers produced by electrons and photons, which do not have a high penetration power. It is based on lead absorbers and liquid argon as active material, where the absorber and electrodes are arranged in an accordion geometry for full coverage in ϕ. It consists of several parts that cover $|\eta| < 3.2$ with a minimum of two layers and a high-precision region with three layers for $|\eta| < 2.5$, where the first layer in the high-precision region is very finely segmented in η. The central part is covered by the electromagnetic barrel ($|\eta| < 1.475$) and the outer part is covered by the electromagnetic end caps ($1.375 < |\eta| < 3.2$). It is important to note that there is a transition region between the two calorimeter parts, that contains a comparatively large amount of dead material and is usually excluded from the reconstruction of electromagnetic objects. Additionally, a liquid argon pre-sampler is installed in the central region ($|\eta| < 1.8$). Electromagnetic calorimetry in the forward region ($3.1 < |\eta| < 4.9$) is performed by the forward calorimeter, with copper absorbers and liquid argon as active material [58].

The hadronic calorimeter surrounds the electromagnetic calorimeter and is optimized to contain hadronic showers. While also hadronic particles typically start to shower in the electromagnetic calorimeter, their showers have a high penetration power and are typically only stopped in the hadronic calorimeter. It comprises three sub-detectors, the Tile calorimeter ($|\eta| < 1.7$), which uses steel plates as absorbers and scintillating plastic tiles as active material, the hadronic endcap calorimeter ($1.5 < |\eta| < 3.2$), which uses copper absorbers and liquid argon as active material and the forward calorimeter ($3.1 < |\eta| < 4.9$), which uses tungsten absorbers in the hadronic part and liquid argon as active material [58][73]. The relative energy resolution of calorimeters is typically parametrised as

$$\frac{\sigma_E}{E} = \frac{a}{\sqrt{E}} \oplus \frac{b}{E} \oplus c, \tag{3.3}$$

where the first term is caused by stochastic fluctuations in the shower development, the second term is due to electronic noise and the third term accounts for imperfections in the calorimeter and fluctuations in the leakage losses [58]. The resolution improves towards higher energies E [72].

The ATLAS calorimeters were designed to achieve a relative resolution of $\frac{\sigma_E}{E} \approx \frac{10\,\%}{\sqrt{E}}$ for the EM calorimeter and $\frac{\sigma_E}{E} \approx \frac{50\,\%\text{ to }100\,\%}{\sqrt{E}}$ for the hadronic calorimeter [58].

3.2.4. Muon Spectrometer

The muons produced in the particle collisions are typically minimally ionizing. This means that they can penetrate a large amount of material, especially both calorimeters. Therefore a tracking system dedicated to muons is used in ATLAS. This MS provides detection and high-precision tracking and momentum measurement for muons in the region $|\eta| < 2.7$ [58]. The schematic layout is given in Figure 3.2. Monitored drift tubes ($|\eta| < 2.7$) and cathode strip chambers ($2 < |\eta| < 2.7$) serve as detection chambers mainly used in the track measurement. They are arranged in three layers, with the cathode strip chambers only used in the first layer, for improved rate capability. The magnetic field for the momentum measurement is provided by the superconducting air-core toroid. The MS is also equipped with a trigger system, which relies on resistive plate and thin gap chambers [58].

3.2.5. Trigger System

The ATLAS trigger system is designed to reconcile the very high proton-proton interaction rate of about 1 GHz with the limited event data recording capabilities of 1.2 kHz, by rejecting a factor of 1×10^6 of minimum-bias events, while recording interesting physics events with very high efficiency. This is accomplished by a two level trigger system, consisting of the Level-1 Trigger (L1) and the High-Level Trigger (HLT) [74].

In a first step, the L1 system uses custom built hardware that processes reduced detector information from the calorimeters and the MS to achieve a rate reduction to 100 kHz. The decision for each collision event has to be taken within a latency of 2.5 µs. In a second step, the HLT, a very large cluster of commercial computers, uses the full detector information and sophisticated particle reconstruction and identification algorithms, similar to those used in the offline data analysis, to make a final decision on the events seeded by the L1 system in up to 4 s per event. Events selected by the HLT are written to permanent storage [74]. Event selection and analysis performed on the HLT level is referred to as *online* in the following and that performed on the permanently recorded data is referred to as *offline*.

The trigger system is configured with so-called *trigger items*. These specify the requirements that an event has to fulfil in order to pass the trigger selection. These requirements can include among other criteria the particle type, the minimum energy or transverse momentum of the particle and also more sophisticated particle identification criteria. Several hundred trigger items exist that are usually tailored for the need of physics analyses.

Trigger Prescale

The p_T spectrum of the final state particles typically rises exponentially towards lower p_T. Interesting physics collisions on the other hand usually contain high-p_T particles. Therefore a common strategy to keep the trigger rates within a level acceptable for permanent storage

is to only record all events above a certain p_{T} or energy threshold for a given physics object and given particle identification criteria [74].

However physics analyses often require information about events with lower p_{T} objects, for example to perform background estimates. This is accomplished by using trigger prescales. This means that events triggered by trigger items below the minimum p_{T} threshold are still recorded, but with a lower rate. If a trigger item is configured with a prescale of X events triggered by this item are randomly chosen for permanent storage with a probability of $P = \frac{1}{X}$ [74].

3.3. Data used in the Measurement

The data analysed in this measurement encompasses the full Run 2 dataset recorded with the ATLAS detector from 2015 to 2018. In total an integrated luminosity of $153\,\mathrm{fb}^{-1}$ was delivered by the LHC, of which $147\,\mathrm{fb}^{-1}$ were recorded by the ATLAS detector[75]. Not the full delivered luminosity is recorded due to data acquisition inefficiencies, and operation related inefficiencies (e.g. start of detector components after the LHC beams are stable). $139\,\mathrm{fb}^{-1}$ pass the basic quality criteria for data analysis , e.g. full detector readiness and good object quality, and form the full Run 2 dataset[75].

During the collision of the proton bunches in the LHC typically several protons collide per bunch crossing. This effect is referred to as pile-up and leads to challenges for physics analyses, since typically only the collision products from the hard scattering process are of interest. Final state particles from other proton-proton collisions in the same bunch crossing need to be removed or their effects need to be accounted for. The pile-up conditions vary depending on the LHC beam conditions. The average pile-up has evolved from 13.4 in 2015 to 36.1 in 2018[75]. The differences in the pile-up conditions between the different years need to be taken into account when performing the measurement and often require separate treatment of data recorded in different years, especially in many of the background estimation methods.

The vertex belonging to the hard scattering process is defined as the primary vertex (PV). Collision vertices are determined using tracks from the ID with an energy above 400 MeV and a vertex-finding algorithm [76][77]. The PV is then defined as the vertex with highest associated $\sum p_{\mathrm{T}}^2$.

4. Measurement Strategy

The goal of this analysis is a precise measurement of the vector boson plus jet production cross sections. This poses several challenges, which motivate the strategy of the measurement and are discussed in the following.

The first challenge is related to *background processes* that produce collision events, which are indistinguishable from the boson plus jet final states. The contributions from these processes need to be estimated and subtracted from the measured data.

The second challenge is related to the *systematic uncertainties* on the measurement. These affect the measurement in two ways. Firstly, the systematic uncertainties on the subtracted backgrounds are propagated to the measured cross sections. Therefore it is necessary to reduce their impact on the background estimates. Secondly, the systematic uncertainties also affect the boson plus jet signal processes. These uncertainties can be constrained by combining information from several boson plus jet measurements, since many systematic uncertainties are correlated between the different processes. To properly leverage this correlation, it is necessary to measure the boson plus jet production cross sections in a coherent way.

The third challenge are *detector effects* on the measured data. These effects, like limited resolution and efficiency, distort the measured spectra. Therefore the detector effects are removed from the data to obtain the cross sections.

The strategy to measure the boson plus jet cross sections is designed to meet these challenges. It is outlined in the following, with a graphical overview shown in Figure 4.1.

For each boson plus jet process a separate *measurement region* is defined. For the $Z \to \nu\nu$ + jets process this region is called the *Signal Region* (SR), since it has sensitivity to many models for BSM physics, especially for DM production. The measurement regions for the other boson plus jet processes are called *Auxilliary Measurement* (AM) regions. The AM regions are: $W \to e\nu$ + jets AM region, $W \to \mu\nu$ + jets AM region, $Z \to ee$ + jets AM region, $Z \to \mu\mu$ + jets AM region and γ+jets AM region. The boson plus jet process for which a given region has been defined is called the *SM signal process* of that region. Each of these regions is designed to enhance the contribution from the SM signal process and to reduce the contributions from background processes. The regions are defined in a coherent way to ensure a high degree of correlation between the systematic uncertainties.

One essential ingredient to achieve this coherence is the definition of a common proxy for the transverse momentum (p_{T}) of the boson in each region. In the SR the boson p_{T} can only be determined indirectly by measuring the hadronic recoil against the Z boson, since the neutrinos in the final state are invisible to the detector. Therefore the boson p_{T} in all other regions is also measured via the hadronic recoil of the corresponding boson. The definition of the measurement regions and of the boson p_{T} proxy are discussed in more detail in Chapter 5.

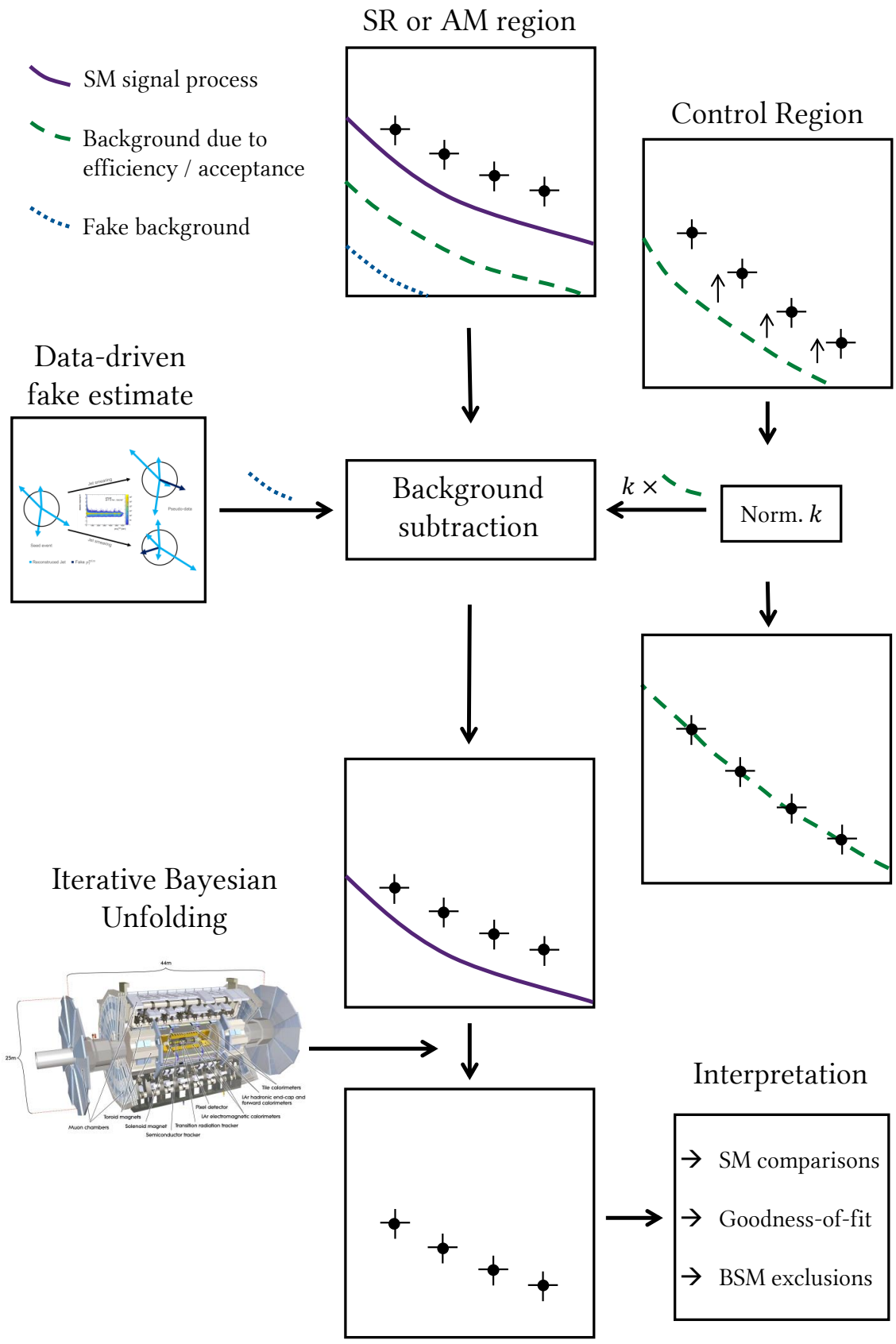

Figure 4.1.: Overview of the measurement strategy.

In each measurement region two phase spaces are defined, which enhance a different production mechanism of the boson plus jet final states. These are the monojet phase space and the VBF phase space. In each phase space several observables are measured: The boson p_{T} is measured in both in monojet and VBF phase space and in the VBF phase space the invariant jet mass of the first two leading jets and the signed azimuthal angle between the first two leading jets is measured in addition.

The next step in the measurement is the estimation of the background contributions to the different regions. The backgrounds can be grouped into two categories. The first category are backgrounds due to mis-identified objects, also called fake objects (e.g a hadronic jet in a dijet event is reconstructed as a photon and the event enters the γ+jets AM region). The background contributions due to these fake objects are estimated using dedicated data-driven techniques.

The second category are backgrounds that enter a given region due to the limited efficiency and acceptance of the detector (e.g. a $W \to e\nu$ + jets event is selected in the SR, because the electron is missed by the detector). The dominant backgrounds of this category are estimated using shape templates derived from MC simulation that are normalized to data in dedicated control regions (CRs). For each dominant background process a separate CR is introduced. Minor backgrounds of this category are estimated purely from MC simulation.

The final in step in the measurement is to correct the background-subtracted data for detector-effects. This is achieved with an iterative Bayesian unfolding technique. The resulting cross sections are used in the interpretation of the measurement.

The measured cross sections are interpreted in different ways. Firstly they are used to validate the theory predictions made with the Sherpa MC generator. Secondly they are used in a goodness-of-fit test to investigate the compatibility of the measurement with the SM. And finally it is demonstrated that the cross sections can be used to constrain models for BSM physics.

The measurement is performed with a *blinding* strategy in the SR. This means that all steps described above are developed and tested only on a subset of the entire collision data that is analysed in the end. This helps to avoid biasing the measurement. The blinded dataset used in the SR is limited to approximately 25 % of the entire data. Once all parts of the measurement were fixed, tested and validated, the full dataset was *unblinded* and the final results produced with the full dataset. All figures shown in the following contain the unblinded data.

The measurement contains many different regions and phase spaces which are not all statistically independent. To track correlations and to properly account for them the bootstrap method is used. It is based on replicas of the measurement, which are created by introducing correlated Poisson fluctuations for each event that is filled in any histogram [78]. These replica can then be used at any given point in the measurement to calculate statistical uncertainties or correlations. An introduction to the bootstrap technique is given in Appendix G. 10 000 bootstrap replica are used in the measurement, unless stated otherwise. This represents the computational limit and allows for a precise accounting of the statistical uncertainties.

5. Reconstruction of Physics Objects and Selection of Events

To measure the boson plus jet cross sections, collision events that belong to the SR or one of the AM regions must be identified. To achieve this it is necessary to first associate the signals measured by the detector, like the energy depositions in the calorimeters or the hits in the ID, to the final state particles produced in the hard scattering process of each event. This procedure is called particle *reconstruction* and the results are a set of particle candidates in each event. For example an energy deposition in the electromagnetic calorimeter that has an associated track formed from hits in the ID could be an electron candidate, whereas the same energy deposition without an associated track could be a photon candidate.

In the next step, a subset of particles is selected from the candidate particles using more sophisticated methods like the analysis of the shower shapes. This is necessary since not all particle candidates correspond to the respective particle in the final state of the hard scattering process. For example an electron candidate can also be formed from a hadronic shower that is narrow and stopped early in the calorimeter. The particle reconstruction and selection is discussed in the first section of this chapter.

The final step of the selection process is the classification of the collision events in the SR or one of the AM regions, according to the selected particles in each event. In addition, specific trigger criteria need to be fulfilled for each region. The selection of the collision events is discussed in the second section of this chapter.

In addition to the selection of events on the detector level it is also necessary to select particles and events on the particle level of the simulation. This selection is used in the unfolding procedure as the fiducial phase-space of the measurement and is discussed in the third part of this chapter. More information on the simulation is given in the next chapter.

5.1. Reconstruction and Selection of Particles and Event-level Quantities

For each of type of particle (electron, muon, tau, photon and jet) different reconstruction algorithms and selection criteria are used depending on the properties of the particle type and its interaction with the detector material. Therefore the reconstruction and selection is discussed separately for each particle type in the following. Please note that anti-particles are reconstructed in the same way as particles and are not separately discussed.

There are two different selection classes for most particle types: the *baseline* selection and the *signal* selection. Baseline objects are characterized by permissive selection criteria and

are for example used to construct background-enriched regions for the fake object estimates. Signal objects have to fulfil strict selection criteria in order to improve background rejection and increase the signal purity of a given region.

The signal selection for electrons is not the same between the $W \to e\nu$ + jets AM and $Z \to ee$ + jets AM region. The reason is that contribution from background processes is expected to be larger in the $W \to e\nu$ + jets AM regions, requiring a stricter selection. In the $Z \to ee$ + jets AM region the background contributions is much smaller, due to the very clean Z boson selection.

The definition of the selection criteria for different objects is not mutually exclusive. Therefore it is possible that a single energy deposition in the calorimeter is reconstructed and as two different objects. A procedure called *overlap removal* is used to remove these duplicated objects from the events.

Finally the selected objects are used to construct event level quantities, especially the *missing transverse momentum* that quantifies the amount of momentum that was carried out of the detector by invisible particles.

The reconstruction, selection and calculation of all these quantities is discussed in the following. Additional details that go beyond the brief overview presented here are given in the references.

5.1.1. Electrons

Electrons are charged and interact with the detector by leaving an ionization track in the identification and depositing the largest part of their energy in the EM calorimeter in the form of an electromagnetic shower. Therefore electron candidates are reconstructed from clusters of energy deposits in the EM calorimeter and charged-particle tracks measured in the ID.

The electromagnetic clusters are built using a topological nearest-neighbour clustering algorithm on EM calorimeter cells. Only cells with a significant energy deposition above the electronic and pile-up noise are included in the formation of these clusters [79].

The charged-particle tracks are built from hits in the ID tracking layers using track fitting based on pattern recognition algorithms that take the curvature of the particle tracks in the magnetic field of the detector into account, as well as energy losses due to Bremsstrahlung [80].

The topo-clusters are matched to high quality tracks that have minimum number of four hits in the silicon tracking detectors. The matched topo-clusters are further processed by a supercluster-building algorithm. This algorithm adds near topo-clusters together if one of the clusters is likely to have originated from a secondary shower, for exampled from a bremsstrahlung photon emitted by the original electron [79]. The calorimeter energy associated to the supercluster is then calibrated using both MC simulation and data [81].

Starting from the electron candidates, the baseline electrons and the signal electrons for the $W \to e\nu$ + jets AM and $Z \to ee$ + jets AM region are defined.

Selection of Baseline Electrons

Baseline electrons are required to have $p_{\mathrm{T}} > 7\,\mathrm{GeV}$ to guarantee high reconstruction efficiency and $|\eta| < 2.47$ to be within the precision region of the electromagnetic calorimeter. The transition region $1.37 < |\eta| < 1.52$ is excluded, since it contains a comparatively large amount of dead material, leading to large energy uncertainties [80]. Baseline electrons are further required to fulfil certain calorimeter quality criteria, especially that the associated electromagnetic cluster is not affected by defective front-end boards or high-voltage modules in the first calorimeter layers or defective calorimeter cells in the cluster core. Finally the electrons have to pass a relatively permissive likelihood-based identification (called *loose identification*) based on the shape of the electromagnetic shower in the calorimeter and information from the tracking system. Since electromagnetic showers have a different shape than hadronic showers, this allows one to distinguish the electrons from hadrons. The loose identification is chosen because it has a high signal efficiency, which is important to guarantee an efficient veto on events containing additional electrons not present in the targeted final state. In addition, the loose identification only has a comparatively weak background rejection, which is important for the fake electron estimate (see Section 8.4), where baseline electrons are used to define a background-enriched region.

Selection of Signal Electrons for the $W \to e\nu$ + jets Auxiliary Measurement Region

Signal electrons in the $W \to e\nu$ + jets AM region have to fulfil the baseline electron criteria. Further requirements are motivated by the need for background rejection. The electrons have to be associated with the primary vertex in the event, to reject electrons from pile-up events. This is done in a procedure called track-to-vertex-association (TTVA) that places requirements on both the transverse and longitudinal impact parameters of electron track with respect to the primary vertex [82][83]. The electrons also have to pass a strict likelihood-based identification (called *tight identification*), which is optimized for background rejection, while preserving good signal efficiency [80]. Furthermore an strict *calorimeter isolation* requirement is placed on the hadronic activity around the electron (called *tight isolation*) [80]. This isolation requirement helps to reject background electrons from heavy flavour decays, which typically are surrounded by significant hadronic activity from the jet remnant. A detailed discussion of the role of identification and isolation in the context of background rejection is given in Section 8.4.

Selection of Signal Electrons for the $Z \to ee$ + jets Auxiliary Measurement Region

Signal electrons in the $Z \to ee$ + jets AM region have to fulfil the baseline electron criteria and pass the TTVA. Furthermore they have to pass an intermediate likelihood-based identification (called *medium identification*), which has good background rejection, while preserving a higher signal efficiency than the tight identification. The electrons are also required to pass the tight isolation. However an additional correction of the calorimeter isolation is performed in this case, since the electrons can de-isolate each other. This happens especially in a boosted scenario with high Z boson p_{T}, when the electrons are close. In case a single electron would fail the isolation requirement, i.e. there is a significant energy deposition

around the electron, it is verified that this energy deposition is not caused by clusters or tracks associated to a second nearby electron. If the energy deposition is associated to a nearby second electron, the isolation is re-evaluated, with the clusters and tracks that are associated to the second electron removed. This prevents the electrons from a boosted Z boson decay to de-isolated each other and improves the selection efficiency.

5.1.2. Muons

Muons are charged and leave tracks both in the ID and the MS, with a small amount of energy also deposited in the calorimeters. Therefore muon candidates are reconstructed using both the MS and the ID. Hits in both subdetectors are used independently in several consecutive pattern recognition and fit steps to reconstruct first track segments and then track candidates. Track candidates from the two subdetectors are then used in a combined fit to reconstruct the actual muon candidates. In regions with reduced acceptance of the MS ($|\eta| < 0.1$) muon candidates are reconstructed by extrapolating track candidates from the ID to the MS and accepting the candidate already if the extrapolated track can be associated with at least one track segment in the MS [84].

Starting from these muon candidates, two types of muons are defined in this analysis, which are described in the following.

Baseline Muons

Baseline muons are required to have $p_{\mathrm{T}} > 7\,\mathrm{GeV}$ to be consistent with the baseline electron selection and $|\eta| < 2.5$ to be within the acceptance of the ID. In addition, permissive quality criteria (called loose identification) are applied to the tracks. These quality criteria require compatibility between the charge and momentum measurement done with the ID and the MS, as well as a minimum amount of hits in both subdetectors [84][85]. They are optimized to maximise the signal efficiency.

Signal Muons

Signal muons have to fulfil the baseline muon criteria combined with additional requirements to improve the background rejection. They have to fulfil the TTVA [82] and are required to fulfil tighter identification requirements than the baseline muons (called the medium identification). This identification specifically does not allow muons, which have been constructed by track extrapolation within $|\eta| < 0.1$. Furthermore an isolation requirement is placed on the activity around the muon, to reject background muons from hadronic sources . Both a permissive track and calorimeter isolation (called loose isolation) are applied, since neither additional tracks nor additional calorimeter activity is expected to be associated with the muons [85].

5.1.3. Hadronic Taus

A large fraction of tau leptons decays hadronically (65 %), of which 72 % (22 %) are decays involving one (three) charged pion(s) in the final state [86], called one-prong (three-prong)

decays. Therefore the tau candidate reconstruction is seeded by hadronic jets reconstructed using the anti-k_t [87] algorithm with a radius parameter of $R = 0.4$. Only jets within the acceptance of the tracking system ($|\eta| < 2.5$) are used, since tracks play an important part in the tau identification. For each tau candidate a tau vertex is associated using a dedicated algorithm. For the further identification steps only tracks from this tau vertex are kept. The tracks are classified as belonging to the core ($R < 0.2$) or isolation ring ($0.2 < R < 0.4$) of the tau candidates, since the showers in the calorimeter from hadronic tau decays are expected to be much narrower than those of gluon- or quark-induced jets [86][88][89].

The tau candidates reconstructed in this way contain a large amount of background from these jets [86], which is reduced in an identification step described in the following.

Baseline Taus

Baseline taus are selected from tau candidates by requiring $p_{\mathrm{T}} > 20\,\mathrm{GeV}$ and $|\eta| < 2.47$, with the transition region $1.37 < |\eta| < 1.52$ excluded and calorimeter quality criteria similar to the baseline electron selection. Furthermore, the taus are required to pass a multivariate identification, which uses several input variables to distinguish taus from quark- and gluon-induced jets [89]. These variables are motivated by the different shower development between the two types of jets. In addition for tau decays tracks are expected to originate only from the charged pions, therefore the number of jets associated with the tau is smaller than in a quark- or gluon-induced jet and these tracks are typically associated with the core region of the tau. A full description of all input variables is given in [89]. For the baseline taus a configuration of the multivariate identification method with high signal efficiency (called loose identification) is used [89].

Signal Taus

Signal taus are selected analogously to baseline taus, but with a stricter requirement on the multivariate identification, called medium identification, providing good signal efficiency and better background rejection than the loose identification.

5.1.4. Photons

Photons interact with the detector in a similar way as electrons. However since they are not charged, they do not leave a track in the ID unless they undergo pair production, also called conversion, in the material of the ID. They also deposit most or all of their energy in an electromagnetic shower in the calorimeter. Therefore the reconstruction of photon candidates proceeds similar to that of electrons. At low η about 20 % of the photons undergo conversion and up to about 65 % at high η. The topo-clustering is the same as for electrons, but the reconstructed tracks are input to a vertex finding algorithm, to find photon conversion vertices [81] which are then matched to topo-clusters. The supercluster-building algorithm proceeds in the same way as for electrons, but without the requirement for a matched track to the seed topo-cluster. For photons the supercluster-building algorithm adds near topo clusters, if they

are likely to belong to a photon conversion [79]. As for electrons, the calorimeter energy associated to the supercluster is then calibrated using both MC simulation and data [81]. An ambiguity resolution is performed for superclusters that are reconstructed as both an electron and a photon [81].

Baseline Photons

Baseline photons are selected from photon candidates by requiring $p_{\mathrm{T}} > 7$ GeV and $|\eta| < 2.47$, with the transition region $1.37 < |\eta| < 1.52$ excluded and calorimeter quality criteria similar to the baseline electron selection. For baseline photons similar to baseline electrons, loose identification requirements are applied to the shape of the electromagnetic shower in the calorimeter. These reduce the contributions from hadronic jets, but still guarantee a high signal efficiency [79].

Signal Photons

Signal photons are required to fulfil the baseline photon criteria together with stricter requirements on the identification (tight identification). Similar to signal electrons, signal photons have to fulfil a calorimeter isolation requirement to remove background from jets that involve the decay of a π_0 to a photon pair [79]. In addition signal photons also have to fulfil a *track isolation* criterium, which places an upper limit on the p_{T} from tracks associated to the photon. This is possible, since photons are not charged and do not produce tracks in the ID, apart from conversion tracks [79]. The isolation requirements are called the tight isolation. Both the photon identification and the two types of isolation are described in more detail in Section 8.3.

5.1.5. Jets

The hadronisation products of quarks and gluons produced in the final state leave tracks in the ID, if they are charged and cause energy depositions both in the EM and hadronic calorimeters in the form of hadronic showers. In this section an overview of the reconstruction, calibration and resolution of these particle jets is given and the signal jet definition is discussed.

Jet Reconstruction

The jet candidates are clustered from energy deposits in both calorimeters and the tracking system using the anti-k_t algorithm with a radius parameter of $R = 0.4$. The input signals to the clustering are determined with a particle flow algorithm [90], which is described briefly in the following. The idea of particle flow jets is to not solely use the energy depositions in calorimeter in the form of topo-clusters[1] in the reconstruction, but to incorporate track

[1] These topo-clusters are constructed with the same algorithm as those used in the electron reconstruction, however also the cells of the hadronic calorimeter are included in the clustering.

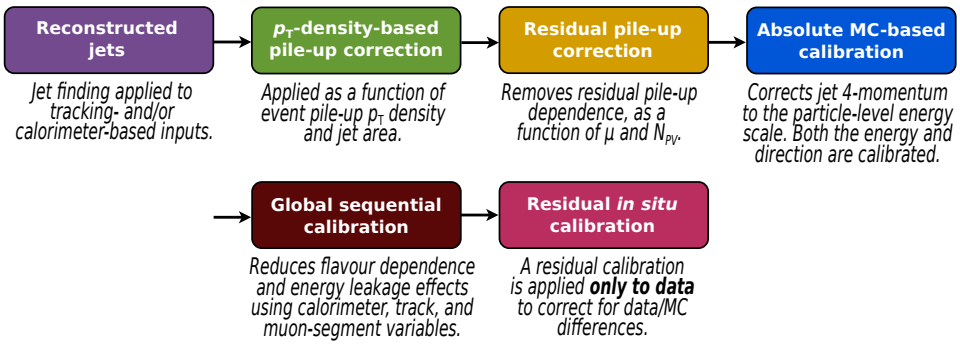

Figure 5.1.: Stages of the jet energy calibration [91].

information for charged particles from the ID in addition. This is beneficial, since the momentum resolution of the tracker is better than the energy resolution of the calorimeter for low p_{T} charged particles. Further benefits include better angular resolution for single charged particle tracks and improved pile-up stability, since the tracking information can be used to reject signals from pile-up vertices. In order to avoid double counting, calorimeter clusters of particles which have a reconstructed track matched loosely to the primary vertex are removed before the jet clustering, which is run on the ensemble of tracks matched to the primary vertex and the remaining calorimeter clusters [90]. To prevent inaccurate removal of calorimeter clusters, especially in the core of high-p_{T} jets and to fully benefit from the excellent calorimeter performance at higher energies, the particle flow algorithm starts to truncate the removal around $p_{\mathrm{T}}^{\mathrm{track}} = 40\,\mathrm{GeV}$. Above $p_{\mathrm{T}}^{\mathrm{track}} = 100\,\mathrm{GeV}$ only calorimeter information is used [91].

Jet Calibration

An extensive calibration procedure is used to correct the jet energy as measured in the calorimeter to that of jets reconstructed at the particle level [91]. A brief overview is given here, since the jet calibration uncertainty is of great importance in this measurement. More detail can be found in [91].

Figure 5.1 shows the complete calibration chain, starting with the reconstructed jets. Only the derivation of the final calibration step involves measured data, all earlier steps are derived from MC simulation. All steps are applied to both data and MC simulation and scale the four-momentum vector of the jets. The first two calibration steps correct the jets for additional energy due to pile-up interactions in the same and the neighbouring bunch-crossings. The first calibration step is an area based energy subtraction, based on the area of the jet in the $y - \phi$ plane and the event pile-up p_{T} density ρ. Since ρ is determined in the central region of the detector, some residual dependence of the jet p_{T} on the pile-up remains after the first step. This is corrected in the second step with an additional correction factor that is a function of the mean number of interactions per bunch-crossing (μ) and the number of reconstructed vertices in the event (N_{PV}). The third step encompasses both the absolute energy scale and η calibration based on MC simulation to account amongst others for energy

losses from passive material, the non-compensating nature of the calorimeter and biases in η in the jet reconstruction. For the energy scale correction, the average jet energy response is determined and used to bring the energy scale of the jets from detector to particle level. A similar correction factor is determined for the jet η. The second to last step is the so-called global sequential calibration that does not change the average jet response, but improves the jet resolution, by correcting fluctuations in the response from jet to jet due to different flavour content, varying energy distributions of the jet constituents and differences in shower shape. The dependence of the jet response on six different variables (e.g. number of tracks, energy fractions in different calorimeter layers, etc.) is corrected. The residual in-situ correction is the final step in the calibration procedure, where measurements in data are used to correct differences between the jet response in data and simulation (e.g. due to imperfect modelling of the materials and physics processes in the detectors). This in-situ correction especially contains an eta intercalibration analysis, where a p_{T} balance in dijet events is used to correct the energy scale of forward jets to that of central jets.

Jet Energy Resolution

The precise knowledge of the jet energy resolution (JER) in data is important, since it is known that the JER is not well modelled in the simulation. This mismodelling needs to be corrected to perform a precise measurement.

The jet energy resolution can be parametrized similarly to the calorimeter resolution with a noise term, a stochastical term and a constant term. These are measured in physics data using a dijet balance method [91]. This method is based on the assumed p_{T} balance of dijet events, which are back-to-back in the transverse plane of the detector. Deviations from the balance arise due resolution effects, additional radiation and method biases. These deviations are measured and the jet resolution is extracted. A detailed description is given in [91].

The measured jet energy resolution is used to improve the description of the data by the simulation. For regions of jet p_{T} where the resolution in the simulation is better than in data, the simulated jets are smeared using the measured JER until the average resolution of the jets matches that in data. In regions where the simulation has worse resolution than the data, no smearing is applied (i.e. the data resolution is not artificially worsened) [91].

Signal Jets

The jets used in the analysis are selected from the jet candidates by requiring $p_{\mathrm{T}} > 30\,\mathrm{GeV}$ and $|y| < 4.4$. In addition jets have to pass basic quality criteria ensuring the correct operation of the calorimeter of the event, also called the loose identification. To suppress pile-up jets, low p_{T} jets are required to pass the jet vertex tagger (JVT) [92], a likelihood discriminant that employs tracking information from the ID to identify pile-up jets. Only jets up to 60 GeV are required to pass the JVT, since the pile-up jet p_{T} spectrum is rapidly falling and the removal of high-p_{T} hard-scatter jets should be avoided [92]. The JVT is only available in the central region of the detector, since it relies on tracks from the ID. Therefore a separate tagger for forward jets, called fJVT, is used. It calculates for each pile-up vertex reconstructed in the central region the vectorial transverse sum of the jet and track momenta associated to that

vertex, to determine if p_{T} is missing[2] for that vertex. The fJVT then checks for each forward jet if the jet p_{T} is compatible with the missing p_{T} of a pile-up vertex and then it tags the forward jet accordingly [93]. In addition the leading jet in p_{T} in each event must satisfy a so-called tight identification in order to reject beam-induced background. This is discussed in detail in Section 8.2.

5.1.6. Removal of Overlapping Physics Objects

The reconstructed and selected physics objects as defined above are not mutually exclusive and one physics objects interacting with the detector can be reconstructed as two different objects. Therefore a procedure is required to remove these overlaps. Detailed studies have been performed by the ATLAS collaboration on the overlaps [94]. In the following, an overview of the main effects and the removal steps applied in this measurement are given based on [94].

Muons can be reconstructed as electrons. This typically happens if a final state radiation photon is emitted collinear to the muon or if the muon radiates a Bremsstrahlung photon. These photons lead to an electromagnetic shower in the calorimeter, which together with the track from the muon in the ID leads to the reconstruction of an electron. However a genuine electron can not cause a track in the MS, which is required for a muon to be reconstructed. Therefore electrons are removed from the event if they share an ID track with a muon.

Hadronic taus, electrons and muons can be reconstructed as jets. In the case of hadronic taus this is clear, since the hadronic tau reconstruction starts with a seed jet. Electrons are also usually clustered as jets, because the same topo clusters used in the electron reconstruction are also used in the jet reconstruction. Therefore all jets that are within $\Delta R < 0.2$ of a tau or an electron are removed from the event. A muon can be reconstructed as a jet, if a bremsstrahlung or FSR photon is emitted. In this case the jet will only have few associated tracks. Therefore jets are removed if they have fewer than three tracks and are closer than $\Delta R < 0.2$ to a muon.

Electrons and muons can be produced as part of a heavy flavour decay, in which case they are typically close to a genuine hadronic jet. Therefore electrons and muons are removed if they have a distance of $0.2 < \Delta R < 0.4$ to a jet. This also serves as an additional isolation criterium for genuine electrons and muons that are close-by to a genuine jet, since in these cases the reconstruction is typically biased and the modelling in simulation is difficult, so the removal of the close-by leptons is favourable.

Hadronic taus can be both faked by electrons and muons. For electrons this happens because the electron are typically reconstructed as jets, which can then seed taus. In the case of muons an anomalous energy loss in the calorimeter, which is reconstructed as a jet can lead to the fake reconstruction as a tau. Therefore taus which are closer to electrons or muons than $\Delta R < 0.2$ are removed.

[2] The sum of all momenta associated to a vertex is expected to be zero in the transverse plane.

5.1.7. Missing Transverse Momentum

One of the most important observables used in this measurement in the missing transverse momentum. It allows to quantify the transverse momentum carried out of the detector by invisible particles, like neutrinos or potentially DM and other invisible BSM particles. The reconstruction of the missing transverse momentum relies on the conservation of momentum in the transverse plane, which means that the sum of the p_{T} of all finals state particles is zero. Therefore the transverse momentum sum of the invisible particles can be calculated as the negative vectorial sum of the visible particles. This is discussed in the following.

The reconstruction of the missing transverse momentum from invisible particles $p_{\mathrm{T}}^{\mathrm{miss,real}}$ relies on the calibrated *hard objects* described above, namely electrons (e), muons (μ), hadronically decaying taus (τ), photons (γ) and jets. All energy deposits in the calorimeters and the ID are matched to those hard objects and an overlap removal is performed to avoid double counting. All energy deposits in the ID not matched to the hard objects are collected in the *soft term.*

The vector $\underline{p_{\mathrm{T}}}^{\mathrm{miss,real}}$ is then calculated along the x and y axes as

$$p_{\mathrm{x(y)}}^{\mathrm{miss,real}} = p_{\mathrm{x(y)}}^{\mathrm{miss,e}} + p_{\mathrm{x(y)}}^{\mathrm{miss},\mu} + p_{\mathrm{x(y)}}^{\mathrm{miss},\tau} + p_{\mathrm{x(y)}}^{\mathrm{miss},\gamma} + p_{\mathrm{x(y)}}^{\mathrm{miss,jets}} + p_{\mathrm{x(y)}}^{\mathrm{miss,soft}}, \tag{5.1}$$

where the terms are calculated as the negative vectorial sum of tracks of charged particles and transverse momenta of energy deposits of the corresponding particles [95][96]. Then $p_{\mathrm{T}}^{\mathrm{miss,real}}$ is calculated as $p_{\mathrm{T}}^{\mathrm{miss,real}} = \left|\underline{p_{\mathrm{T}}}^{\mathrm{miss,real}}\right|$.

For the SR the $p_{\mathrm{T}}^{\mathrm{miss,real}}$ is a proxy for the boson p_{T}, since the neutrinos from the $Z \to \nu\nu$ + jets decay can not be reconstructed directly. For the AM regions a similar proxy for the boson p_{T}, called $p_{\mathrm{T}}^{\mathrm{miss}}$, is defined. It is constructed in each region of the measurement by summing the $\underline{p_{\mathrm{T}}}^{\mathrm{miss,real}}$ and the transverse momentum vectors of the signal leptons or photon in that region (e.g. in the SR $\underline{p_{\mathrm{T}}}^{\mathrm{miss}} = \underline{p_{\mathrm{T}}}^{\mathrm{miss,real}}$, in the $W \to e\nu$ + jets AM region $\underline{p_{\mathrm{T}}}^{\mathrm{miss}} = \underline{p_{\mathrm{T}}}^{\mathrm{miss,real}} + \underline{p_{\mathrm{T,e}}}$, etc.). Note that since $p_{\mathrm{T}}^{\mathrm{miss,real}}$ is calculated as the negative vectorial sum of all hard objects and the soft term, adding a hard object in this way effectively removes it from the $p_{\mathrm{T}}^{\mathrm{miss,real}}$ and treats it as if it were invisible to the detector. This is done even in regions where no genuine $p_{\mathrm{T}}^{\mathrm{miss,real}}$ is expected from the final state. Defining $p_{\mathrm{T}}^{\mathrm{miss}}$ in this way has the advantage that the experimental systematic uncertainties in the AM regions remain closely correlated to those in the SR. This is especially important for the jet experimental systematic uncertainties, since the jet recoil systems are expected to be very similar in all regions and are taken into account in the same way in the calculation of $p_{\mathrm{T}}^{\mathrm{miss}}$ and $p_{\mathrm{T}}^{\mathrm{miss,real}}$.

5.2. Selection of Collision Events

Collision events are selected according to their selected physics objects content into the six different measurement regions and the two jet phase spaces in different steps. In a first step a dedicated set of analysis triggers is used to select all events that possibly enter in any region

of the measurement from the ATLAS data stream. This is discussed in the first part of this section.

In a next step, event quality criteria are applied to the triggered events, to ensure that the detector was fully functional at the time the event was recorded. This is discussed in the second part of this section.

In a final step the events are selected into the different regions according to the reconstructed, calibrated and selected physics objects. These event selection criteria have two aims that need to be reconciled: To improve the statistical precision of the measurement the selection should be as inclusive as possible. However, to reduce contributions from background events and improve the purity of the signal process, additional selection constraints are necessary in certain cases. The third part of this section discusses and motivates the selection cuts applied in the measurement. Please note that additional regions, like control or validation regions for the background estimates, are discussed in the relevant chapters.

5.2.1. Trigger Selection

The analysis triggers are selected to be as inclusive as possible to allow for the highest possible statistical precision in the measurement. Therefore the lowest unprescaled triggers for each physics object are used. Table 5.1 shows the main analysis trigger items. The trigger item names include the name of the object (electron:e, photon: g, $p_{\mathrm{T}}^{\mathrm{miss,real}}$: xe) followed by the p_{T} or $p_{\mathrm{T}}^{\mathrm{miss,real}}$ threshold and in some cases further information on the applied selection (e.g.: medium likelihood identification: lhmedium). A detailed description of all trigger items names used in the measurement is given in Section A.1. The main analysis triggers are discussed in the following.

The lowest unprescaled triggers evolve for different years, mostly to cope with the harsher pile-up conditions [76], therefore the trigger items change for different years. The requirements placed on the triggered objects typically become looser towards higher p_{T}, since the trigger rate decreases due to the falling p_{T} spectra. In most cases a logical "or" of several triggers is used to ensure maximum efficiency.

For the SR, $p_{\mathrm{T}}^{\mathrm{miss,real}}$ triggers are used, since the SM signal process $Z \to \nu\nu$ + jets and also BSM physics like DM produce large $p_{\mathrm{T}}^{\mathrm{miss}}$. For the $W \to \mu\nu$ + jets AM and $Z \to \mu\mu$ + jets AM regions the $p_{\mathrm{T}}^{\mathrm{miss}}$ triggers are also used. This is possible, since muons are not included as hard objects in the online $p_{\mathrm{T}}^{\mathrm{miss}}$ calculation, thus they are "invisible" to the HLT and their p_{T} is part of the online $p_{\mathrm{T}}^{\mathrm{miss}}$.

For the $W \to e\nu$ + jets AM region single electron triggers are used, since electron triggers have a much lower threshold than $p_{\mathrm{T}}^{\mathrm{miss}}$ triggers. Single electron triggers are also used in the $Z \to ee$ + jets AM region. For the γ+jets AM region single photon triggers are used.

5.2.2. Event Quality Criteria

Each event that is selected for analysis has to fulfil basic criteria to ensure all relevant detector components are in a ready state. This is not trivial, since the ATLAS detector is a very

Region	Trigger requirement
Signal Region, $W \to \mu\nu$ + jets AM & $Z \to \mu\mu$ + jets AM	2015: HLT_xe70 2016: HLT_xe90_mht_L1XE50 HLT_xe110_mht_L1XE50 2017: HLT_xe110_pufit_L1XE55 2018: HLT_xe110_pufit_xe70_L1XE50 HLT_xe120_pufit_L1XE50 HLT_xe110_pufit_xe65_L1XE50
$W \to e\nu$ + jets AM & $Z \to ee$ + jets AM	2015: HLT_e24_lhmedium_L1EM20VH HLT_e60_lhmedium HLT_e120_lhloose 2016: HLT_e24_lhmedium_nod0_L1EM20VH HLT_e60_lhmedium HLT_e26_lhtight_nod0_ivarloose HLT_e60_lhmedium_nod0 HLT_e140_lhloose_nod0 HLT_e300_etcut 2017: HLT_e26_lhtight_nod0_ivarloose HLT_e60_lhmedium_nod0 HLT_e140_lhloose_nod0 HLT_e300_etcut 2018: HLT_e26_lhtight_nod0_ivarloose HLT_e60_lhmedium_nod0 HLT_e140_lhloose_nod0 HLT_e300_etcut
γ+jets AM	2015: HLT_g120_loose HLT_g200_etcut 2016-2018: HLT_g140_loose HLT_g300_etcut

Table 5.1.: A summary of the trigger requirements applied to the SR and the AM regions over the Run 2 data taking period.

complex instrument. In addition events with errors or increased noise either in the calorimeters or the ID are rejected. Each event is required to have a reconstructed PV with at least 2 associated tracks.

5.2.3. Measurement Regions and Jet Phase Spaces

In this section the definition of the regions in the measurement is given. The SR and the γ+jets AM region definitions are shown in Table 5.2 and the definitions of the remaining regions are given in Table 5.3 and discussed in the following.

The value of the $p_{\mathrm{T}}^{\mathrm{miss}}$ selection requirement in the SR is motivated by the suppression of fake $p_{\mathrm{T}}^{\mathrm{miss}}$ background that rises strongly towards lower $p_{\mathrm{T}}^{\mathrm{miss}}$ and by the trigger efficiency of the lowest unprescaled $p_{\mathrm{T}}^{\mathrm{miss,real}}$ triggers. The $p_{\mathrm{T}}^{\mathrm{miss}}$ requirement of the SR is also applied in the other regions, to achieve a coherent selection.

The minimum p_{T} requirement for the leading photon in the γ+jets AM region and the leading electron in the $W \to e\nu$ + jets AM region are chosen to ensure that the triggers used to select the events are fully efficient. This requirement has to be larger than the trigger threshold since the the offline and online p_{T} are not identical, but have a different resolution. This leads to a turn-on effect, where the efficiency of the trigger rises not sharply to 100 %, but gradually following an error-function like form [97].

The minimum p_{T} requirement for the leading electron (muon) and the selection cut on the invariant mass $m_{\ell\ell}$[3] of the di-lepton system around the Z boson mass in the $Z \to ee$ + jets AM ($Z \to \mu\mu$ + jets AM) region are chosen to increase the signal over background ratio for the SM signal process $Z \to ee$ + jets ($Z \to \mu\mu$ + jets).

The $p_{\mathrm{T}}^{\mathrm{miss,real}}$ cut and the cut on the transverse mass m_{T}[4] in the $W \to e\nu$ + jets AM region are applied to reduce the fake electron background. They are not applied in the $W \to \mu\nu$ + jets AM region, since the fake muon background is much smaller [22].

	Signal Region	γ+jets AM region
$p_{\mathrm{T}}^{\mathrm{miss}}$	> 200 GeV	
signal photon multiplicity	N/A	1
photon $\lvert\eta\rvert$	N/A	$0 < \lvert\eta\rvert < 1.37$ or $1.52 < \lvert\eta\rvert < 2.47$
leading photon p_{T}	N/A	> 160 GeV
additional baseline e, μ, τ	Strictly none	

Table 5.2.: A summary of the selection cuts defining the Signal Region and the γ+jets AM region.

[3] The invariant mass is calculated as the positive square root of $m_{\ell\ell}^2 = p_1 \times p_2$, with p_1 and p_2 the momentum four vectors of the leptons.

[4] The transverse mass is defined as $m_{\mathrm{T}} = \sqrt{2(p_{\mathrm{T}}^{e} p_{\mathrm{T}}^{\mathrm{miss,real}} - \underline{p_{\mathrm{T}}^{e}}\,\underline{p_{\mathrm{T}}^{\mathrm{miss,real}}})}$, p_{T}^{e} is the electron p_{T} and $\underline{p_{\mathrm{T}}^{e}}$ is the corresponding vector in the transverse plane.

	Lepton-based AM regions	
	$W \to e\nu$ + jets AM & $W \to \mu\nu$ + jets AM	$Z \to ee$ + jets AM & $Z \to \mu\mu$ + jets AM
$p_{\mathrm{T}}^{\mathrm{miss}}$	> 200 GeV	
lepton multiplicity	1 signal lepton	2 signal leptons, opposite charge
lepton $\lvert\eta\rvert$ (muons)	$\lvert\eta\rvert < 2.5$	
lepton $\lvert\eta\rvert$ (electrons)	$0 < \lvert\eta\rvert < 1.37$ or $1.52 < \lvert\eta\rvert < 2.47$	
leading lepton p_{T}	> 30 GeV for e, > 7 GeV for μ	> 80 GeV
sub-leading lepton p_{T}	N/A	> 7 GeV
di-lepton mass	N/A	$66\,\mathrm{GeV} < m_{\ell\ell} < 116\,\mathrm{GeV}$
transverse mass	$30\,\mathrm{GeV} < m_{\mathrm{T}} < 100\,\mathrm{GeV}$ for e only	N/A
$p_{\mathrm{T}}^{\mathrm{miss,real}}$	> 60 GeV for e only	N/A
additional baseline e, μ, τ	Strictly none	

Table 5.3.: A summary of the selection cuts defining the lepton-based *AM* regions.

In each of the six regions, two different phase spaces are defined. These are the monojet phase space and the VBF phase space. The selection cuts for the two phase spaces are chosen to enhance the respective jet topology. They are shown in Table 5.4 and discussed in the following.

In each of the phase spaces a large separation in ϕ between the first four leading jets and the $p_{\mathrm{T}}^{\mathrm{miss}}$ is required ($\Delta\phi(\mathrm{jet}_i, p_{\mathrm{T}}^{\mathrm{miss}}) > 0.4$) to reduce the contribution from multijet events with fake $p_{\mathrm{T}}^{\mathrm{miss}}$. This is due to a topological characteristic of the fake $p_{\mathrm{T}}^{\mathrm{miss}}$ background that leads to the alignment of the fake $p_{\mathrm{T}}^{\mathrm{miss}}$ with a jet. This is discussed in more detail in Section 8.1. Furthermore the p_{T} cuts on the leading and sub-leading jets are chosen to avoid threshold effects with respect to the $p_{\mathrm{T}}^{\mathrm{miss}}$ cut.

For the VBF topology a large rapidity separation between the jets from the quark remnants is expected. Therefore the VBF topology is enhanced in the VBF phase space by requiring a large invariant jet mass m_{jj}, calculated as

$$m_{jj} = 2 p_T^{j1} p_T^{j2} \left(\cosh\left(\eta_{j1} - \eta_{j2}\right) - \cos\left(\phi_{j1} - \phi_{j2}\right)\right), \tag{5.2}$$

from the first two leading jets. The large m_{jj} requirement thus leads to an angular separation of the first two leading jets. In addition a rapidity separation of $\left|\Delta y_{jj}\right| > 1$ is required. Since the quark remnants are not colour connected in the VBF topology, no additional jets are expected in the rapidity gap between the quark remnants. Therefore a veto on additional jets in the gap is applied.

The monojet and the VBF phase spaces are share events and are correlated. This correlation is taken into account with the consistent use of the bootstrap method throughout the analysis.

	Monojet	VBF
$\Delta\phi(\text{jet}_i, p_{\text{T}}^{\text{miss}})$	> 0.4, where $i = 1, \ldots 4$ runs over the four highest p_{T} jets	
leading jet $\lvert\eta\rvert$	< 2.4	
leading jet p_{T}	> 120 GeV	> 80 GeV
sub-leading jet p_{T}	N/A	> 50 GeV
m_{jj}	N/A	> 200 GeV
$\lvert\Delta y_{jj}\rvert$	N/A	> 1
In-gap jets	N/A	Strictly None

Table 5.4.: A summary of the selection cuts defining the monojet and the VBF phase spaces. These cuts apply to the SR and all five AM regions.

5.3. Selection Criteria for Simulated Events on Particle Level

Simulated events are used in the unfolding procedure discussed in Chapter 11 to correct the measured data for detector effects. In this procedure events have to be selected on the particle level of the simulation in order to define the fiducial phase-space volume. To minimize the extrapolation between the detector level and the unfolded particle level and reduce the dependence on the MC simulation, the selection criteria for the events are the same on the particle level and on the detector level, wherever that is applicable. More details on the MC simulation are given in the next chapter.

The particle-level objects in the simulation used to select the particle-level events are discussed in the following. These object definitions are also motivated by the reduction of the extrapolation.

Charged leptons (electrons or muons) are required to be prompt. This means that they do not originate from the decay of a hadron. Dressed leptons are used, meaning that the four-momenta of photons within a cone of $\Delta R < 0.1$ from Bremsstrahlung are added to the four-momentum of the lepton.

Photons are required to be prompt and isolated. The truth level photon isolation is used to reject photons from fragmentation processes. It is chosen such that it mimics the isolation requirement at detector level [98].

Jets are reconstructed using the anti-k_t jet algorithm [87] with $R = 0.4$. All stable final-state particles are used as input to the jet algorithm except prompt leptons from W, Z, Higgs and tau decays and prompt photons from Higgs decays. The excluded prompt leptons are dressed as described above.

Any jets that contain a hadron coming from the decay of a tau are classified as hadronically decaying taus.

The particle-level $p_{\text{T}}^{\text{miss}}$ is defined as the truth boson p_{T} of the corresponding signal or AM regions.

6. Simulation of Collision Events

The simulation of the proton-proton collisions at the LHC and the interactions of the collision products with the ATLAS detector is an important tool in the measurement. It helps to understand the measured data, to optimize the event selection criteria, estimate the contributions from background processes and systematic uncertainties and to enable comparisons of theory predictions to data.

The full simulation chain typically includes the calculation of the cross section of a given scattering process using Monte Carlo integration methods, parton shower and hadronisation models and the ATLAS detector simulation. As Monte Carlo techniques are used it is often referred to as Monte Carlo (MC) simulation [3].

The simulation produces event samples, which can be treated as collision events. This includes the application of selection criteria. In this way, theory predictions can be obtained for a specific event selection after the MC simulation sample is generated. This facilitates the consistent comparison of the predictions and the measured collision data.

The first section of this chapter discusses the general steps in the generation of the MC simulation samples, while the different MC generators and simulation samples used in the measurement are described in the second section. The final section of this chapter explains several improvements which are applied to the MC simulation in order to achieve a better description of the measured data.

6.1. Generation of the Simulation Samples

The generation of the MC simulation samples is a complex procedure that combines calculations at fixed order in perturbation theory of QED and QCD with parton distribution functions measured in data and empirical models for showering and hadronization. This is necessary due to the complex theoretical structure of QCD and the breakdown of perturbation theory at low energies. This section gives a brief overview over the main steps of the MC event generation, which is inspired loosely by [3].

The major steps of the MC generation are sketched in Figure 6.1. The first step is perturbative calculation of the matrix element of the hard process to a given order in perturbation theory of QCD, typically at next-to-leading order (NLO) or next-to-next-to-leading order (NNLO). The PDF sets for the proton that enter these calculations are typically determined from a combination of measurements [33].

The next step is called parton showering and takes into account that the ingoing partons and also potential outgoing partons are QCD objects and thus can radiate gluons, which in turn can radiate additional gluons or produce quark-antiquark pairs. This process typically evolves perturbatively down from the scale of the hard process to some cut-off scale, where

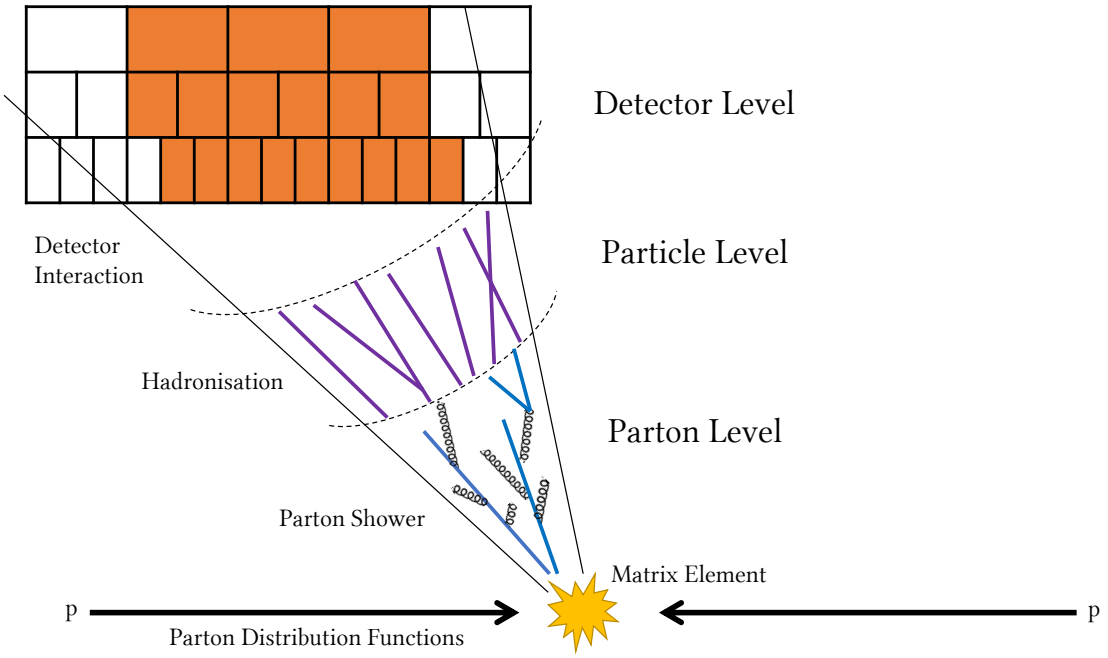

Figure 6.1.: Majors stages of the MC simulation beginning with the calculation of the matrix element using PDF sets. The nomenclature used for the objects generated by the simulation at the various stages is also shown. Objects that are present after parton showering are on *parton level*, objects that are produced in the hadronization stage are on *particle level* and objects that are reconstructed in the detector are on *detector level*.

perturbation theory breaks down. It is also possible that more than two partons interact. These multi-partonic interactions of the proton remnant are rather involved and typically approximated by an empirical model [3].

The simulation of electroweak radiation and subsequent showers is typically also simulated using the perturbative part of the parton showering algorithm, allowing for both types of showers to be simulated simultaneously [3]. In some cases, analytic calculations are used [99].

The partons present after the parton shower define the *parton* level of the simulated event.

The partons produced in the parton shower are not stable, but undergo hadronization, due to the confining nature of QCD. This is is typically simulated using a phenomenological model, since the processes involved are in the non-perturbative regime of QCD [3]. The same is true for the simulation of the decay of non-stable hadrons that decay to lighter hadrons after hadronization has taken place [3].

The stable hadrons that are the result of this procedure are clustered with a the anti-k_t jet algorithm [87] to be used for studies on the so-called truth- or *particle level*. The physics object present on particle level are for example used when determining the detector corrections discussed in Chapter 11.

In a final step the final state particles from the MC event generator are passed through the

ATLAS detector simulation, which is based on GEANT4 [100]. This complex software simulates the interaction of the particles with the detector material, using measured interaction cross section. Furthermore it simulates the signal generation of the detector electronics. This simulation step allows to correctly take detector effects into account. These are for example the limited detector efficiency and acceptance, as well as energy, momentum and angular resolutions. The results of the detector simulation are reconstructed and processed with the same algorithms as the physics data. The resulting objects are said to be on the so-called reco or *detector level*.

Running the full chain outlined above allows for a direct comparison of theory predictions with the measured data. However the simulation process is very costly in terms of computing power. The average time to generate the particle level event is around half a minute [101] and the detector level simulation using the full GEANT4 setup takes an additional three minutes on average[1] [102]. Several billion events have to be generated to provide enough statistical precision not to be limited by the simulation event statistics. Therefore the MC simulation samples used in the measurement are all centrally produced and provided by the ATLAS collaboration. They are described in more detail in the following section.

6.2. Simulation Samples used in the Measurement

Simulated events are used for all relevant SM signal and background processes as well as a BSM signal process. The MC simulation samples involving SM processes include the full GEANT4 simulation.

The MC simulation samples used for the SM processes are shown in Table 6.1. The table also includes the event and parton shower generator, the accuracy of the matrix element calculation, the PDF set and the relevant references. The generators are chosen to provide the highest available accuracy for the given process. The samples for the SM signal processes are discussed in the following.

For all V+jets processes the EWK and the QCD production mode is distinguished. The EWK V+jets diagrams are generated using SHERPA v2.2.11, which is LO-accurate for up to two jets for this process. For detector level comparisons, the QCD diagrams for W/Z+jets are generated using SHERPA v2.2.1, which is NLO-accurate for matrix elements with up to two jets, and LO-accurate for the emission of a third or fourth jet.

The QCD production mode of the γ + jets process is simulated with SHERPA v2.2.2, which is NLO-accurate for matrix elements with up to two jets, and LO-accurate for the emission of a third or fourth jet. An alternative sample for the QCD production is simulated with PYTHIA v8.186. This generator applies a different approach to model fragmentation photons and is used to determine a modelling uncertainty related to fake photon background estimate discussed in Section 8.3.

To improve the accuracy of the QCD V+jets simulation samples produced with SHERPA, an event-by-event reweighting is applied to account for higher order electroweak effects. The reweighting is performed as a function of boson p_{T} at particle level as prescribed in [103].

[1] The actual generation time of a signal event varies strongly, depending on the final state particle content.

Physics Process	Generator	Parton Shower	Accuracy of cross section	PDF Set	Reference
QCD W/Z+jets	Sherpa v2.2.1	Sherpa v2.2.1	NLO	NNPDF3.0nnlo	[107, 6][108]
EWK V+dijets	Sherpa v2.2.11	Sherpa v2.2.11	LO	NNPDF3.0nnlo	[107, 6]
QCD γ + jets	Sherpa v2.2.2	Sherpa v2.2.2	NLO	NNPDF3.0nnlo	[6]
γ + jets	Pythia v8.186	Pythia v8.186	LO	NNPDF2.3lo	[109]
VV (semileptonic)	Sherpa v2.2.1	Sherpa v2.2.2	NLO	NNPDF3.0nnlo	[107] [110]
VV (fully leptonic)	Sherpa v2.2.2	Sherpa v2.2.2	NLO	NNPDF3.0nnlo	[107][110]
VVV	Sherpa v2.2.2	Sherpa v2.2.2	NLO	NNPDF3.0nnlo	[107][110]
$t\bar{t}$	Powheg-Box v2	Pythia v8.230	NNLO+NNLL	NNPDF3.0nlo	[111, 112, 113, 114][104]
Single top (Wt)	Powheg-Box v2	Pythia v8.230	NLO	NNPDF3.0nlo	[115, 112, 113, 114]
Single top (t-channel)	Powheg-Box v2	Pythia v8.230	NLO	NNPDF3.0nlonf4	[116, 112, 113, 114]
Single top (s-channel)	Powheg-Box v2	Pythia v8.230	NLO	NNPDF3.0nlo	[117, 112, 113, 114]

Table 6.1.: Simulated event samples used in the measurement with the corresponding matrix element and parton shower generators, accuracy of the matrix element and PDF set. Please note that the γ + jets samples produced with Pythia v8.186 are solely used to define an uncertainty on the fake photon background estimate.

All MC samples include soft QCD processes that overlay the event from the hard scattering to simulate pile-up contributions. This overlay is simulated with Pythia 8.186 [104] using the NNPDF2.3lo PDF set [105][106].

The MC calculation of the simplified axial-vector mediator DM model is performed with the Powheg-Box generator [117, 112, 113, 114] using the NNPDF3.0nlo PDF. For the parton showering it is interfaced to Pythia 8.205, with the A14 tune [118]. This MC simulation sample is not passed through the Geant4 simulations, as it is used with the detector-corrected cross sections.

6.3. Data-driven Improvement of the Simulation

The modelling of the ATLAS detector in the Geant4 simulation can be improved. One example is the shower development of electrons in the calorimeter, which is known to be mismodelled by the simulation[79]. This mismodelling leads to differences between data and MC simulation in the performance of the reconstruction, trigger, identification and isolation algorithms for charged leptons and photons.

To improve the description of the data, each simulated event is reweighted with scale-factors derived from physics data. These scale factors are determined in dedicated analyses and improve the MC simulation modelling on the object level. They are typically derived as a function of object p_{T} and η, since the modelling depends on the particle kinematics and the instrumentation of the detector. The scale factors are applied for each lepton/photon in the event. An exception are the trigger scale factors. These are only applied for the lepton/photon that triggered the event[2]. The size of the scale-factors is typically in the few percent range, but can be larger in specific cases (e.g. the turn-on region of the triggers for the trigger scale-factors).

Scale-factors for the reconstruction and identification algorithms are applied for all charged leptons [79]. For muons and electrons scale-factors for the isolation algorithms are applied

[2]This is possible in MC simulation, where the full trigger chain is modelled.

as well [85][79]. Trigger scale-factors are only available for electrons [119][75]. For photons, identification and isolation scale-factors are applied[79]. Scale factors are not available for all objects, either because the modelling is considered good enough, or because the relevant analysis to determine them has not yet concluded.

In addition, the MC simulation is reweighted such that its pile-up profile matches that of the data. This is necessary, since the MC simulation is typically generated before the data is taken, so the exact pile-up profile is not known. The reweighting is done on an event-by-event basis and the weights are provided by the ATLAS collaboration [120].

7. Sources of Systematic Uncertainty Considered in the Measurement

All quantities measured with the ATLAS detector are subject to systematic uncertainty. This includes for example the energy measured in the calorimeters or the curvature of tracks in the ID, but also higher level objects like the shape variables used to quantify electromagnetic showers in the detector or the algorithms used to reconstruct and identify particles using the detector inputs.

The effect of the very large number of systematic uncertainties on the measured particles (e.g. on the p_{T} of a jet or the reconstruction efficiency of an electron) are measured in dedicated analyses by the ATLAS collaboration, usually by comparing data and MC simulation. The resulting uncertainties are encoded in sets of nuisance parameters. Each nuisance parameter (NP) represents the combined effect of many underlying sources of systematic uncertainty. The NPs are used to propagate the impact of these systematic uncertainties to all measured observables. This is achieved by shifting the variables affected by the NP (e.g. the jet p_{T}) by $\pm 1\sigma_{NP}$ and repeating the whole analysis chain with the shifted variables for each shift separately. In total 215 NPs related to the detector or experimental techniques are considered in this measurement.

Also the theory predictions have significant systematic uncertainties attached. These are related to uncertainties on the size of the QCD coupling constant α_S, the PDF sets and missing higher order corrections. In total 109 theory variations are considered in this measurement, which are propagated through the measurement whenever theory predictions are used. For the final result they are encapsulated in 3 NPs.

In the first section of this chapter, the experimental systematic uncertainties due to the detector and the various analysis techniques used in the measurement are described. In the second section the theory uncertainties applied to the MC simulation predictions for both SM and BSM physics processes and their impact on the measurement are discussed.

7.1. Experimental Uncertainties

Experimental uncertainties affect all physics objects (jets, electrons, muons, taus, photons) measured with the detector, as well as the event-level quantities ($p_{\mathrm{T}}^{\mathrm{miss}}$, pile-up reweighting), the integrated luminosity and the analysis methods (background estimates and unfolding).

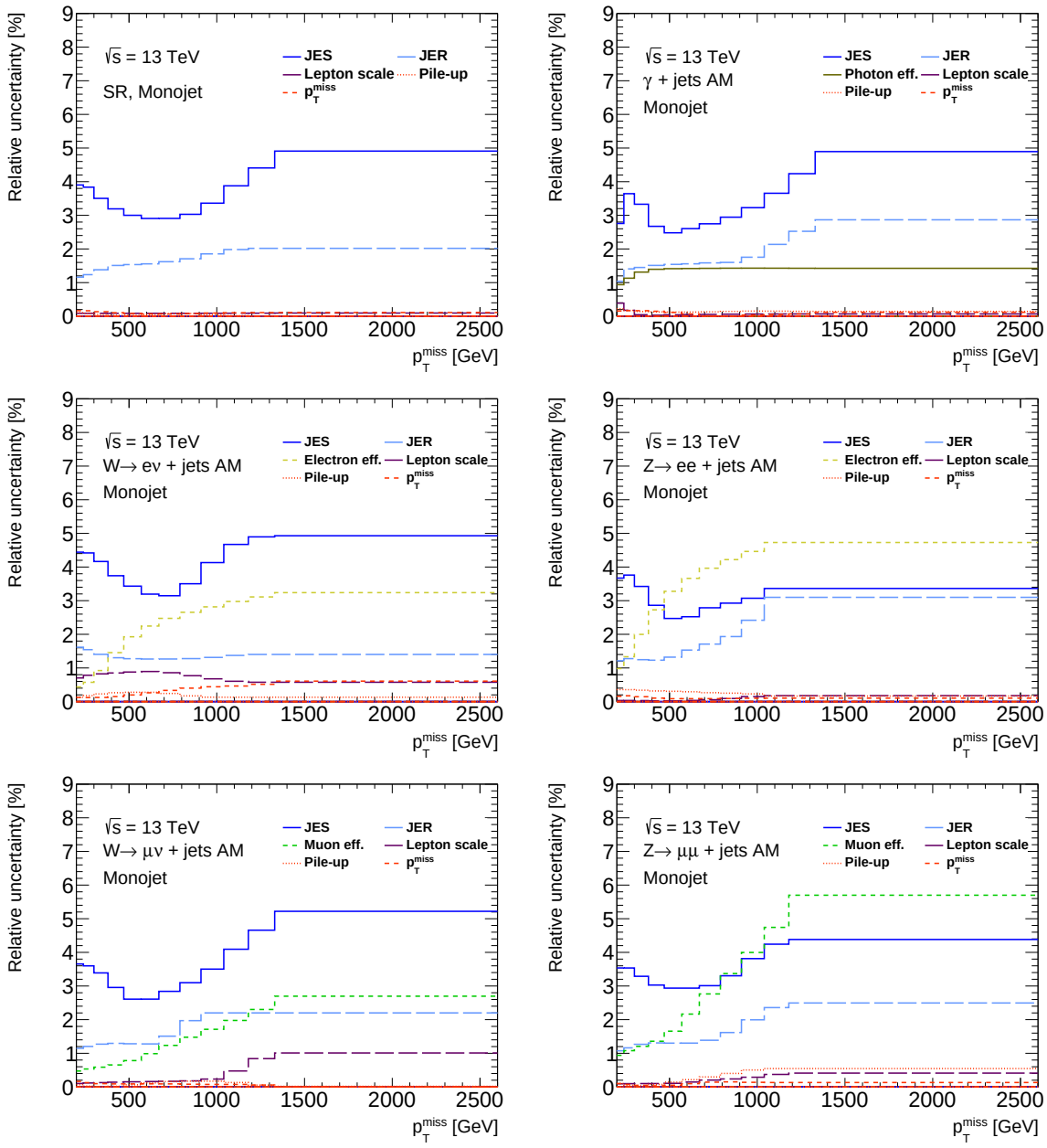

Figure 7.1.: Relative experimental systematic uncertainties in percent on the SM signal process in the SR (top left) and the γ+jets AM (top right), the $W \rightarrow e\nu$ + jets AM (middle left), the $Z \rightarrow ee$ + jets AM (middle right), the $W \rightarrow \mu\nu$ + jets AM (bottom left) and the $Z \rightarrow \mu\mu$ + jets AM (bottom right) regions for $p_{\mathrm{T}}^{\mathrm{miss}}$ in the monojet phase space. The following uncertainty groups are shown: jet energy scale (JES, dark blue), jet energy resolution (JER, light blue), electron efficiency (yellow), muon efficiency (green), photon efficiency (yellow), lepton energy scale and resolution (violet), pile-up reweighting (red) and $p_{\mathrm{T}}^{\mathrm{miss}}$ (teal).

An overview of the impact of the systematic uncertainties of the objects and event-level

quantities on the SM signal process are shown in Figure 7.1. Each panel of the figure shows the relative uncertainty as a function of $p_{\mathrm{T}}^{\mathrm{miss}}$ in the monojet phase space. Here all NPs belonging to a certain group of uncertainties have been added in quadrature for easier visibility. Both the $+1\sigma$ and the -1σ variation of the NPs are shown. These are symmetric, apart from statistical fluctuations. The details of the different uncertainty groups are discussed in the remainder of this section. Due to the large number of NPs only a summary is given here, with more details available in the references.

7.1.1. Uncertainties on the Jet Energy Scale and Resolution

The jet uncertainties are the dominant experimental systematic uncertainties in most regions of the measurement. They affect the measured distributions either directly (e.g. calculation of $p_{\mathrm{T}}^{\mathrm{miss}}$) or indirectly (e.g. selection requirements of the monojet phase space). The shape and magnitude of the relative systematic uncertainty is similar in all regions, since the jet system recoiling against the boson is very similar. The jet systematic uncertainties comprise two main parts, those related to the jet energy scale (JES) and those related to the jet energy resolution (JER). Both are shown in Figure 7.1. The JES NPs originate from the jet calibration and induce shifts of the jet energy of each jet that depend on the p_{T} and/or η of the jet [91]. In total there are 125 NPs, related to the JES and it is not feasible, or necessary, to process all of them separately. Therefore the 98 NPs from the in-situ analyses are combined into several reduced sets using eigenvector decomposition. The largest orthogonal terms are kept as separate NPs and the rest are combined to a residual term [91]. Table 7.1 shows an overview of the 29 uncorrelated NPs used for the JES. The largest component is the JET_Flavor_Response, which covers the different calorimeter response for quark- and gluon-initiated jets [91].

The JER uncertainties originate from the smearing of the MC simulation to match the data [91]. They are propagated to the measurement by smearing individual jets according to a Gaussian with the width given by the NP. A similar decorrelation method as for the JES is applied to the NPs related to the measurement of the JER. The 13 uncorrelated NPs are shown in Table 7.1. More details on the JES and JER NPs is given in [91].

Nuisance parameter (group)	# NPs	Nuisance parameter (group)	# NPs
JET_EffectiveNP_Detector	2	JET_Flavor_Composition	1
JET_EffectiveNP_Mixed	3	JET_Flavor_Response	1
JET_EffectiveNP_Modelling	4	JET_Pileup	4
JET_EffectiveNP_Statistical	6	JET_Others	3
JET_EtaIntercalibration	5	JET_JER	13

Table 7.1.: JES/JER NPs or NP groups used in the measurement.

7.1.2. Uncertainties on Charged Leptons and Photons

The systematic uncertainties on charged leptons and photons are split into two groups: energy scale and resolution uncertainties and efficiency uncertainties. The energy scale and resolution uncertainties induce shifts of the object p_{T} similar to the JES. They impact the

regions in the measurement in different ways depending on the particle content of the final state.

If a lepton/photon is part of the final state in a given region, then the variation of the p_{T} of leptons/photons, which are close in p_{T} to the selection cut of the region, will affect the number of events passing the region selection. This happens because a lepton might fail the selection after the variation even though it passed it before, or vice-versa.

If a lepton is not part of the final state of a given region the variation in the lepton p_{T} still has an impact, as the number of leptons that pass the baseline lepton definition will vary, due to the minimum lepton p_{T} requirement. This leads to a varying number of events passing or failing the lepton veto. If an event does not contain a baseline lepton in the varied event but contains one in the nominal event, that event passes the lepton veto in the varied case, but fails in the nominal case.

Figure 7.1 shows that the impact of the lepton scale and resolution NPs is typically small. In total there are two such NPs for electrons [79], four for muons [84], five for taus [88] and two for photons [79].

The efficiency uncertainties cover the systematic uncertainties on the scale-factors used to improve the agreement between the MC simulation and the data. The NPs induce variations of the scale-factors that are applied to the event for each lepton present in the final state. Therefore these NPs only affect events with the corresponding lepton in the final state.

In total there are 117 such NPs for electrons [79], 8 for muons [85], 14 for taus [121] and 6 for photons [79]. The impact of the efficiency uncertainties, shown in Figure 7.1, is typically larger in the region containing two leptons in the final state, since each lepton is affected separately by the uncertainty. They are dominant at high $p_{\mathrm{T}}^{\mathrm{miss}}$ in the $Z \to ee$ + jets AM and $Z \to \mu\mu$ + jets AM region.

7.1.3. Uncertainties on the Analysis Methods

Several analysis methods are used in this measurement which require the development and definition of a systematic method uncertainty. For completeness the NPs defined for the different methods are shown in Table 7.2. A detailed discussion for these NPs is given in the relevant chapters.

7.1.4. Other sources of systematic uncertainties

The systematic uncertainty on the $p_{\mathrm{T}}^{\mathrm{miss,real}}$ consists of two parts. The first part is related to the hard term of $p_{\mathrm{T}}^{\mathrm{miss,real}}$ and is calculated by propagating the systematic uncertainties on the objects that enter the hard term of the $p_{\mathrm{T}}^{\mathrm{miss,real}}$ calculation. The second part is related to the soft term. The soft term uncertainty is derived from comparisons of the modelling of the $p_{\mathrm{T}}^{\mathrm{miss,real}}$ resolution and scale in MC simulation and data [96]. It is encoded in three NPs. As shown in Figure 7.1, the impact of this uncertainty is below 1 % in all regions of the measurement.

The systematic uncertainty on the pile-up reweighting covers modelling differences in the vertex multiplicity between the data and the MC simulation [120]. It is generally small, below

Nuisance parameter	Description
FAKE_MET_SYS	Fake $p_{\mathrm{T}}^{\mathrm{miss}}$ background estimates (SR)
FAKE_PHOTON	Fake photon background estimate (γ+jets AM region)
FAKE_ONE_ELECTRON	Fake background estimate ($W \to e\nu$ + jets AM region)
FAKE_TWO_ELECTRON	Fake background estimate ($Z \to ee$ + jets AM region)
FAKE_ONE_MUON	Fake background estimate ($W \to \mu\nu$ + jets AM region)
FAKE_TWO_MUON	Fake background estimate ($Z \to \mu\mu$ + jets AM region)
SM_BKG_SR	Background normalization (SR)
SM_BKG_WENU	Background normalization ($W \to e\nu$ + jets AM region)
SM_BKG_WMUNU	Background normalization ($W \to \mu\nu$ + jets AM region)
UNFOLD_DDC	Unfolding uncertainty

Table 7.2.: NPs on the background estimates and the unfolding.

1 %.

The relative systematic uncertainty on the full Run 2 luminosity is 1.7 % [75]. This uncertainty translates into a flat relative uncertainty on the measured cross sections.

7.1.5. Propagation of the Experimental Uncertainties through the Measurement

The experimental systematic uncertainties can be grouped in three categories: Uncertainties that affect both the SM signal process and the background processes, uncertainties that affect only the background processes and uncertainties that affect only the final cross section. Each category is propagated differently through the measurement. This is discussed in the following.

Uncertainties related directly to the measured physics object or event-level quantities, like the lepton scale or efficiency uncertainties are estimated using MC simulation. This has two advantages: Firstly the MC simulation samples typically have much higher statistical precision than the data, which allows for a statistically significant determination of the impact of the NPs even in sparsely populated bins of the measured distribution. Secondly the MC simulation allows to determine the impact of the NPs for each signal and background process independently. In this way effects of the topology of the final state in a given process are taken correctly into account. Examples are the lepton p_{T} and η distributions or the jet p_{T}, η and multiplicity distributions, which can vary for different processes (e.g. higher jet multiplicities in backgrounds involving top quark decays compared to the $W \to \tau\nu$ + jets background).

These uncertainties affect both the SM signal and the background in a region and therefore enter the measurement in two places. Firstly the backgrounds determined from MC simulation are varied according to the NP before subtraction from the data. For the dominant background processes the impact of these uncertainties is first constrained in additional control regions - this is discussed in Chapter 9. Secondly the SM signal process in a given region is varied according to the NP. Technically this is done in the unfolding procedure after

the subtraction of the varied backgrounds, by varying the response matrix. This is discussed in Chapter 11. The whole analysis chain is repeated for each NP, and the backgrounds and the signal are varied simultaneously. The simultaneous variation is necessary to correctly account for the correlations of the uncertainties.

The uncertainties on the fake background estimates and on the background normalization procedure affect only the respective backgrounds. Therefore they are propagated by varying the corresponding background estimate according to the NP before subtracting it from the data and repeating the whole analysis chain.

The unfolding and luminosity uncertainties only affect the final cross sections and are applied directly to them.

7.2. Theory Uncertainties

Three sources of systematic theory uncertainty are considered and discussed in the following. They follow the PDF4LHC recommendations [122].

The uncertainty on the strength of the strong coupling $\alpha_S = 0.118$ includes experimental uncertainties in the determination of α_S and uncertainties due to missing higher orders when evaluating α_S at a scale other than the Z boson mass. It is evaluated by shifting the value of α_S by ± 0.001 and calculating a symmetric uncertainty [122] as

$$\delta^{\alpha_S}(\sigma) = \frac{\sigma\left(\alpha_S^{down}\right) - \sigma\left(\alpha_S^{up}\right)}{2}. \tag{7.1}$$

In order to evaluate the uncertainty on the PDF set used in the MC simulation the PDF variations provided by the NNPDF group are used. These include experimental uncertainties on the data entering the PDF fits and uncertainties on the fitting method. In total there are 100 PDF varations from toy experiments provided by NNPDF and the uncertainty is calculated as the root-mean-square of these variations [33].

The impact of missing higher order in the calculation of the matrix element due to the removal of divergences are also evaluated. To this end the renormalization (μ_R) and factorization (μ_F) scales are varied according to the 7-point variation

$$\{\mu_R, \mu_F\} \times \{0.5, 0.5\}, \{1, 0.5\}, \{0.5, 1\}, \{1, 1\}, \{2, 1\}, \{1, 2\}, \{2, 2\}. \tag{7.2}$$

The scale uncertainty is determined from this variations as the difference between the maximum envelope and the nominal prediction [122].

8. Background Contributions due to Fake Objects

Backgrounds due to fake objects occur for example when a physics object in the final state (e.g. a jet) in an event is reconstructed as a different object (e.g. a photon). Another possible cause for fake backgrounds are energy fluctuations (e.g. in the jet p_{T}) that lead to fake $p_{\mathrm{T}}^{\mathrm{miss}}$. Events in which these processes have happened can be selected into one of the regions of the measurement, even though the events do not contain the correct signature in the final state.

The background contributions due to fake processes are estimated and subtracted in each of the SR and the AM regions. Since the physics mechanisms that play a role in the generation of the fake backgrounds depend on the final state of a given region, different estimation methods are used in different regions. These mechanisms and methods are discussed in this chapter.

The fake background contribution to the SR is dominated by multijet events, where the energy of one or more jets has undergone a large fluctuation and produced fake $p_{\mathrm{T}}^{\mathrm{miss}}$. This background is estimated with the Jet Smearing method and discussed in Section 8.1. A second fake background contribution to the SR originates from events containing beam background muons. This background is discussed in Section 8.2.

The fake background contribution to the γ+jets AM region consists of events containing fake photons. This background is estimated using a 2D-sideband method and is discussed in Section 8.3.

In the $W \to e\nu$ + jets AM regions the fake background contribution consists of events with fake electrons. The background contribution is estimated using the Matrix Method, which is discussed in Section 8.4.

The fake backgrounds in the $Z \to ee$ + jets AM, $W \to \mu\nu$ + jets AM and $Z \to \mu\mu$ + jets AM regions also consist of events with fake electrons and muons. However in these regions the relative background contribution is smaller than in the remaining regions. Therefore they are estimated using a simplified version of the matrix method. As the matrix method is already discussed in detail, no further discussion is given on the simplified method. Please see [22] for more details.

8.1. Multijet Background in the Signal Region

Collision events with jets and no prompt invisible particles in the final state can enter the SR. This typically happens because of jet energy fluctuations in multijet events. These fluctuations either originate from heavy flavour jet decays that produce neutrinos which carry away some of the jet momentum undetected or from instrumental effects that cause the measured jet p_{T} to deviate from the true jet p_{T}. Both cases can lead to a momentum imbalance in the transverse plane and the reconstruction of $p_{\mathrm{T}}^{\mathrm{miss}}$. The $p_{\mathrm{T}}^{\mathrm{miss}}$ generated in this way is called fake $p_{\mathrm{T}}^{\mathrm{miss}}$.

The probability of producing enough fake $p_{\mathrm{T}}^{\mathrm{miss}}$ in multijet events to pass the $p_{\mathrm{T}}^{\mathrm{miss}}$ cut of the SR is low[123]. However, due to the very high jet production cross section at the LHC this type of fake $p_{\mathrm{T}}^{\mathrm{miss}}$ background is produced at a similar rate as the SM signal process $Z \to \nu\nu$ + jets, if no rejection cuts are applied.

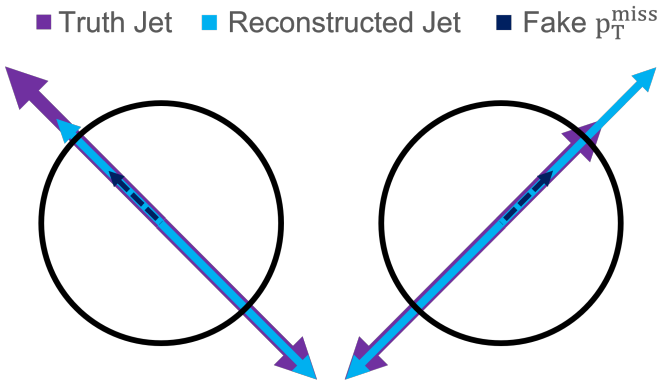

Figure 8.1.: Sketch of a dijet event in the transverse plane of the detector. The dijets are balanced on truth level (violet). A fluctuation of the jet energy at detector-level (light blue) leads to an energy imbalance in the transverse plane and the reconstruction of fake $p_{\mathrm{T}}^{\mathrm{miss}}$ (dark blue). Typically the fake $p_{\mathrm{T}}^{\mathrm{miss}}$ is close to one of the jets in ϕ.

The fake $p_{\mathrm{T}}^{\mathrm{miss}}$ background can be rejected very efficiently by vetoing events that have a highly energetic jet close to the $p_{\mathrm{T}}^{\mathrm{miss}}$ in the transverse plane of the detector. The veto exploits a topological characteristic related to the reconstruction of the fake $p_{\mathrm{T}}^{\mathrm{miss}}$, which is illustrated in Figure 8.1 for a dijet event in the transverse plane. At particle-level both jets are balanced in p_{T} due to momentum conservation. If a fluctuation of the jet energy happens at the detector-level, the fake $p_{\mathrm{T}}^{\mathrm{miss}}$ is reconstructed pointing along the same axis as the fluctuating jet in the transverse plane.

This motivates the $\Delta\phi\left(jet, p_{\mathrm{T}}^{\mathrm{miss}}\right)$ veto for the first four leading jets, which is applied in the SR. Figure 8.2 shows the effect of this veto on the signal efficiency and background rejection for different veto values, using the $Z \to \nu\nu$ + jets signal MC simulation and a fake background sample. The generation of this background sample is discussed in the following section. At the chosen veto value of $\Delta\phi\left(jet, p_{\mathrm{T}}^{\mathrm{miss}}\right) < 0.4$ a background rejection of 98.1 % is achieved, while retaining 91.7 % of the signal.

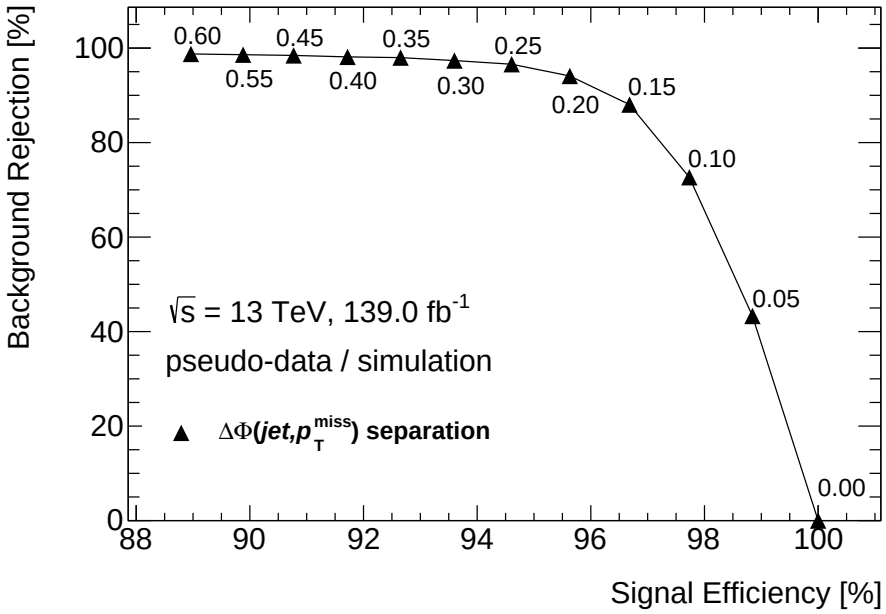

Figure 8.2.: Background rejection and signal efficiency for the fake $p_{\mathrm{T}}^{\mathrm{miss}}$ background and the $Z \rightarrow \nu\nu$ + jets signal for different values of the $\Delta\phi\left(jet, p_{\mathrm{T}}^{\mathrm{miss}}\right)$ cut. The pseudo-data for the fake $p_{\mathrm{T}}^{\mathrm{miss}}$ background is generated using the Jet Smearing method.

The residual background that remains after the veto is estimated using the Jet Smearing method discussed in the following section.

8.1.1. The Jet Smearing Method

The multijet background is estimated using a data-driven procedure called the Jet Smearing method [123], since it is difficult to estimate in MC simulation. One reason for this is that jet energy fluctuations that generate enough $p_{\mathrm{T}}^{\mathrm{miss}}$ to enter the SR are rare. This makes it challenging to generate sufficient MC simulation statistics[123]. Furthermore, the effects of high jet multiplicity and the non-Gaussian tail of the $p_{\mathrm{T}}^{\mathrm{miss}}$ resolution distribution are typically not well modelled[96][123].

The Jet Smearing method is based on the idea that it is possible to reproduce the jet energy fluctuations that lead to the reconstruction of fake $p_{\mathrm{T}}^{\mathrm{miss}}$ and create a pseudo-data sample that mimics the background behaviour. This pseudo-data sample is then used for the background estimation. A brief overview of the method is given in this paragraph and a detailed description of each step is provided in the subsequent sections.

The first step of the Jet Smearing method is the selection of a sample of well-measured seed multijet seed events in which the jets have undergone only little energy fluctuations. The second step is to produce the pseudo-data by varying the momenta of these jets according to the calorimeter jet response, which encodes the sources of the jet energy fluctuations. In the final step the pseudo-data is used to determine the shape of the background in the SR.

This shape is then normalised in a control region (CR) using collision data.

Selection of the Seed Events

The seed event sample is built by first selecting a set of multijet events and then choosing the subsample where the jets have undergone only little fluctuations of the jet energy. To select the events at least two jets are required and events with leptons in the final state are removed. The leading jet has to fulfil $p_{\mathrm{T}} > 50\,\mathrm{GeV}$ to ensure adequate separation from the lowest leading jet p_T cut used in the analysis ($p_{\mathrm{T}} > 80\,\mathrm{GeV}$ in the VBF phase space). This is necessary to properly account for events migrating at the phasespace boundary, i.e. to account for events with a low p_{T} leading jet that enter because the jet energy fluctuates up.

Dedicated single jet triggers are used to pre-select the events for the multijet sample. The triggers have to be fully efficient at the selection cut value of $p_{\mathrm{T}} > 50\,\mathrm{GeV}$. The trigger with the highest threshold that fulfils this criterium is the HLT_j35. However, the low p_{T} single jet triggers are heavily prescaled, which would lead to poor statistical precision if only the HLT_j35 was used. To maximise the available statistics the events are split into several regions according to the leading jet p_{T} in each event and the events in each region are selected using a dedicated single jet trigger. The p_{T} regions and triggers are shown in Table 8.1. In this way it is possible to benefit from the lower prescales of the higher p_{T} single jet triggers.

Trigger	Leading jet p_{T} threshold [GeV]	Average prescale
HLT_j35	49.5	6.4×10^5
HLT_j45	60.5	1.8×10^5
HLT_j60	75.5	1.6×10^4
HLT_j85	104.5	1.5×10^4
HLT_j110	131.0	1.9×10^3
HLT_j175	205.5	2.9×10^2
HLT_j260	297.5	4.2×10^1
HLT_j360	416.5 (2017/18 only)	1.1×10^1
HLT_j380	436.0 (2015/16 only)	1
HLT_j420	463.5 (2017/18 only)	1

Table 8.1.: Single jet trigger used to select seed events. The thresholds are chosen such that the corresponding trigger is fully efficient[76].

The leading jet p_{T} thresholds are selected such that the corresponding trigger is fully efficient above the threshold. The triggered events are then each corrected for the corresponding prescale P_X by applying the weight $w_X = \frac{1}{P_X}$ to the event [120].

The next step in the seed selection is to determine the subset of multijet events that have undergone only little fluctuations in the jet energy. The simplest solution to this would be to place an upper limit on the absolute $p_{\mathrm{T}}^{\mathrm{miss}}$ in the event. However, it has been shown in [123] that such a cut biases the jet p_{T} distribution of the seed events. This can be understood as follows. For the $p_{\mathrm{T}}^{\mathrm{miss}}$ resolution $\sigma\left(p_{\mathrm{T}}^{\mathrm{miss}}\right)$ it is known that $\sigma\left(p_{\mathrm{T}}^{\mathrm{miss}}\right) \propto \sqrt{\sum p_{\mathrm{T}}}$, where $\sum p_{\mathrm{T}}$ is the p_{T} sum of the jets contributing to $p_{\mathrm{T}}^{\mathrm{miss}}$ [96]. As the $p_{\mathrm{T}}^{\mathrm{miss}}$ in multijet events is generated

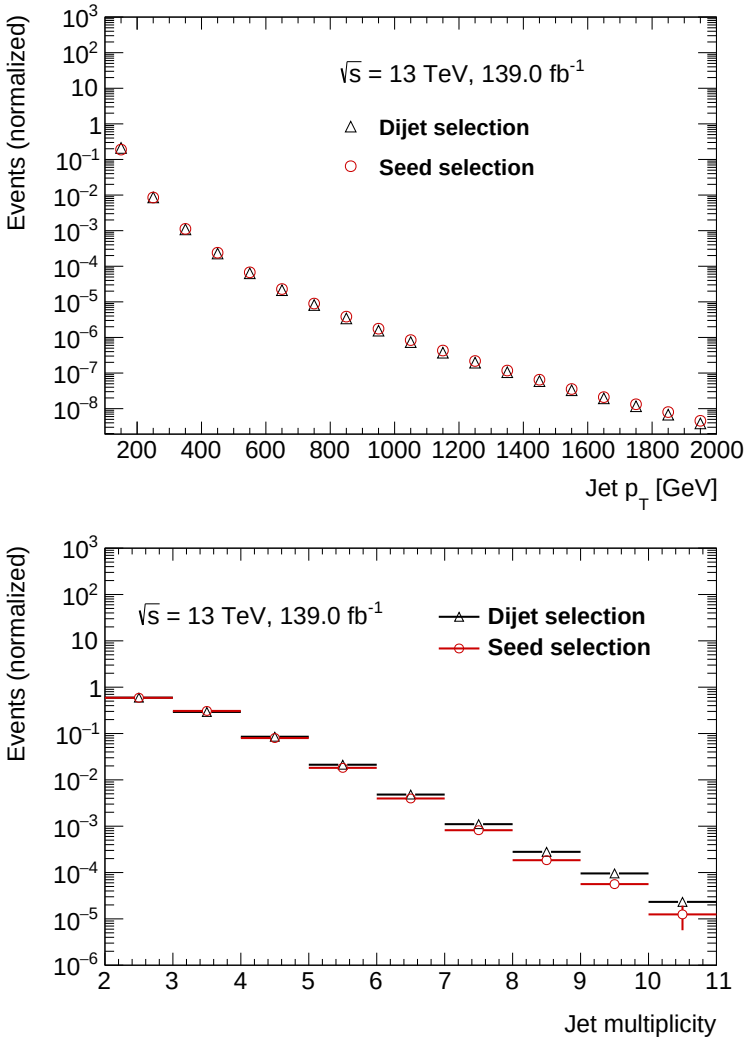

Figure 8.3.: Inclusive jet p_{T} (top panel) and jet multiplicity (bottom panel) distributions for events before (black) and after (red) the seed selection.

by jet energy fluctuations, a cut on the absolute $p_{\mathrm{T}}^{\mathrm{miss}}$ in the event would therefore bias the jet p_{T} distribution, as events with a large $\sqrt{\sum p_{\mathrm{T}}}$ would be perferably removed.

To remove the dependence of the cut on the $p_{\mathrm{T}}^{\mathrm{miss}}$ resolution $\sigma\left(p_{\mathrm{T}}^{\mathrm{miss}}\right)$, a new observable is constructed as proposed in [123]. Since $\sigma\left(p_{\mathrm{T}}^{\mathrm{miss}}\right)$ is proportional to $\sqrt{\sum p_T}$ a cut on the $p_{\mathrm{T}}^{\mathrm{miss}}$ significance

$$S = \frac{p_{\mathrm{T}}^{\mathrm{miss}}}{\sqrt{\sum p_T}} < 0.5 \tag{8.1}$$

is applied, which does not lead to a bias in the jet p_{T} distribution.

This is demonstrated in Figure 8.3 for the inclusive jet p_{T} distribution and the jet multiplicity. The nominal dijet selection is shown in black and the seed selection with the additional

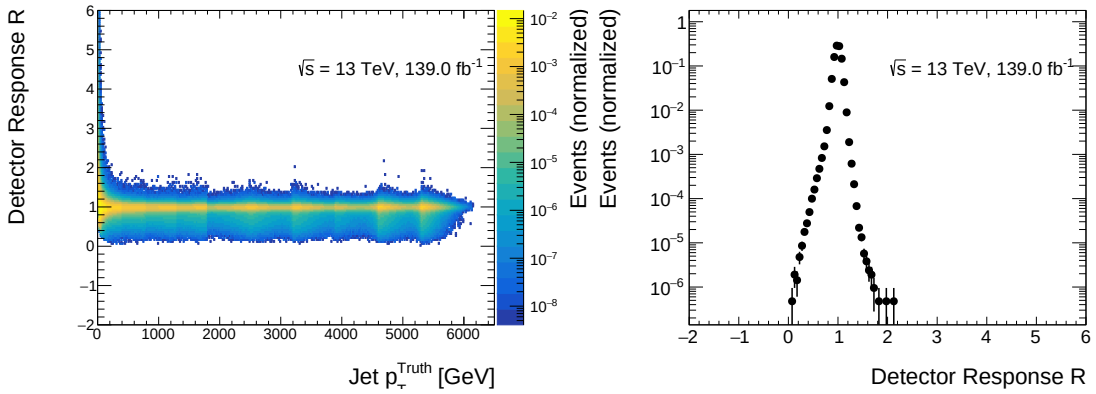

Figure 8.4.: Left panel: Data-constrained jet response as a function of truth jet p_{T}. Right panel: Example of the response for a truth jet p_{T} slice (260 GeV to 280 GeV).

$p_{\mathrm{T}}^{\mathrm{miss}}$ significance cut applied is shown in red. In both cases the shape of the distributions agree well, with only a small bias at very large jet multiplicities.

Derivation of the Jet Response

To apply the jet energy fluctuations observed in data to the seed events, data-constrained jet response maps are used. These are provided centrally by the ATLAS collaboration. In this paragraph a brief overview of their derivation is given, more details can be found in [123].

The jet response R as a function of truth jet p_{T}, shown in Figure 8.4, is derived from dijet MC simulation on a per-jet basis as the ratio of reconstructed jet p_{T} and true jet p_{T}

$$R = \frac{p_T^{reco}}{p_T^{truth}}, \tag{8.2}$$

for isolated jets ($\Delta R > 0.2$). To correct for the known mismodelling of the jet energy resolution in MC the four momenta of the reconstructed jets in MC simulation are smeared to agree with the broader resolution observed in data[91]. Furthermore, the tails of the jet response are also constrained using a measurement in data. This is especially important since large energy fluctuations are typically involved when producing the large fake $p_{\mathrm{T}}^{\mathrm{miss}}$ needed for a background event to enter the SR.

Generation and Validation of the Pseudo-data

The central step of the Jet Smearing method is the artificial fluctuation of the jet energies in the seed events according to the jet response to generate the pseudo-data. The procedure is sketched in Figure 8.5 and described in the following.

The seed events are selected to be well-measured, therefore their reconstructed p_{T} is very similar to their true p_{T}. To apply the jet response to a given jet, the four momentum vector of that jet is scaled with a factor drawn randomly from the corresponding truth p_{T} slice in the jet response map shown in Figure 8.4. This procedure is applied to each jet. This

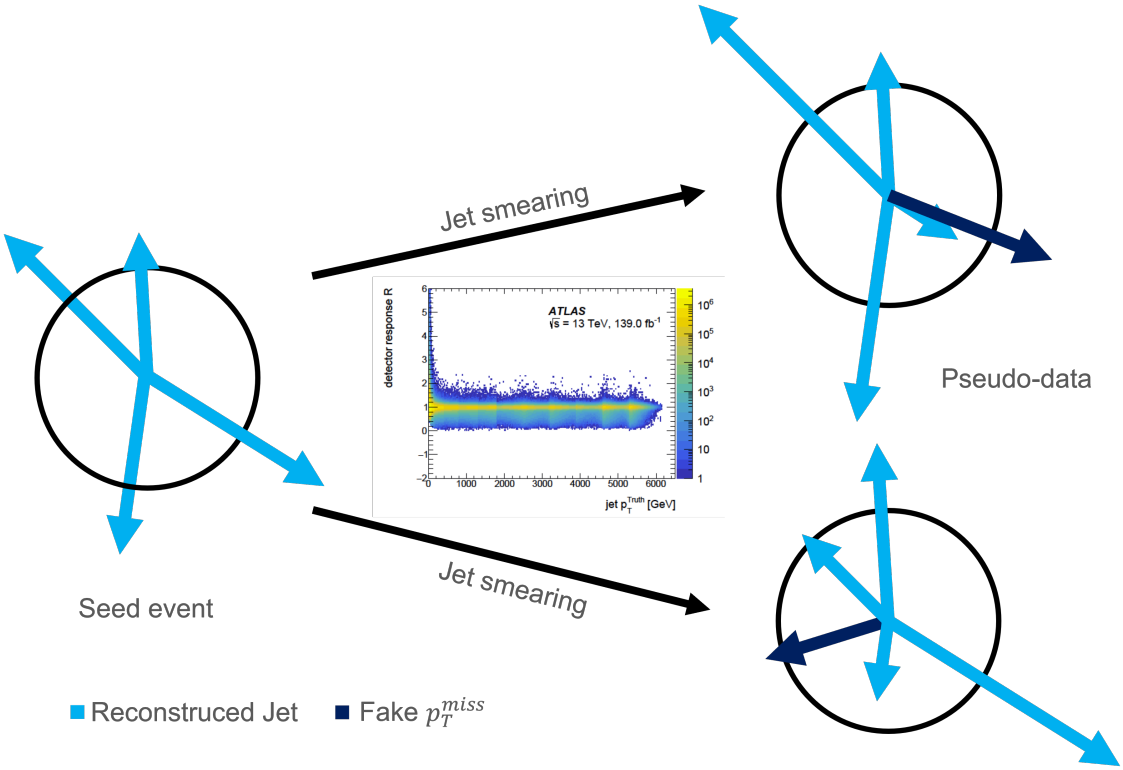

Figure 8.5.: Sketch of the pseudo-data generation. Each jet (light blue) in a well-measured seed event is fluctuated according to the calorimeter jet response (middle) to generate a pseudo-event (right) with fake $p_{\mathrm{T}}^{\mathrm{miss}}$ (dark blue). This procedure is repeated 2000 times for each seed event.

leads to deviations from the momentum balance between the jets in the transverse plane and the generation of fake $p_{\mathrm{T}}^{\mathrm{miss}}$. This procedure is repeated 2000 times for each seed event and allows for the generation of a large set of pseudo-data. As the jet energy fluctuations produced by the artificial smearing with the jet response are expected to reproduce those energy fluctuations in multijet events leading to fake $p_{\mathrm{T}}^{\mathrm{miss}}$ in the detector, this pseudo-data is used to model the fake $p_{\mathrm{T}}^{\mathrm{miss}}$ background.

It is necessary to verify that no biases in are introduced in jet kinematic distributions in the the pseudo-data with respect to the seed events during the smearing, to ensure a proper background modelling. Therefore several quantities are compared before and after the smearing. The two most important ones are shown in Figure 8.6. The top panel shows the leading jet p_{T}, where a small bias towards a softer spectrum is observed. This is addressed during the validation of the method described in below.

The bottom panel shows an observable called M_{eff}, which describes the sum of $p_{\mathrm{T}}^{\mathrm{miss}}$ and the hadronic activity in the event and is defined as

$$M_{\mathrm{eff}} = p_{\mathrm{T}}^{\mathrm{miss}} + H_{\mathrm{T}} = p_{\mathrm{T}}^{\mathrm{miss}} + \sum_{jets} p_{\mathrm{T}}. \tag{8.3}$$

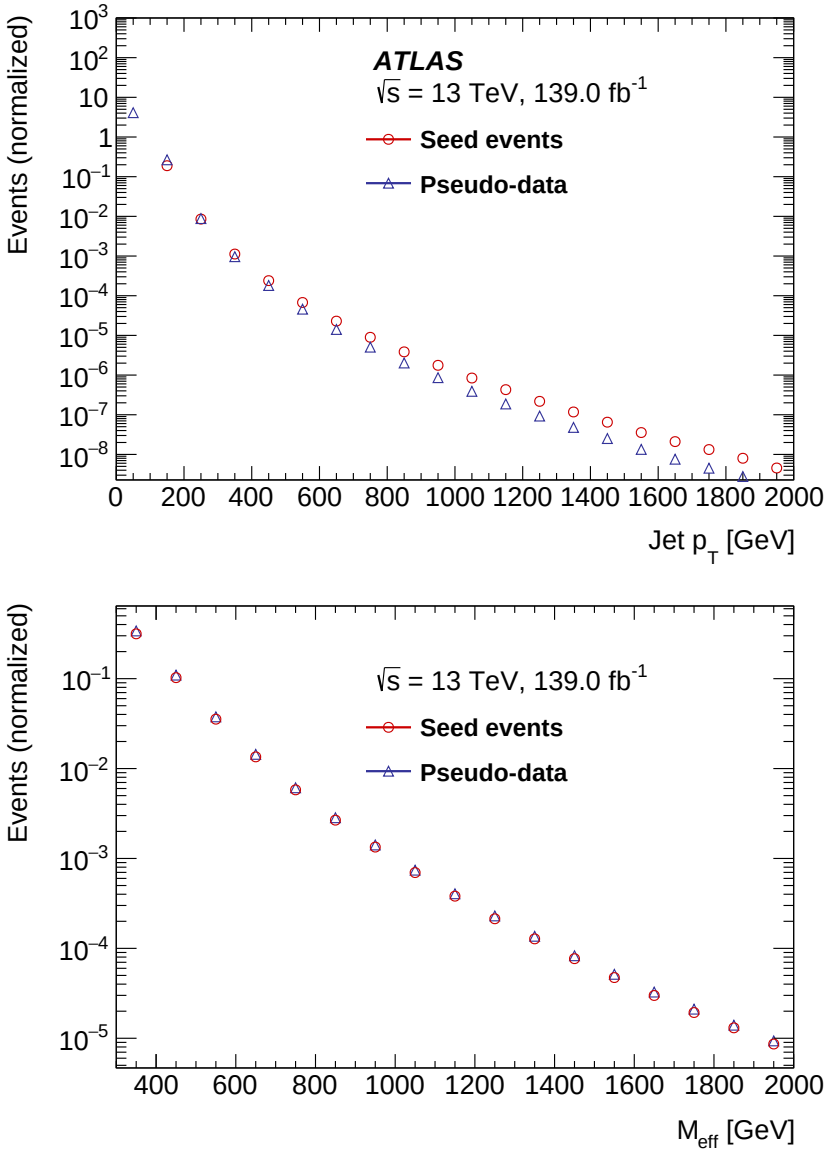

Figure 8.6.: Jet p_{T} (top panel) and M_{eff} (bottom panel) for seed events (red) and pseudo-data events (blue). The pseudo-data distribution has been normalised to the seed event distribution.

Any deviation of M_{eff} after the smearing procedure from the original distribution would indicate a bias, since during the smearing transverse energy is only shifted between its component terms. No deviation is observed.

The ability of the pseudo-data to describe the shape of the multijet background is also tested in collision data. To this end a background-enriched multijet CR is defined by inverting the $\Delta\phi\left(jet, p_{\mathrm{T}}^{\mathrm{miss}}\right)$ veto and requiring at least one jet in the event to be closer to the $p_{\mathrm{T}}^{\mathrm{miss}}$ than $\phi\left(\Delta\phi\left(jet, p_{\mathrm{T}}^{\mathrm{miss}}\right)\right) < 0.3$. To keep this CR close to the actual SR, all other SR cuts are applied in addition. The definition of the SR and CR as a function of $\Delta\phi\left(jet, p_{\mathrm{T}}^{\mathrm{miss}}\right)$ is shown in

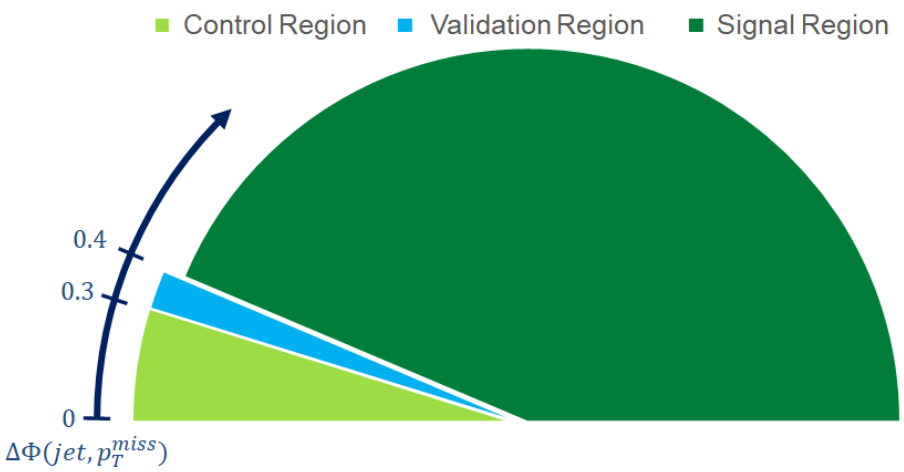

Figure 8.7.: Definition of the control and validation regions used for the fake $p_{\mathrm{T}}^{\mathrm{miss}}$ estimate relative to the signal region in $\Delta\phi\left(jet, p_{\mathrm{T}}^{\mathrm{miss}}\right)$.

Figure 8.7.

The multijet CR has a very large multijet background component as is demonstrated in the top panel of Figure 8.8. The top part shows the data distribution in the CR together with the MC simulation of the relevant SM processes as a function of $p_{\mathrm{T}}^{\mathrm{miss}}$ in the VBF phase space and the ratio of the two in the bottom part. The very large disagreement between data and MC simulation in the bulk of the distribution is due to the presence of multijet background, which is not described by the simulation. The disagreement in the last bin of the distribution is attributed to poor modelling in the MC simulation, since the multijet background contribution drops strongly towards high $p_{\mathrm{T}}^{\mathrm{miss}}$ [123].

The pseudo-data generated with the Jet Smearing method provides a very good shape description of the multijet background. This is demonstrated in the bottom panel of Figure 8.8[1], which shows the same data and MC simulation distributions as the top panel, but with the multijet background component determined from the pseudo-data (dark blue) added to the predictions. Excellent shape agreement within the statistical and systematic uncertainties is observed in the bulk of the distribution where the multijet background is dominant. The multijet background component has been determined by applying all cuts and selection criteria of the multijet CR to the pseudo-data and normalising it to the difference between data and MC simulation, thereby providing a shape test. The systematic uncertainty on the background estimate is discussed in more detail in Section 8.1.1.

[1]The corresponding distributions for the monojet phase space are shown in Section B.1.1.

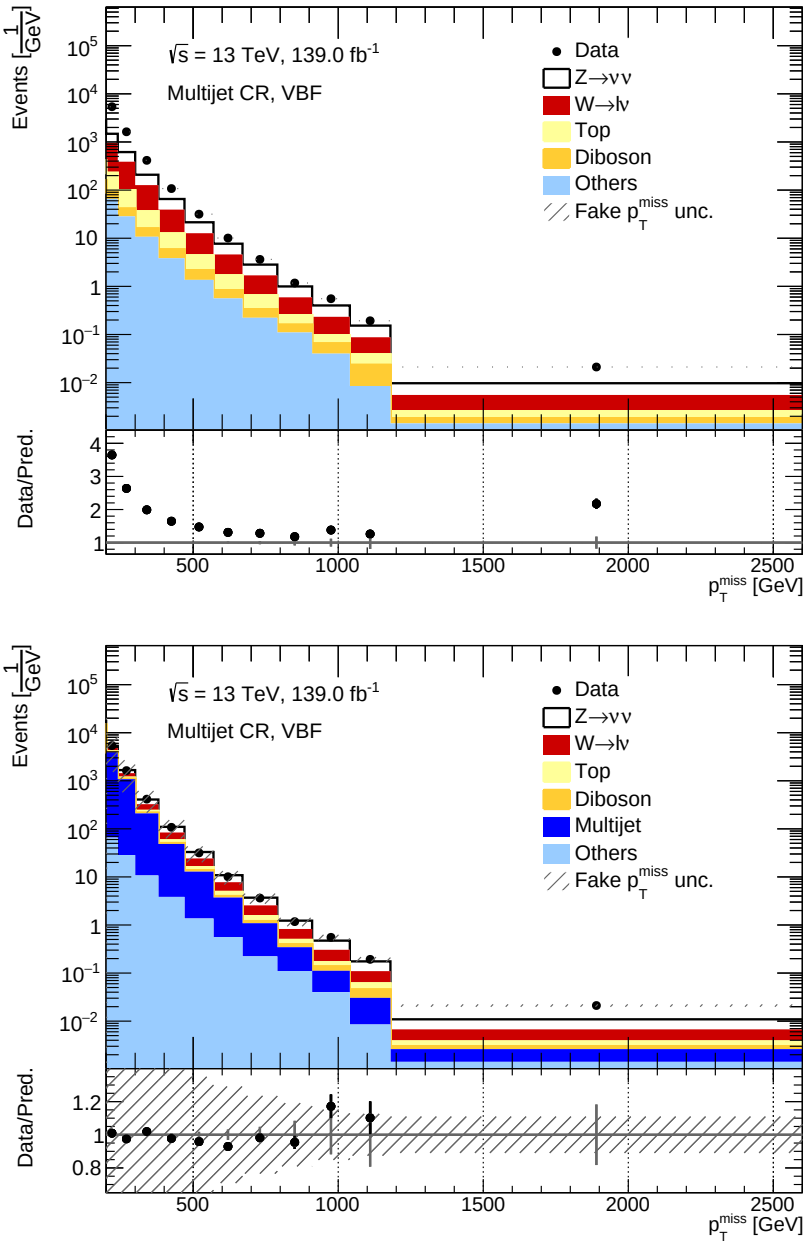

Figure 8.8.: $p_{\mathrm{T}}^{\mathrm{miss}}$ distribution in the multijet CR in the VBF phase space for collision data and MC simulation predictions alone (top panel) and collision data, MC simulation and normalised pseudo-data in dark blue (bottom panel). The bottom part of each figure shows the ratio of the data and the sum of the various process predictions, with the statistical uncertainty on the data shown in grey and the statistical uncertainty on the predictions shown in black. The systematic uncertainty on the background estimate is shown as a shaded band.

Multijet Background Estimate

The estimate of the multijet background in the SR is performed in a two step procedure. First a background shape template is determined by applying all selection criteria of the SR to the pseudo-data. In a second step a normalisation factor is calculated using the multijet CR introduced in the previous section. This normalisation factor is given by

$$\frac{N^{tot}_{CR,data} - N^{tot}_{CR,MC}}{N^{tot}_{CR,pseudo-data}}, \tag{8.4}$$

which is the ratio of the total difference in number of events between data ($N^{tot}_{CR,data}$) and MC simulation ($N^{tot}_{CR,MC}$) in the multijet CR and the total number of pseudo-data events ($N^{tot}_{CR,pseudo-data}$) in the multijet CR. This is valid under the assumption that the difference between data and MC simulation in the multijet CR is entirely caused by multijet background. This assumption is justified by the construction of the multijet CR, which leads to a very high multijet background contribution in the multijet CR. However, a further validation of the method is performed below to test if this assumption is valid.

The final multijet background estimate in the SR in a bin i is therefore given by

$$N^{i}_{SR} = N^{i}_{SR,pseudo-data} \frac{N^{tot}_{CR,data} - N^{tot}_{CR,MC}}{N^{tot}_{CR,pseudo-data}}, \tag{8.5}$$

where $N^{i}_{SR,pseudo-data}$ is the number of pseudo-data events in the background shape template in bin i, which is multiplied by the normalisation factor. Please note that same pseudo-data set is used to determine the templates in the SR and the number of multijet background events in the multijet CR, such that the final multijet background estimate is independent of the amount of pseudo-data generated.

The result of the background estimate as a function of $p_{\mathrm{T}}^{\mathrm{miss}}$ in the monojet phase space is shown in Figure 8.9[2] together with the statistical and systematic uncertainty on the background estimate. The largest background contribution is in the first bin of the $p_{\mathrm{T}}^{\mathrm{miss}}$ distribution and the relative background contribution strongly decreases towards higher $p_{\mathrm{T}}^{\mathrm{miss}}$. This systematic uncertainty on the background estimate is discussed in the following section. Tables with the number of estimated background events per bin in each observable are shown in Section B.1.3.

Validation of the Background Estimate

The multijet estimation method using the Jet Smearing method is validated in collision data to verify several additional assumptions that enter into the procedure. These are: the premise that the sources of fake $p_{\mathrm{T}}^{\mathrm{miss}}$ due to energy fluctuations can be properly described by the data-constrained response maps, that energy fluctuations are the dominant contributor to the fake $p_{\mathrm{T}}^{\mathrm{miss}}$, that the jet response is independent of event-level quantities and therefore

[2] The results for the VBF phase space are shown in Section B.1.2.

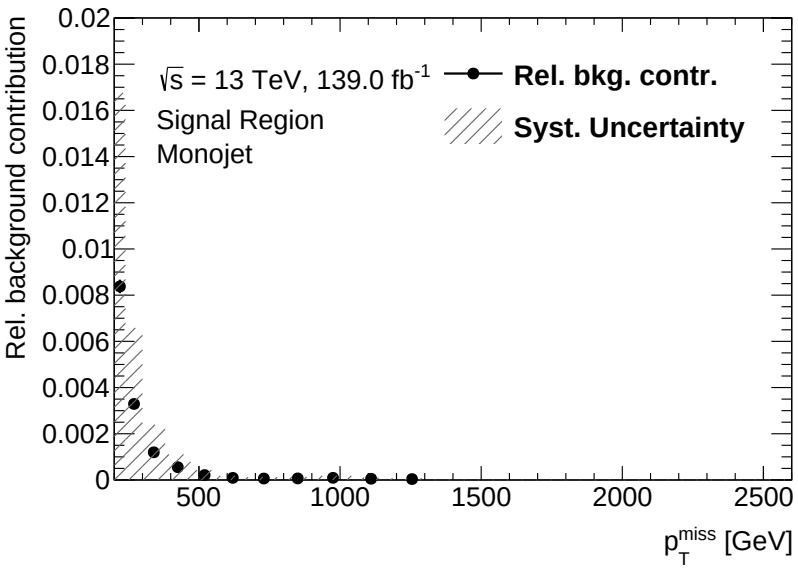

Figure 8.9.: Relative contribution of the multijet background to SR as a function of $p_{\mathrm{T}}^{\mathrm{miss}}$ in the monojet phase space. The statistical uncertainty is shown as error bars on the points and the systematic uncertainty on the background estimate is shown as a grey hashed band.

applicable on a jet-by-jet basis and that the background normalisation can be determined from the difference between data and MC simulation in the multijet CR [123].

To test the assumptions and to make certain that the small biases observed in the seed selection and smearing described above do not pose a problem, a validation region (VR) is defined that is very close but orthogonal to the SR. It differs from the SR selection only by the $\Delta\phi\left(jet, p_{\mathrm{T}}^{\mathrm{miss}}\right)$ veto, which is modified to $0.3 < \Delta\phi\left(jet, p_{\mathrm{T}}^{\mathrm{miss}}\right) < 0.4$ (see Figure 8.7 for the definition of the VR with respect to the SR and the multijet background-enriched CR).

Following all steps described above, a full background estimate is performed for the VR, with the same systematic uncertainty of 100 % of the event yield per bin. Figure 8.10 shows the comparison of data, MC simulation and the multijet background estimate in the validation region together with the systematic uncertainty on the background estimate as a function of $p_{\mathrm{T}}^{\mathrm{miss}}$ in the monojet phase space[3]. In general good agreement within the systematic uncertainty is observed, validating the application of the Jet Smearing method.

The systematic uncertainty on the background estimate is taken to be 100 % of the event yield, which is very conservative. However a more precise estimation of the uncertainty would be very involved, as the Jet Smearing method has many different parts, which have a systematic uncertainty associated. Since the background contribution in the $p_{\mathrm{T}}^{\mathrm{miss}}$ distribution in the SR is very small, this is deemed acceptable.

[3]The distributions for all observables in the validation region are shown in Section B.1.4.

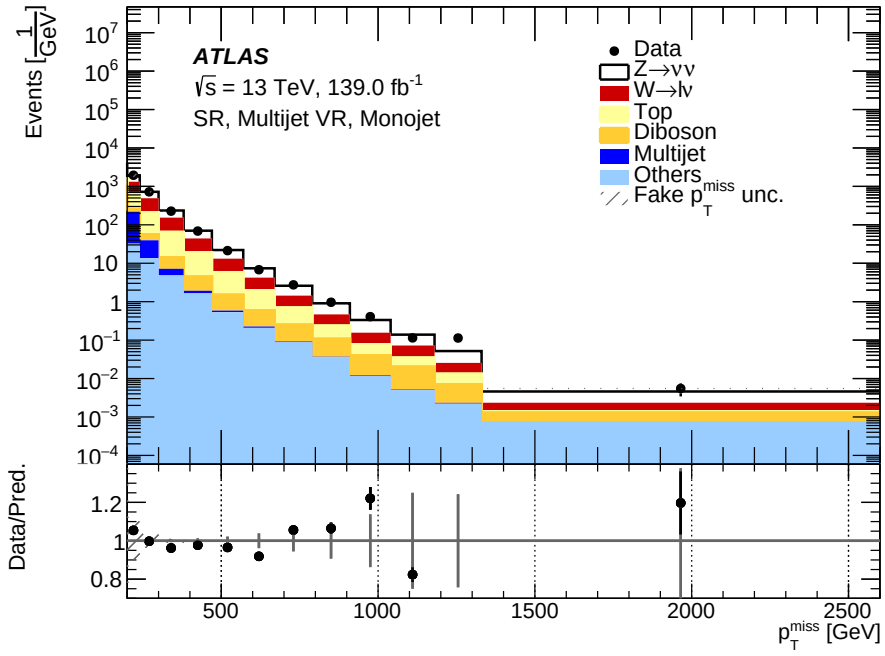

Figure 8.10.: Data, MC simulation and multijet background estimate as a function $p_{\mathrm{T}}^{\mathrm{miss}}$ in the monojet phase space. The bottom part of each figure shows the ratio of the data and the sum of the various process predictions, with the statistical uncertainty on the data shown in grey and the statistical uncertainty on the predictions shown in black. The systematic uncertainty on the background estimate is shown as a shaded band.

8.2. Beam-induced Background in the Signal Region

Another type of background event that can contain large fake $p_{\mathrm{T}}^{\mathrm{miss}}$ and enter the SR is caused by decay products of the LHC beam halo penetrating into the ATLAS detector, as well as elastic and inelastic beam-gas interactions [124]. The beam halo is constituted by protons that have drifted out of the core of the LHC beams or by protons undergoing elastic scattering on the beam gas [125]. To prevent damage to the machine, especially the superconducting magnets, this halo is constantly removed by a sophisticated cleaning system. This system consists of several sets of collimators and absorbers distributed throughout the LHC ring, which are used to induce shower cascades of the beam halo protons and absorb the decay products [126][127]. In addition, the physics experiments are protected by heavy shielding which absorbs most of the remaining particles produced in the halo showers [58]. This is illustrated in Figure 8.11.

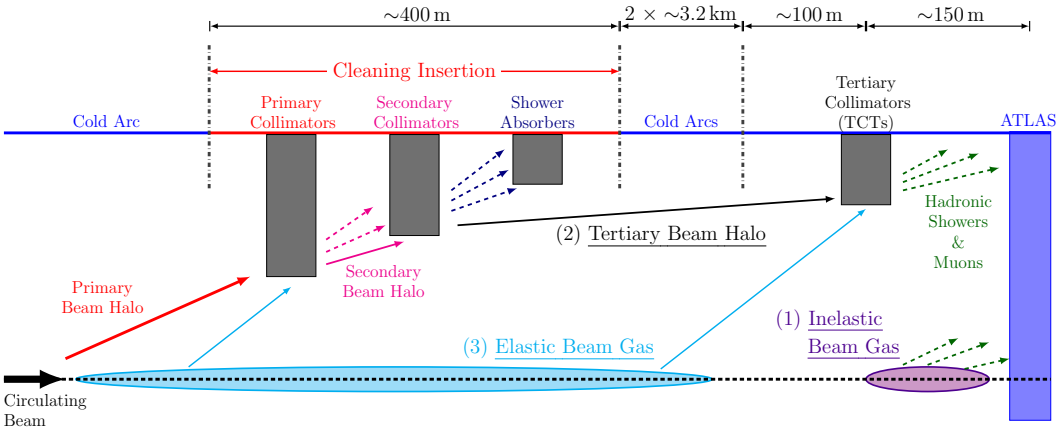

Figure 8.11.: Schematic illustration of the three sources of BIB reaching ATLAS: (1) nearby inelastic beam–gas collisions, (2) tertiary beam halo losses on the TCT and (3) protons deflected by elastic beam–gas collisions and hitting the TCT. The distance from the beam to the collimators is a few millimetres. Typically beam-induced background at higher radii can reach the calorimeters and cause fake jets. Adapted from [128].

However, highly energetic beam-background muons from these showers can pass the detector shielding and cause fake $p_{\mathrm{T}}^{\mathrm{miss}}$+jets events [127]. This is illustrated in Figure 8.12 with an event display of a typical *beam-induced background* (BIB) event. A beam-background muon enters the detector from the right (b) and deposits energy in the calorimeter via Bremsstrahlung, which is reconstructed as a highly energetic fake jet. This fake jet is not balanced by additional energy deposits in the transverse plane of the detector (a), which leads to the reconstruction of large fake $p_{\mathrm{T}}^{\mathrm{miss}}$ (dashed red line). This type of event can enter the SR if enough fake $p_{\mathrm{T}}^{\mathrm{miss}}$ is produced.

The contribution of BIB to $p_{\mathrm{T}}^{\mathrm{miss}}$ + *jets* events measured in data is of the same order of magnitude as the signal process $Z \rightarrow \nu\nu$ + jets, therefore efficient removal techniques are

needed [124]. The strategies employed to remove these kind of events and the method used to estimate the residual background after the removal are discussed in the following sections.

8.2.1. Characteristics and Removal of Beam-induced Background

The fake jets in BIB events have characteristic energy deposition and timing properties that allow for their efficient removal. These characteristics also allow to estimate the residual background after removal. This is discussed in the following sections.

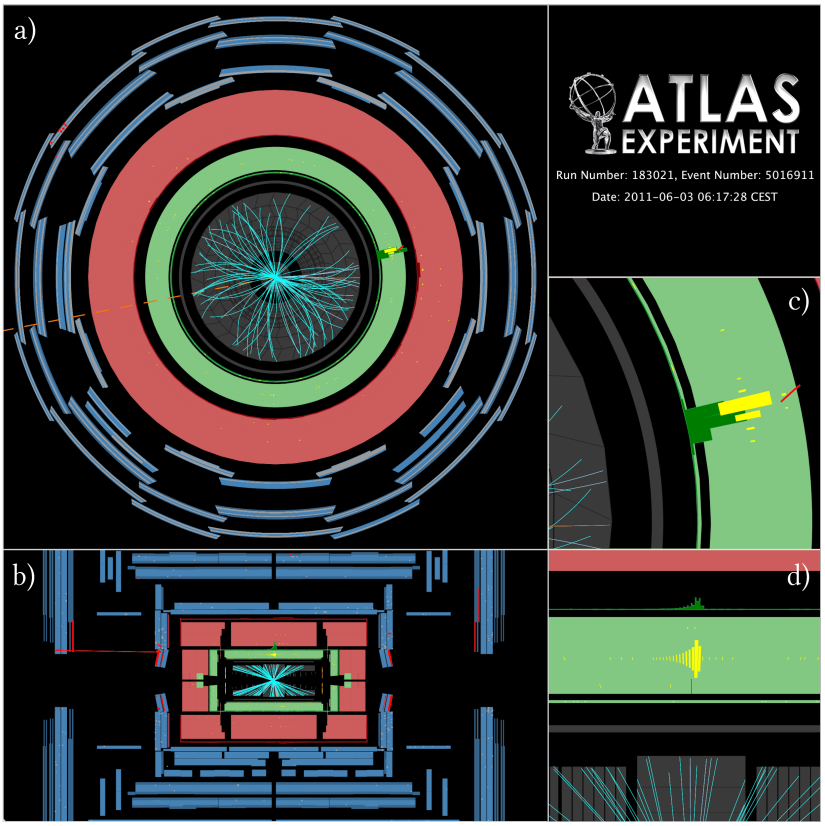

Figure 8.12.: Example of BIB event with the beam-induced muon entering from the right and causing a fake jet. In the longitudinal projection (b), chambers of the muon system with hits (highlighted in red) are seen on both sides. Electromagnetic calorimeter cells (yellow) in-between contain large energy (green towers) that forms a fake jet. A muon track (red line) parallel to the z-axis is reconstructed on the left side of the detector. The transverse projection (a) shows $p_{\mathrm{T}}^{\mathrm{miss}}$ (dashed line) opposite to the fake jet. The reconstructed tracks (blue) in the inner tracking detector do not point towards the fake jet. A detailed view (c) shows that the calorimeter cells and the muon track are aligned in ϕ. Focusing on the energy depositions in the electromagnetic calorimeter in the longitudinal projection (d) reveals that the fake jet consists of a cluster elongated in the z-direction. Adapted from [125].

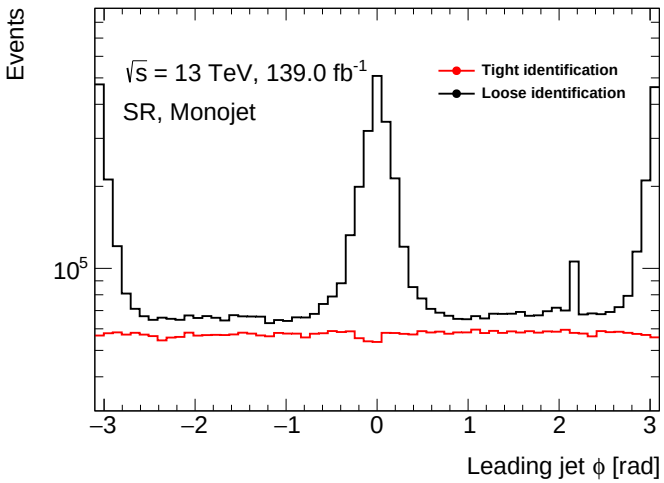

Figure 8.13.: Leading jet ϕ distribution in the monojet phase space in the SR, with the loose (black) and tight (red) identification applied.

Energy Deposition Characteristics and Tight Jet Identification

The energy deposition topology of BIB events in the calorimeters can be understood by considering the typical path a beam-induced muon takes in the detectors.

The beam-induced muons, typically enter the detector in parallel to the beam-line and therefore deposit most of their energy in a single layer of the ATLAS calorimeters (Figure 8.12 b) and d)). This is characterised by the maximum sampling fraction f_{max}, defined as the maximum energy fraction in a single calorimeter layer, which is expected to be high for the corresponding fake jet.

The energy deposition produced by the muon also has no associated tracks to the primary vertex in the event (Figure 8.12 c)). This leads to a low value of the charge fraction f_{ch}, defined as the fraction of the p_{T} of the tracks associated to the jet and the total jet p_{T} [129].

To reject this type of fake jet, a cut on the ratio of these two variables given by

$$\frac{f_{ch}}{f_{max}} > 0.1 \tag{8.6}$$

has proven useful [129] [4]. The combination of the loose jet identification and the cut given in Equation 8.6 form the tight identification for jets, which is required for the leading jet in the event selection. Since the charge fraction can only be determined in the acceptance of the ATLAS tracking system, the tight identification can only be applied in the corresponding η range.

The tight jet identification allows to remove most of the BIB events, while keeping $> 99\,\%$ of the signal events [129]. This is demonstrated in Figure 8.13, which shows the ϕ distribution of the leading jet in the monojet phase space in data before (black) and after (red) applying the tight identification to the leading jet. A clear structure in ϕ is visible in the original

[4] The cut value of 0.1 is optimized by the ATLAS JET/ETmiss group [124].

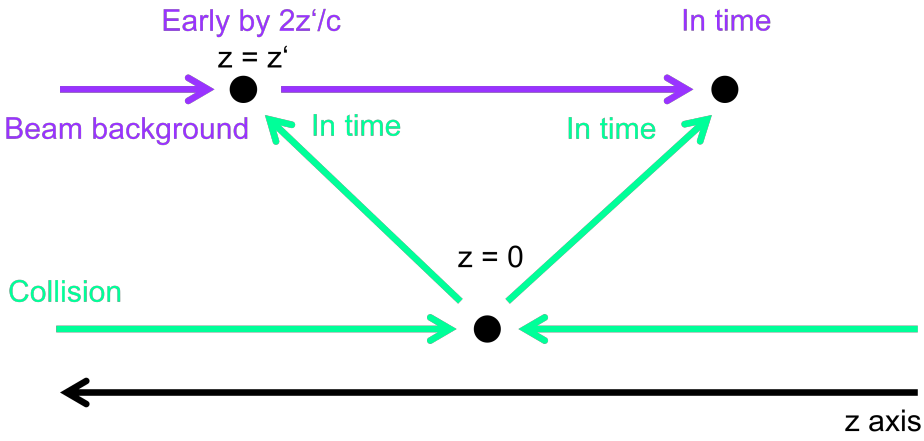

Figure 8.14.: Sketch of the flight path of BIB (violet) and the normal collision process (green). The time of the collision corresponds to $t = 0$. Collision products are always in time, due to time-of-flight corrections. The timing of the BIB depends on the z coordinate.

distribution, with prominent peaks at $\phi = 0$ (towards the center of the LHC) and $\phi = \pm\pi$ (away from the center of the LHC). This structure is caused by the dipole magnets of the LHC which are bending the trajectories of the beam-induced muons in a way similar to the beam. [5]

Jet Timing

Another important characteristic of the BIB is the timing of the fake jets, which is typically early with respect to the collision products in the detector. This is illustrated in Figure 8.14 for muons passing into the detector from the left. The muons enter the detector at the same time as the proton bunch associated to the original halo protons that produced them. Therefore they arrive always early with respect to the collision products, as the proton bunch first has to travel to the interaction point to produce a collision, whereas the muons enter directly into the calorimeters.

The timing of the fake jets depends on its z-position with respect to the interaction point ($z = 0$), since the timing determined at a given point in the detector is corrected for the time-of-flight from the interaction point. This is further illustrated in Figure 8.15, which shows the timing t of the leading jet as a function of η. While the jets originating from genuine collisions form a band around $t = 0$, there are two clear arcs visible for $t < 0$, which are caused by the fake jets from the BIB. There is a clear correlation between timing and η for these jets, with those further away from the interaction point occurring at earlier times. There are also two

[5] An additional structure is slightly visible in Figure 8.13 as an asymmetry between the top side ($\phi = \frac{\pi}{2}$) and the bottom side ($\phi = -\pi/2$) of the detector. It is caused by the longer distance from the beam pipe to the ceiling of the LHC tunnel (2 m) than to the floor (1 m). This allows for different free drift times for kaons/pions of the halo showers, depending on their direction. Hence a lower number of muons is expected in the lower hemisphere of the detector [125].

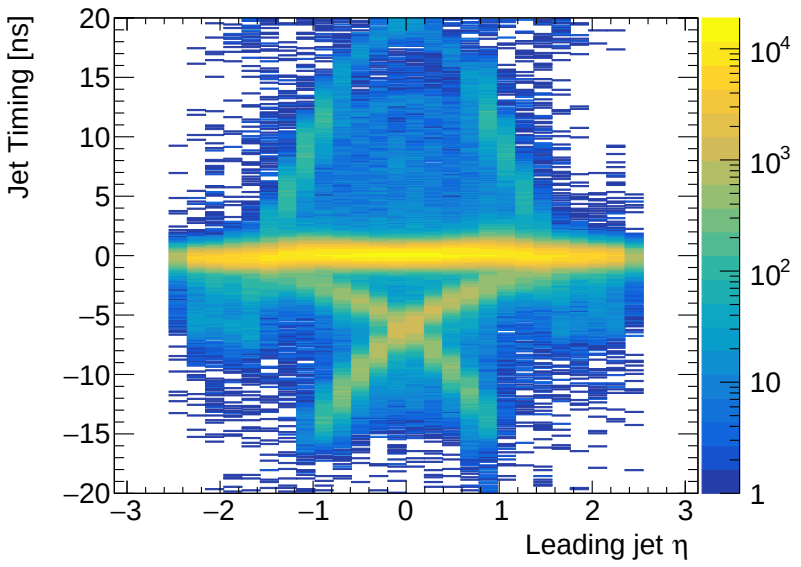

Figure 8.15.: Timing of the leading jet as a function of η.

similar arcs visible for $t > 0$. These are caused by fake jets from BIB belonging to the next proton bunch, which is separated by $\Delta t = 25\,\text{ns}$.

Figure 8.16 shows a direct comparison of the timing distributions in the SR (left panel), which has a clear peak from in-time collision events around $t = 0\,\text{ns}$ and a BIB-enriched CR, which has a broad distribution of out-of-time BIB events. The BIB-enriched CR is defined like the SR, but with the tight jet identification inverted[6].

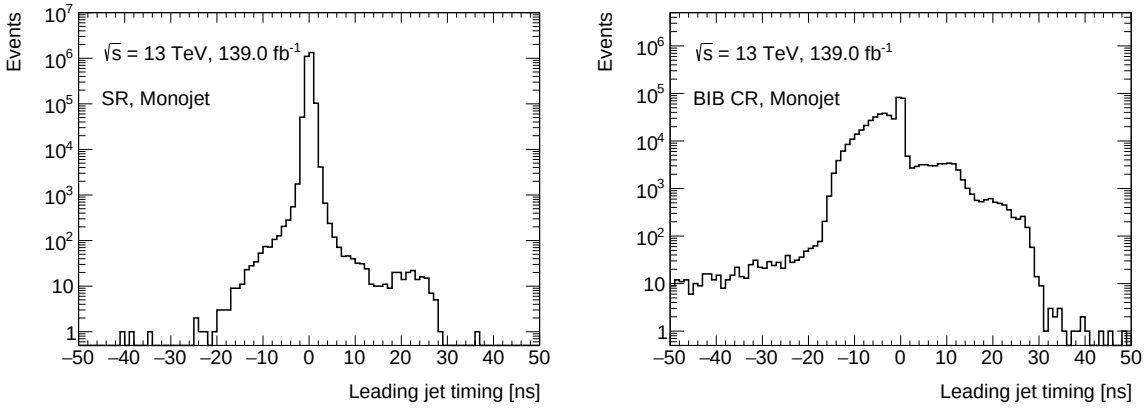

Figure 8.16.: Timing of the leading jet in the SR (left panel) a BIB-enriched CR (right panel).

[6]Rejecting jets that fulfil the tight jet identification and selecting those that fail it.

8.2.2. Beam-induced Background Estimate

The residual background that is not removed by the jet cleaning is estimated using the information provided by the tight jet identification and the jet timing variable.

Region	Selection criteria
SR	tight leading jet
BIB-enriched CR	non-tight leading jet

Table 8.2.: Definition BIB-enriched CR orthogonal to the SR.

In a first step, a BIB-enriched CR orthogonal to the SR is defined by inverting the tight identification (c.f. Table 8.2). In a next step, events are tagged as *positive out-of-time* if the leading jet timing is $t > 5\,\text{ns}$ or *negative out-of-time (n)* if $t < -5\,\text{ns}$. The timing variable and the identification criteria can be assumed to be uncorrelated [125]. This means that the ratio of out-of-time events and all events is independent of the identification and it follows that

$$\frac{N^{\text{CR}}_{t<5\,\text{ns}}}{N^{\text{CR}}_{t<0\,\text{ns}}} = \frac{N^{\text{SR}}_{t<5\,\text{ns}}}{N^{\text{SR}}_{t<0\,\text{ns}}}, \quad \frac{N^{\text{CR}}_{t>5\,\text{ns}}}{N^{\text{CR}}_{t>0\,\text{ns}}} = \frac{N^{\text{SR}}_{t>5\,\text{ns}}}{N^{\text{SR}}_{t>0\,\text{ns}}}. \tag{8.7}$$

The total number of background events is then determined bin-by-bin using

$$N^{\text{SR}} = N^{\text{SR}}_{t<0\,\text{ns}} + N^{\text{SR}}_{t>0\,\text{ns}} = \frac{N^{CR}_{t<0\,\text{ns}}}{N^{CR}_{t<5\,\text{ns}}} N^{SR}_{t<5\,\text{ns}} + \frac{N^{CR}_{t>0\,\text{ns}}}{N^{CR}_{t>5\,\text{ns}}} N^{SR}_{t>5\,\text{ns}}. \tag{8.8}$$

The result of the background estimate is presented in Figure 8.17. The figure shows the relative background contribution to the monojet phase space in the SR as a function of $p_{\text{T}}^{\text{miss}}$, together with the statistical and systematic uncertainties. The relative systematic uncertainty is defined to be 100 % in each bin. Also in the case of the BIB this conservative uncertainty is chosen, as the relative background contribution is small. Tables containing the results for all observables are given in Section B.2.

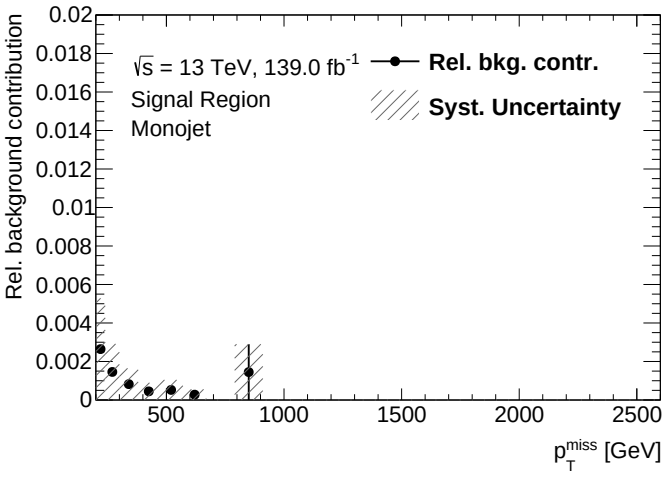

Figure 8.17.: Relative contribution of the BIB estimate to the SR as a function of $p_{\mathrm{T}}^{\mathrm{miss}}$ in the monojet phase space. The statistical uncertainty is shown as error bars on the points and the systematic uncertainty on the background estimate is shown as a grey hashed band.

8.3. Fake Photon Background

Hadronic jets can be reconstructed as photon candidates in the detector. This typically happens if the jets contain a neutral meson, like a π^0 or K^0, which carries a large fraction of the jet momentum and decays into a pair of non-prompt photons, which cause an electromagnetic shower in the EM calorimeter [130]. It is also possible for a hadron to be directly reconstructed as a photon, if a significant amount of energy is deposited in the EM calorimeter [130]. These misidentified jets are called fake photons in the following. The fake photons can in turn lead to background events without prompt photons to enter the γ+jets AM region.

The first section of this chapter discusses the methods used to distinguish fake photons from prompt photons and how they are rejected in this measurement. In the second section the estimation of the residual background caused by the fake photons which pass the rejection cuts is described.

8.3.1. Rejection of Fake Photons

The rejection of fake photons is based on the differences in the energy deposition patterns of prompt and fake photons in the calorimeter and the tracking system. Prompt photons produce narrow electromagnetic showers without any associated tracks. Fake photons tend to have a broader shower, as well as associated tracks and can be accompanied by additional calorimeter activity around the energy depositions from the electromagnetic shower. Therefore fake photons are rejected using two strategies, namely cuts on the *shower shape* in the calorimeters and *isolation* requirements on the activity around the photon in the calorimeters and the tracker. These strategies are discussed in the following.

Shower Shape Identification

The shower shape identification is based on a series of selection cuts on a set of variables quantifying the shape of the electromagnetic shower in the calorimeter. A list of all variables is given in appendix Section B.3.1 and a selection is discussed in the following. The ensemble of these cuts constitutes the tight photon identification. It is very efficient in rejecting fake photons while keeping most of the prompt photons (signal efficiency: $\gtrsim 90\,\%$, background rejection: $\gtrsim 60\,\%$ for photons above 160 GeV [79]). The signal photon is required to fulfil the tight identification.

The variables employing the highly granular first layer of the EM calorimeter are especially useful in separating collimated photon pairs produced in neutral meson decays from prompt photons. This is illustrated is Figure 8.18, which shows an event display of the EM calorimeter for a prompt photon (left panel) and a photon pair from a neutral pion decay (right panel). The shower caused by the photon pair from the pion decay in the first layer is much broader than that caused by the photon and has a non-central energy distribution. Therefore the tight identification requires a narrow shower width in the first calorimeter layer (w_{stot}, w_{s3}) with the highest energy contained in the centre of the shower (f_{side}, f_1). Furthermore it is visible that the energy deposition of the photon pair from the pion decay has a distinctive

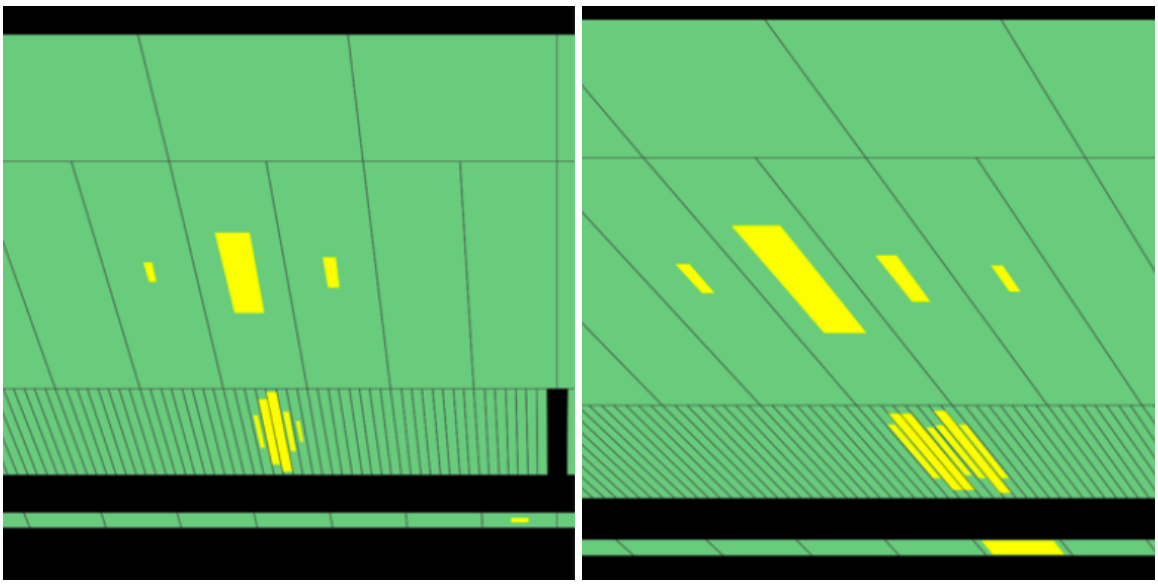

Figure 8.18.: Event display of the showers in the EM calorimeter for a prompt photon (left) and a pion decaying to a photon pair (right). The calorimeter layers from bottom to top are: the presampler, the highly segmented first calorimeter layer, the second and the third calorimeter layer. Adapted from [131].

double peak structure, whereas the prompt photon only shows one peak. Therefore the tight identification also requires a large separation in energy between the first and second energy maximum of the shower (E_{ratio}, ΔE_s) in the first calorimeter layer.

The remaining cuts of the tight identification are focused on the general shape differences between electromagnetic and hadronic showers, mainly the narrower shower width in the second calorimeter layer of the electromagnetic showers (R_η, R_ϕ, w_{η_2}) and their lower penetration depth into the hadronic calorimeter (R_{had}, R_{had_1}) [79].

In addition to the tight identification, a relaxed set of shower shape cuts is defined. It allows to select a sample of fake photons, which is used to study the fake photon background in data. This so-called loose^{IV} identification is based on the tight identification with four[7] shower shape cuts in the first calorimeter layer removed (w_{s3}, f_{side}, E_{ratio}, ΔE_s) [79]. To select the fake photon samples, photon candidates are required to pass the loose^{IV} identification but fail the tight identification. This is called non-tight identification in the following.

Isolation

Strict requirements are placed on the maximum energy deposition in calorimeter cells around the photon (calorimeter isolation), as well as on the maximum p_{T} from tracks associated with the photon (track isolation). Both are helpful in rejecting fake photons, since a prompt photon is neither expected to be associated with calorimeter activity outside of its electromagnetic shower, nor does it cause signals in the tracking system, apart from conversion tracks in

[7] It is also possible to remove a different number of shower shape cuts from the tight identification to define the relaxed set. This is done in Section 8.3.3 to define an uncertainty on the fake photon background estimate.

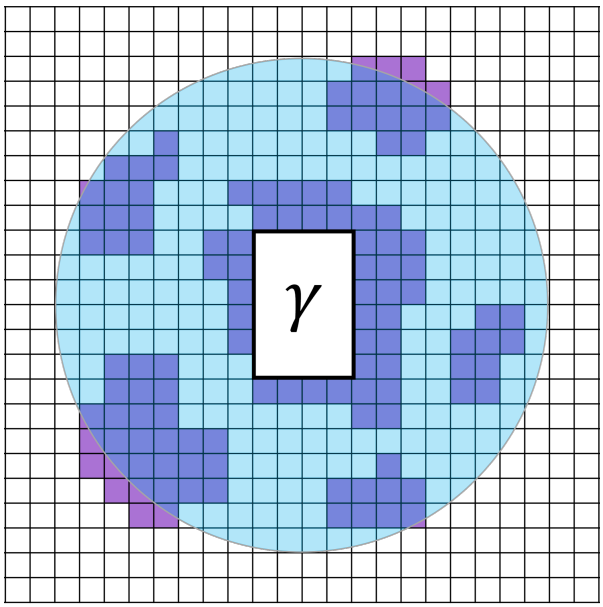

Figure 8.19.: Sketch of the calorimeter isolation, where the $\eta-\phi$ grid represents the calorimeter cells and a purple cell indicates an energy deposition. The cone used to sum the calorimeter cells that enter the raw isolation energy $E_{\mathrm{T,raw}}$ is shown in blue and the cells that form the photon shower are depicted as the white 5×7 square.

pair production, which are included in the photon reconstruction. Both the calorimeter isolation and the track isolation play an important part in the fake photon background estimate and are discussed in the following.

Calorimeter Isolation The signal photon is required to fulfil a so-called tight calorimeter isolation, given by

$$E_{\mathrm{T}}^{\mathrm{cone40}} < 0.022 \times E_{\mathrm{T}} + 2.45\,\mathrm{GeV}. \tag{8.9}$$

The term depending on the photon E_{T} is used to improve the signal efficiency of the isolation cut at high E_{T}, by loosening the isolation requirement. The optimization of the numerical factors is discussed in [79].

The isolation energy E_{T}^{cone40} is calculated as

$$E_{\mathrm{T}}^{\mathrm{cone40}} = E_{\mathrm{T,raw}}^{\mathrm{cone40}} - E_{\mathrm{T,core}} - E_{\mathrm{T,leakage}} - E_{\mathrm{T,pile-up}}. \tag{8.10}$$

The main components in the calculation of $E_{\mathrm{T}}^{\mathrm{cone40}}$ are illustrated in Figure 8.19. The grid in $\eta-\phi$ represents the calorimeter cells in the second calorimeter layer and cells marked in purple represent energy depositions. All energy depositions above a certain noise cut within a radius of $R = 0.4$ around the photon barycentre (blue circle) are summed to form the raw isolation energy $E_{T,raw}^{cone40}$. These still contain the energy from the photon shower itself, which is calculated as the energy sum $E_{T,core}$ of the 5×7 cells around the photon barycentre and

which needs to be subtracted. The window for this sum is larger in ϕ direction, since the shower is broadened in that direction by the magnetic field in the detector [81].

The third term $E_{\mathrm{T,leakage}}$ is used to correct for showers that do not fit in the 5×7 window and leak energy to the outside and is optimised in MC simulation as a function of E_{T} and η. The fourth term $E_{\mathrm{T,pile-up}}$ corrects for energy depositions due to underlying events. The $E_{\mathrm{T}}^{\mathrm{cone40}}$ calculated in this way is further corrected by applying data-driven corrections to improve agreement with the MC simulation, which predicts a distribution shifted by a few GeV due to known mismodelling in the lateral shower development [79].

The shape modelling of the calorimeter isolation variable $E_{\mathrm{T}}^{\mathrm{cone40}} - 0.022 E_{\mathrm{T}}$ is validated in data. This is necessary, since this variable plays an important role in the estimation of the residual background discussed below. Figure 8.20[8] shows the data distribution (black) of the calorimeter isolation variable in the γ+jets AM region. Also shown are a template for the fake photons (blue) and the sum (yellow) of the MC simulation used to model the prompt photons and the fake photon template[9]. The fake photon template has been derived by requiring the non-tight identification instead of the tight identification on the signal photon. To allow for a shape comparison, the template is normalised to the data for $E_{\mathrm{T}}^{\mathrm{cone40}} - 0.022 E_{\mathrm{T}} > 10$.

It is shown that the calorimeter isolation distribution in data is well modelled by the sum of the MC simulation and the fake photon template. The peak region, containing *isolated* photons, is dominated by the MC simulation and the tail region, containing photons failing the calorimeter isolation, is dominated by the fake template. This demonstrates that the non-tight selection can be used to model the tight selection in the *non-isolated* regime. This is a pre-requisite of the background estimation method discussed below, which assumes that the non-tight identification is decorrelated from the isolation variable.

Track Isolation In addition to the calorimeter isolation, the signal photon is required to fulfil a so-called tight track isolation, given by

$$p_{\mathrm{T}}^{\mathrm{cone20}} < 0.05 \times E_{\mathrm{T}}, \tag{8.11}$$

which is E_{T}-dependent to improve the selection efficiency for high-E_{T} photons. The optimisation for the prefactor is taken from [79]. $p_{\mathrm{T}}^{\mathrm{cone20}}$ is constructed in a very similar way to $E_{\mathrm{T}}^{\mathrm{cone40}}$. All tracks in a radius of $R = 0.2$ around the photon barycentre that fulfil certain quality criteria outlined in [79] are summed. Tracks belonging to photons which have undergone pair-production are excluded.

The modelling of the track isolation is also validated in data. The result is shown in Figure 8.21 for the data distribution (black) in the γ+jets AM region without the track isolation cut applied[10]. The figure also shows a fake template (blue) derived by requiring the non-tight identification instead of the tight identification on the signal photon and the sum of the simulation prediction and the fake template (yellow). To allow for a shape comparison, the fake template is normalised to the tight data for $p_T^{cone20} - 0.05 \times E_T > 10$. Good agreement similar to the calorimeter isolation is observed.

[8] For this figure, the cut on the calorimeter isolation ($E_{\mathrm{T}}^{\mathrm{cone40}} - 0.022 \times E_{\mathrm{T}} < 2.45$ GeV) is not applied.

[9] The corresponding distributions for the VBF phase space are shown in Section B.3.3.

[10] The corresponding distributions for the VBF phase space are shown in Section B.3.3.

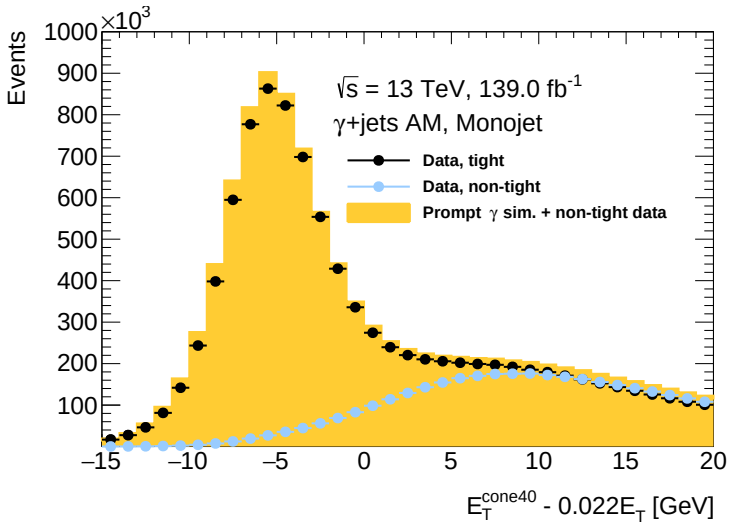

Figure 8.20.: Calorimeter isolation energy distribution in the γ+jets AM region and the monojet phase space without the calorimeter isolation requirement applied for events in data with tight leading photons (black), non-tight leading photons (blue, normalised to the tight data for $E_{\mathrm{T}}^{\mathrm{cone40}} - 0.022E_{\mathrm{T}} > 10$). The sum of the simulation and non-tight data (yellow) adequately describes the tight data.

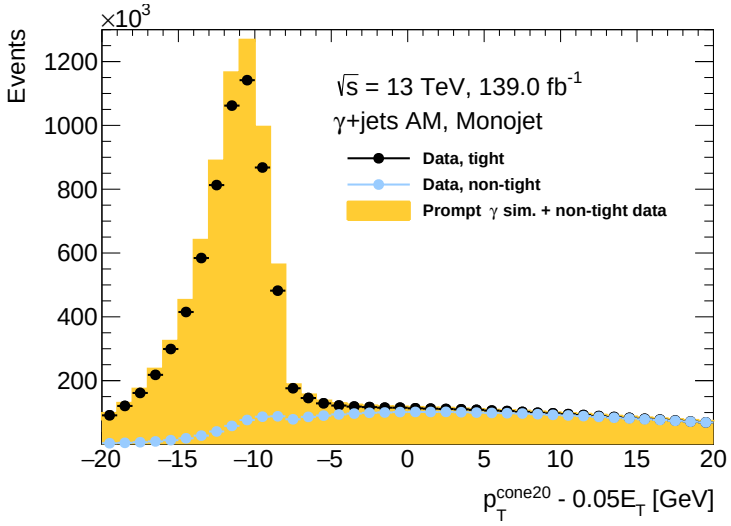

Figure 8.21.: Track isolation energy distribution in γ+jets AM region and the monojet phase space without the track isolation requirement applied for events in data with tight leading photons (black), non-tight leading photons (blue, normalised to the tight data for $p_T^{cone20} - 0.05 \times E_T > 10$. The sum of the simulation and non-tight data (yellow) adequately describes the tight data.

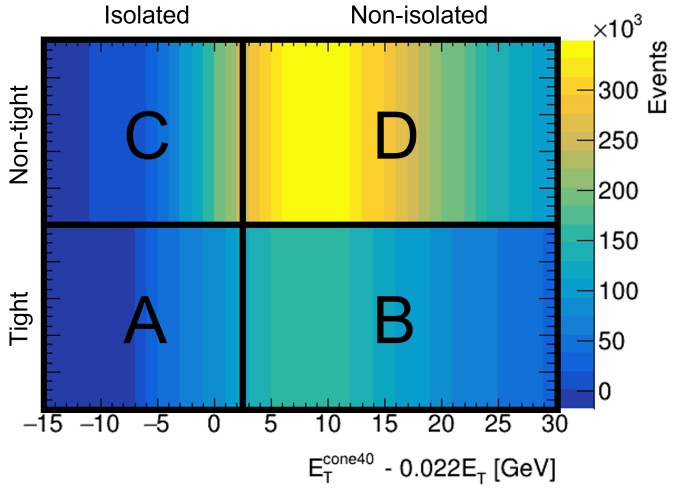

Figure 8.22.: Sketch of the control region definition used for the 2D-sideband method (the two sidebands are B-D and C-D) as a function of the calorimeter isolation variable. The z-axis shows the expected background distribution. Please Note: This is a sketch for visualisation purposes only. The actual control region definition also includes the track isolation.

8.3.2. Estimation of the Residual Background using the 2D-sideband Method

The general idea to estimate the number of fake photon events which pass the tight identification and isolation requirements of the γ+jets AM region is outlined in the following. First, the number of fake photon events passing the tight identification is measured in a background-enriched region orthogonal to the γ+jets AM region. This region is defined by inverting the isolation requirements (*non-isolated*). Then a transfer factor is determined by measuring the fraction of *isolated* and *non-isolated* fake photon events. Since this transfer factor needs to be measured in an independent set of fake photon events, it is determined from two additional regions which are background-enriched by requiring the photon to fulfil the non-tight identification. A sketch of these regions is given in Figure 8.22 together with the expected contribution of fake photons in each region.

The number of tight and isolated fake photon events is then determined as

$$N_{\text{fake}}^{\text{tight,isolated}} = R \times N_{\text{fake}}^{\text{tight,non-isolated}} \frac{N_{\text{fake}}^{\text{non-tight,isolated}}}{N_{\text{fake}}^{\text{non-tight,non-isolated}}}, \tag{8.12}$$

where the correlation factor R has been introduced to account for a potential correlation between the identification and isolation requirements. Typically, the assumption of non-correlation ($R = 1$) is good and is justified by the construction of non-tight identification, which differs from tight only in variables not sensitive to the photon isolation and also supported by the shape studies of the isolation variables discussed in the previous sections. The

Region	Selection criteria
A (=γ+jets AM region)	*tight, isolated*
B	*tight, non-isolated*
C	*non-tight, isolated*
D	*non-tight, non-isolated*

Table 8.3.: Definition of the 2D-sideband regions used for the estimation of the fake photon background.

correlation factor R is measured in data and deviations from $R = 1$ are assigned as a systematics uncertainty. This is discussed in Section 8.3.3.
In the derivation of the background estimate given in the following, an abbreviated notation is used for the different regions and given in Table 8.3. With the abbreviated notation, Equation 8.12 becomes

$$N_{\mathrm{A,bkg}} = R \times N_{\mathrm{B,bkg}} \frac{N_{\mathrm{C,bkg}}}{N_{\mathrm{D,bkg}}}, \tag{8.13}$$

with $N_{X,bkg}$ the number of fake photon events in the four regions A, B, C and D.

The number of events N_{X} measured in one of the background-enriched regions B, C and D is not the number of fake background events, since each of these regions has a varying degree of contamination with events containing prompt photons $N_{\mathrm{X,sig}}$. Therefore the number of fake photon events is expressed as $N_{\mathrm{X}} - N_{\mathrm{X,sig}}$ and Equation 8.13 becomes

$$N_{\mathrm{A,bkg}} = R N_{\mathrm{B,bkg}} \frac{N_{\mathrm{C,bkg}}}{\mathrm{N_{D,bkg}}} = R \left(N_{\mathrm{B}} - N_{\mathrm{B,sig}} \right) \frac{N_{\mathrm{C}} - N_{\mathrm{C,sig}}}{N_{\mathrm{D}} - N_{\mathrm{D,sig}}}. \tag{8.14}$$

The $N_{\mathrm{X,sig}}$ are determined in a partially data-driven way as

$$N_{\mathrm{X,sig}} = \epsilon_{\mathrm{X}} N_{\mathrm{A,sig}} = \epsilon_{\mathrm{X}} \left(N_{\mathrm{A}} - N_{\mathrm{A,bkg}} \right), \tag{8.15}$$

based on $N_{\mathrm{A,sig}}$, the measured number of signal events in the γ+jets AM region in data. ϵ_{X} is a transfer factor, also called *(signal) leakage fraction*, which is determined from simulation as

$$\epsilon_{\mathrm{X}} = \frac{N^{\mathrm{MC}}_{\mathrm{X,sig}}}{N^{\mathrm{MC}}_{\mathrm{A,sig}}}. \tag{8.16}$$

In this way the simulation is only used to determine the relative number of signal events in the different regions, but the estimate remains independent of the absolute cross section predicted by the MC simulation, which is known to be poorly modelled (see Chapter 10). The assumption that the relative number of signal events can be extracted from the MC simulation depends on the proper modelling of the isolation and identification variables, which has been verified in data as described in the previous section and also more extensively in [79].

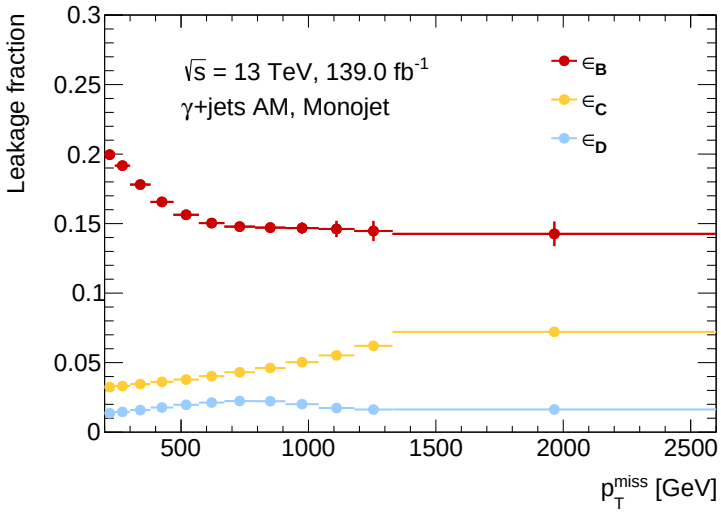

Figure 8.23.: Leakage fractions for regions B (red), C (yellow) and D (blue) as a function of $p_{\mathrm{T}}^{\mathrm{miss}}$ in the monojet phase space.

The *leakage fractions* for the $p_{\mathrm{T}}^{\mathrm{miss}}$ distribution in the monojet phase space are shown in Figure 8.23 [11]. The behaviour of the *leakage fractions* as a function of $p_{\mathrm{T}}^{\mathrm{miss}}$ can be explained by the signal efficiencies of the corresponding identification and isolation working points of the leading photon[12]. The leakage into region B (*tight* and *non-isolated*) depends on the signal efficiency of the isolation working point, which rises with photon p_{T} and reaches a plateau only above 500 GeV [79]. This leads to a decreasing *leakage fraction* in region B. The leakage into region C (*non-tight* and *isolated*) depends on the signal efficiency of the identification working point, which is in general higher than that of the isolation working point, leading to a lower leakage and which decreases slightly at very high photon p_{T} [79], explaining the rising trend in the *leakage fraction*. Accordingly the leakage into region D (*non-tight* and *non-isolated*) depends on a combination of both the isolation and identification efficiencies.

Combining Equation 8.13 and Equation 8.14 the background $N_{A,bkg}$ in the γ+jets AM region for an observable in a given bin can be estimated by solving

$$N_{A,bkg} = R(N_B - \epsilon_B(N_A - N_{A,bkg}))\frac{N_C - \epsilon_C(N_A - N_{A,bkg})}{N_D - \epsilon_D(N_A - N_{A,bkg})}. \tag{8.17}$$

This is done numerically for each measured variable and bin using the SymPy package [132]. As the γ+jets AM region has no other background contributions, the result is expressed in terms of the purity, defined as

$$P = 1 - \frac{N_{A,bkg}}{N_A}. \tag{8.18}$$

[11] The *leakage fractions* for the VBF phase space are shown in Section B.3.3

[12] Note that $p_{\mathrm{T}}^{\mathrm{miss}}$ in the γ+jets AM regions corresponds mostly to the p_{T} of the leading photon, with some fluctuations from the residual $p_{\mathrm{T}}^{\mathrm{miss}}$ resolution

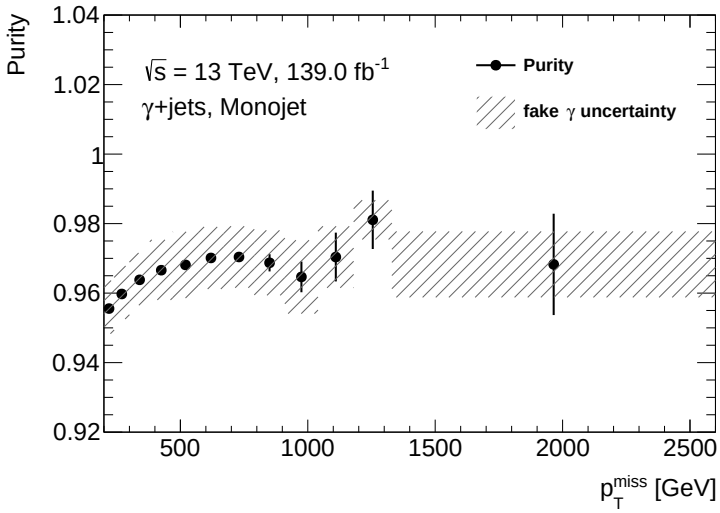

Figure 8.24.: Purity as a function of $p_{\mathrm{T}}^{\mathrm{miss}}$ in the monojet phase space. The grey bands show the systematic uncertainty from the background estimate and the black error bars show the statistical uncertainty on the purity.

The purities determined with the 2D-sideband method are above 95 % for the γ+jets AM region, as shown in Figure 8.24[13] for the $p_{\mathrm{T}}^{\mathrm{miss}}$ distribution in the monojet phase space. The statistical uncertainty has been determined using the bootstrap method. The systematic uncertainty on the background estimate is determined as described in the following section.

8.3.3. Systematic Uncertainty on the Background Estimate

Three different sources of systematic uncertainties are considered for the fake background estimate in the γ+jets AM region: The definition of the non-tight identification in terms of shower shape variables, residual correlations of the background contributions in the regions A,B,C and D ($R \neq 1$ in Equation 8.13) and a dependence of the *leakage fractions* on the MC generator. These sources are discussed in the following. The total uncertainty is determined by summing the single uncertainties in quadrature, as they are expected to be uncorrelated. The single uncertainties are first rebinned, to reduce the impact of statistical fluctuations.

Definition of the Non-tight Identification

The background estimate depends on the exact definition of the non-tight identification, which is used to select events for the background-enriched regions. Therefore the background estimate is redone three times with varied non-tight IDs. These are constructed analogue to the nominal non-tight identification, but replace the loose^{IV} identification with loose^{II}, loose^{III} and loose^{V} respectively, where a different number of shower shape variables are removed from the tight identification (see Table 8.4).

[13] The purity distributions for the VBF phase space are shown in Section B.3.4.

identification working point	Define
loose^{II}	tight without w_{s3}, f_{side}
loose^{III}	tight without w_{s3}, f_{side}, ΔE_s
loose^{IV}	tight without w_{s3}, f_{side}, ΔE_s, E_{ratio}
loose^{V}	tight without w_{s3}, f_{side}, ΔE_s, E_{ratio}, w_{stot}

Table 8.4.: Variations of the loose^{IV} identification used to determine the systematic uncertainty on the fake photon estimate.

The systematic uncertainty due to the definition of the loose^{IV} identification is then determined as the envelope of the three variations. The resulting relative uncertainty on the background estimate is shown in Figure 8.25[14]. The different magnitude of the up and down variation are due to the different impact of the three alternative definitions of the non-tight identification.

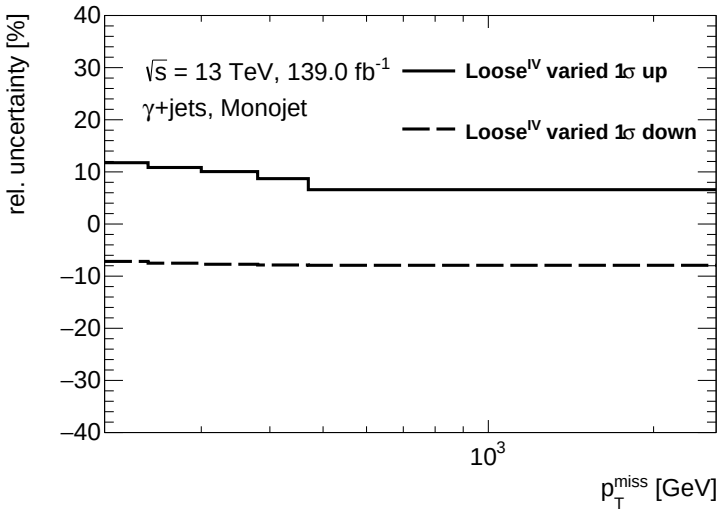

Figure 8.25.: Relative uncertainty on the fake photon background estimate due to the choice of the loose^{IV} identification as a function of $p_{\mathrm{T}}^{\mathrm{miss}}$ in the monojet phase space.

Residual Correlations between Isolation and Identification

The correlation factor R used in Equation 8.12 is estimated from data and differences from $R = 1$ are symmetrized and assigned as a systematic uncertainty. This accounts for the fact that the identification and isolation requirements are not fully uncorrelated.

The correlation factor R is estimated in a highly background-enriched region in data. To achieve this, the regions enriched with events failing the isolation cut (B and D) are further subdivided into B', D',E and F as defined in Table 8.5 and illustrated in Figure 8.26. The

[14]The distributions for the VBF phase space are shown in Section B.3.5

Region	Selection criteria	Isolation Cuts
B'	*tight, non-isolated*	$E_{T,cone40} - 0.22p_T < 11\,\text{GeV}$ & $p_{T,cone20} - 0.05p_T < 11\,\text{GeV}$
D'	*non-tight, non-isolated*	$E_{T,cone40} - 0.22p_T < 11\,\text{GeV}$ & $p_{T,cone20} - 0.05p_T < 11\,\text{GeV}$
E	*tight, non-isolated*	$E_{T,cone40} - 0.22p_T > 11\,\text{GeV}$ & $p_{T,cone20} - 0.05p_T > 11\,\text{GeV}$
F	*non-tight, non-isolated*	$E_{T,cone40} - 0.22p_T > 11\,\text{GeV}$ & $p_{T,cone20} - 0.05p_T > 11\,\text{GeV}$

Table 8.5.: Definition of 2d sideband regions used for the determination of the correlation R.

division cut of 11 GeV in the table is chosen such that the statistical precision is still high enough in regions E and F. The correlation factor R for fake photon events is then extracted for a given observable and bin using

$$R = \frac{\left(N_{B'} - \epsilon'_B(N_A - N_{A,bkg})\right)\left(N_F - \epsilon_F(N_A - N_{A,bkg})\right)}{\left(N_{D'} - \epsilon'_D(N_A - N_{A,bkg})\right)\left(N_E - \epsilon_E(N_A - N_{A,bkg})\right)}, \tag{8.19}$$

where the $N_{A,bkg}$ are the solutions of Equation 8.17 obtained above and the *leakage fractions* ϵ_X are determined as in Equation 8.16.

The relative systematic uncertainty on the background estimate derived from the varied correlation factor R is shown in Figure 8.27 for the $p_{\text{T}}^{\text{miss}}$ distribution in the monojet phase space[15]. It is the dominant component of the total systematic uncertainty on the background estimate.

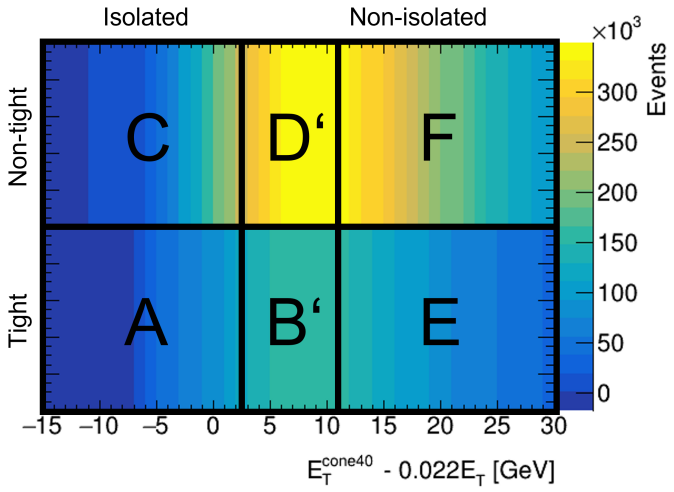

Figure 8.26.: Sketch of the control region definition used to determine the correlation factor R' in the 2D-sideband method as a function of the calorimeter isolation variable. The z-axis shows the expected background distribution. Please note: This is a sketch for visualization purposes only. The actual control region definition also includes the track isolation.

[15]The distributions for the VBF phase space are shown in Section B.3.5

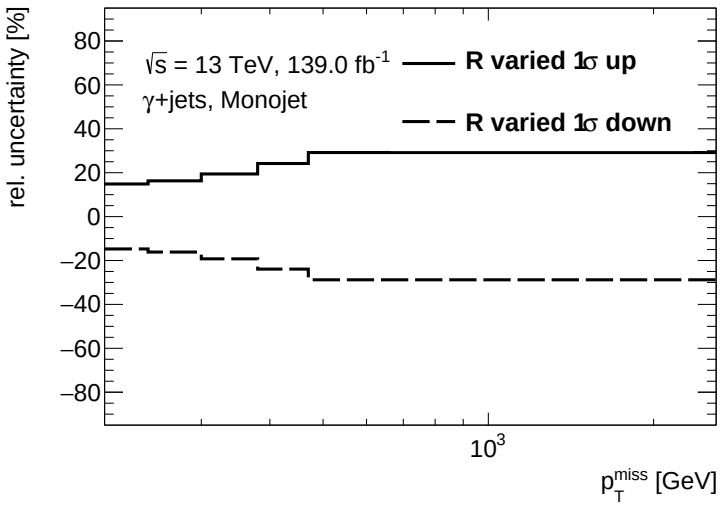

Figure 8.27.: Relative uncertainty on the fake photon background estimate due to residual correlations between isolation and identification as a function of $p_{\mathrm{T}}^{\mathrm{miss}}$ in the monojet phase space.

Dependence of the Leakage Fractions on the Monte Carlo Generator

The leakage fractions depend on the modelling of the contribution from fragmentation photons in the MC simulation. Photons from fragmentation processes are typically accompanied by hadronic activity and therefore not isolated. This means that especially the leakage fractions for the non-isolated regions have a dependence on the MC generator.

To account for this, the signal leakage fractions ϵ_X are redetermined using an alternative MC generator (Pythia). Pythia is chosen, since it models the fragmentation processes differently from Sherpa (see [133] for more details on the Sherpa modelling and [134] for more details on the Pythia modelling). Figure 8.28 shows a comparison of the *leakage fractions* determined with Sherpa and Pythia. While the leakage fractions are similar for the isolated region C, there is a significant difference observed in non-isolated regions B and especially D.

The background estimate is repeated with the alternative leakage fractions and the difference to the nominal estimate is symmetrized and assigned as a systematic uncertainty. The resulting relative systematic uncertainty is shown in Figure 8.29[16].

[16]The distributions for the VBF phase space are shown in Section B.3.5

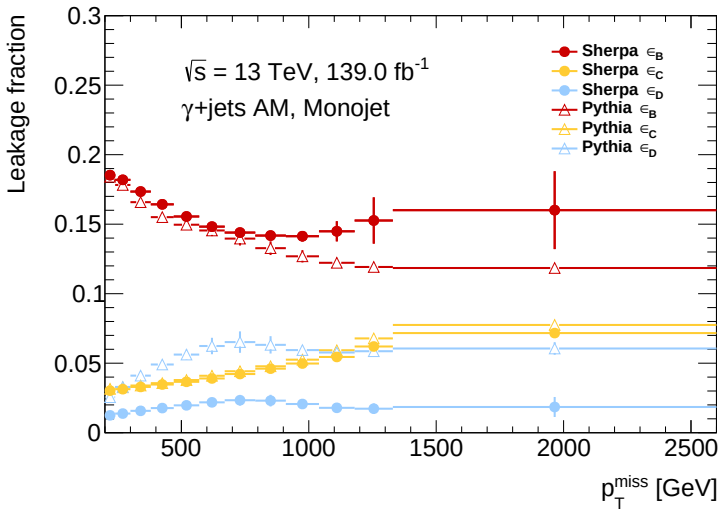

Figure 8.28.: Comparison of the *leakage fractions* between SHERPA and PYTHIA as function of $p_{\mathrm{T}}^{\mathrm{miss}}$ in the monojet phase space.

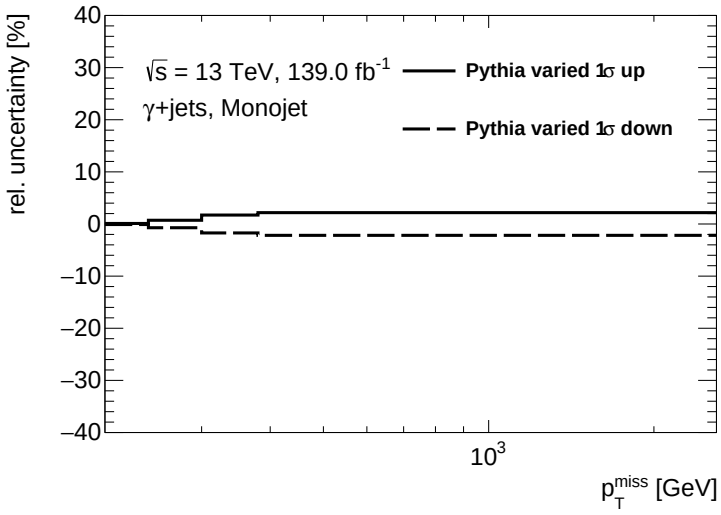

Figure 8.29.: Relative uncertainty on the fake photon background estimate due to the MC generator dependence as a function of $p_{\mathrm{T}}^{\mathrm{miss}}$ in the monojet phase space.

8.4. Fake Electron Background in the $W \to e\nu$ + jets Auxilliary Measurement Region

Photons and jets can be reconstructed as *electron candidates* in the detector. This typically happens when tracks from other sources are matched to the electromagnetic clusters in the calorimeter caused by an electromagnetic shower from a photon, if a jet develops an electron-like shower in the calorimeters or if a heavy hadron undergoes a weak decay involving an electron. The electron candidates reconstructed from these objects are collectively referred to as *fake electrons*.

Fake electron candidates are rejected very efficiently by the selection criteria for signal electrons. In addition, the background rejection cuts applied in the $W \to e\nu$ + jets AM region help reduce the fake electron background contributions. These are the cut on the W boson transverse mass ($30\,\text{GeV} < m_\text{T} < 100\,\text{GeV}$) and the minimum requirement for real missing transverse momentum ($p_\text{T}^{\text{miss,real}} > 60\,\text{GeV}$) expected from the neutrinos in the $W \to e\nu$ + jets final state.

However, a residual number of events with fake electrons can enter the measurement in the $W \to e\nu$ + jets AM region. The contribution of these fake background events is estimated using a data-driven method called the *matrix method*.

The first section of this chapter discusses the sources of fake electrons and the methods used to reject them in more detail. The remainder of the chapter focusses on the background estimation with the matrix method.

8.4.1. Sources and Rejection of Fake Electrons

The dominant sources of fake electrons are weak decays of light and heavy hadrons and photons with mismatched tracks. A general overview of the relative composition of all sources is given in Figure 8.30, which was determined in [135] from a relatively loose electron sample for the Drell-Yan process. The exact composition in a tighter sample like the $W \to e\nu$ + jets AM region is difficult to determine in practice, due to limited MC statistics and the various dependencies on the energy of the objects involved, their localization in the detector, due to varying instrumentation, the applied electron selection criteria and the phase-space cuts, which have an impact on the jet activity. The main sources are discussed in the following.

Heavy hadrons (blue circles and violet triangles in Figure 8.30), especially B and D mesons, that undergo a weak decay before reaching the detector material, are a main source of electrons which are real, but non-prompt, in the sense that they do not originate directly from the hard scattering process [135]. One method applied to reject these electrons is the track-to-vertex association (TTVA) requirement with respect to the primary vertex, since the hadrons typically have a lifetime long enough for a secondary vertex to be resolved [77]. Another method is the tight isolation requirement placed on the activity in the calorimeter around the electron, which is usually high for this type of non-prompt electron, due to the jet remnant. The isolation requirement is very similar to that applied to photons and more information is given in Section 8.3.1.

Light hadrons (brown boxes in Figure 8.30) are also a source of fake electrons, especially

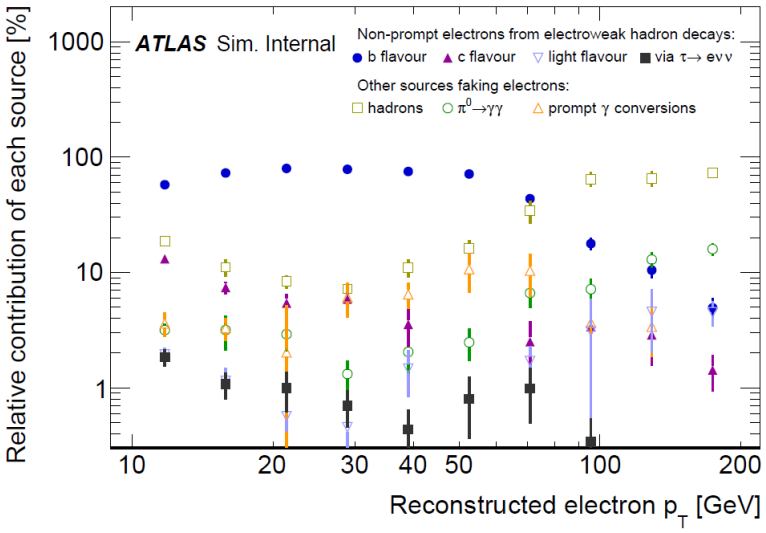

Figure 8.30.: Relative contributions of different sources of fake or non-prompt electrons as function of p_{T} in simulated Drell-Yan processes. Other cumulated sources not displayed contribute to less than 0.5 % in any bin. Error bars represent statistical uncertainties of the simulation. Adapted from [135].

if they are stopped early in the calorimeter and develop a narrow shower similar to that of electrons. In that case the hadrons can be reconstructed as electron candidates. A special case are decays of light mesons to two photons (e.g. $\pi^0 \to \gamma\gamma$), where the photons are highly collimated and form a single cluster in the calorimeter, with tracks stemming from the jet remnant or photon conversion [135].

The main method to reject these fake electrons is the application of a likelihood-based identification using the shape of the shower in the calorimeter as input. This tight identification for electrons is based on the same shower shape variables also used for photons, with the addition of stringent requirements on the quality of the tracks recorded in the ATLAS inner detector and the spatial matching of those tracks to the shower in the calorimeter. A detailed discussion on the shower shape variables is given in Section 8.3.1. The tight identification is very efficient in rejecting fake electrons. The background rejection is roughly a factor 200 to 300 depending on the phase-space in question [76].

Despite the background rejection power of the various methods, the very high jet production cross section at the LHC still leads to a significant amount of residual fake background that enters the $W \to e\nu$ + jets AM region and needs to be estimated.

8.4.2. The Matrix Method

The background in the $W \to e\nu$ + jets AM region caused by fake electrons is estimated using a data-driven method, since the modelling of the different background sources in simulation is very challenging. Furthermore, due the low probability for a fake electron to enter the $W \to e\nu$ + jets AM region, a very large amount of MC statistics would be required, which is

impractical to produce [135].

The challenge in the background estimation is that the number of events with real ($N^R_{W\to e\nu+jetsAM}$) and fake electrons ($N^F_{W\to e\nu+jetsAM}$) that enter the $W \to e\nu$ + jets AM region is difficult to measure directly. However, two related quantities are easily accessible. These are the number of events with signal electrons that enter the $W \to e\nu$ + jets AM region (N_S) and the number of events with non-signal electrons ($N_{!S}$) that pass the $W \to e\nu$ + jets AM region selection, if the signal electron criteria are dropped. Non-signal electrons are defined as baseline electrons that fail the signal electron selection. A summary of the properties[17] of the different types of electrons is given in Table 8.6.

The idea of the *matrix method* is to measure N_S and $N_{!S}$ and relate them to $N^R_{W\to e\nu+jetsAM}$ and $N^F_{W\to e\nu+jetsAM}$ via a set of efficiencies that can also be measured[18]. This relation is derived in the following.

Electron type	Selection criteria
signal (S)	tight identification, tight isolation, TTVA
baseline (B)	loose identification
non-signal ($!S$)	pass baseline, fail signal

Table 8.6.: Definition of signal, baseline and non-signal electrons.

In a first step N_S and $N_{!S}$ are expressed as a function of the number of events with real (N^R_B) and fake electrons (N^F_B) that pass the baseline selection.

$$\begin{aligned} N_S &= \epsilon_R N^R_B + \epsilon_F N^F_B \\ N_{!S} &= (1-\epsilon_R)\, N^R_B + (1-\epsilon_F)\, N^F_B, \end{aligned} \tag{8.20}$$

where the real efficiency ϵ_R and the fake efficiency ϵ_F are defined as

$$\epsilon_R = \left(\frac{N_S}{N_B}\right)_R \quad \text{and} \quad \epsilon_F = \left(\frac{N_S}{N_B}\right)_R \tag{8.21}$$

and are determined in a sample of real (R) and fake (F) electrons. $\epsilon_R(\epsilon_F)$ is the probability for an event containing a real (fake) electron that passes the baseline selection to also pass the signal selection. The measurement of these efficiencies as a function of electron p_T and η is discussed in detail in Section 8.4.3 and Section 8.4.4.

Equation 8.20 can be expressed in matrix form

$$\begin{pmatrix} N_S \\ N_{!S} \end{pmatrix} = \begin{pmatrix} \epsilon_R & \epsilon_F \\ (1-\epsilon_R) & (1-\epsilon_F) \end{pmatrix} \begin{pmatrix} N^R_B \\ N^F_B \end{pmatrix}, \tag{8.22}$$

giving the method its name. In a second step the matrix is inverted to determine the number of events with fake electrons in the baseline selection (N^F_B)

[17] The exact definition is given in Section 5.1.1.

[18] Both N_S and $N_{!S}$, as well as $N^R_{W\to e\nu+jetsAM}$ and $N^F_{W\to e\nu+jetsAM}$ are independent, since by definition a signal electron is never a non-signal electron and a real electron is never fake.

$$N_B^F = \frac{1}{\epsilon_R - \epsilon_F} \left[\epsilon_R N_{!S} - (1 - \epsilon_R) N_S\right]. \tag{8.23}$$

In a third step the number of events with fake electrons in the $W \rightarrow e\nu$ + jets AM region $N^F_{W\rightarrow e\nu+jetsAM}$ is determined from N_B^F by multiplying with the fake efficiency ϵ_F

$$N^F_{W\rightarrow e\nu+jetsAM} = \epsilon_F N_B^F = \frac{\epsilon_F}{\epsilon_R - \epsilon_F} (\epsilon_R - 1) N_S + \frac{\epsilon_F}{\epsilon_R - \epsilon_F} \epsilon_R N_{!S}. \tag{8.24}$$

The final result is determined using Equation 8.24 on an event-by-event basis, where a weight w_i is assigned to each event i, depending if the leading electron fulfils the signal or non-signal criteria according to

$$w_i = \begin{cases} \frac{\epsilon_F}{\epsilon_R - \epsilon_F} (\epsilon_R - 1) & \text{if leading electron fulfils signal selection criteria} \\ \frac{\epsilon_F}{\epsilon_R - \epsilon_F} \epsilon_R & \text{if leading electron fulfils non-signal selection criteria} \end{cases} \tag{8.25}$$

and $N^F_{W\rightarrow e\nu+jetsAM}$ is given by the sum of the weights

$$N^F_{W\rightarrow e\nu+jetsAM} = \sum_i w_i. \tag{8.26}$$

The statistical uncertainty on $N^F_{W\rightarrow e\nu+jetsAM}$ is determined with the bootstrap technique (bootstrap replica are created for all quantities entering Equation 8.26).

The real and fake efficiencies are determined as a function of electron p_{T} and η, since they depend on the energy of the electron (reflecting the energy dependence of the shower development in the calorimeter), as well as the spatial location in the detector (reflecting the varying instrumentation in the detector). Their derivation is discussed in detail in the following sections.

8.4.3. Real Electron Efficiencies

The real electron efficiencies are determined using MC simulation. This has the advantage of easy access to a clean sample of real electrons and also provides high statistical precision. It is justified by a relatively good description of electron efficiencies by the ATLAS MC simulation [79] and the application of additional scale factors to the MC simulation that improve on that already good description of the data. A truth matching is performed on each simulated event, which requires the electron on detector-level to be within a radius of $R < 0.2$ in (η, ϕ) of a prompt electron on particle-level. Events that do not pass the truth matching are not used. This ensures that fake electrons, which also have a small contribution in the MC simulation, are not included in the calculation of the real efficiencies.

In order to determine the real efficiencies the number of electrons passing the signal (N_S) and baseline (N_B) selection criteria in the $W \rightarrow e\nu$ + jets AM region and the monojet phase space are counted as a function of p_{T} and η and are used to calculate the ϵ_R according to Equation 8.21. These efficiencies are found to be very similar in the VBF phase spaces, therefore they are only derived in the monojet phase space. The resulting efficiencies are shown

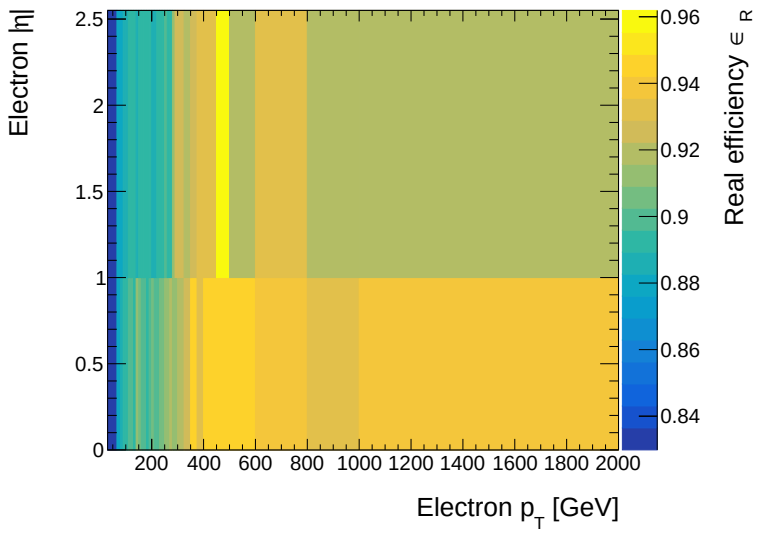

Figure 8.31.: Real electron efficiency as a function of electron p_{T} and electron η for the 2017 data period.

in Figure 8.31 as a function of p_{T} and η for the 2017 data period[19]. The binning is determined such as to reduce fluctuations of the efficiencies due to the limited statistics of the MC simulation.

For better visibility the one dimensional distributions are shown in Figure 8.32 for all data periods. The efficiency shown for the 2015/16 period is usually slightly higher than for 2017 and 2018. This is due to a different gas mixture used in the *TRT* of the ATLAS tracking system and the residual pile-up dependence, with lower efficiencies for higher pile-up [79]. It can further be seen that the real efficiency rises as a function of p_{T} (top panel) from around 85 % to 95 %. This behaviour directly reflects that of the tight identification and tight isolation criteria applied to the signal electron as function of p_{T}, which have an improved performance at high p_{T}, where the electrons are easier to distinguish from background events [76][79]. A structure is visible in the η distribution (bottom panel), with a higher efficiency in the central region and lower efficiency in the more forward region. This is an effect of the varying instrumentation in the different detector regions, especially the larger amount of material in front of the endcap calorimeters ($|\eta| > 1.375$), which leads to a lower efficiency [76][80].

8.4.4. Fake Electron Efficiencies

The fake electron efficiencies are determined from data, since, the MC simulation is insufficient to properly model all sources of fake electrons. To this end a fake-enriched control region is defined, which is discussed in the first part of this section. To collect an unbiased data sample of baseline electrons it is necessary to use events recorded using prescaled triggers, this is discussed in the second part of this section. The resulting fake efficiencies are presented in the final part of this section.

[19]The real efficiencies for the other data periods are shown in Section B.4.1.

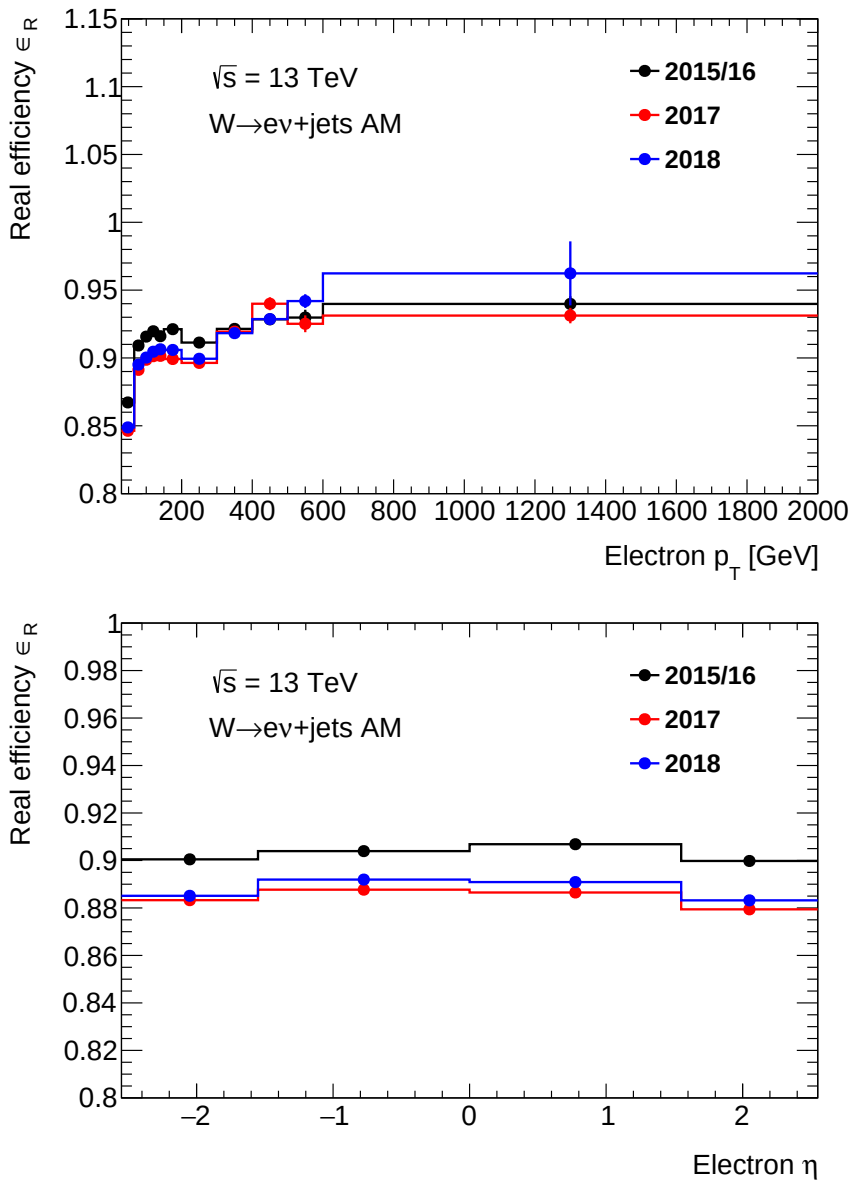

Figure 8.32.: Real electron efficiency as a function of electron p_{T} (top panel) and electron η (bottom panel) for the 2015/16 (black), 2017 (red) and 2018 (blue) data period.

Fake Electron-enriched Control Region

The fake-enriched control region is defined by inverting or dropping the cuts that are used to reject the fake electron background in the $W \to e\nu$ + jets AM region, namely

- inverting the cut on $p_{\mathrm{T}}^{\mathrm{miss,real}}$, to reduce contributions from events containing W bosons ($p_{\mathrm{T}}^{\mathrm{miss,real}} < 60\,\mathrm{GeV}$).

- dropping the cut on the W boson invariant transverse mass m_{T}, to increase the number of events with fake electrons.
- dropping the cut on $p_{\mathrm{T}}^{\mathrm{miss}}$ (W boson momentum), to increase the available statistics.

This ensures that the control region is enriched by fake background processes, but still remains close to the $W \to e\nu$ + jets AM region in terms of the event topology, especially the jet system. This is necessary to minimize the amount of extrapolation in the background estimate.

Triggering Events with Baseline Electrons

The prescaled triggers *HLT_e26_lhvloose_nod0* and *HLT_e60_lhvloose_nod0* are used in addition to the nominal analysis triggers below an electron p_{T} of 150 GeV to obtain an unbiased event sample with baseline electrons. The nominal triggers alone are not sufficient, since they apply either tight (*HLT_e26_lhtight_nod0_ivarloose*) or medium (*HLT_e60_lhmedium_nod0*) shower shape identification cuts on the electrons at trigger level. While these identification requirements on trigger level are not exactly identical to those applied to the electrons in the offline analysis[20], they are considerably tighter than the baseline requirements, which makes them unsuitable for use in the fake-enriched control region. Above an electron p_{T} of 150 GeV the *HLT_e140_lhloose_nod0* nominal analysis trigger can be used, which is the lowest unprescaled loose single electron trigger consistently enabled throughout all data periods.

The prescale factor for a given event depends on the exact run conditions and the trigger, however they typically lie between $\frac{1}{60}$ and $\frac{1}{1400}$. Events collected with the prescaled triggers need to be corrected for the prescale. This is done in the same way as described in Section 8.1.1, by defining p_{T} ranges for each trigger item, where the corresponding trigger is fully efficient and solely used. Each event in this p_{T} range is then weighted by the inverse of the corresponding prescale value. The exact p_{T} ranges and triggers used for each data taking year are shown in Table 8.7.

Range [GeV]	2016-2017	2018
$30 < p_{\mathrm{T}} < 70$	HLT_e26_lhvloose_nod0_L1EM20VH	HLT_e26_lhvloose_nod0_L1EM22VH
$70 < p_{\mathrm{T}} < 150$	HLT_e60_lhvloose_nod0	
$p_{\mathrm{T}} > 150$	HLT_e140_lhloose_nod0 or HLT_e300_etcut	

Table 8.7.: Triggers used to select the baseline electron events in different p_{T} ranges and years.

Note that the exact trigger definition evolves throughout Run 2, in order to keep the trigger rate constant or improve the trigger efficiency. This affects the fake efficiencies as discussed below and important changes are therefore discussed briefly in the following. Firstly, as shown in Table 8.7, the L1 seed trigger is changed from *L1EM20VH* to *L1EM22VH* in

[20] The two main reasons why the identification algorithms used on trigger level are not identical to those used in the offline analysis is that the calculation of some discriminating variables is too CPU-intensive for the *HLT* and the limited resolution available for the objects reconstructed on trigger level [80].

2018. Secondly, also for the triggers keeping the same name, the underlying configuration changes [119]. Especially relevant for the fake efficiencies are:

- Introduction of the NeuralRinger algorithm starting with the 2017 data-taking. This improves the removal of fake electrons at trigger level.
- New likelihood tunes for electron identification at trigger level in the 2018 data-taking.

No direct fake background estimate is performed for 2015 data; instead the luminosity ratio between 2015 and 2016 is used to extrapolate the expected background. This is necessary, since no loose triggers were consistently operational for low-p_{T} electrons in 2015 and no unbiased baseline sample as defined above can be collected.

Comparison between Data and Simulation in the fake-enriched Control Region

The fake-enriched control region contains contributions from real electrons. These contributions are estimated using MC simulation and are discussed in the following

Figure 8.33 shows the $p_{\mathrm{T}}^{\mathrm{miss,real}}$ (top panel), low electron p_{T} (middle panel) and high electron p_{T} (bottom panel) distributions for baseline (left panels) and signal (right panels) electrons together with the ratio of data and MC simulation for each distribution. The strong disagreement between data and simulation for both classes of events is attributed to events with fake electrons, that are not modelled by the MC simulation. This demonstrates the large fake electron background contribution in the the fake-enriched control region. It is also visible that the disagreement is smaller for the signal electron selection, since it provides stronger fake background rejection.

Several additional features can be observed. Firstly, the relative background contribution increases towards lower $p_{\mathrm{T}}^{\mathrm{miss,real}}$. This is typical for fake background from light hadrons (e.g. dijet events without prompt invisible particles). Secondly, the relative background increases towards low electron p_{T}, where the electrons are less well separated from background in many of the discriminating variables used in the likelihood identification [76]. Thirdly, the relative background increases towards high electron p_{T}, this is most likely a feature of the isolation, which is optimized for good background rejection at low p_{T} and large signal efficiency at high p_{T}. The consequence of the high signal efficiency is a slightly worse background rejection [79]. The jump visible around 300 GeV in the baseline electron p_{T} distribution (bottom left) is caused by the onset of the *HLT_e300_etcut*, which increases the relative contribution of fake electron events, since it places less stringent electron identification requirements than the other triggers. Since mostly fake electron events are affected by this, the jump is not visible in the MC simulation. A detailed discussion of the trigger effect on the fake efficiencies is given in the following section.

Fake Efficiencies

The fake efficiencies are calculated as a function of η and p_{T} using Equation 8.21 in the fake-enriched control region. The contributions from processes containing real electrons are estimated using MC simulation and subtracted from the data. Figure 8.34 shows the resulting

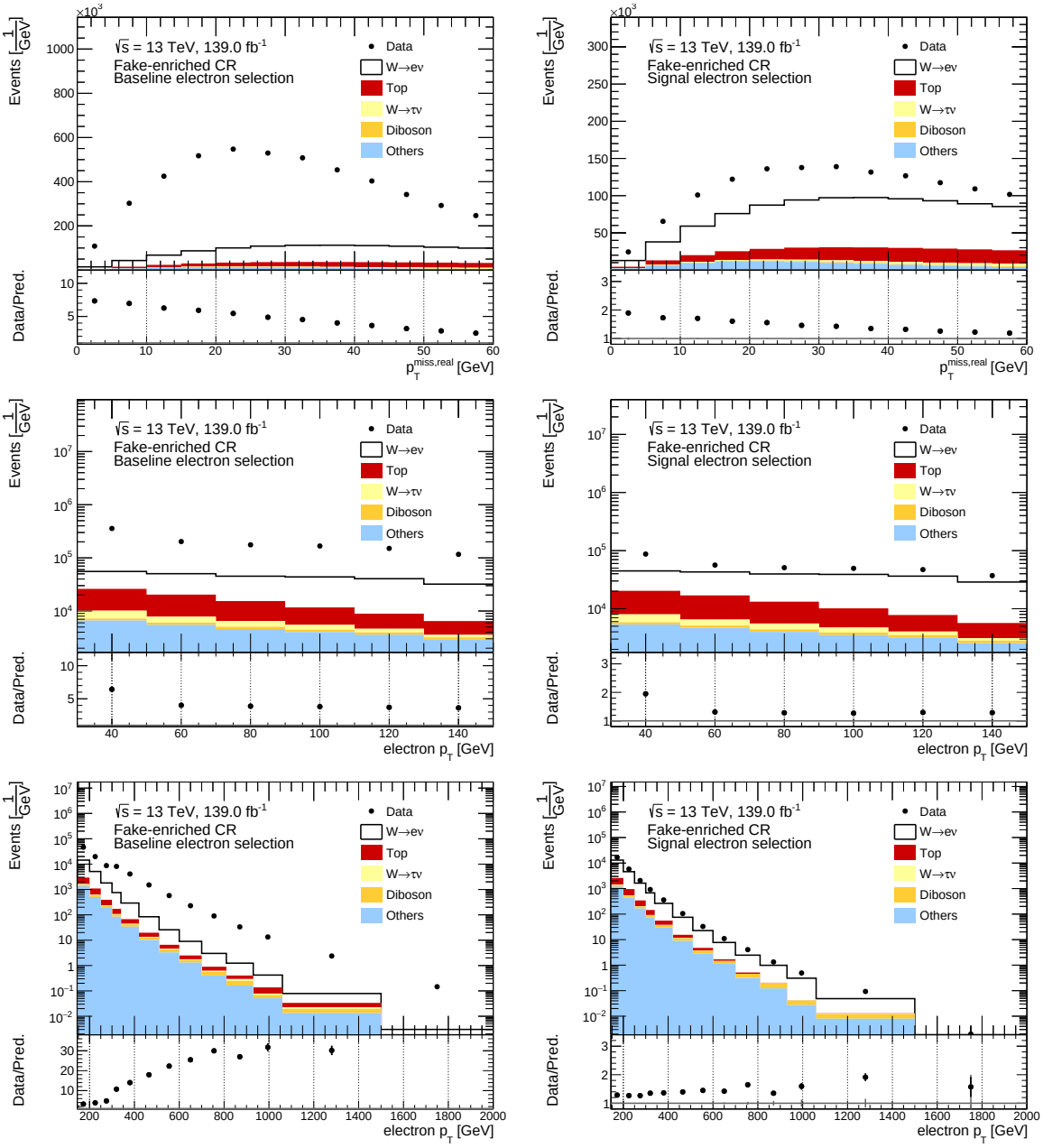

Figure 8.33.: Comparison of data and MC simulation in the fake-enriched control region for the baseline electron selection (left panel) and the signal electron selection (right panel). Top row: $p_{\mathrm{T}}^{\mathrm{miss,real}}$ distribution, middle row: low electron p_{T} distribution, bottom row: high electron p_{T} distribution.

fake efficiencies as a function of p_{T} and η for the 2017 data period[21]. The binning is chosen to minimize statistical fluctuations due to the limited statistical precision of the data in the fake-enriched control region.

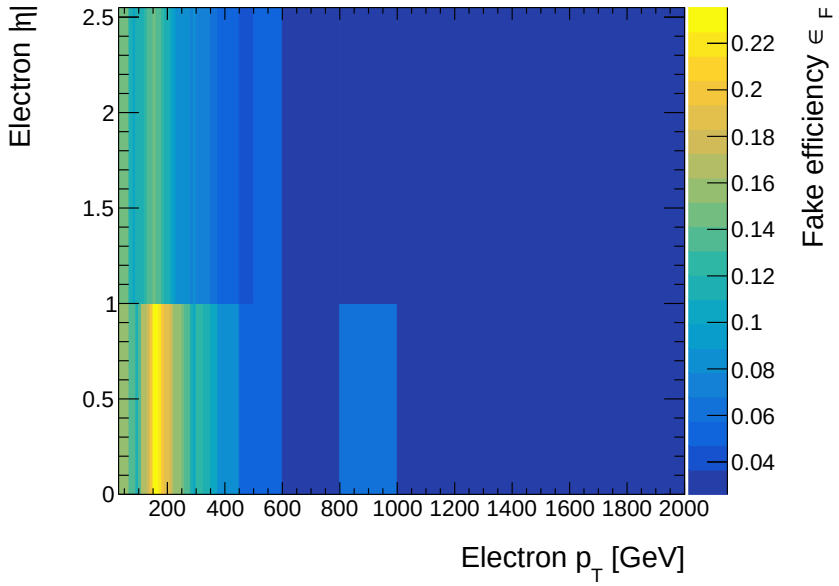

Figure 8.34.: Fake electron efficiency as a function of p_{T} and η for the 2017 data period.

For better visibility the one dimensional distributions are shown in Figure 8.35 for all data periods. There is a rise in the fake efficiencies towards very low electron p_{T} and a decrease towards very high electron p_{T}. The behaviour of the fake efficiencies as a function of a given observable depends strongly on the chosen signal and baseline criteria. In this case, the background contribution to the baseline selection rises stronger towards high p_{T} than to the signal selection, leading to a decreasing efficiency.

Several additional features can be observed that are a consequence of the trigger selection (see [119]). Firstly, it is visible that the fake efficiencies in 2017/18 are higher than those in 2015/16. This is caused by the introduction of the NeuralRinger algorithm mentioned above, in addition to the increase expected from the different pile-up conditions. It reduces the number of fake electron events that pass the trigger, thus leading to a tighter baseline in the denominator of Equation 8.21 and consequently a higher efficiency.

Secondly, it is visible that the efficiency increases slightly when moving from HLT_e60_lhvloose_nod0 to HLT_e140_lhloose_nod0, since the *lhloose* identification working point of the latter has a stronger background rejection than the *lhvloose* (=*very loose*) working point of the former trigger[22]. This leads to a slightly tighter baseline above 150 GeV and a higher efficiency. Thirdly, there is an increase in the 2018 efficiency compared to 2017

[21] The fake efficiencies for the other data periods are shown in Section B.4.3.

[22] Note that even though the baseline selection requires a loose trigger in the offline selection, the effect from the *vloose* trigger in the online selection is still visible, because the offline and online definition of the shower shape identification are similar, but not identical.

above 150 GeV. The reason for this is a new tune for the *lhloose* working point on trigger level, introduced in 2018, that reduces the fake rate passing the trigger and thus tightens the baseline in the efficiency calculation. Furthermore, the slight increase in efficiency in the lowest p_T bin is caused by the change of the Level-1 seed trigger and the application of Level-1 isolation (L1_EM20VH vs L1_EM20VHI). Finally, there is a drop in the efficiency around 300 GeV which is caused by the onset of the HTL_e300_etcut which has a much more permissive selection than the HLT_e140_lhloose_nod0, since no likelihood identification requirements are applied to the electron on HLT level, leading to a looser baseline and thus a lower efficiency. The lack of identification requirements on the HLT electron candidate also means that the HLT_e300_etcut is not affected by the improvements to the triggers discussed above. This explains why the fake efficiencies above 300 GeV are identical within statistical uncertainties between the years.

These changes in the baseline caused by the constraints of the trigger selection do not impair the applicability of the matrix method, since it is only important that the baseline is consistent for any given bin of p_T. It has been verified that the baseline changes have no impact on the final result (see Figure B.15).

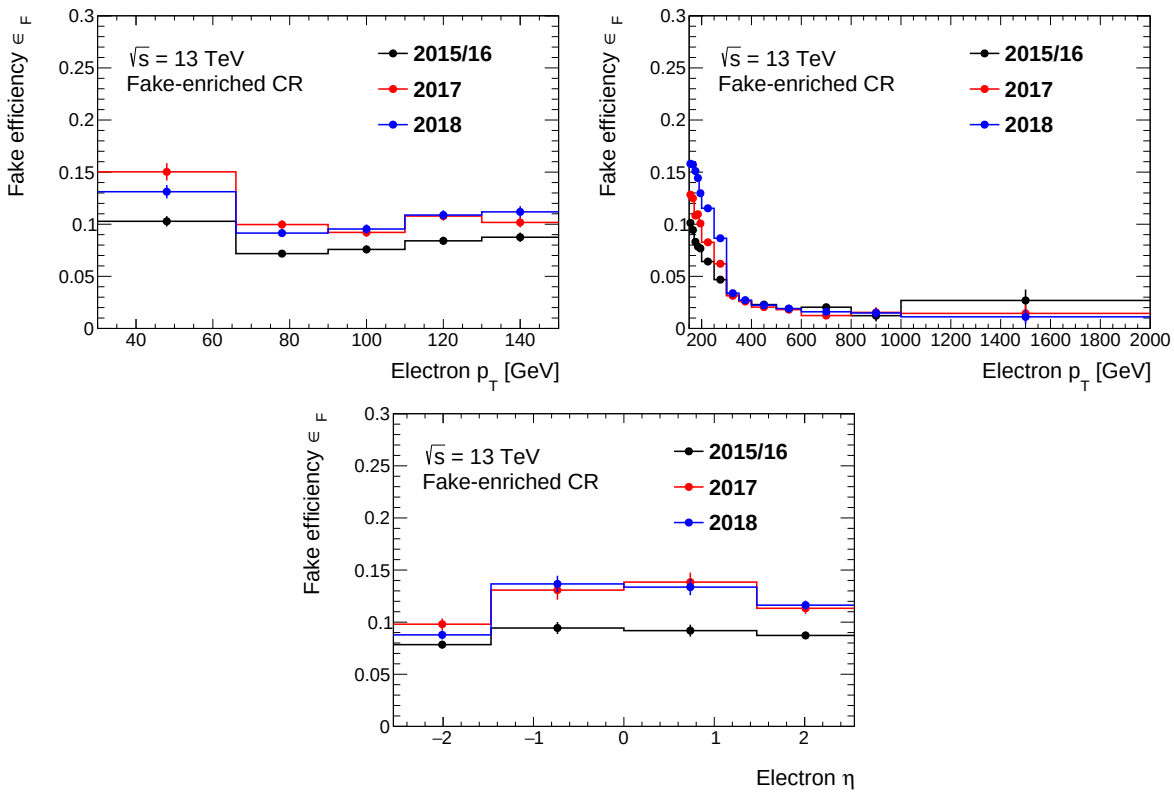

Figure 8.35.: Fake electron efficiency as a function of electron p_T (top panel, split in low p_T on the left and high p_T on the right) and electron η (bottom panel) for the 2015/16 (black), 2017 (red) and 2018 (blue) data period.

8.4.5. Result of the Background Estimate

The final background estimate is obtained by applying Equation 8.26 directly to the prescale corrected data making use of the weights w_i determined event-by-event and the real and fake efficiencies determined as a function of electron p_{T} and η in each event.

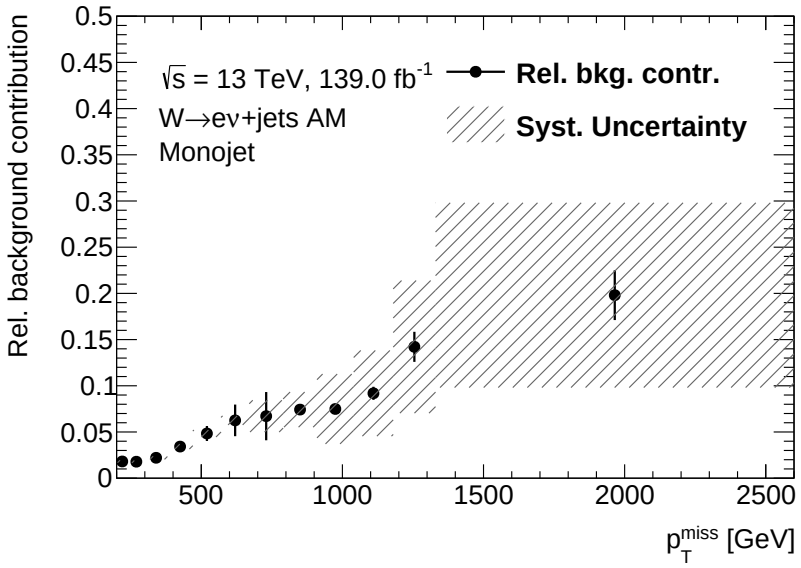

Figure 8.36.: Relative contribution of the fake electron background to $W \rightarrow e\nu$ + jets AM region as a function of $p_{\mathrm{T}}^{\mathrm{miss}}$ in the monojet phase space. The statistical uncertainty is shown as error bars on the points and the systematic uncertainty on the background estimate is shown as a grey hashed band.

The results of the background estimate for the $p_{\mathrm{T}}^{\mathrm{miss}}$ distribution in the monojet phase space are shown in Figure 8.36[23]. It shows the relative fake electron background contribution to the $W \rightarrow e\nu$ + jets AM region together with the statistical uncertainty (error bars) and the systematic uncertainty (grey hashed band) on the background estimate. The relative background contribution is small at low $p_{\mathrm{T}}^{\mathrm{miss}}$ ($\approx 1.8\,\%$), but rises considerably towards higher $p_{\mathrm{T}}^{\mathrm{miss}}$ ($\approx 20\,\%$ relative contribution in the highest bin). The determination of the systematic uncertainty is explained in Section 8.4.7. The statistical uncertainty on the fake background estimate takes into account the statistical uncertainty on the real and fake efficiencies as well as the statistical uncertainty on the signal (N_S) and baseline (N_B) data and is derived with the bootstrap method. The main contribution to the statistical uncertainty comes from the baseline data, which has a relatively large statistical uncertainty at low electron $p_{\mathrm{T}} < 150$ GeV due to the prescaled triggers used to collect it. This causes the statistical fluctuations with large statistical uncertainties in some bins (e.g. $[570, 670, 790]$ GeV) if an event with receives a large weight from the prescale correction.

[23] The results in the VBF phase space is shown in Section B.4.4.

8.4.6. Validation of the Background Estimate

The background estimate is validated in a dedicated background-enriched validation region in data. This is necessary since several assumptions enter its determination, that are difficult to test in the MC simulation. Firstly, the control region used to extract the fake efficiencies is using events with low $p_{\mathrm{T}}^{\mathrm{miss,real}} < 60\,\mathrm{GeV}$, whereas the $W \to e\nu$ + jets AM region requires high $p_{\mathrm{T}}^{\mathrm{miss,real}} > 60\,\mathrm{GeV}$. This potentially changes the composition of the background sources, especially the relative heavy flavour jet content. Secondly, for the control region the cut on $p_{\mathrm{T}}^{\mathrm{miss}} > 200\,\mathrm{GeV}$ is dropped, which means that the fake efficiencies are measured in the bulk of W boson p_{T} distribution whereas the $W \to e\nu$ + jets AM region measures the high p_{T} tail.

The validation region is defined similar to the $W \to e\nu$ + jets AM region, with some background rejection cuts dropped, namely

- cut on $p_{\mathrm{T}}^{\mathrm{miss,real}} > 60\,\mathrm{GeV}$ is dropped.
- cut on the W invariant transverse mass m_T is dropped.

Figure 8.37 shows the agreement between data and MC simulation without the fake electron estimate (top panel) and including the fake electron estimate (bottom panel) for the electron p_{T} distribution in the monojet phase space in the validation region, with the systematic uncertainty shown as a shaded band. Including the fake estimates strongly improves the description of the data, especially in the high p_{T} tail. The agreement between data, simulation and background estimate in the validation region for the $p_{\mathrm{T}}^{\mathrm{miss}}$ distribution in the monojet phase space is shown in Figure 8.38. Good agreement within the systematic uncertainty on the background estimate is observed.

8.4.7. Systematic Uncertainty on the Background Estimate

The main source of systematic uncertainty on the background estimate is the derivation of the fake efficiencies[24], since the composition of the fake background in the fake-enriched control region depends on the selection cuts. To estimate this dependence, the selection criteria of the fake-enriched control region are varied and the fake efficiencies and the background estimate are repeated using the varied selection. The maximum difference to the nominal estimate per bin is symmetrized and assigned as the systematic uncertainty.

The selection criterium that has the strongest impact on the fake efficiencies is the $p_{\mathrm{T}}^{\mathrm{miss,real}}$ selection cut (nominal value: $p_{\mathrm{T}}^{\mathrm{miss,real}} < 60\,\mathrm{GeV}$). Therefore this cut is varied as follows to obtain a systematic uncertainty:

- Low: $p_{\mathrm{T}}^{\mathrm{miss,real}} < 20\,\mathrm{GeV}$, leading to higher fake efficiencies and a larger background estimate.

[24] No additional systematic uncertainty is applied for the real efficiencies, since the modelling of the data by the MC simulation is known to be good with the application of the scale factors (cf. Section 6.3). In addition, any residual MC dependency will be reduced in the efficiency ratio.

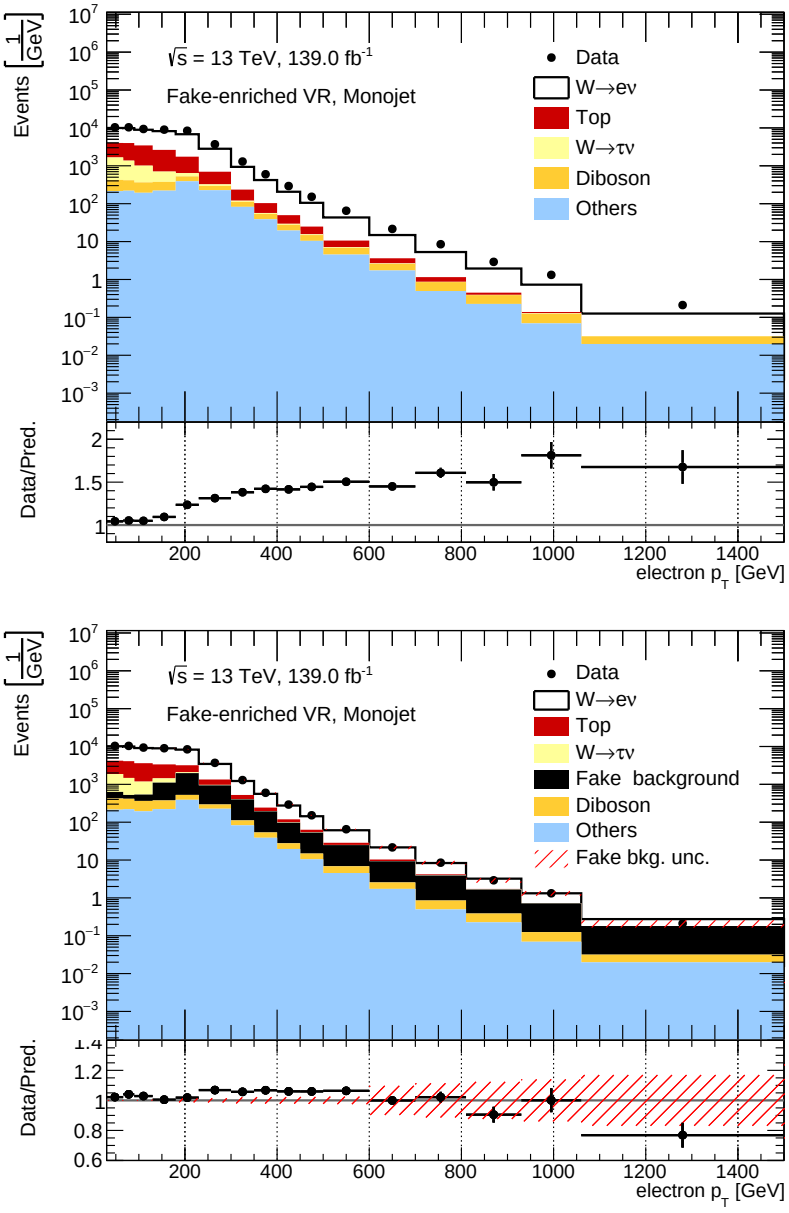

Figure 8.37.: Electron p_{T} distribution in the validation region for the fake electron background in the $W \to e\nu$ + jets AM region in the monojet phase space. Top panel: Distribution of data and MC simulation, together with the ratio of the data and the sum of the MC simulation samples. Bottom panel: Distribution of data, MC simulation and fake electron background estimate together with the ratio of data and the sum of the fake background prediction and the MC simulation samples. The shaded band shows the systematic uncertainty on the fake electron background estimate.

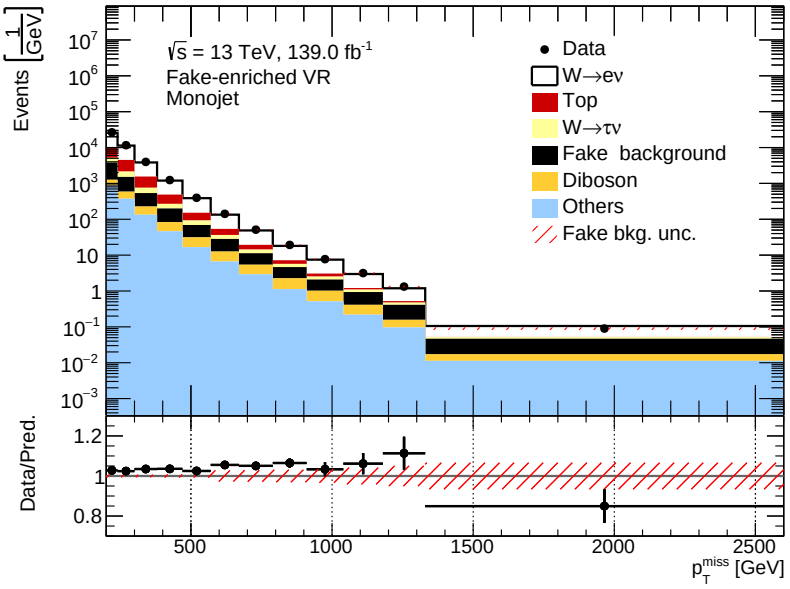

Figure 8.38.: $p_{\mathrm{T}}^{\mathrm{miss}}$ distribution in the validation region for the fake electron background in the $W \to ev$ + jets AM region in the monojet phase space. Distribution of data, MC simulation and fake electron background estimate together with the ratio of data and the sum of the fake background prediction and the MC simulation samples. The shaded band shows the systematic uncertainty on the fake electron background estimate.

- High: $20\,\mathrm{GeV} < p_{\mathrm{T}}^{\mathrm{miss,real}} < 60\,\mathrm{GeV}$, leading to lower fake efficiencies and a smaller background estimate.

The resulting relative systematic uncertainty on the fake estimate are shown in Section B.4.5.

9. Background Contributions due to Limited Detector Efficiency and Acceptance

The SR and the AM regions receive background contributions from SM processes with charged leptons in the final state. These backgrounds typically enter a given region, because a charged lepton is not reconstructed due to the limited detector efficiency and acceptance. An example is a $W \to e\nu$ + jets event, where the electron flies in the forward direction. For large $p_{\mathrm{T}}^{\mathrm{miss,real}}$ from the neutrino, this event is indistinguishable from a $Z \to \nu\nu$ + jets event and can be reconstructed in the SR.

Process	Region					
	SR	$Z \to ee$ AM	$Z \to \mu\mu$ AM	$W \to e\nu$ AM	$W \to \mu\nu$ AM	γ AM
$Z \to \nu\nu$ + jets	**55%**	0%	0%	0%	0%	0%
$Z \to ee$ + jets	0%	**94%**	0%	0%	0%	0%
$Z \to \mu\mu$ + jets	0%	0%	**95%**	0%	2%	0%
$W \to e\nu$ + jets	6%	0%	0%	**68%**	0%	0%
$W \to \mu\nu$ + jets	9%	0%	0%	0%	**67%**	0%
$W \to \tau\nu$ + jets	20%	0%	0%	5%	7%	0%
γ + jets	0%	0%	0%	0%	0%	**100%**
top	7%	3%	2%	25%	21%	0%
Others	3%	3%	3%	2%	3%	0%

Table 9.1.: Process composition for the SR and the AM regions. For this table the region name has been abbreviated (e.g. $Z \to ee$ AM corresponds to the $Z \to ee$ + jets AM region). All background processes involving top quark decays in the matrix element are summed and shown in the "top" row. "Others" includes di-boson, tri-boson and $Z \to \tau\tau$ + jets processes. Background contributions from fake processes are not shown.

This type of background is the dominant background contribution in several regions of the measurement. This is illustrated in Table 9.1, which shows the signal (bold font) and background contributions from various SM processes to the measurement[1]. The background contributions are largest in the SR ($\approx$ 45 %), the $W \to \mu\nu$ + jets AM region ($\approx$ 33 %) and the

[1]The contributions for this table are determined using MC simulation. Background contributions from fakes are not shown.

$W \to e\nu$ + jets AM region ($\approx 32\,\%$). For the remaining regions the contributions are smaller ($\leq 6\,\%$)[2].

The contributions from these backgrounds have to be *subtracted* from the measured data, in order to perform the cross section measurements of the SM signal process in each region. To do this, this contribution has to be estimated.

The estimation of the backgrounds using only MC simulation is not optimal, since some of the background processes are poorly modelled in the simulation. In addition, large uncertainties on the predictions of the backgrounds would have to be taken into account in the cross section measurement due to the subtraction. This would lead to a large uncertainty on the final results for regions with a large background contribution. One example is the uncertainty on the renormalisation and factorization scales used in the MC simulation, which can be up to 20 % for $W \to \ell\nu$ + jets processes in the region $p_{\mathrm{T}}^{\mathrm{miss}} > 200\,\mathrm{GeV}$. Considering that $W \to \ell\nu$ + jets processes contribute with about 35 % to the total event yield in the SR, this would lead to an additional uncertainty on the measurement of the $Z \to \nu\nu$ + jets cross section of approximately 7 % from the scale uncertainty alone. This is larger than the expected experimental systematic uncertainty on the cross section from the $Z \to \nu\nu$ + jets process in the SR, which is about 6 %.

Therefore the estimation of the dominant background processes is performed in a data-driven way. A background process is considered dominant in a region, if it contributes more than 5 % to the total event yield to that region. Smaller backgrounds are estimated purely based on MC simulation, since they have no large impact on the uncertainties of the measured cross sections.

In the data-driven method, the *normalisation* of the MC simulation of each dominant background process is determined in data and the *shape* predicted by the simulation is validated in data. The method also helps to constrain the impact of the theoretical and experimental systematic uncertainties of the backgrounds on the measured cross section. The background estimation method is discussed in the remainder of this chapter.

Dominant backgrounds that need to be determined in a data-driven way are only present in the SR, the $W \to e\nu$ + jets AM and the $W \to \mu\nu$ + jets AM region. The backgrounds in the $Z \to ee$ + jets AM, $Z \to \mu\mu$ + jets AM and the γ+jets AM regions are subdominant.

9.1. Shape and Normalisation Determination of the Dominant Background Processes

The estimation of the contributions from the dominant background processes is split into two parts: The determination of the *shape* and the measurement of the *normalisation* of each background component.

The *shape* of the background components is taken from MC simulation. It is difficult to measure directly in data, because these backgrounds occur, if one or more charged leptons

[2]Please note that a small part of the di- and tri-boson contributions is not due to limited detector acceptance and efficiency, when the bosons decay invisibly. However, since this contribution is small and estimated purely with MC simulation it is not treated separately.

in the final state of the background processes are not measured in the detector. This happens either because leptons are outside of the detector acceptance - be it geometrically (e.g. the tracking range, for electrons) or energetically (e.g. low-p_{T} objects below the detection threshold) - or they are missed due to detector inefficiencies. It is however possible to define control regions (CRs) in data and use them to validate the shapes predicted by the MC simulation. These CRs are also used to measure the *normalisation* of each background component.

The general idea behind the definition of the CRs is to keep them as close as possible to the original regions, but require in addition a lepton corresponding to the background process to be validated and normalised (e.g. the CR used to validate and normalise the $W \to e\nu$ + jets background in the SR is defined by requiring the SR selection plus one electron). In this way the extrapolation to the actual background processes due to out-of-acceptance and out-of-efficiency leptons is kept minimal. The specific definition of these CRs and the shape validation and the extraction of the background normalisation from data is discussed in the following sections.

9.2. Signal Region Backgrounds

In the SR the dominant background processes are $W \to e\nu$ + jets, $W \to \mu\nu$ + jets, $W \to \tau\nu$ + jets and processes involving top quark decays, called top in the following, where the top contribution is dominated by leptonic $t\bar{t}$ decays ($> 85\%$)[3]. For each of these background processes a CR is defined according to Table 9.2.

For the $W \to \ell\nu$ + jets CRs the respective charged lepton is added to the SR selection. For electrons and muons the signal lepton definition for the corresponding $W \to \ell\nu$ + jets AM regions is used and for taus the *signal tau* definition is used (see Section 5.1). A minimum lepton p_{T} 30 GeV, which is the minimum p_{T} possible for signal electrons, is required for all CRs, to achieve a coherent selection.

Please note that $W \to \ell\nu$ + jets CRs and the $W \to \ell\nu$ + jets AM regions are not identical. A major difference is that in the $W \to \ell\nu$ + jets CR $p_{\mathrm{T}}^{\mathrm{miss,real}} > 200\,\mathrm{GeV}$ is required, as in the SR selection. In the $W \to \ell\nu$ + jets AM regions the selection cut is on the boson p_{T}-proxy $p_{\mathrm{T}}^{\mathrm{miss}} > 200\,\mathrm{GeV}$. Despite this difference the regions are correlated. The impact of these correlations on the background estimate is discussed in Section C.3.

$W \to e\nu$ + jets CR	$W \to \mu\nu$ + jets CR	$W \to \tau\nu$ + jets CR	top CR
SR selection			
1 signal electron	1 signal muon	1 signal tau	1 signal muon 1 signal electron opposite charge
lepton $p_T > 30\,\mathrm{GeV}$			

Table 9.2.: Definition of the CRs used to validate and constrain the MC simulation predictions for the dominant background processes in the SR.

[3] See Section C.1 for further details.

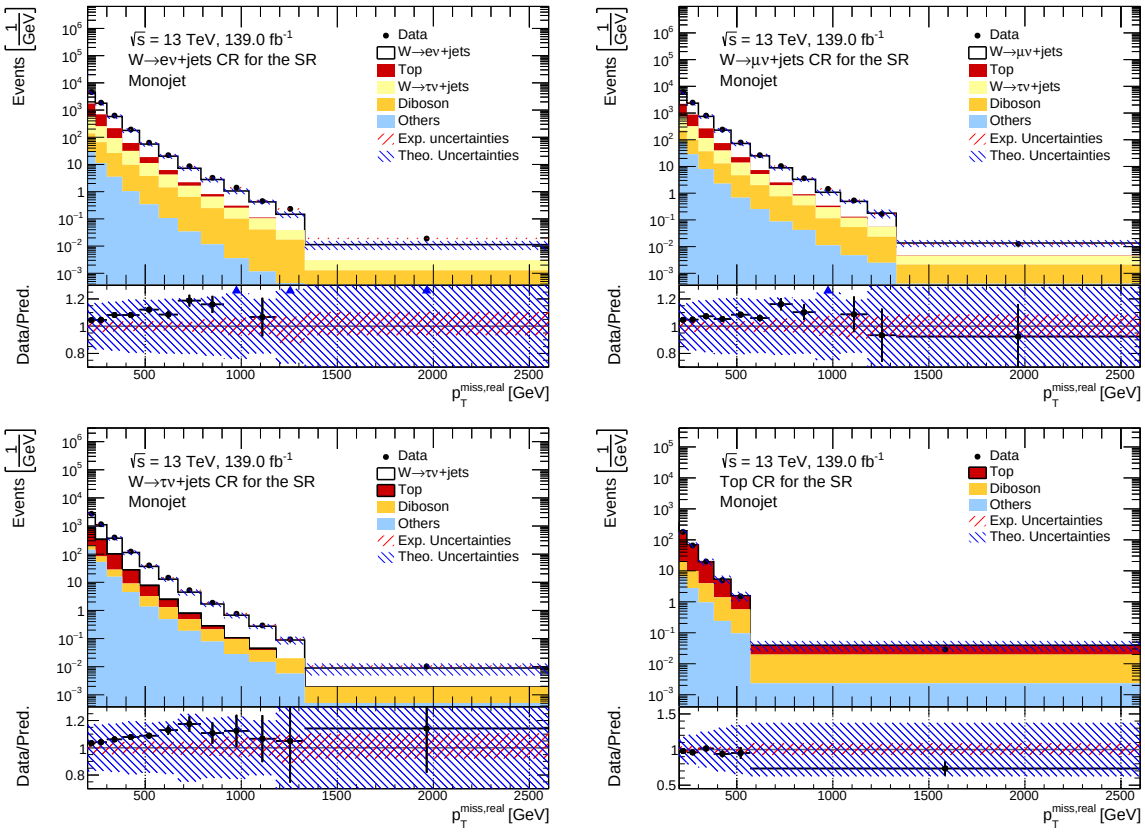

Figure 9.1.: Comparison of data and MC simulation in the CRs used to normalise and validate the dominant backgrounds in the SR in the monojet phase space as a function of $p_{\mathrm{T}}^{\mathrm{miss,real}}$. The bottom panel of each plot shows the ratio between data and MC simulation prediction. The bands show the experimental (red) and theoretical (blue) systematic uncertainties. The black error bars show the combined statistical uncertainty on the data and the MC simulation. Top left panel: $W \to e\nu$ + jets CR, top right panel: $W \to \mu\nu$ + jets CR, bottom left panel: $W \to \tau\nu$ + jets CR, bottom right panel: top CR.

For the top background processes a fully leptonic $t\bar{t}$ selection is used, by requiring an oppositely charged electron-muon pair in addition to the SR selection. Same flavour lepton pairs are excluded to reduce the contribution from $Z \to \ell\ell$ + jets decays. These selection criteria are chosen to ensure a high signal efficiency in the CR.

All other background processes in the SR (di-boson, tri-boson and $Z \to \ell\ell$ + jets processes) are considered subdominant and are estimated and subtracted purely based on MC simulation.

The comparison of data and MC simulation in the CRs is shown in Figure 9.1 as a function of $p_{\mathrm{T}}^{\mathrm{miss,real}}$ in the monojet phase space[4]. The top panel of each plot shows the measured data (black points) and the MC simulation predictions. The bottom panel shows the ratio of

[4]See Section C.2.1 for the VBF phase space.

data and the total prediction. The shaded bands show the experimental (red) and theoretical (blue) systematic uncertainties on the MC simulation. Good shape agreement and a constant normalisation offset is observed for the $W \to e\nu$ + jets CR (top left), $W \to \mu\nu$ + jets CR (top right) and $W \to \tau\nu$ + jets CR (bottom left). The difference between data and MC simulation prediction is covered by the systematic uncertainties. The top CR (bottom right) shows good shape and also normalisation agreement, with the ratio of data and prediction close to unity. These plots demonstrate that the shape predicted by the MC simulation agrees well with the shape observed in data.

In a next step the CRs are used in a combined fit to determine the normalisation of the MC simulation samples from data. To achieve this a system of linear equations, built according to the template shown in Equation 9.1, is constructed. In the equation template k_X is the normalisation factor of the MC simulation sample of background process X, MC_Y^X the integrated yield of simulated events of background process X in CR Y, $data_Y$ the integrated event yield in CR Y and MC_Y^{bkg} the integrated yield of simulated events of the subdominant background MC samples (diboson, triboson, $Z \to \ell\ell$) in CR Y.

$$k_{W\to e\nu} MC_Y^{W\to e\nu} + k_{W\to \mu\nu} MC_Y^{W\to \mu\nu} + k_{W\to \tau\nu} MC_Y^{W\to \tau\nu} + k_{top} MC_Y^{top} = data_Y - MC_Y^{bkg} \quad (9.1)$$

This system of equations is then solved to extract the normalisation factor k_X of each background process. The bootstrap method is used to obtain a statistical uncertainty on the normalisation factors. The highest number of bootstrap replica that is still computationally feasible (10 000) is used. The advantage of this simple system of equations is that it is fast to calculate. This is important since the fit has to be repeated many times, once for each bootstrap replica and also for the systematic variations.

This extraction of the normalisation factors is performed independently for the monojet and the VBF phase space, since different normalisation offsets are possible, due to the different phase space selections.

The normalisation factors k_X obtained from solving Equation 9.1 are shown in table Table 9.3. The first column of uncertainties gives the statistical uncertainty and the second column gives the systematic uncertainty, which is further discussed in Section 9.5. All $W \to \ell\nu$ regions show a largely consistent normalisation offset within the uncertainties in each phase space, which is expected, since the same MC generator is used in all cases and the only difference in the process is the lepton flavour in the final state.

The consistency of the normalisation factors k_X is verified by comparing the agreement of data and the normalised MC simulation samples. This is shown in Figure 9.2 for the monojet phase space together with the systematic uncertainties [5]. In all cases good agreement between data and the normalised MC samples is observed within the systematic uncertainties. This validates the use of the normalised MC simulation to determine the contributions of the dominant background processes to the SR. The reduction of the systematic uncertainties after the fit is discussed in Section 9.4.

[5] see Section C.2.2 for the VBF phase space.

Background process	Normalisation factor k_X	
	Monojet phase space	VBF phase space
$W \to e\nu$ + jets	$1.09 \pm 0.01 \pm 0.01$	$1.10 \pm 0.01 \pm 0.02$
$W \to \mu\nu$ + jets	$1.08 \pm 0.01 \pm 0.03$	$1.10 \pm 0.01 \pm 0.04$
$W \to \tau\nu$ + jets	$1.08 \pm 0.01 \pm 0.03$	$1.13 \pm 0.01 \pm 0.06$
top	$0.97 \pm 0.01 \pm 0.01$	$0.98 \pm 0.01 \pm 0.03$

Table 9.3.: Normalisation factors determined from data for the dominant backgrounds in the SR for the monojet and VBF phase spaces. The first error column gives the statistical uncertainty and the second error column gives the systematic uncertainty.

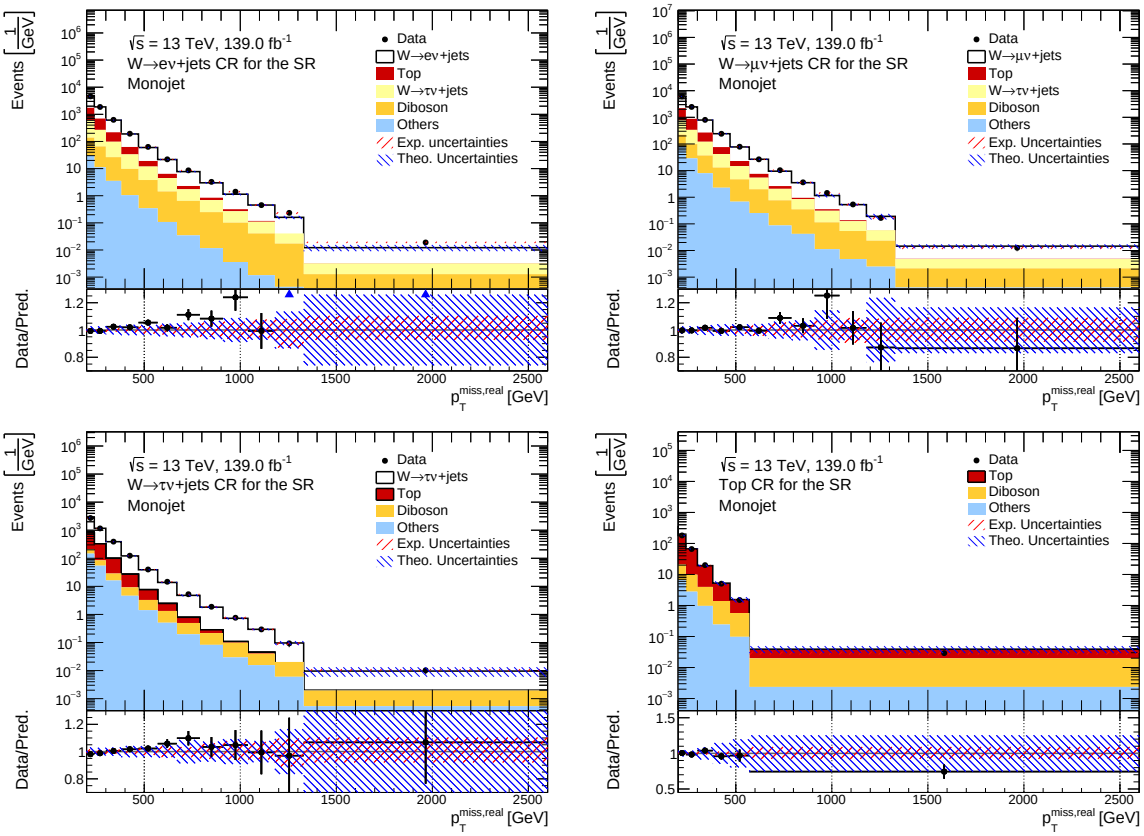

Figure 9.2.: Comparison of data and MC simulation in the CRs used to normalise and validate the dominant backgrounds in the SR in the monojet phase space. The dominant background processes determined from MC simulation are scaled with the normalisation factors k_X. The bottom panel of each plot shows the ratio between data and MC simulation prediction. The bands show the experimental (red) and theoretical (blue) systematic uncertainties. The black error bars show the combined statistical uncertainty on the data and the MC simulation. Top left panel: $W \to e\nu$ + jets CR, top right panel: $W \to \mu\nu$ + jets CR, bottom left panel: $W \to \tau\nu$ + jets CR, bottom right panel: top CR.

9.3. Backgrounds in the $W \to e\nu$ + jets and $W \to \mu\nu$ + jets Auxiliary Measurement Regions

In the $W \to e\nu$ + jets AM and $W \to \mu\nu$ + jets AM regions the dominant background processes are top and $W \to \tau\nu$ + jets, where the top contribution is dominated by leptonic $t\bar{t}$ decays ($> 85\,\%$)[6]. For each of these processes a CR is defined according to Table 9.4.

For the top backgrounds separate CRs are defined for the $W \to e\nu$ + jets AM and the $W \to \mu\nu$ + jets AM region, by adding a jet multiplicity requirement of six or more jets to the respective region selection. This greatly enhances the relative top contribution, due to the high jet multiplicity in $t\bar{t}$ decays.

For the $W \to \tau\nu$ + jets backgrounds the CR is defined by requiring a signal tau lepton, with a cut around the invariant transverse mass m_{T} of the W boson to suppress potential fake tau backgrounds and a requirement of $p_{\mathrm{T}}^{\mathrm{miss,real}} > 160\,\mathrm{GeV}$, to ensure that the $p_{\mathrm{T}}^{\mathrm{miss}}$ trigger used to trigger these events is 100 % efficient. The $W \to \tau\nu$ + jets CR is defined in the identical way for both the $W \to e\nu$ + jets AM and the $W \to \mu\nu$ + jets AM region, since the only relevant difference between both is the m_{T} cut. This cut can not be relaxed in the $W \to \tau\nu$ + jets CR, as it is needed for the fake background suppression.

Top CR		$W \to \tau\nu$ + jets CR
$W \to e\nu$ + jets AM	$W \to \mu\nu$ + jets AM	
$W \to e\nu$ + jets AM selection	$W \to \mu\nu$ + jets AM selection	1 signal tau
$n_{jets} \geq 6$		$30\,\mathrm{GeV} < m_{\mathrm{T}} < 100\,\mathrm{GeV}$
		$p_{\mathrm{T}}^{\mathrm{miss,real}} > 160\,\mathrm{GeV}$
lepton $p_{\mathrm{T}} > 30\,\mathrm{GeV}$		

Table 9.4.: Definition of the CRs used to validate and normalise the MC simulation predictions for the dominant background processes in the $W \to e\nu$ + jets AM and $W \to \mu\nu$ + jets AM regions. Note that the $W \to \tau\nu$ + jets CR as defined here is used for both the $W \to e\nu$ + jets AM and the $W \to \mu\nu$ + jets AM regions.

The comparison of data and MC simulation in these CRs is shown in Figure 9.3 for the monojet phase space as a function of $p_{\mathrm{T}}^{\mathrm{miss}}$. Good shape and normalisation agreement is observed in case of the $W \to \tau\nu$ + jets CRs (top panels). For the top CRs (bottom panels) good shape agreement is observed, but also consistent normalisation offset, where the event yield is overestimated by the MC simulation. All discrepancies, except for what is likely a statistical fluctuation in one bin of the $W \to \tau\nu$ + jets CRs, are covered by the systematic uncertainties on the theory predictions.

The same procedure as described in the previous section is applied to extract the factors used to normalise the background MC samples from these CRs. Separate fits are performed for the $W \to e\nu$ + jets AM and the $W \to \mu\nu$ + jets AM regions, to take potential differences due to the different selection criteria for both regions into account.

[6] See Section C.1 for further details.

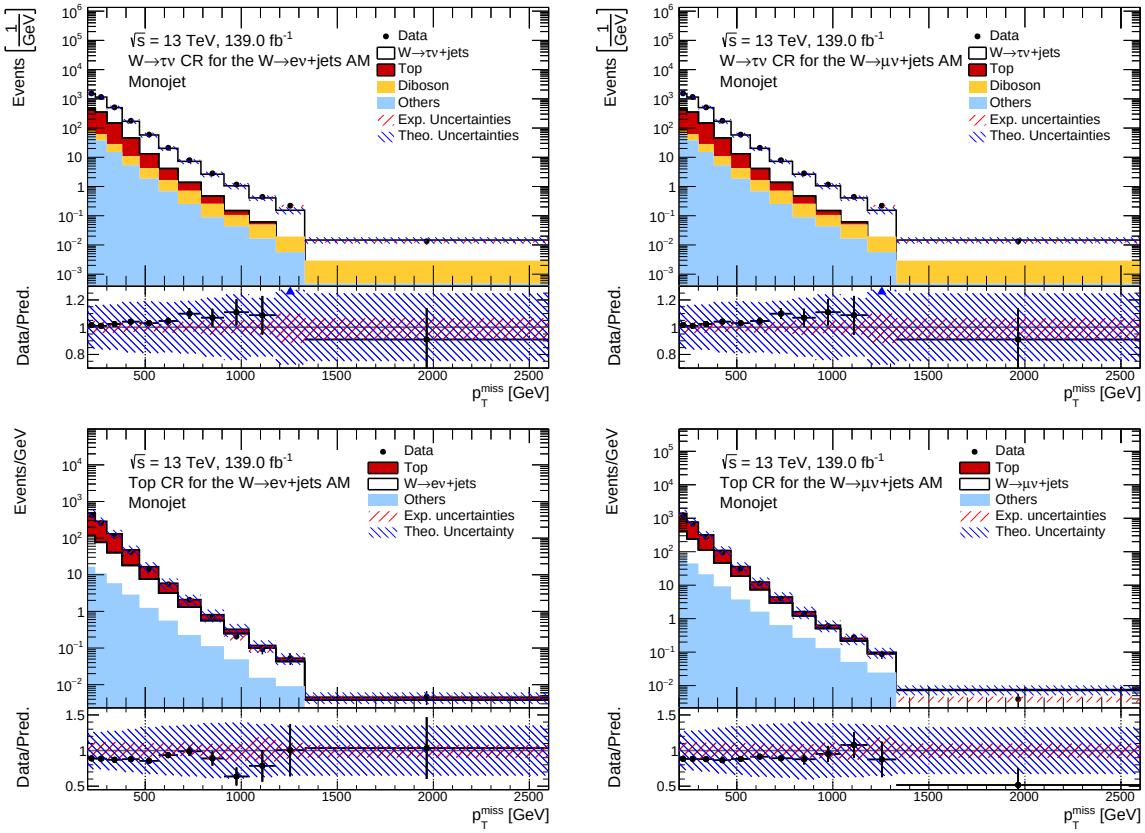

Figure 9.3.: Comparison of data and MC simulation in the CRs used to normalise and validate the dominant backgrounds in the $W \to e\nu$ + jets AM and $W \to \mu\nu$ + jets AM regions for $p_{\mathrm{T}}^{\mathrm{miss}}$ in the monojet phase space. The bottom panel of each plot shows the ratio between data and MC simulation prediction. The bands show the experimental (red) and theoretical (blue) systematic uncertainties. The black error bars show the combined statistical uncertainty on the data and the MC simulation. Top left panel: $W \to \tau\nu$ + jets CR for the $W \to e\nu$ + jets AM region, top right panel: $W \to \tau\nu$ + jets CR for the $W \to \mu\nu$ + jets AM region, bottom left panel: top CR for the $W \to e\nu$ + jets AM region, bottom right panel: top CR for the $W \to \mu\nu$ + jets AM region.

The resulting normalisation factors are shown in Table 9.5 for the $W \to e\nu$ + jets AM region and Table 9.6 for the $W \to \mu\nu$ + jets AM region, with the first error column giving the statistical and the second error column the systematic uncertainty on the normalisation factors. A good agreement of the normalisation factors for $W \to \tau\nu$ + jets and top is observed between the $W \to e\nu$ + jets AM and $W \to \mu\nu$ + jets AM region within the uncertainties. The difference of the top normalisation factor between the $W \to e\nu$ + jets AM and $W \to \mu\nu$ + jets AM regions and the SR is attributed to the different phase-space selection.

The consistency of the normalisation factors is verified by comparing the agreement of the data and the normalised MC simulation samples. This is shown in Figure 9.4 for $p_{\mathrm{T}}^{\mathrm{miss}}$ in the monojet phase space together with the experimental and theoretical systematic uncertainties.

Background process	Normalisation factor k_X	
	Monojet phase space	VBF phase space
$W \to \tau\nu$ + jets	$1.10 \pm 0.01 \pm 0.01$	$1.10 \pm 0.01 \pm 0.02$
top	$0.78 \pm 0.01 \pm 0.02$	$0.70 \pm 0.04 \pm 0.05$

Table 9.5.: Normalisation factors determined from data for the dominant Standard Model backgrounds in the $W \to e\nu$ + jets AM region for the monojet and VBF phase spaces. The first error column gives the statistical uncertainty and the second error column gives the systematic uncertainty.

Background process	Normalisation factor k_X	
	Monojet phase space	VBF phase space
$W \to \tau\nu$ + jets	$1.11 \pm 0.01 \pm 0.02$	$1.10 \pm 0.01 \pm 0.03$
top	$0.75 \pm 0.01 \pm 0.01$	$0.70 \pm 0.02 \pm 0.03$

Table 9.6.: Normalisation factors determined from data for the dominant Standard Model backgrounds in the $W \to \mu\nu$ + jets AM region for the monojet and VBF phase spaces. The first error column gives the statistical uncertainty and the second error column gives the systematic uncertainty.

In all cases good agreement between data and the scaled MC samples is observed within the systematic uncertainties.

To rule out a potential bias in the top CRs due to the selection cut on the jet multiplicity, the jet multiplicity distributions before and after the normalisation procedures are compared in Figure 9.5 for both the $W \to e\nu$ + jets AM (left) and the $W \to \mu\nu$ + jets AM (right) regions. It is shown that the MC simulation without the normalisation factors applied (top row) describes the jet multiplicity distribution only poorly, with the discrepancy between data and simulation ranging from +20 % to −20 %. This improves greatly after the application of the normalisation factors to the respective MC samples (bottom row) and good compatibility with unity is observed in the comparison between data and MC simulation.

Please note that the improvement of the description of the jet multiplicity distribution shown in Figure 9.5 is non-trivial, since the shape of the background components predicted by the MC simulation is not changed, only the normalisation.

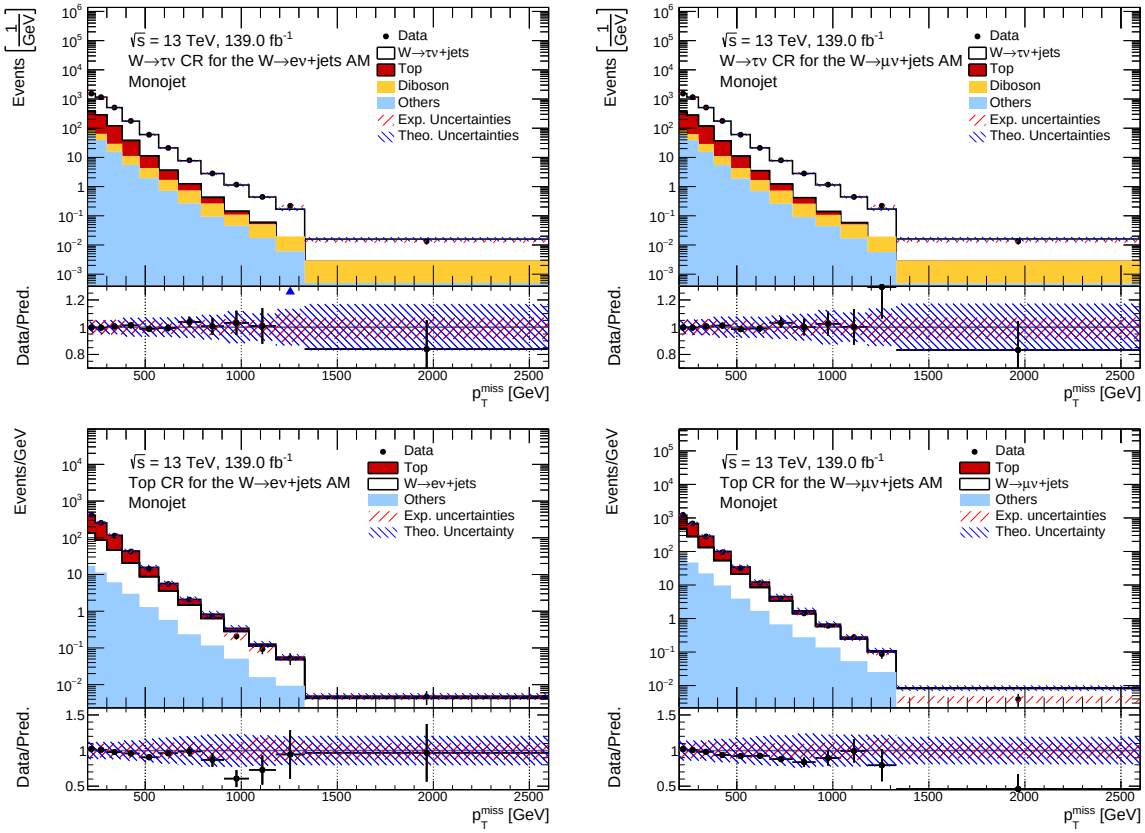

Figure 9.4.: Comparison of data and MC simulation in the CRs used to normalise and validate the dominant backgrounds in the $W \to e\nu$ + jets AM and $W \to \mu\nu$ + jets AM regions for $p_{\mathrm{T}}^{\mathrm{miss}}$ in the monojet phase space. The dominant background processes determined from MC simulation are scaled with the the normalisation factors k_X. The bottom panel of each plot shows the ratio between data and MC simulation prediction. The bands show the experimental (red) and theoretical (blue) systematic uncertainties. The black error bars show the combined statistical uncertainty on the data and the MC simulation. Top left panel: $W \to \tau\nu$ + jets CR for the $W \to e\nu$ + jets AM region, top right panel: $W \to \tau\nu$ + jets CR for the $W \to \mu\nu$ + jets AM region, bottom left panel: top CR for the $W \to e\nu$ + jets AM region, bottom right panel: top CR for the $W \to \mu\nu$ + jets AM region.

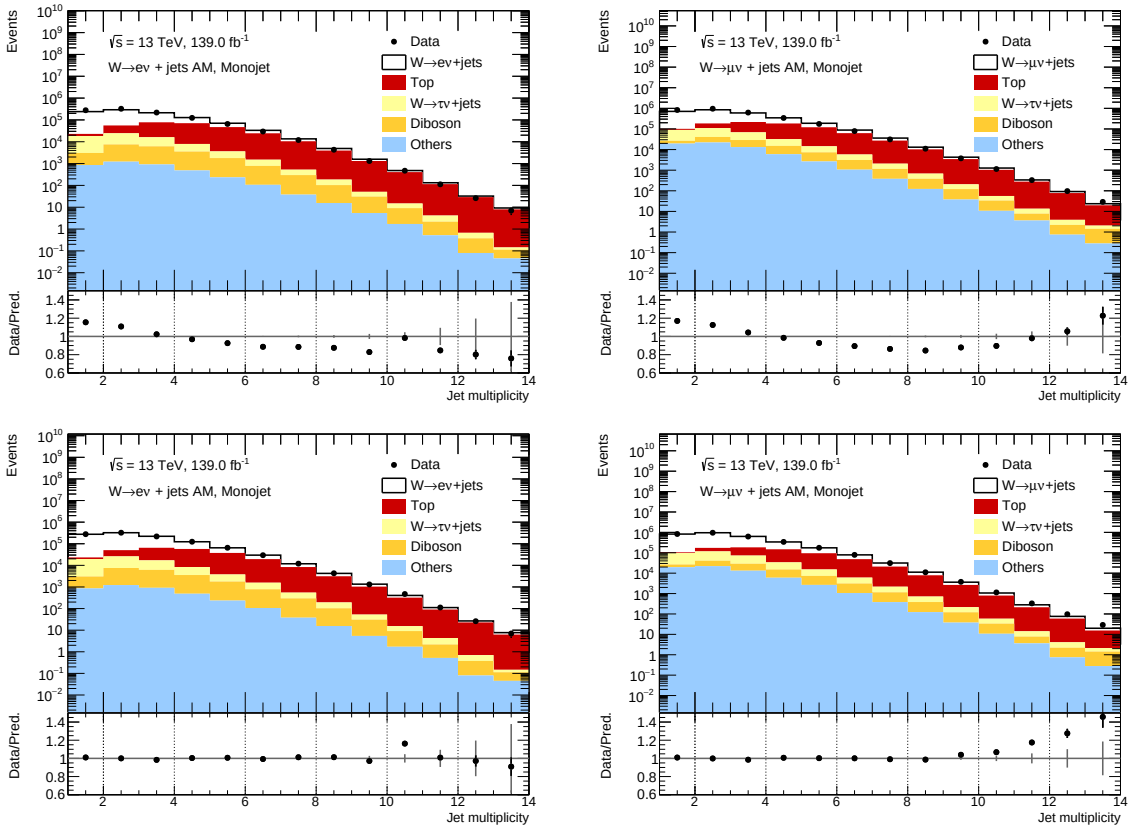

Figure 9.5.: Comparison of data and MC simulation for the jet multiplicity distribution in the monojet phase space for the $W \to e\nu$ + jets AM region (left) and the $W \to \mu\nu$ + jets AM region (right), before (top) and after (bottom) the application of the normalisation factors. The bottom panel of each plot shows the ratio between data and MC simulation. The grey error bars show the statistical uncertainty on the data the black error bars show the statistical uncertainty on the MC simulation.

9.4. Constraining the Impact of Systematic Uncertainties

The normalisation procedure is also used to constrain the impact of the experimental and theoretical systematic uncertainties on the dominant backgrounds. This is an important step which contributes to the precision of the measurement. To constrain impact of the systematic uncertainties, the complete fit procedure outlined above is repeated for each theoretical and experimental systematic variation and a new set of normalisation factors $k_{Syst,X}$ is determined for each variation. The following discussion is based on several example variations.

This is illustrated for two examples in Figure 9.6 for the $W \to \tau\nu$ + jets background in the $W \to \tau\nu$ + jets CR for the SR. The left column shows `JET_EffectiveNP_Modelling1RecoMET`, a $\pm 1\sigma$ variation of the jet energy scale. The top row shows the relative systematic uncertainty on the $p_{\mathrm{T}}^{\mathrm{miss,real}}$ distribution in the $W \to \tau\nu$ + jets CR due to the variation. It is symmetric and relatively flat around 1.5 %. The middle row shows the the relative variation of the corresponding normalisation factor $k_{Syst,X}$ with respect to the nominal normalisation factor k_X.

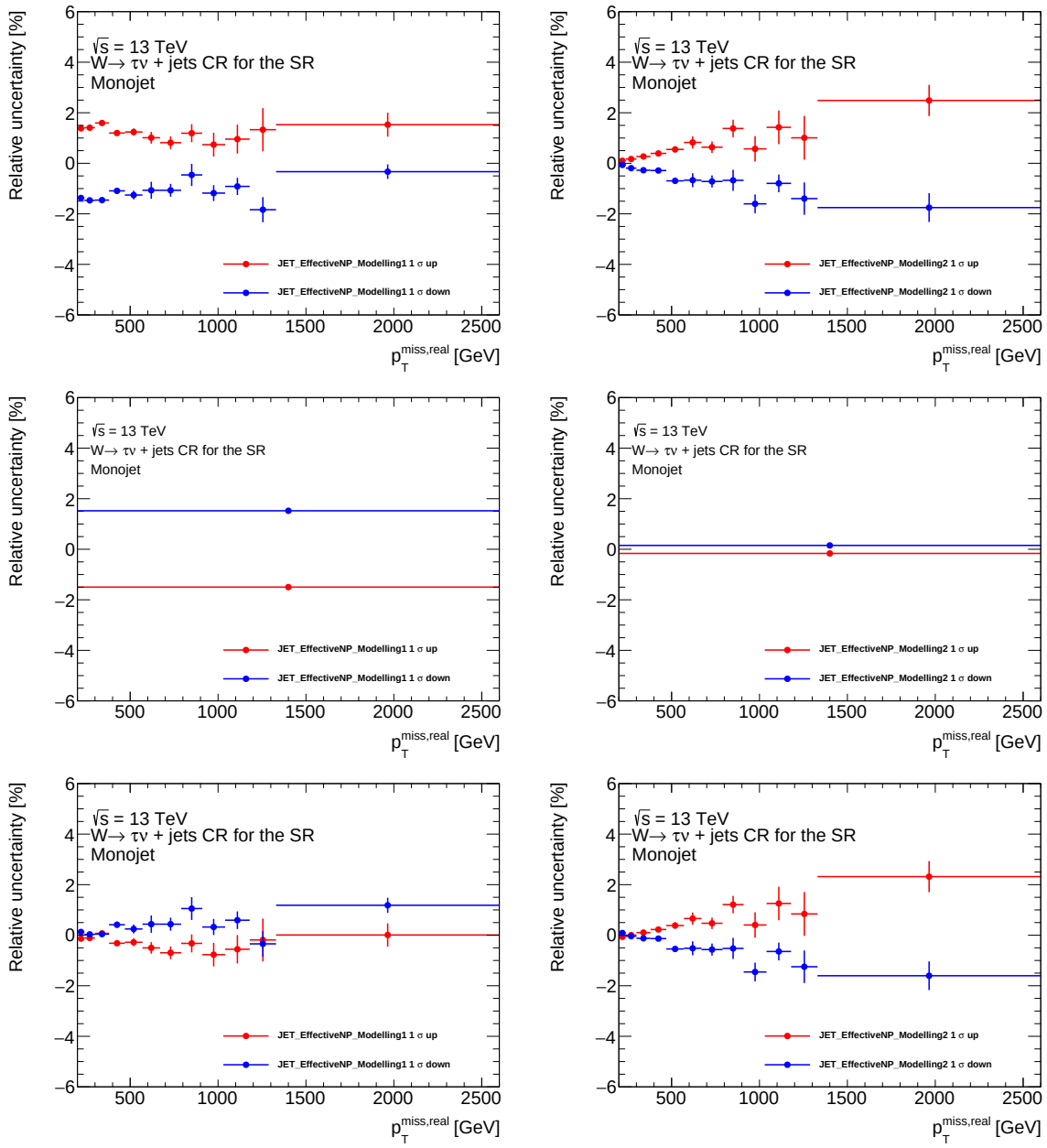

Figure 9.6.: Relative systematic uncertainty on the $W \rightarrow \tau\nu$ + jets background due to two jet energy scale variations: `JET_EffectiveNP_Modelling1` (left) and `JET_EffectiveNP_Modelling2` (right). The $+1\sigma$ variation is shown in red, the -1σ variation is shown in blue. Top panel: Relative systematic uncertainty as a function of $p_{\mathrm{T}}^{\mathrm{miss,real}}$. Middle panel: Relative shift of the normalisation factors $k_{W\rightarrow\tau\nu+jets}$ due to the systematic variation. Bottom panel: Relative systematic uncertainty as a function of $p_{\mathrm{T}}^{\mathrm{miss,real}}$ after application of the normalisation factors.

The relative size of the varied normalisation factor is similar to the relative systematic uncertainty, with the variation $+1\sigma$ leading to a smaller normalisation factor and -1σ variation leading to a larger normalisation factor. The bottom row shows the relative uncertainty on the $W \to \tau\nu$ + jets background after application of the varied normalisation factor $k_{Syst,X}$, which demonstrates a strongly reduced systematic uncertainty.

The right column of Figure 9.6 shows the same type of plots for `JET_EffectiveNP_Modelling2RecoMET`, a different variation of the jet energy scale. Here it is visible that the relative systematic uncertainty (top row) has a relatively strong shape, growing in absolute values towards higher $p_{\mathrm{T}}^{\mathrm{miss}}$ and relatively small at low $p_{\mathrm{T}}^{\mathrm{miss}}$. The resulting relative variation on the normalisation factor $k_{Syst,X}$, is much smaller than in the previous case, since the normalisation is dominated by the first few bins of the spectrum, which contain most events. Consequently the resulting relative systematic uncertainty on the normalised $W \to \tau\nu$ + jets background (bottom panel) is slightly reduced but still prominent, since only the normalisation is constrained, but not the shape. Therefore the normalisation procedure is very powerful to constrain the impact of systematic uncertainties that result in a flat shift of the spectrum.

All residual systematic uncertainties that remain after the normalisation procedure, are propagated to the final result.

9.5. Systematic Uncertainties on the Data-driven Method

A systematic uncertainty on the normalisation factors is determined by varying the main cuts used in the event selection of the CRs. These variations allow to asses the robustness of the method and to encapsulate the dependence of the MC simulation on the selection cuts in a NP that is used in addition to the residual experimental and theoretical uncertainties described in the previous section.

The CRs used for the SR region (defined in Table 9.2) are varied according to:

- Reduce lepton p_{T} cut to $p_{\mathrm{T}} = 20\,\mathrm{GeV}$.
- Raise lepton p_{T} cut to $p_{\mathrm{T}} = 40\,\mathrm{GeV}$.
- Apply a cut on the invariant transverse mass of the W boson $30\,\mathrm{GeV} < m_{\mathrm{T}} < 100\,\mathrm{GeV}$.

The CRs used for the $W \to \ell\nu$ + jets AM regions (defined in Table 9.4) are varied according to:

- Reduce lepton p_{T} cut to $p_{\mathrm{T}} = 27\,\mathrm{GeV}$.
- Raise lepton p_{T} cut to $p_{\mathrm{T}} = 40\,\mathrm{GeV}$.
- Reduce n_{jet} cut to $n_{jet} \geq 5$.
- Raise n_{jet} cut to $n_{jet} \geq 7$.

where applicable. For each variation the extraction of the normalisation factors is repeated. The final uncertainty for each normalisation factor is obtained as the maximum difference of any single variation to the nominal. This uncertainty is then symmetrised. The resulting uncertainties on the normalisation factors are shown in Table 9.3, Table 9.5 and Table 9.6.

To propagate this systematic uncertainty to the measured cross sections, one NP each is defined for SR, the $W \to e\nu$ + jets AM region and the $W \to \mu\nu$ + jets AM region, by coherently varying all normalised backgrounds by $\pm 1\sigma$ and the performing the background subtraction with the varied backgrounds.

10. Detector-level Modelling of the Measured Observables

In this chapter the quality of the description of the data by the combination of the SM signal MC simulation and the background estimates is investigated. This step is important to verify that the signal and background modelling is understood within the theoretical and systematic uncertainties, before the backgrounds are subtracted for the determination of the cross section.

The results of the comparison between data and the estimates of the different contributions are shown in in Figure 10.1, Figure 10.2 and Figure 10.3 for a selection of observables and discussed in the remainder of this chapter. The distributions for all regions, phase spaces and observables are shown in Appendix D.

The figure for each observable is split in two parts. The top panel shows the data (black points) together with the SM signal MC simulation and the background estimates. The SM signal process is always shown in white. Only the dominant background contributions and the fake background estimates are shown. Subdominant contributions are summed together as "Others". The bottom panel shows the ratio of the data to the total MC simulation and the background estimates (black points), together with the experimental systematic uncertainties (red hashed bands) and the theoretical systematic uncertainties (blue hashed bands). The statistical uncertainties on the data, the MC simulation and the background estimates are summed in quadrature and shown as black error bars on the points.

Figure 10.1 shows the $p_{\mathrm{T}}^{\mathrm{miss}}$ distribution in the monojet phase space in the SR (top panel) and the γ+jets AM region (bottom panel).

In the SR the shape of the spectrum is well described by the the combination of the different contributions. The fake $p_{\mathrm{T}}^{\mathrm{miss}}$ background estimate is especially important to achieve a good modelling in the first bin of the distribution. There is a normalization offset of roughly 10 %. This offset is similar to what is observed in the control regions used to normalize the backgrounds discussed in Chapter 9. As the dominant backgrounds are all normalized to data and the fake $p_{\mathrm{T}}^{\mathrm{miss}}$ background contributes below 0.2 % for $p_{\mathrm{T}}^{\mathrm{miss}} > 300\,\mathrm{GeV}$, this is attributed to missing higher order corrections in the MC simulation of the $Z \to \nu\nu$ + jets process. The offset is covered by the systematic theory uncertainty on the MC simulation and is also present in the $p_{\mathrm{T}}^{\mathrm{miss}}$ distributions of the remaining regions with charged leptons in the final state. It is also observed that there is a fluctuation in one bin ($[1040, 1180]$GeV).

For the γ+jets AM region a similar shape agreement is observed, however the normalization offset is in the different direction around roughly -10 %. As the fake photon background contributes less than 5 % below a $p_{\mathrm{T}}^{\mathrm{miss}}$ of 500 GeV and less than 3 % above, this normalization offset is attributed to poor modelling of the γ + jets process in the MC simulation, which is discussed in more detail in Chapter 12.

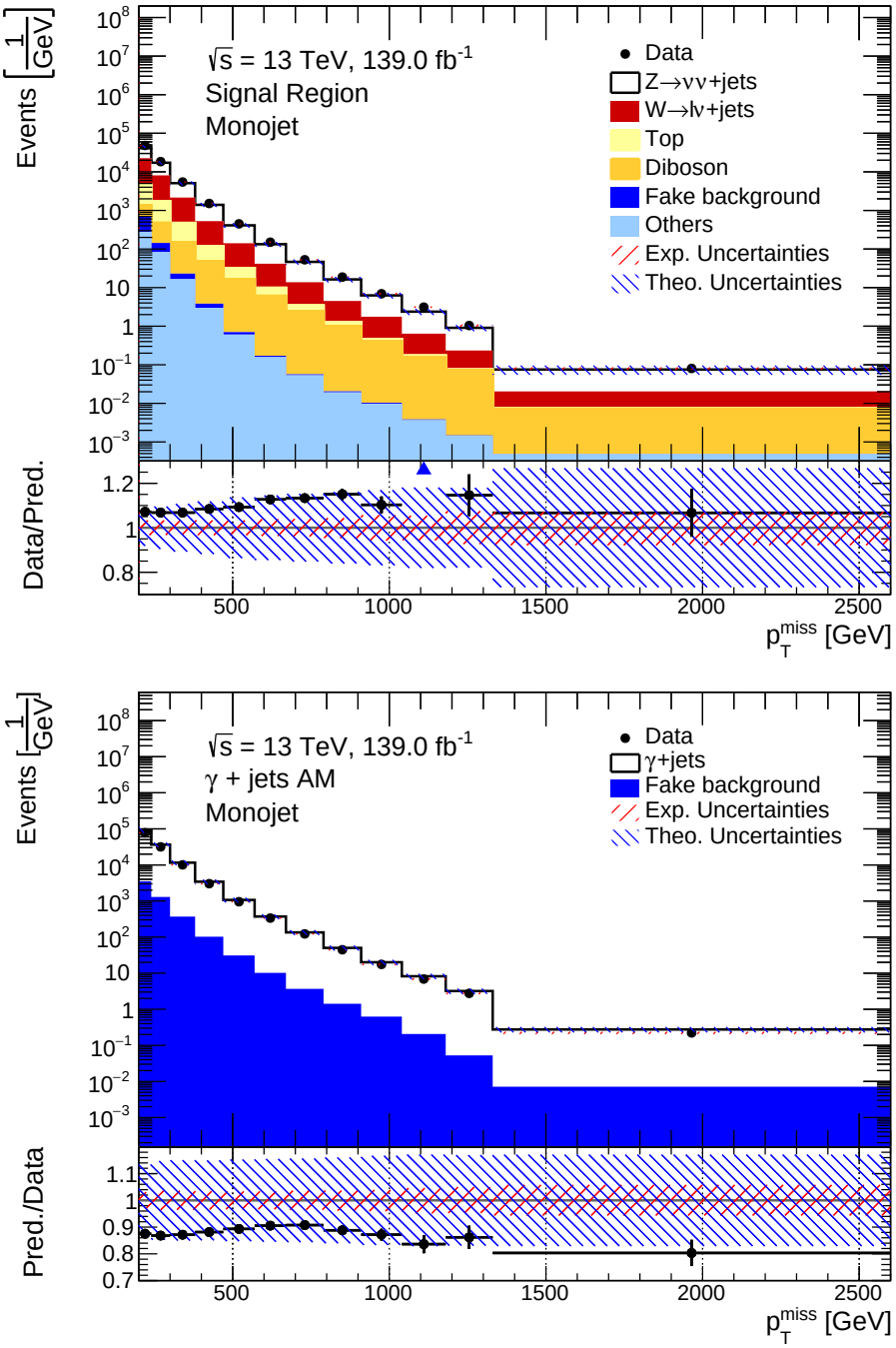

Figure 10.1.: Signal and background process composition as a function of $p_{\mathrm{T}}^{\mathrm{miss}}$ in the monojet phase space in the SR (top) and the γ+jets AM region (bottom). The error bars include the statistical uncertainty on the data, the MC simulation and the fake background estimates. The experimental (red) and theoretical (blue) systematic uncertainties are shown as hashed bands.

The top panel of Figure 10.2 shows the $p_{\mathrm{T}}^{\mathrm{miss}}$ distribution in the monojet phase space in the $W \to e\nu$ + jets AM region. A good shape agreement with a similar normalization offset as in the SR is seen. The fake electron background estimate plays an important role for this shape agreement, especially at medium and high $p_{\mathrm{T}}^{\mathrm{miss}}$. This also explains the higher experimental systematic uncertainty in last bin ($\approx$ 20 %) compared to the the $p_{\mathrm{T}}^{\mathrm{miss}}$ distribution in the SR ($\approx$ 8 %), since in this bin the total uncertainty is dominated by the uncertainty on the fake background estimate.

The $p_{\mathrm{T}}^{\mathrm{miss}}$ distribution in the VBF phase space in the $W \to \mu\nu$ + jets AM region is shown in the bottom panel of Figure 10.2. In general the observed features are similar to what is seen in the monojet phase space. However the relative contribution of the fake muon background is much smaller than in the $W \to e\nu$ + jets AM region. This is due to the fact that muons are easier to distinguish from fake background objects.

Figure 10.3 shows the $\Delta\phi_{jj}$ distribution in the VBF phase space in the $Z \to ee$ + jets AM region (top panel) and the m_{jj} distribution in the VBF phase space in the $Z \to \mu\mu$ + jets AM region (bottom panel). The $\Delta\phi_{jj}$ distribution exhibits a two peak structure, around $\left|\Delta\phi_{jj}\right| = 0.5$. The reason for this is that at leading order in α_{s} the jets are recoiling against the vector boson, which has a high transverse momentum ($p_{\mathrm{T}} > 200$ GeV). Therefore the jets receive a boost in the transverse plane and move closer together in ϕ. The shape of the $\Delta\phi_{jj}$ distribution is well modelled in general, although there is a slight modulation as a function of $\Delta\phi_{jj}$, especially in the first and last bin of the distribution. The shape of the m_{jj} distribution is poorly modelled, with the ratio between data and the sum of MC simulation and fake background estimate going from a 20 % offset at low m_{jj} to a -10 % offset at high m_{jj}. This is a known feature of the Sherpa generator used to produce the predictions[8]. Despite the poor modelling of the shape of the distribution in this case, the differences between data and MC simulation are covered by the theoretical uncertainties on the MC simulation.

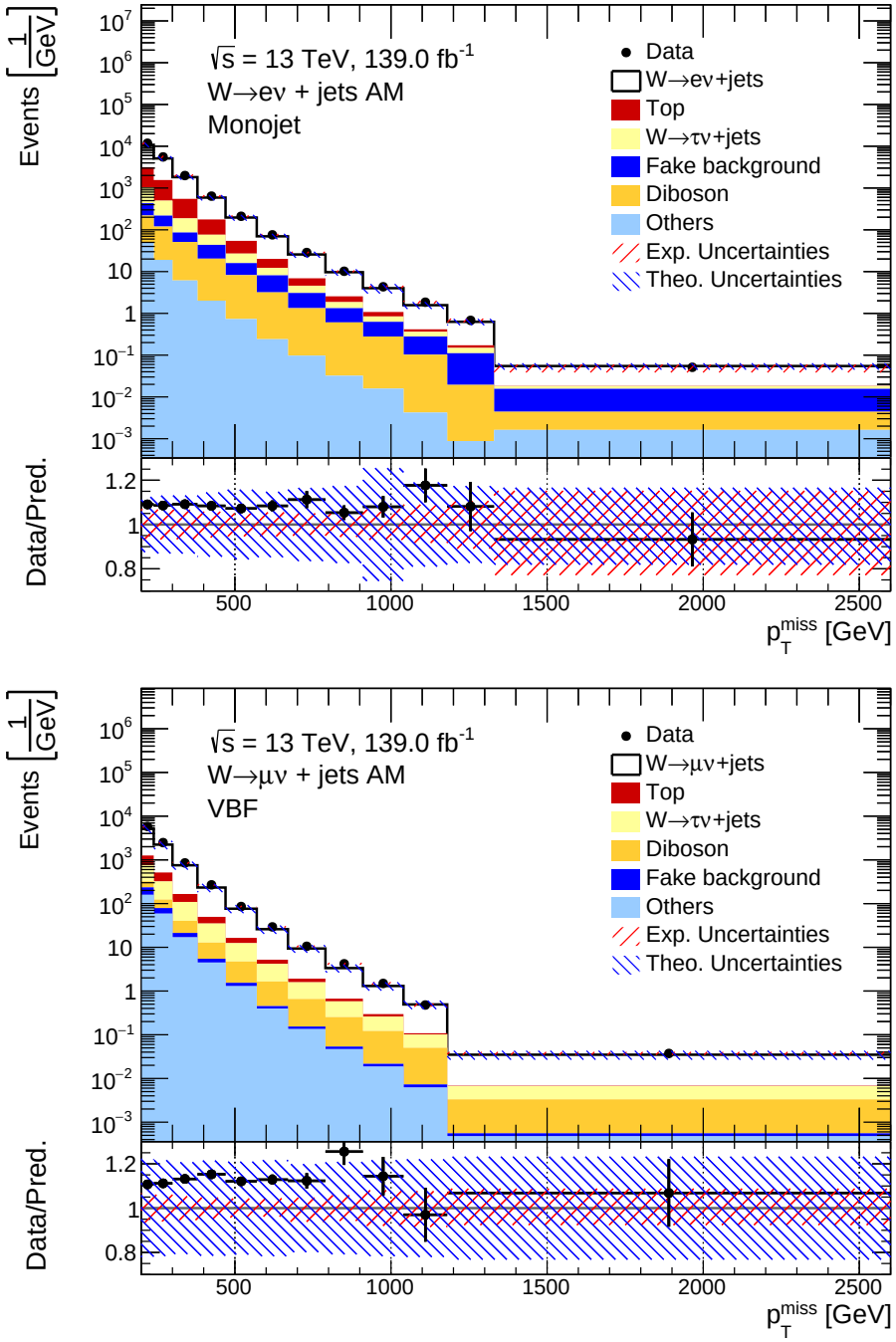

Figure 10.2.: Signal and background process composition as a function of $p_{\mathrm{T}}^{\mathrm{miss}}$ in the monojet phase space in the $W \rightarrow e\nu$ + jets AM region (top) and $p_{\mathrm{T}}^{\mathrm{miss}}$ in the VBF phase space in the $W \rightarrow \mu\nu$ + jets AM region. The error bars include the statistical uncertainty on the data, the MC simulation and the fake background estimates. The experimental (red) and theoretical (blue) systematic uncertainties are shown as hashed bands.

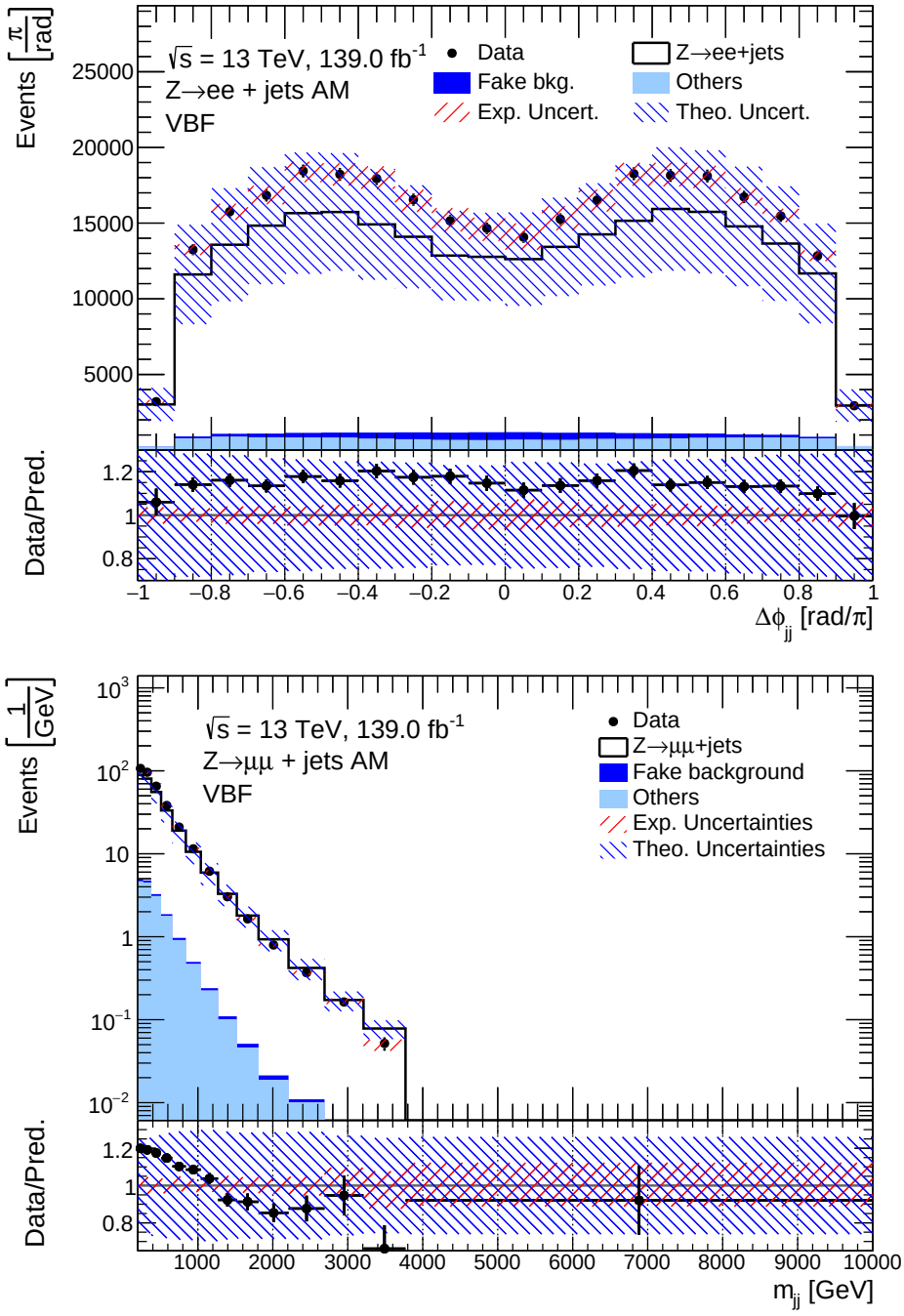

Figure 10.3.: Signal and background process composition as a function of $\Delta\phi_{jj}$ in the VBF phase space in the $Z \rightarrow ee$ + jets AM region (top) and as a function of m_{jj} in the VBF phase space in the $Z \rightarrow \mu\mu$ + jets AM region (bottom). The error bars include the statistical uncertainty on the data, the MC simulation and the fake background estimates. The experimental (red) and theoretical (blue) systematic uncertainties are shown as hashed bands.

11. Correction of Detector Effects on the Measured Data

The goal of this analysis is to measure cross sections and compare them to predictions made by the SM and models for BSM physics. However the background-subtracted distributions determined from the histogram shown in Chapter 10 are not the *true* cross sections, but rather a convolution of the cross section and the detector response.

The detector response can have different effects on the spectrum:

- Events are missed because the measured particles are outside of the detector acceptance (e.g. beamline, dead material) or they are missed due to detector inefficiencies.
- Events migrate between bins due to the finite detector resolution.
- The spectrum is shifted due to a non-linear detector response.

These effects can be accounted for in two ways in order to compare the measured data to predictions: Either the detector effects are applied to the predictions - this is called *folding* - or the inversion problem is solved and the effects are removed from the measured distributions, this is usually referred to as *unfolding* [136][137][138].

Folding detector effects on the prediction is typically the easier solution for the problem, since it only involves processing the predictions with the appropriate detector MC simulations. However it has several drawbacks: Firstly the full detector simulation based on GEANT4 is very complex and computationally expensive. This can be limiting, if many different predictions are to be compared to the data. Secondly the GEANT4 simulation is not publicly available. This means that to compare predictions to the published data outside of the ATLAS collaboration less refined parametric simulations like Delphes [139] have to be used.

Unfolding the measured data allows for the incorporation of the full knowledge of the ATLAS detector simulation and numerous data-driven improvements from both test-beam and collision data into the published result. This improves the longevity and general usability of the data.

In this analysis the measured observables are unfolded to particle level, in order to facilitate further use of the measured data. This means that only detector effects are corrected by the unfolding, but physics effects like parton showering still need to be applied to the predictions.

The first section of this chapter discusses the mathematical formulation of the unfolding problem and the *Bayesian* unfolding technique that is used in this measurement. The second section discusses the determination of the ingredient needed to apply the Bayesian unfolding to the measured observables. The third section discusses the uncertainties on the unfolded

result. The last sections discuss the propagation of statistical and experimental systematic uncertainties through the unfolding procedure and the conversion of the unfolded distributions into cross sections.

11.1. Introduction to Unfolding

In this section a general introduction to the unfolding problem is given and a specific solution based on Bayes theorem is presented. Detector level quantities are denoted by r or R for *reco(nstruction)*, whereas particle level quantities are denoted by t or T for *truth*.

11.1.1. The Unfolding Problem

The unfolding problem can be formulated mathematically as a Fredholm integral equation of the first kind [136]

$$\int K(r,t)\, f(t)\, dt + b(r) = g(r)\,, \tag{11.1}$$

where $f(t)$ is the distribution of the true observable t, $g(r)$ is the distribution of the measured observable r, $b(r)$ is the distribution of potential backgrounds and $K(r,t)$ is a kernel function that contains the detector response. The unfolding problem then consists of solving this equation to extract the true distribution $f(t)$.

When applied to a particle physics analysis, Equation 11.1 is usually discretized and expressed in matrix form as

$$\underline{\underline{A}}\,\underline{t} + \underline{b} = \underline{r}, \tag{11.2}$$

where $\underline{r}$ is and n-vector that contains the binned observable, $\underline{t}$ is an n-vector of the unknown bins of the true distribution and $\underline{\underline{A}}$ is the n-by-n response matrix[1] that encodes the detector response.

The response matrix $\underline{\underline{A}}$ is usually constructed for each observable using a MC simulation sample of the physics process that is to be unfolded (e.g. $Z \to \nu\nu$ + jets in the SR) chained with the detector simulation. This allows to account for process specific effects in a given phase space.

The elements A_{ij} are the conditional probability to observe an event in bin i on detector level that is in bin j on particle level

$$A_{ij} = P(\text{observed in bin } i \,|\text{true value in bin } j)\,. \tag{11.3}$$

It is important to note, that the response matrix has limited statistical precision, depending on the statistical precision of the MC simulation.

[1] It is also possible in principle to choose a m-by-n response matrix and have different numbers of bins on particle and detector level.

The unfolding problem as defined in Equation 11.1 and Equation 11.2 belongs to a class of problems called improper problems [140]. These have in common, that the naive solution by matrix inversion

$$\underline{t} = \underline{\underline{A}}^{-1} (\underline{r} - \underline{b}) , \tag{11.4}$$

usually produces results with strong fluctuations. This happens because typically some eigenvalues of $\underline{\underline{A}}$ are effectively zero within their statistical uncertainty (even though their numerical value will not be exactly zero). This means that the response matrix has an effective rank $p \leq n$. Only eigenvectors belonging to the first p eigenvalues will contribute meaningfully to the result. The rest will typically give large random contributions. See [136] for more details.

The unfolding method used in this measurement avoids the difficulty of spurious oscillations by solving the unfolding problem without inversion of the response matrix. This approach is discussed in the following section.

11.1.2. Iterative Bayesian Unfolding

Iterative Bayesian unfolding is used to unfold the measured data in this analysis. This method avoids the difficulties related to the inversion of the response matrix by using Bayes theorem and interpreting unfolding as a probabilistic process[2]. In this process the knowledge on the true distribution is improved, by using the measured data and the detector response matrix. In this section a brief summary of the method based on the original publication [138] and also [141] is given. The reader is referred to these for additional information. The implementation of the method provided by the RooUnfold package [142] is used throughout.

Bayes Theorem

Bayes theorem

$$P(A|B) = \frac{P(B|A)\, P(A)}{P(B)} \tag{11.5}$$

connects the *initial* or *prior probability* for an event A to occur $P(A)$ with the conditional probability for "A to occur given B" $P(A|B)$, via the conditional probability for "B to occur given A" $P(B|A)$, normalised by the probability for B to occur $P(B)$.

Already in the form of Equation 11.5, Bayes theorem exhibits some features, which are important in the context of this discussion.

- An intuitive way to "update" our knowledge of a true physical distribution A, given a measurement B.

[2]Following the argument given in [138] it is natural to view unfolding as a probabilistic problem, rather than the deterministic one, since the measurement itself is always limited by finite sample statistics. Indeed it is only in the limit of the number of events n going to infinity that the assumptions underlying the treatment of unfolding as a rotation of vectors are valid. For a more detailed discussion see [141].

- A way to "invert" probabilities $P(B|A) \rightarrow P(A|B)$. Indeed $P(B|A)$ is later identified with the response matrix $\underline{\underline{A}}$.

The generalized version of Bayes theorem with multiple events A_i is given by

$$P(A_i|B) = \frac{P(B|A_i)\,P(A_i)}{\sum_k P(B|A_k)\,P(A_k)}, \tag{11.6}$$

where the normalisation factor in the denominator now has to be summed over all possible events A_i.

Formulation of Bayesian unfolding

In the following a solution to the unfolding problem using Equation 11.6 is formulated.

The probability that an event is in bin i of the true distribution, given that is was measured in bin j on detector level, is

$$P\left(T_i|R_j\right) = \frac{P\left(R_j|T_i\right)P_0\left(T_i\right)}{\sum_k P\left(R_j|T_k\right)P_0\left(T_k\right)}. \tag{11.7}$$

Here the $P\left(R_j|T_i\right)$ are identified with the elements A_{ji} of the response matrix. $P_0\left(T_i\right)$ is the truth prior, which contains the prior probability to find an event in bin i of the true distribution. As usual in Bayesian statistics it should be constructed in such a way that it contains the best knowledge about the true distribution previous to the measurement. A detailed discussion about the choice and importance of the prior is given in the following section.

A few additional comments on Equation 11.7:

- For proper normalisation it is assumed that $\sum_i P_0\left(T_i\right) = 1$ and $\sum_i P\left(T_i|R_j\right) = 1$. This means that for each event in a detector level bin, there is a corresponding particle level bin. In case the fiducial definition leads to events that pass the event selection on detector but not on particle level, it is necessary to account for this by adding additional bins $P\left(T_i|R_j\right)$ to the response matrix. This events are called *fakes* and are discussed in Section 11.2.2.

- The efficiency to reconstruct an event which is in bin i on particle level is given by $\epsilon_i = 0 \leq \sum_j P\left(R_j|T_i\right)\big) \leq 1$. The efficiencies are discussed in more detail in Section 11.2.2.

Assuming a set of bins $n\left(R_j\right)$ with the measured events, the distribution of true events $\hat{n}\left(T_i\right)$ can be estimated as

$$\hat{n}\left(T_i\right) = \frac{1}{\epsilon_i}\sum_j n\left(R_j\right)P\left(T_i|R_j\right), \tag{11.8}$$

where the $P\left(T_i|R_j\right)$ are calculated using Equation 11.7 and the division by ϵ_i is used to correct for the efficiency.

The estimate of the new total number of events on particle level $\hat{N}_{true}$ is then given by

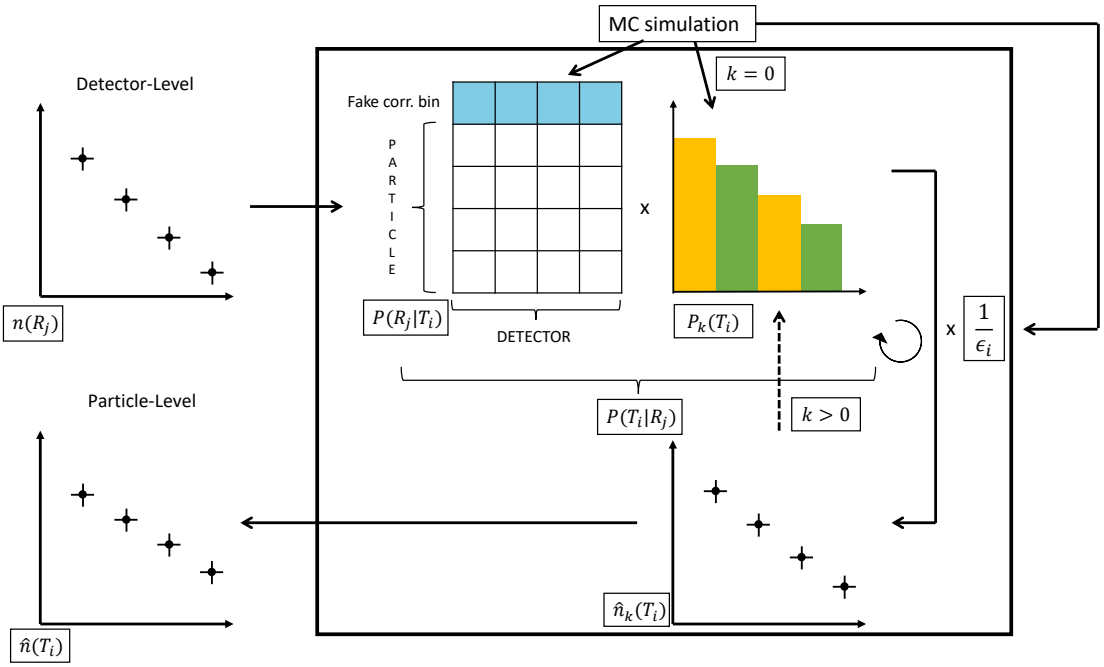

Figure 11.1.: Illustration of the iterative Bayesian unfolding.

$$\hat{N}_{true} = \sum_i \hat{n}(T_i) \tag{11.9}$$

and "updated" probabilities for an event to be in particle bin i can be calculated as

$$\hat{P}(T_i) = \frac{\hat{n}(T_i)}{\hat{N}_{true}}. \tag{11.10}$$

In principle Equation 11.8 already gives an unfolded distribution. However the question how strong this distribution is influenced by the choice of the prior and which prior to use still remains open. This is discussed in the following section.

Choice of the Prior and Iterative Unfolding

In Bayesian statistics the choice of the proper prior should usually guided by "the best available previous knowledge" on the probability density functions in question, then Equation 11.5 is to be used to update that knowledge. This is of course inherently subjective and very dependent on the problem in question.

In the case of a particle physics measurement, the "best available knowledge" is usually encoded in an up-to-date MC simulation. Therefore an intuitive choice for the prior $P_0(T_i)$ is the particle level distribution predicted by the MC simulation.

However the unfolded result as given in Equation 11.8 will have a dependence on the MC simulation prior and different priors can lead to different unfolded results. To reduce this dependence an iterative unfolding procedure is used, as suggested in [138]. The idea is to use

the MC simulation prior only in the first step and then switch to the unfolded distributions themselves as priors for the next steps. The algorithm described in [138] is outlined in the following and illustrated in Figure 11.1.

1. Use MC simulation to calculate the particle level prediction as the initial prior $P_{k=0}(T_i)$.
2. Take the detector level data $n(R_j)$ and perform an unfolding iteration using Equation 11.8 to obtain $\hat{n}_k(T_i)$ and calculate the updated probabilities $\hat{P}_k(T_i)$ using Equation 11.10.
3. Take $\hat{P}_k(T)$ as the new truth prior. Go to step 2. and repeat until the optimal number of iterations is reached.

The iterative procedure is typically very efficient in reducing the dependence on the truth prior. The residual dependence depends on the details of the distributions and is evaluated and discussed in Section 11.3.

11.2. Application of Iterative Bayesian Unfolding in the Measurement

This section discusses the application of the Iterative Bayesian unfolding to the measured distributions and the determination of the components of the unfolding. These components are: The measured *data distribution* on detector level, the *initial truth prior*, the *detector response* matrix and the *corrections for efficiencies and fakes*.

The *data distribution* measured on detector level that is to be unfolded is prepared for the unfolding by subtracting all contributions from background processes.

The *initial truth prior* is determined using the MC simulation of the SM signal process corresponding to the distribution that is to be unfolded (e.g. the $Z \rightarrow \nu\nu$ + jets simulation for a distribution in the SR). This is justified, since all backgrounds from other processes are subtracted from the data before the unfolding. The prior is determined by applying the particle level selection[3] corresponding to the distribution that is to be unfolded to the MC simulation.

The determination of the *detector response* matrix and the *corrections for efficiencies and fakes* is more involved and discussed in the following.

11.2.1. Derivation of the Detector Response Matrices

The detector response matrices describe bin-to-bin event migrations between the particle and the detector level due to detector-effects, especially due to resolution effects. These effects depend on the particles in the final state, as well as on their topology, since the detector resolution varies for different physics objects, as well as for differently instrumented parts of the detector. Therefore the detector response matrices are determined from the MC simulation

[3] See Section 5.3 for the particle level selection.

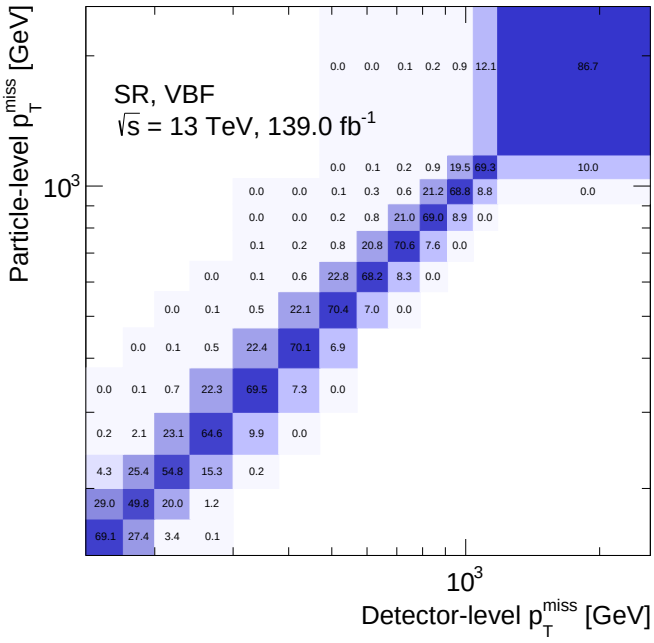

Figure 11.2.: Detector response matrices for $p_{\mathrm{T}}^{\mathrm{miss}}$ in the VBF phase space in the SR. The entries indicate the probability $P\left(R_j|T_i\right)$ in percent to find an event in $p_{\mathrm{T}}^{\mathrm{miss}}$ bin j on detector level given it is found in $p_{\mathrm{T}}^{\mathrm{miss}}$ bin i on particle level.

of the SM signal process corresponding to the distribution that is unfolded (e.g. the $Z \rightarrow \nu\nu$ + jets simulation for a distribution in the SR).

To correctly describe the migrations only events that pass both the particle and the detector level selection are used in the construction of the response matrices. This is called event-level matching.

In addition an object-level matching is applied both for the $\Delta\phi_{jj}$ and m_{jj} distributions in the VBF phase space. It requires the first and second leading jet in p_{T} to be uniquely matched between particle and detector level according to $\Delta R\left(jet_{\mathrm{i,detectorlevel}}, jet_{\mathrm{i,particlelevel}}\right) < 0.2$. The reason for this is that both observables have a dependence on the detailed structure of the jet system, since both depend only on the first two leading jets in the event. This structure can be different between the particle and the detector level. For example, the first two jets can change places, leading to a different sign of $\Delta\phi_{jj}$ on particle and detector level. Another example is a third jet that switches places with one of the first two jets on either detector or particle level, breaking the correlation of m_{jj} between particle and detector level. The presence of these effects introduces a strong dependence of the event migrations on the MC simulation, especially on the modelling of details of the jet system. The object-level matching ensures that these events are not part of the response matrix.

Events that either fail the event- or the object-level matching are accounted for in the efficiency and fake corrections discussed in Section 11.2.2.

All events of the SM signal MC simulation sample for a given region that fulfil both the

Observable	γ+jets AM region	all other regions
$p_{\mathrm{T}}^{\mathrm{miss}}$	$[170, 200]$ GeV	$[140, 170, 200]$ GeV
m_{jj} in VBF	$[140, 170, 200]$ GeV	

Table 11.1.: Underflow bins used during the unfolding procedure.

event- and object-level matching criteria are used to construct the response matrices. For each event, the matrix is filled according to the observable value on particle and detector level.

An example of a detector response matrix is shown in Figure 11.2[4] for the $p_{\mathrm{T}}^{\mathrm{miss}}$ distribution in the VBF phase space in the SR. The matrix is normalised such that the entries indicate the probability $P\left(R_j|T_i\right)$ in percent to find an event in bin j on detector level given it is found in bin i on particle level. The detector effects are clearly visible, with considerable off-diagonal elements indicating non-negligible migrations to the next and also the next-to-next bins. The size of these migrations depends on the resolution of the given observable and the bin size, where better resolution or larger bin size lead to less migrations.

The migrations can be further quantified for diagnostic purposes by the *purity* and the *stability*. These are discussed in Section E.2.

Accounting for Migrations at the Observable Boundary

Event migrations due to detector-effects also occur on the boundary of an observable (e.g. the $p_{\mathrm{T}}^{\mathrm{miss}} > 200\,\mathrm{GeV}$ requirement in the SR). Under the assumption that the description of the MC simulation of the data at this boundary is good, the unfolding correctly accounts for these event migrations in and out of the phase space. However, to be less dependent on the modelling of the MC simulation at the boundary and to avoid threshold effects, the correction of the migrations is performed with the unfolding matrix. The binning used in the measurement is defined such, that the highest bin of the spectrum includes all overflow events, therefore only migrations happening at the lower end of the spectrum have to be treated specially. No special treatment is needed for the $\Delta\phi_{jj}$ observable, since it is defined without a boundary.

To correctly account for the migration effects, all histograms used in the unfolding are extended with underflow bins - this includes the detector response matrices. The unfolding then migrates events in and out of the underflow bin during the unfolding procedure and thus correctly accounts for the migrations at the boundary of the observable. After the unfolding the underflow bins are removed from the unfolded result. The underflow bins defined in the measurement are shown in Table 11.1. Wherever possible two underflow bins are defined to also account for long-term migrations. For the γ+jets AM region only one underflow bin is defined in $p_{\mathrm{T}}^{\mathrm{miss}}$, since measurements lower than 170 GeV are not possible due to trigger limitations.

[4]The full set of response matrices for all phase spaces and regions is given in Section E.1.

11.2.2. Efficiency and Fake Corrections

An important part of the unfolding procedure it the correction for unmatched events, i.e. events that either only pass the detector level selection or the particle level selection, but not both. There is a wide range of possibilities, why an event is not matched. One example are efficiency or acceptance effects of the detector, where a physics object present at particle level is not reconstructed at detector level (e.g. due to a fluctuation of the shower shape in the calorimeter, which leads to a rejection by the identification requirements). A second example are resolution effects at the phase-space boundary where selection cuts are placed, e.g. an electron passes the p_{T} selection criteria on detector level but not on particle level due to the finite resolution of the p_{T} measurement.

Events that pass the particle level selection but fail the detector level selection are quantified by the efficiency and events that pass the detector level selection, but fail the particle level selection are quantified by the fake fraction. Both types of event are accounted for in the unfolding and discussed in the following. Please note that this fraction of events is "fake" in the sense of an event reconstructed inside the fiducial volume due to detector effects, even though it is outside the fiducial volume on particle level. This is different from the mis-identified objects discussed in Chapter 8.

The efficiency for bin i is defined as the fraction of particle level events also passing the detector level selection (in any bin on detector level)

$$\text{efficiency} = \epsilon_i = \frac{\text{matched particle level events in bin } i}{\text{all particle level events in bin } i}. \tag{11.11}$$

Figure 11.3 show the efficiency for the $p_{\mathrm{T}}^{\mathrm{miss}}$ distribution in the monojet phase space for all regions [5]. The efficiency has a strong dependence on the phase space and physics process. This reflects the differences in instrumentation and detection methods for different types of final state particles measured with the detector that each come with their own efficiencies. However a few general features are discussed in the following. First, it is visible that the efficiency is highest for $Z \to \nu\nu$ + jets, as the only final state particles are jets in this case, whereas all other regions have lepton/photon reconstruction efficiencies contributing in addition. Second, it is visible that the processes involving electrons in the final state have consistently lower efficiencies than processes involving muons, due to the lower efficiency of the electron reconstruction compared to muons and the stricter identification and isolation requirements applied to electrons [79][84]. Third, it is visible that the efficiency for $Z \to \mu\mu$ + jets AM is dropping towards higher $p_{\mathrm{T}}^{\mathrm{miss}}$. This is caused by the increasing collimation of the muons for higher Z boson p_{T}, which leads to a reduced reconstruction efficiency for the muon pair if it is very close. For $Z \to ee$ + jets this is effect is not visible, due to the close-by correction[6] that is applied. Fourth, the efficiency for the $Z \to \mu\mu$ + jets process is lower than that for the $W \to \mu\nu$ + jets process, since the muon efficiency affects these events for each muon present in the event. This feature is not visible for $Z \to ee$ + jets and $W \to e\nu$ + jets, due to the additional cuts applied to the $W \to e\nu$ + jets region to reject the fake electron

[5] The full set of efficiency distributions for all phase-spaces and regions is given in Section E.3.

[6] For electrons this effect would be much stronger, necessitating the application of the close-by correction.

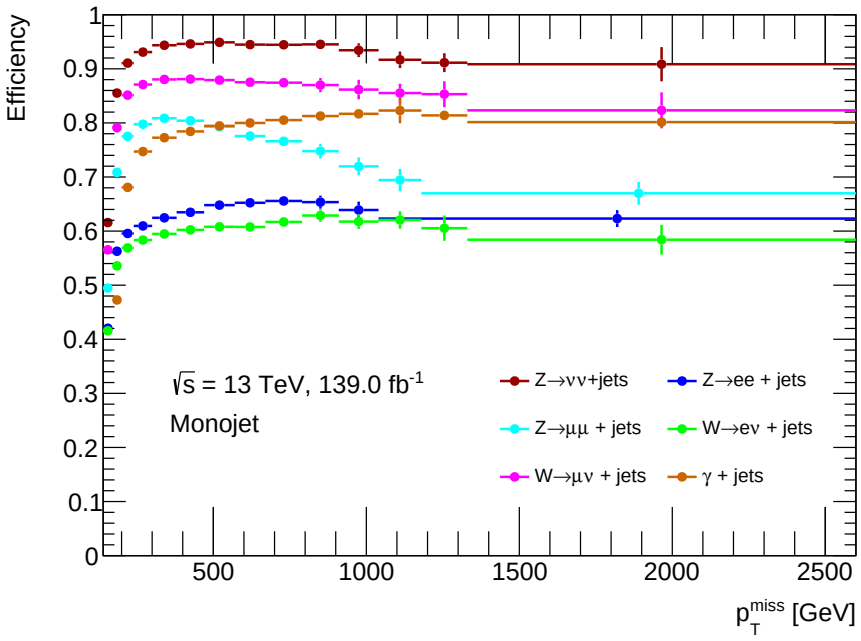

Figure 11.3.: Efficiency as a function of p_T^{miss} in the monojet phase space in the SR (dark red) and the $Z \to ee$ + jets AM (dark blue), $Z \to \mu\mu$ + jets AM (light blue), $W \to e\nu$ + jets AM (green), $W \to \mu\nu$ + jets AM (pink) and γ+jets AM (brown) regions.

background. These cuts on $p_T^{miss,real}$ and the transverse mass of the W boson are affected by the $p_T^{miss,real}$ resolution of the detector, leading to a lower efficiency.

All efficiencies show a strong turn-on behaviour in the first two bins. The reason for this are threshold effects due to the phase space boundary. As underflow bins are used these threshold effects only weakly affect the efficiency in the measured part of the spectrum, which starts in the third bin ($p_T^{miss} > 200$ GeV). This demonstrated a benefit of the underflow bins.

The fake fraction for bin i is defined as one minus the fraction of detector level events also passing the particle level selection (in any bin on particle level)

$$\text{fake fraction} = 1 - \frac{\text{matched detector level events in bin } i}{\text{all detector level events in bin } i}. \tag{11.12}$$

Figure 11.4 shows the fake fraction for the p_T^{miss} distribution in the monojet phase space for all regions[7]. In general it is well below 10 % for most processes and bins, with the high values in the lowest underflow bin related to the phase-space boundary effects already discussed above. The notable exception is the $W \to e\nu$ + jets region which has a fake fraction above 15 %. The reason for this are the $p_T^{miss,real}$ and transverse mass cuts applied in the selection of the W boson in this region, which are both affected by the $p_T^{miss,real}$ resolution of the detector.

[7]The full set of fake fraction distributions for all phase-spaces and regions is given in Section E.3.1

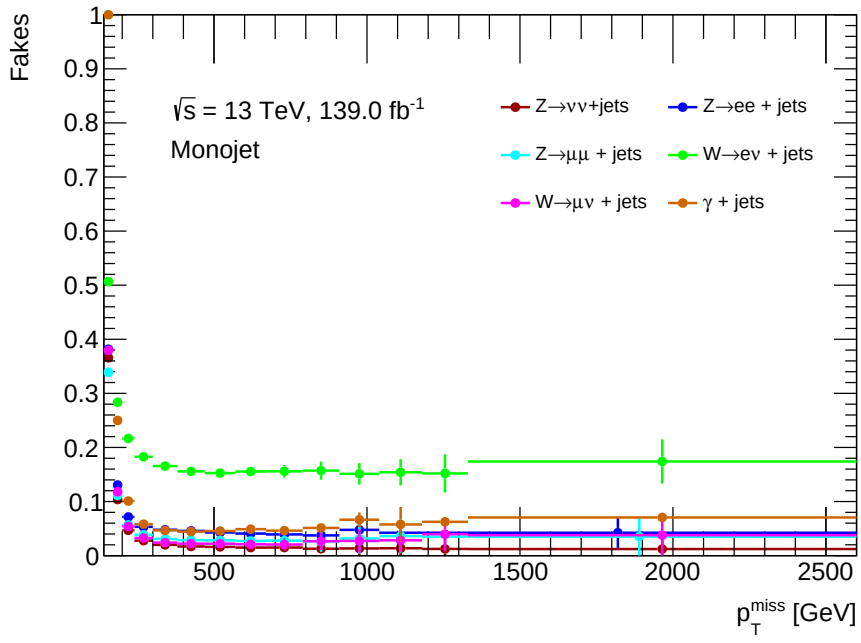

Figure 11.4.: Fake fraction for $p_{\mathrm{T}}^{\mathrm{miss}}$ in the monojet (top panel) phase space in the $Z \to \nu\nu$ + jets (dark red), $Z \to ee$ + jets (dark blue), $Z \to \mu\mu$ + jets (light blue), $W \to e\nu$ + jets (green), $W \to \mu\nu$ + jets (pink) and γ+jets AM (brown) regions.

Events which contribute to the fake fraction need to be taken into account in the unfolding procedure, as they appear in the detector level spectrum even though they are outside of the fiducial definition on particle level. The is achieved by adding an additional particle level bin (called "fake correction bin") to the response matrix as shown in Figure 11.1. During the unfolding a number of events corresponding to the fake fraction will be migrated into this additional particle level bin. This bin is discarded after the unfolding and not part of the final unfolded spectrum.

11.3. Studies of the Dependence of the Unfolding on the Simulation

The unfolding has a potential dependence on the MC simulation, especially on the initial truth prior determined from the simulation. In this section this dependence is studied and quantified. Potential biases due to the dependence on the simulation are assigned as systematic uncertainties on the unfolding method.

Three different tests are performed to quantify potential biases: The *data-driven closure test* that determines biases due to mismodelling of the unfolded observables, the closely related *hidden observable test* that determines biases due to mismodelling of observables that are not unfolded and the *signal injection test* that determines the effect of the unfolding on BSM signals.

In the following the *data-driven closure test* is discussed in detail, since it gives the largest contributions to the unfolding uncertainty. The remaining tests are performed in a very similar manner and give only negligible contributions to the unfolding uncertainty. They are shown for completeness in Section E.3.2 and Section E.3.3.

11.3.1. Bias due to Mismodelling of the Unfolded Observables

The general idea of the data-driven closure test is to quantify the impact of the non-perfect agreement between data and MC simulation on the unfolded result. This is achieved by constructing for each observable an alternative pair of detector and particle level MC simulation spectra by reweighting, such that the alternative detector level spectra agree very good with the measured data.

This alternative detector level MC simulation spectrum is used as pseudo-data and unfolded with the nominal response matrix constructed from the unreweighted (and thus imperfect) SM signal MC simulation sample. The unfolded result is then compared to the alternative particle level spectrum. If the nominal MC simulation describes the data perfectly or if the iterative unfolding procedure completely mitigates the non-perfect description of the data, the agreement of the unfolded results with the alternative particle level spectrum will be perfect within statistical fluctuations (i.e. the test closes). Typically this is not the case and a residual deviation remains. This deviation is then assigned as a systematic uncertainty on the unfolded result for the given observable. The detailed steps of the data-driven closure test are described in the following.

Construction of the Pseudo-data

The goal of the alternative MC simulation is very good description of the data. However a MC simulation that satisfies this requirement for all unfolded observables does currently not exist. Therefore the alternative MC sample is constructed from the nominal MC simulation by performing an event-by-event reweighting.

To make the reweighting as realistic as possible, it is performed as a function of the particle level observable. This means that the reweighting can only be performed for *matched* events. In general the reweighting is non-trivial, since differences to the data appear on detector level, whereas the reweighting is performed on particle level.

An iterative approach has been developed to determine the reweighting function, since the conventional approach of "guessing" a function is impractical due to the numerous distributions, which are unfolded in this measurement.

The basic idea is to compare the detector level spectrum of matched MC events to the data. For this comparison the data is multiplied bin-by-bin with the truth matching efficiency ϵ_i determined in Section 11.2.2. This is necessary, since only matched events in the MC simulation are used in the reweighting. A spline fit is done based on the comparison. The resulting function is then used to reweight the MC simulation and the next iteration is performed on this reweighted MC simulation. The algorithm is as follows.

1. Start with the matched detector level spectrum $m_{k=0}$ determined from the unreweighted nominal MC simulation.

2. Construct the ratio of the efficiency-corrected data to the matched detector level spectrum $\tilde{r} = \frac{d \times \epsilon}{m_k}$.

3. For $k = 0$: $r_k = \tilde{r}$. For $k > 0$: Update the previous ratio (bin-by-bin multiplication): $r_k = r_{k-1} \times \tilde{r}$. For better agreement between MC simulation and data, $\tilde{r}$ is closer to one, and less is changed.

4. Smooth r_k three times using the smoothing algorithm presented in [143].

5. Interpolate the smoothed r_k with a cubic spline f_k

6. Reweight the nominal MC simulation with f_k to obtain the reweighted matched detector level spectrum m_{k+1}.

7. If m_{k+1} agrees sufficiently well with the efficiency-corrected data $d \times \epsilon$ then stop, else go to step 2.) replacing $k \to k + 1$

The algorithm produces good reweighting functions already after a few iterations. This is demonstrated in the following for the m_{jj} observable in the VBF phase space in the $W \to \mu\nu$ + jets AM region. The top panel of Figure 11.5a shows the unreweighted *matched* detector level MC simulation distribution $m_{k=0}$ (step 1.) together with the efficiency-corrected data $d \times \epsilon$ and the bottom panel shows the ratio $\tilde{r}$ between both (step 2.). A strong disagreement between the data and the simulation with a clear shape difference is shown.

Figure 11.5b shows the initial reweighting function f_0 (step 5.) determined from the smoothed ratio (step 4.) shown in the bottom panel of Figure 11.5a[8].

The result of the first reweighting pass $m_{k=1}$ is shown in Figure 11.5c, which already shows a strong improvement of the agreement between data and simulation with respect to the unreweighted distribution. The updated reweighting function determined from the ratio in the bottom panel of Figure 11.5c is shown in Figure 11.5d. For this observable, the agreement is sufficiently good after three iterations. The agreement of the final reweighted *matched* detector level spectrum with the efficiency-corrected data is shown in Figure 11.5.

Additional examples for reweighted distributions are shown in Section E.3.4.

[8] As a spline interpolation is used, the reweighting function is only defined until the last data point and assumed to be constant beyond.

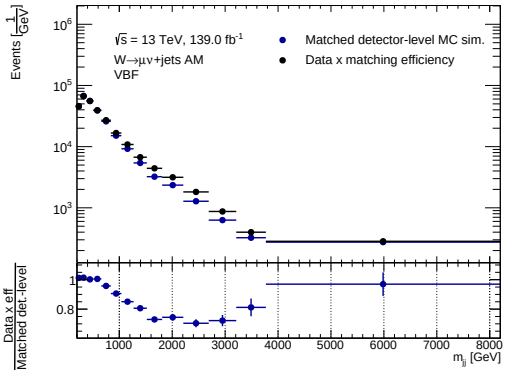

(a) Unreweighted *matched* detector level MC simulation together with the efficiency-corrected data.

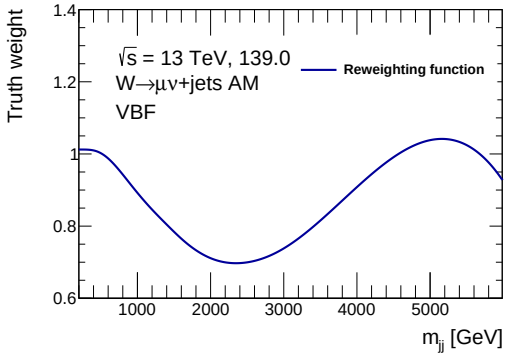

(b) Initial reweighting function.

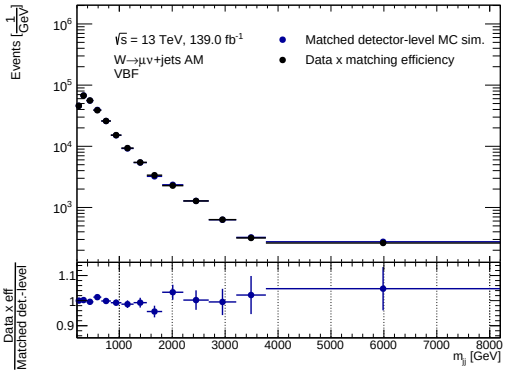

(c) *Matched* detector level MC simulation after the first reweighting step together with the efficiency-corrected data.

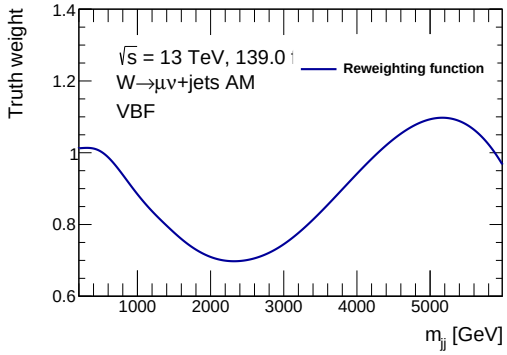

(d) Reweighting function after one iteration.

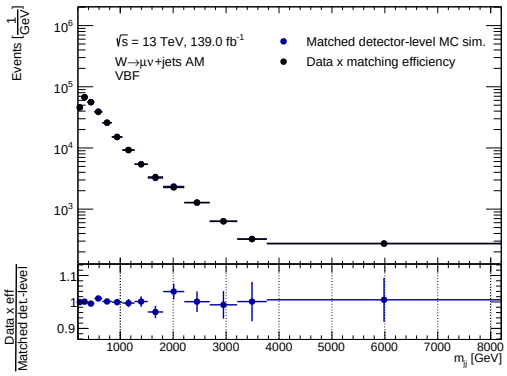

(e) Final *matched* detector level MC simulation together with the efficiency-corrected data.

Figure 11.5.: Several steps in the determination of the reweighting function for the MC simulation used in the data-driven closure test for m_{jj} in the VBF phase space in the $W \rightarrow \mu\nu$ + jets AM region. Panels (a), (c) and (e) show comparisons between the matched MC simulation at various iterations of the reweighting and the efficiency-corrected data. Panels (b) and (d) show the reweighting functions at various iterations of the reweighting.

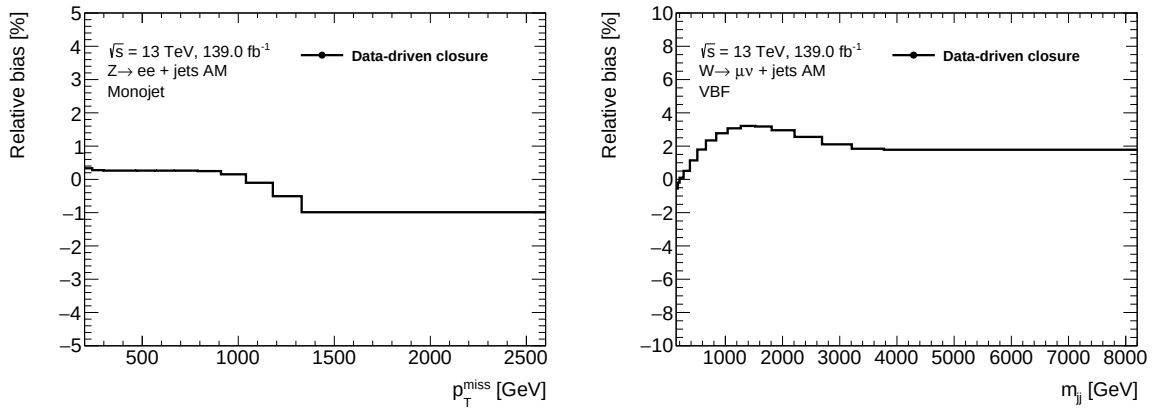

Figure 11.6.: Relative bias determined in the data-driven closure test for $p_{\mathrm{T}}^{\mathrm{miss}}$ in the monojet phase space in the $Z \rightarrow ee$ + jets AM region (left) and m_{jj} in the VBF phase space in the $W \rightarrow \mu\nu$ + jets AM region (right).

Results of the Data-driven Closure Test

The results of the data-driven closure test are discussed for two representative examples. The bias due to the non-closure is determined by using the reweighted matched MC simulation on detector level as pseudo-data and unfolding it with the nominal MC simulation. The resulting unfolded distribution is compared to the particle level of the reweighted matched MC simulation and the deviations are assigned as the bias.

The left panel of Figure 11.6 shows the relative bias for the $p_{\mathrm{T}}^{\mathrm{miss}}$ distribution in the monojet phase space in the $Z \rightarrow ee$ + jets AM region. The bias is small (below 1 %), which is the case for most distributions, since the shape of the data is modelled well by the MC simulation in most cases.

One notable exception is the m_{jj} distribution in the VBF phase space, which is poorly modelled, especially at medium and high values of m_{jj}. This poor modelling is reflected in the bias determined in the data-driven closure test, which is shown as an example for the m_{jj} distribution in the VBF phase space in the $W \rightarrow \mu\nu$ + jets AM region in the right panel of Figure 11.6. The bias is larger than for the $p_{\mathrm{T}}^{\mathrm{miss}}$ distribution, up to 3 % at medium values of m_{jj} and the shape roughly follows the discrepancy between data and MC simulation shown in Figure 11.5a. However, compared to the size of that disagreement between the data and the MC simulation (up to 20 %) the bias is relatively small. This demonstrates that the iterative unfolding procedure mitigates even a poor modelling of the data by the MC simulation to a large extent. Furthermore the data-driven closure test allows to properly quantify any residual biases.

These biases are symmetrized and assigned as a systematic uncertainty on the unfolded result for each distribution.

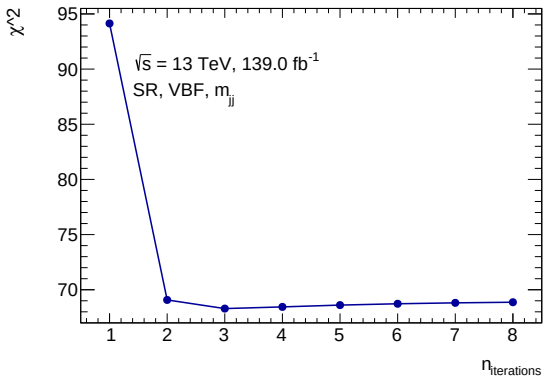

Figure 11.7.: Value of χ^2 between the unfolded detector level spectrum and the particle level spectrum of the reweighted *matched* MC simulation as a function of the number of unfolding iterations n.

11.4. Optimisation of the Number of Iterations

The number of iterations used in the iterative Bayesian unfolding is a priori arbitrary. In the following a procedure is motivated to determine that number.

To optimise the number of iterations used in the iterative unfolding procedure two opposing features of the unfolding have to be considered. Increasing the number of iterations will reduce the dependence on the MC prior and reduce the bias resulting from this dependence. However as the number of iterations increases, the limited statistical precision of the response matrix will lead to growing statistical fluctuations on the unfolded result (this is discussed in detail in [138]). To find the optimal point, where the results are as unbiased as possible, but not yet fluctuating, the *data-driven closure test* described above is repeated for different numbers of unfolding iterations n. For each n, the χ^2 between the unfolded result and the reweighted *matched* MC simulation particle level distribution is calculated and the n for which χ^2 is minimal is taken as the number of iterations for the given observable.

As an example, Figure 11.7 shows the resulting χ^2 as a function of the number of iterations for the m_{jj} distribution in the VBF phase space in the SR. A minimum is found at three iterations. This demonstrates that also for observables with a strong shape disagreement, the iterative unfolding minimises the bias already after a small number of iterations. This optimisation is performed for every unfolded observable.

11.5. Uncertainty Treatment in the Unfolding Procedure

11.5.1. Propagation of Systematic Uncertainties

Since the shape of the distributions is different on detector and particle level, the relative shape of the uncertainties might also be different. Therefore the uncertainties are propagated from the detector to the particle level through the unfolding.

Each systematic variation is unfolded separately, where two different approaches are taken depending on the source of the systematic uncertainty.

- Uncertainties that affect only the backgrounds that are subtracted from the data (e.g. uncertainties on the fake background estimate) are applied directly to the data by shifting the backgrounds according to the uncertainty before the background subtraction. The resulting shifted data is then unfolded with the nominal MC simulation.

- For uncertainties that affect the SM signal process, the MC simulation is shifted according to the systematic variation and the data is unfolded with the shifted MC simulation. This helps to account for migrations that might be slightly different under the systematic variation. Typically such a systematic variation will affect both the signal process and the backgrounds (e.g. for the jet uncertainties). In these cases the backgrounds are shifted according to the systematic variation before subtracting them from the data. The resulting shifted data is then unfolded with the shifted MC simulation, to correctly account for the correlation of a given systematic variation.

11.5.2. Statistical Uncertainty and Correlations

The statistical uncertainty on the unfolded result has two components. One is the statistical uncertainty on the measured data, the other is the statistical uncertainty on the MC simulation. In addition the migration of events between different bins of the spectrum during the unfolding, introduce statistical correlations between bins of the unfolded result. This means that an alternative to the standard $\sqrt{N}$ statistical uncertainty is needed.

In order to correctly account for these effects, the statistical uncertainty is determined using the bootstrap method. As the bootstrap method is coherently used over the entire analysis chain, bootstrap replicas exist for all quantities entering the unfolding: The background-subtracted data, the truth prior, the response matrix and the fake and efficiency corrections. The unfolding is performed independently for each set of bootstrap replicas (e.g. the background-subtracted data replica $B = 1$ is unfolded with response matrix replica $B = 1$ and the efficiency replica $B = 1$ to yield the unfolded result replica $B = 1$ and so on). The final unfolded distribution is obtained by averaging the bootstrap replicas (central value) and calculating their RMS (statistical uncertainty).

The bootstrap method is also used to determine the bin-to-bin correlations of the unfolded distribution. Figure 11.8 shows the bin-to-bin correlations of the background-subtracted data at detector level before unfolding (left) and the after unfolding on particle level (right). It is shown that no correlations are present in the data before the unfolding, within the statistical fluctuations due to the bootstrap replicas. After the unfolding the bins are correlated due to the migrations. These correlations are taken into account when interpreting the unfolded cross sections.

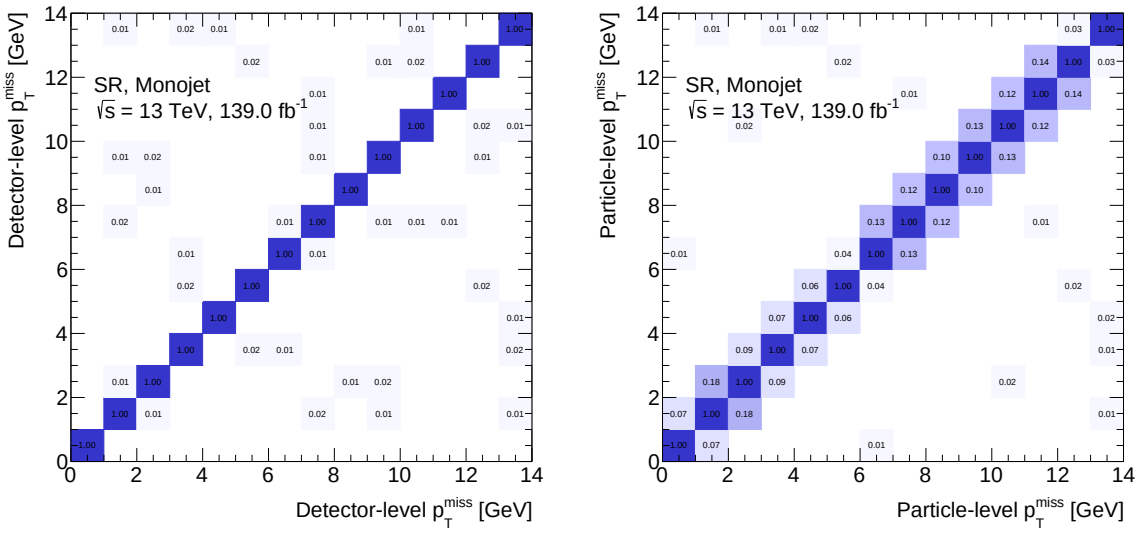

Figure 11.8.: Correlations between bins before (left) and after (right) unfolding for the $p_{\mathrm{T}}^{\mathrm{miss}}$ distribution in the monojet phase space in the SR.

11.6. Conversion of the Unfolded Distributions to Cross Sections

The unfolding procedure corrects for the detector effects on the measured data. To obtain a differential cross section from the background-subtracted and unfolded distributions, additional steps are necessary. First the distributions are corrected for the binning, by dividing the content in each bin by the bin width. Then the differential cross section for an observable X is determined by using Equation 3.1 for a given bin i as

$$\frac{d\sigma_i}{dX} = \frac{N_i}{\int_T \mathscr{L}(t)\,dt}, \tag{11.13}$$

where N_i is the number of detector-corrected events in bin i and the integrated luminosity $\int_T \mathscr{L}(t)\,dt = 139\,\mathrm{fb}^{-1}$ corresponds to the full Run 2 luminosity.

12. Validation of the Standard Model Predictions of Vector Boson plus Jet Production

A key motivation of the measurement is to test the agreement of the data with the theory predictions. This constitutes a test of the SM as the theory underlying the predictions. In this chapter a selection of the differential cross sections obtained after the unfolding procedure are compared to SM predictions produced with the Sherpa generator. The remaining cross section are shown in Appendix F. The following cross sections have been measured:

- production of $Z \to \nu\nu$ + jets as a function of the Z boson p_{T} in the monojet phase space (this chapter) and as a function of the Z boson p_{T}, m_{jj} and $\Delta\phi_{jj}$ in the VBF phase space
- production of $Z \to ee$ + jets as a function of the Z boson p_{T} in the monojet phase space and as a function of the Z boson p_{T}, m_{jj} and $\Delta\phi_{jj}$ (this chapter) in the VBF phase space
- production of $Z \to \mu\mu$ + jets as a function of the Z boson p_{T} in the monojet phase space and as a function of the Z boson p_{T}, m_{jj} (this chapter) and $\Delta\phi_{jj}$ in the VBF phase space
- production of $W \to e\nu$ + jets as a function of the W boson p_{T} in the monojet phase space and as a function the of W boson p_{T}, m_{jj} and $\Delta\phi_{jj}$ in the VBF phase space
- production of $W \to \mu\nu$ + jets as a function of the W boson p_{T} in the monojet phase space and as a function of the W boson p_{T}, m_{jj} and $\Delta\phi_{jj}$ in the VBF phase space
- production of γ + jets as a function of the photon p_{T} in the monojet phase space (this chapter) and as a function of the photon p_{T}, m_{jj} and $\Delta\phi_{jj}$ in the VBF phase space

A selection of observables is shown in Figure 12.1 and Figure 12.3 and discussed in the following. The figure for each observable is split in two parts. The top part shows the measured cross sections in black together with the Sherpa prediction in blue. The bottom part shows the ratio of the prediction and the data. The statistical uncertainty on the cross section and the prediction is shown as black and blue error bars respectively. The experimental systematic uncertainties are shown as a red hashed band and the theoretical systematic uncertainties on the Sherpa predictions are shown as a blue hashed band. In all cases the measured cross section agrees with the prediction within the theoretical systematic uncertainties.

The top panel of Figure 12.1 shows the $Z \to \nu\nu$ + jets cross section as a function of the Z boson p_{T} in the monojet phase space. A normalization offset is observed as well as a slight deviation from a flat shape. This behaviour is very similar to what is observed on the

detector level. The normalization offset is attributed to missing higher order corrections in the SHERPA simulation. The boson p_{T} bin [1040, 1180]GeV shows a deviation, most likely due to a fluctuation, that was also observed on the detector level. The experimental systematic uncertainties on the cross section change from 5 % at low boson p_{T} to around 4 % at medium boson p_{T} to 8 % at high boson p_{T}.

The contributions from the different sources of systematic uncertainty are shown in the top panel of Figure 12.2 together with the statistical uncertainty. The different NPs which belong to each uncertainty group are added in quadrature, since they are uncorrelated. For the Z boson $p_{\mathrm{T}} > 1000\,\mathrm{GeV}$ the statistical uncertainty (red dotted line) dominates. This means that for a more precise measurement at high boson p_{T} more collision data is needed. At lower boson p_{T} the measurement is limited by the systematic uncertainties, mainly by the jet uncertainties (JES in dark blue and JER in light blue). Their impact on the boson p_{T} spectrum is involved, since it is a convolution of the jet uncertainties on the single jets that contribute to the boson p_{T} calculation and the boson p_{T} spectrum. However it is clear that the measurement of the cross section would benefit from a more precise jet measurement. The contribution from the background subtraction method (green) remains below 2.5 % at high boson p_{T} and below 2.0 % and is well below the contributions of the jet uncertainties. This demonstrates that the data-driven method to normalise the backgrounds does not introduce large additional uncertainties to the measurement. This uncertainty also contains the residual theory uncertainties from backgrounds that were not normalised with the data-driven method. The uncertainty from the fake $p_{\mathrm{T}}^{\mathrm{miss}}$ estimates (brown) contributes only in the lowest two bins of the cross section and is small, below 2 %. This demonstrates that the conservative systematic uncertainty of 100 % that is applied to the background estimate does not greatly impact the measurement. The contributions from all other sources of experimental systematic uncertainty (magenta) is well below 1 % in most bins of the spectrum. This includes especially the uncertainty on the $p_{\mathrm{T}}^{\mathrm{miss}}$ soft term, the uncertainty on the pile-up reweighting and the unfolding uncertainties

The bottom panel of Figure 12.1 shows the γ + jets production cross section as a function of the photon p_{T} in the monojet phase space. A shape difference similar to that observed for $Z \to \nu\nu$ + jets final state is also seen here, however as on the detector level, the normalisation offset of the simulation with respect to the data is in the different direction. Several possible explanations exist for this offset that was also observed in previous γ + jets cross section measurements[14] [13]. One possible explanation is a dependence of the predicted cross section on the Frixione[144] isolation criterium that is applied to the photons in the SHERPA generator. This is the major difference to the other boson plus jet processes.

This result demonstrates the need for further developments on the prediction side to achieve a better description of the data by the MC predictions. Measurements of the type presented here are indispensable in these efforts, as the experimental systematic uncertainties on the cross section measurement are much lower than the theoretical uncertainties on the prediction.

The bottom panel of Figure 12.1 also shows that the experimental systematic uncertainties on the γ + jets cross section are smaller than that those on the $Z \to \nu\nu$ + jets cross section. This is discussed in the following. The bottom panel of Figure 12.2 shows the contributions from the different sources of systematic uncertainty. As in the case of $Z \to \nu\nu$ + jets, the

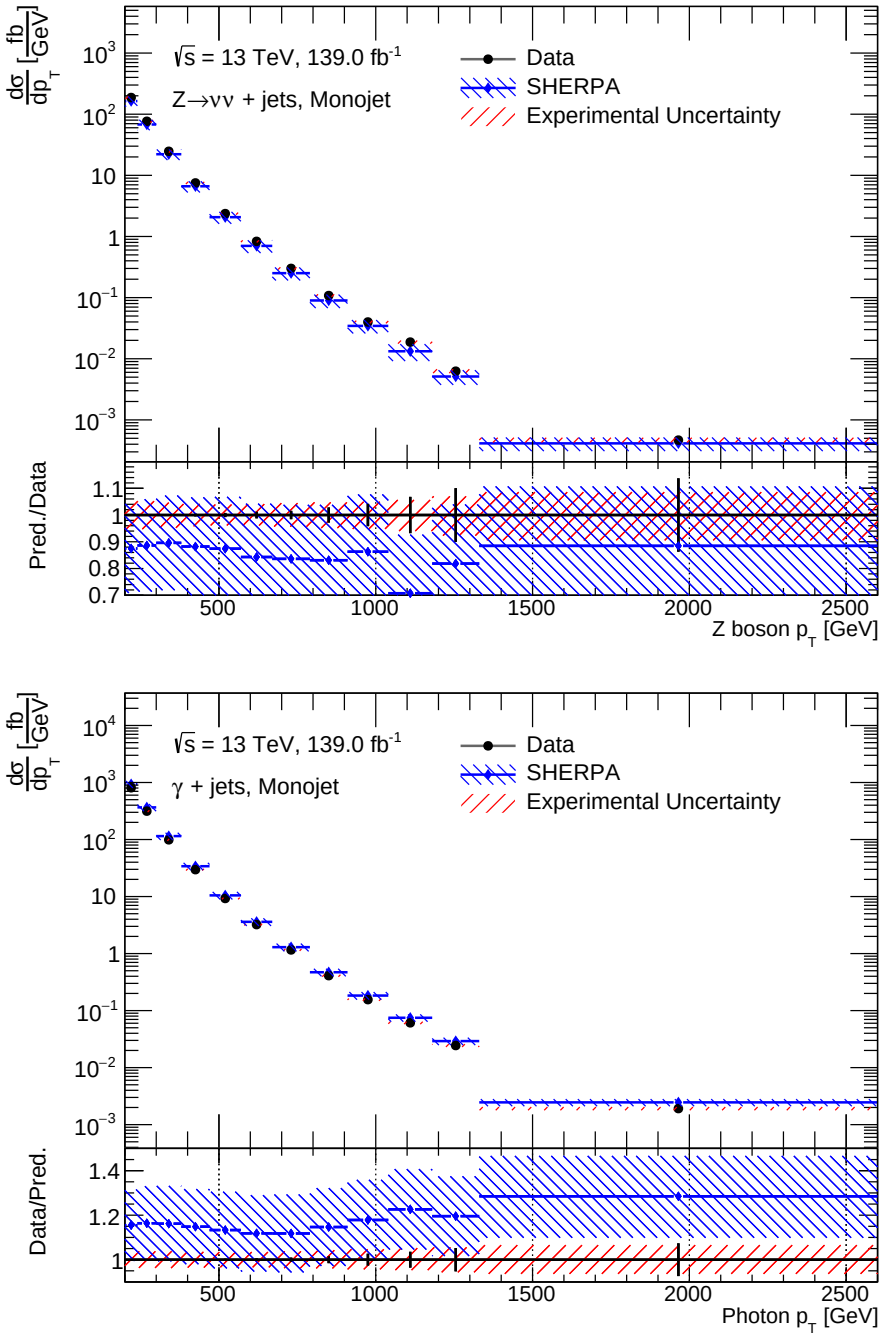

Figure 12.1.: Differential cross sections of $Z \to \nu\nu$ + jets (top) and γ + jets (bottom) production as a function of the boson p_{T} in the monojet phase space. The cross sections predicted by SHERPA are shown in blue. The statistical uncertainty on the cross section (black) and the prediction (blue) is shown as error bars on the respective points. The experimental (red) and theoretical (blue) systematic uncertainties are shown as hashed bands.

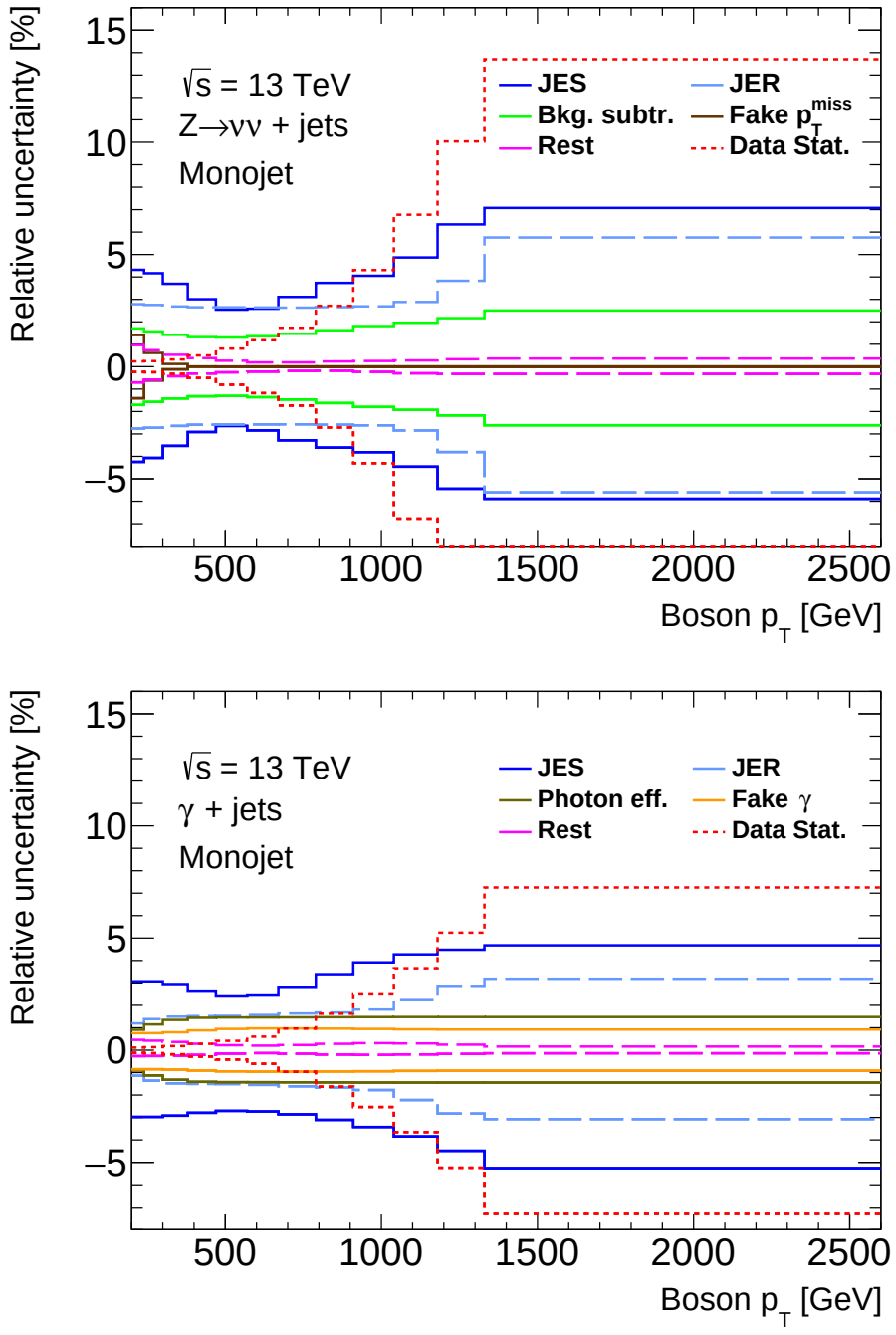

Figure 12.2.: Relative uncertainty for the dominant sources of experimental systematic uncertainty on the cross sections of $Z \to \nu\nu$ + jets (top) and γ + jets (bottom) as a function of the boson p_T in the monojet phase space. The systematic variations contributing to the individual uncertainty groups are added in quadrature.

dominant contributions are from the jet uncertainties, which exhibit a similar shape of the relative systematic uncertainty. This similar behaviour of the jet uncertainties is explained

by the similarity of the hadronic recoil system in both the $Z \to \nu\nu$ + jets and γ + jets process. It is one of the reasons why the boson p_{T} in the AMs is measured via the hadronic recoil and not, as would be possible in the γ + jets case, by directly measuring the photon. As the jet uncertainties are correlated, observables like cross section ratios can be constructed, where the effect of these uncertainties is mitigated. This is discussed below. All other sources of systematic uncertainty remain below 2 %. In general the γ + jets process has the best experimental precision of all the measured boson plus jets processes. The γ + jets process is also measured with the highest statistical precision of all processes in the measurement. This is due to the high cross section of γ + jets production and also due to the high purity of the γ+jets AM region.

Figure 12.3 shows the $Z \to ee$ + jets cross section as a function of $\Delta\phi_{jj}$ (top panel) and the $Z \to \mu\mu$ + jets cross section as a function of m_{jj} (bottom panel) in the VBF phase space. In both cases the agreement between prediction and data is very similar to that observed on detector level. Especially in the case of the m_{jj} distribution, the Sherpa generator shows a poor modelling of the cross section. Also in this case the measurement can provide valuable feedback for the improvement of the MC predictions.

12.1. Cross Section Ratios

The construction of cross section ratios between the boson plus jet processes provides another view on a given observable due to the correlated systematic uncertainties between the different processes that are very similar both in shape and size. Therefore their impact will be reduced in the ratio.

Special care has to be taken with the systematic uncertainties when constructing the ratios. All experimental systematic uncertainties are taken to be correlated, except for the uncertainties on the background estimation methods and the unfolding. Also all theoretical systematic uncertainties are taken to be correlated. The uncertainties are correlated bin-to-bin and region to region.

As an example the cross section ratio R between the $Z \to \nu\nu$ + jets and the $W \to e\nu$ + jets final state is shown in Figure 12.4. The ratio shows a good agreement between the measured cross section and the prediction within the experimental systematic uncertainties[1]. Both the systematic uncertainties on the theory prediction and on the experimental systematic uncertainties are strongly reduced in the ratio. At low boson p_{T} the resulting experimental uncertainty on the ratio is very small since in this p_{T} region the jet uncertainties dominate which are correlated between the $Z \to \nu\nu$ + jets and the $W \to e\nu$ + jets final state. Towards higher boson p_{T}, the experimental systematic uncertainty on the fake electron background estimate starts to dominate. This uncertainty is not reduced in the ratio, since it is not present in $Z \to \nu\nu$ + jets.

While the value of a ratio between different Z boson decay channels can be explained by the branching fractions of the Z boson, this is not as easy for the ratio presented here, due to the differences in W and Z production. The rising ratio towards low boson p_{T} is explained by

[1] The systematic uncertainties on both input distributions are smoothed to reduced statistical fluctuations [143].

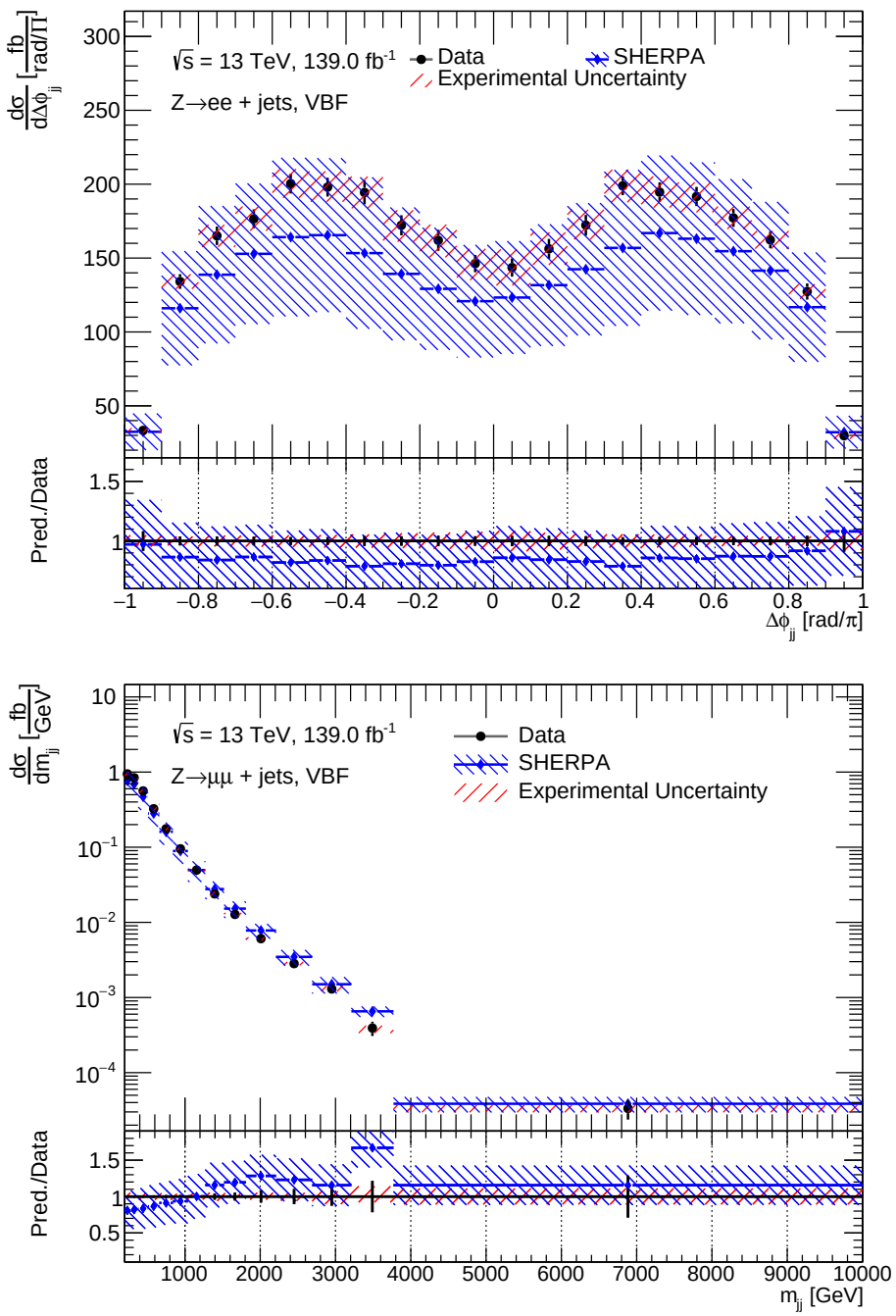

Figure 12.3.: Differential cross sections of $Z \to ee$ + jets production as a function of $\Delta\phi_{jj}$ in the VBF phase space (top) and of $Z \to \mu\mu$ + jets production as a function of m_{jj} in the VBF phase space (bottom). The cross sections predicted by SHERPA are shown in blue. The statistical uncertainty on the cross section (black) and the prediction (blue) is shown as error bars on the respective points. The experimental (red) and theoretical (blue) systematic uncertainties are shown as hashed bands.

the fiducial requirements placed on the electron in $W \to e\nu$ + jets process in the denominator that can not be applied for the neutrinos in the $Z \to \nu\nu$ + jets process in the numerator [10].

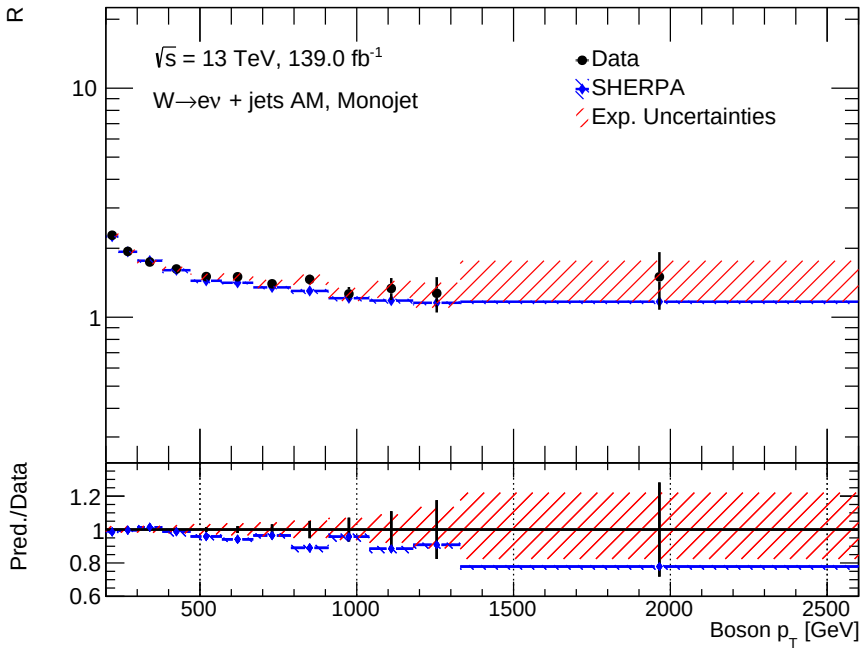

Figure 12.4.: Differential cross section ratio of $Z \to \nu\nu$ + jets and $W \to e\nu$ + jets production as a function of the boson p_T in the monojet phase space. The cross sections predicted by SHERPA are shown in blue. The statistical uncertainty on the cross section (black) and the prediction (blue) is shown as error bars on the respective points. The experimental (red) and theoretical (blue) systematic uncertainties are shown as hashed bands.

13. Quantitative Comparison of the Measured Cross Sections to the Standard Model Predictions

After the general agreement of the cross sections with the SM predictions has been validated in the previous chapter, it is vital to evaluate the agreement between both quantitatively. This is especially true in the context of the search for BSM physics, which would manifest itself in a disagreement between the measured data and the predictions. The typical discovery threshold for BSM physics is a probability of observing the data given the SM prediction of less than 5.7×10^{-7} [136].

The goal of this chapter is to quantify the compatibility between data and theory. This is achieved with a *goodness-of-fit test* based on the maximum likelihood approach. This allows to define a *p-value* that quantifies how often one would obtain a similar or worse agreement between experiment and prediction, if the experiment is repeated many times [136].

In the following an overview of the procedure of the goodness-of-fit test is given. The first step is a maximum likelihood fit. In this fit, the systematic uncertainties are treated as NPs which are allows to float. The statistical uncertainties are accounted for in a covariance matrix. The diagonal elements of this matrix contain information about the statistical fluctuations in each bin of the unfolded cross sections, while the off-diagonal elements encode the information about correlations between different bins. The covariance matrix Cov is determined using the bootstrap method, as the bootstrap replica contain all the relevant information, since they were coherently propagated through the measurement. The likelihood $\mathscr{L}$ used in the fit [22] is given as

$$\mathscr{L}\left(\vec{x} \,|\, \vec{\mu}, \vec{\theta}\right) = \frac{1}{(2\pi)^k \,|\mathrm{CoV}|} \cdot e^{-\frac{1}{2}\chi^2\left(\vec{x},\vec{\mu},\vec{\theta}\right)} \cdot \prod_i G(\theta_i) \tag{13.1}$$

and $\chi^2\left(\vec{x}, \vec{\mu}, \vec{\theta}\right)$ is defined as

$$\chi^2\left(\vec{x}, \vec{\mu}, \vec{\theta}\right) = \left(\vec{x} - \vec{p}\left(\vec{\mu}\right) + \sum_i \theta_i \vec{\epsilon}_i\right)^T \mathrm{Cov}^{-1} \left(\vec{x} - \vec{p}\left(\vec{\mu}\right) + \sum_i \theta_i \vec{\epsilon}_i\right). \tag{13.2}$$

Here $\vec{x}$ is a vector, which contains the measured data bins and $\vec{p}\left(\vec{\mu}\right)$ is a vector which contains the predictions. The θ_i are the k NPs and $\vec{\epsilon}_i$ is the uncertainty amplitude associated with NP θ_i. For each NP a Gaussian constraint term $G(\theta_i)$ with mean $\mu = 0$ and width $\sigma = 1$ is multiplied to the likelihood, since the NPs are assumed to follow a normal distribution. The θ_i are constrained in the fit.

The χ^2 test statistic follows a χ^2 distribution $f_{\chi^2}\left(\chi^2, \text{ndf}\right)$ where the number of degrees of freedom ndf is the number of cross section bins. Then the p-value [136], is defined as

$$p\left(\chi^2_{obs}, N\right) = \int_{\chi^2_{obs}}^{\infty} f(z, N)\, dz, \tag{13.3}$$

with N the number of bins and χ^2_{obs} the observed value of χ^2 after the fit. Typically fit values with a p-value above 0.05 are considered to be good.

13.1. Results of the Goodness-of-fit Test

The goodness-of-fit test is first discussed in detail for the $Z \rightarrow \nu\nu$ + jets production cross section as a function of the Z boson p_{T} in the monojet phase space. In a next step, the goodness-of-fit test is performed separately for each boson plus jet final state as a function of the boson p_{T} and also in a combined fit with all boson plus jet final states.

Figure 13.1 shows the result of the fit for the $Z \rightarrow \nu\nu$ + jets cross section. Very good agreement between the data and the SM prediction is observed, with a p-value of 0.745 and a reduced χ^2 of $\chi^2/\text{NDF} = 7.64/11$.

The figure also shows the pre- and post-fit distributions for the data (pre-fit: grey, post-fit black) and the SM prediction (pre-fit: blue, post-fit: red). The top part of the figure shows the cross sections and the bottom part the ratio of the data to the prediction. Statistical uncertainties are displayed only for the post-fit distributions. The total post-fit systematic uncertainty, including both the experimental and theoretical uncertainties, is given in orange. The x-axis shows the bin number and all bins are displayed equidistant.

The post-fit distributions are determined from the pre-fit distributions by adding the systematic uncertainties according to their post-fit value $\hat{\theta}_i$. They show a post-fit agreement close to unity, with a reduced total systematic uncertainty.

The pre- and post-fit values of the θ_i are shown in Figure 13.2. For most θ_i only a small difference is observed between pre- and post-fit. This indicates that the uncertainties corresponding to these θ_i were evaluated well. This is especially true for the jet and lepton experimental systematic uncertainties and also for the systematic uncertainty on the normalization procedure for the dominant backgrounds in the SR.

The NP *data_syst_FAKEMET_SYS* describes the systematic uncertainty on the fake $p_{\mathrm{T}}^{\mathrm{miss}}$ background estimate and is pulled around 2σ from its pre-fit value. This indicates that the background or its uncertainty are most likely underestimated. This is also visible in the top panel of Figure 13.1, where especially the first bin of the pre-fit data distribution shows a difference (4 %) with respect to the post-fit prediction. This difference is attributed to the underestimated fake $p_{\mathrm{T}}^{\mathrm{miss}}$ background, which has the largest contribution in the first bin of the spectrum. By pulling the NP, the fit compensates for the difference.

Table 13.1 shows the results of the goodness-of-fit test for the differential production cross sections as a function of boson p_{T} for alle measured final states in the monojet and the VBF phase spaces. In addition the result of a combined fit including all final states is also shown. Good agreement is observed between the measured cross sections and the predictions. This demonstrates that the measured data is described by the SM and no excess over the SM

predictions from potential BSM physics is observed within the uncertainties on the measurement.

Region	Monojet Z boson p_T		VBF Z boson p_T	
	χ^2/NDF	p-value	χ^2/NDF	p-value
$Z \to \nu\nu$ + jets	7.64/11	0.75	8.30/10	0.60
$Z \to ee$ + jets	2.56/9	0.98	4.36/7	0.74
$Z \to \mu\mu$ + jets	5.17/10	0.88	9.17/8	0.33
$W \to e\nu$ + jets	6.55/11	0.83	12.04/10	0.28
$W \to \mu\nu$ + jets	18.09/11	0.08	11.71/10	0.31
γ + jets	11.96/11	0.37	2.47/10	0.99
Combined	77.57/68	0.20	52.52/60	0.74

Table 13.1.: Results of the goodness-of-fit test for the cross sections as a function of the boson p_T in the monojet and VBF phase spaces for the measured final states.

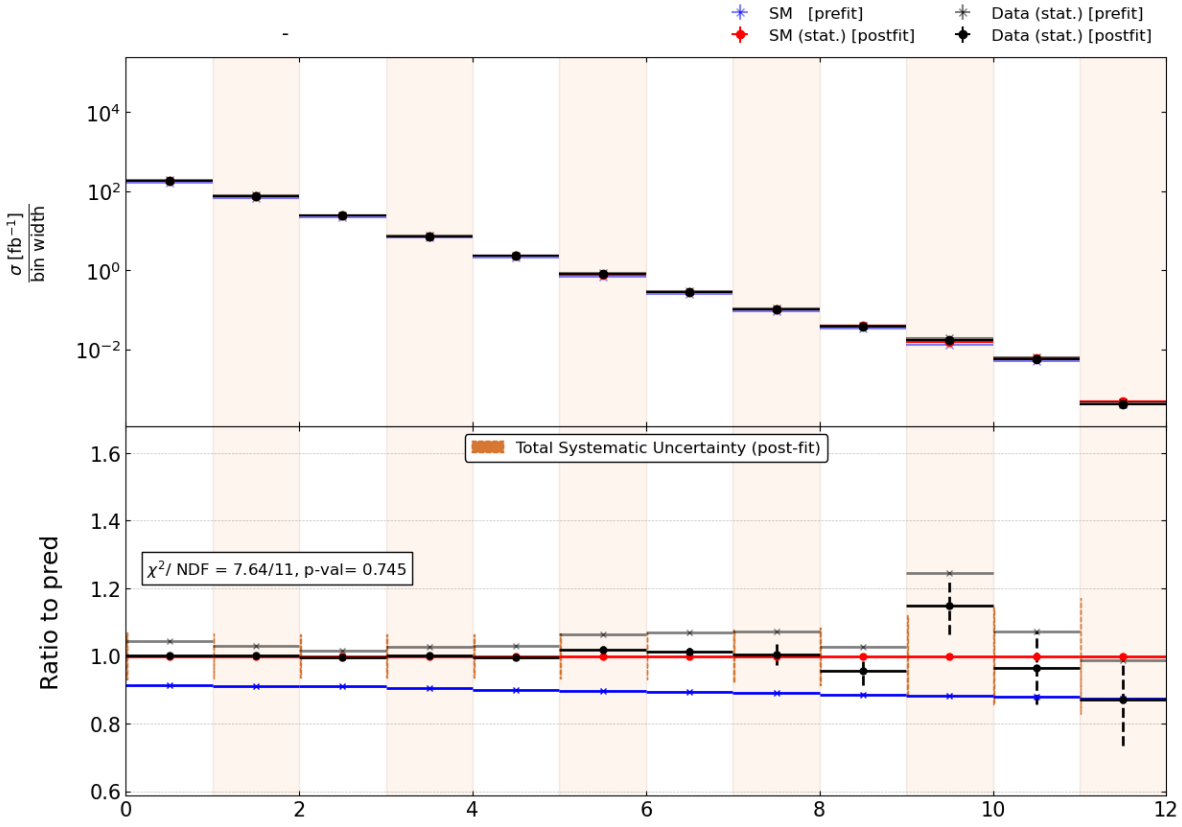

Figure 13.1.: Pre- and post-fit distributions for both the data and the prediction in bins of the Z boson p_T in the monojet phase space for the $Z \to \nu\nu$ + jets final state. The total systematic uncertainty includes both the experimental and the theoretical uncertainties. The stastistical errors are only shown for the post-fit distribution.

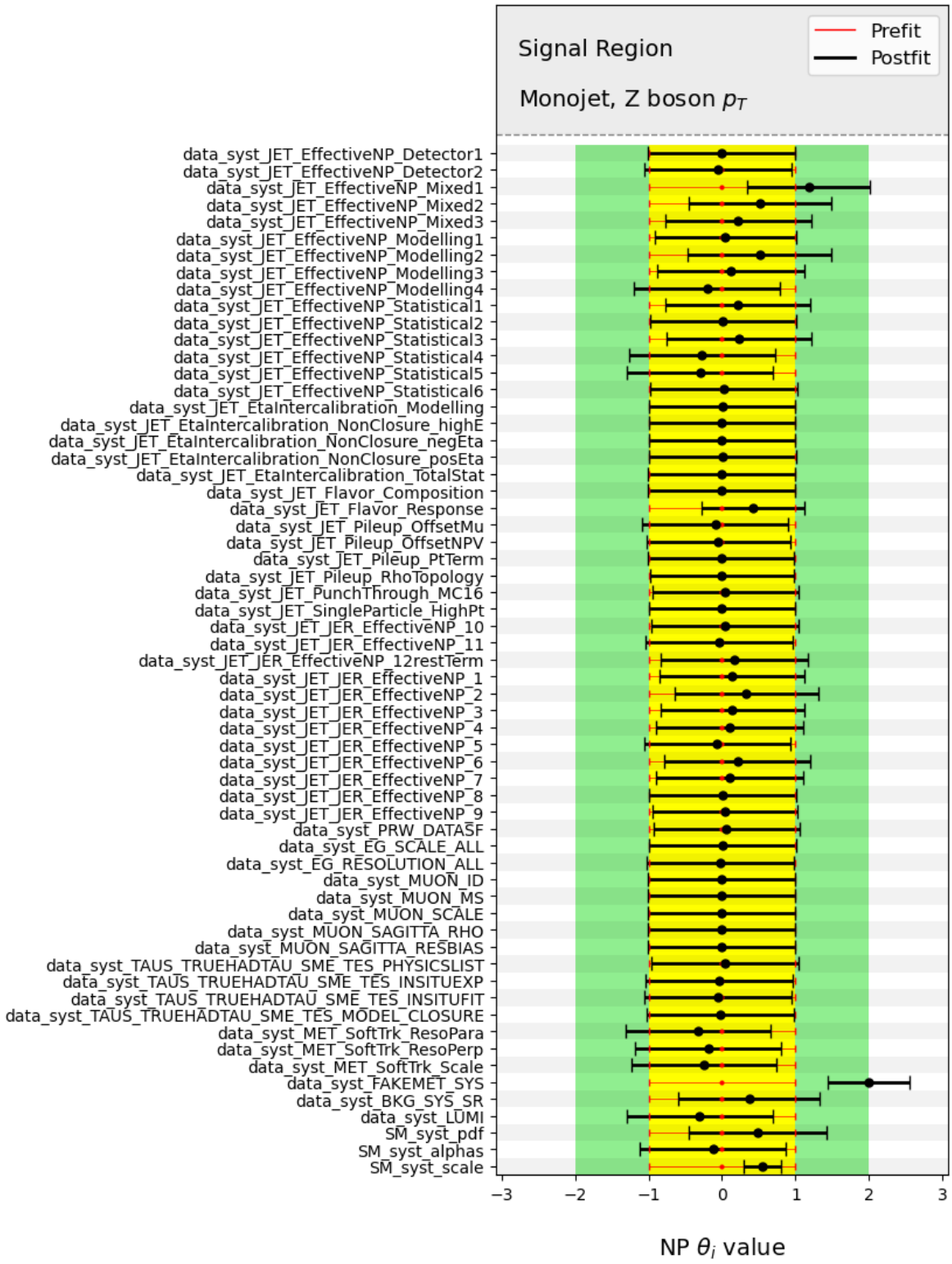

Figure 13.2.: Pre-fit (red) and post-fit (black) values of the NPs θ_i. The yellow band indicates a deviation within one σ from the pre-fit value, the green band indicates a deviation within two σ from the pre-fit value.

14. Interpretation of the Measured Cross Sections in the Context of Physics Beyond the Standard Model

The measured cross sections show good agreement with the SM predictions and no excess due to BSM physics processes is observed. Therefore the data is used to constrain models for BSM physics. In this section this is demonstrated for the example of a DM model with an axial-vector mediator (DMA) (see Section 2.3.2).

The goal is to determine the limitting parameters of the model, under which it is still compatible with the measurement. To achieve this a hypothesis test is performed, which quantifies how much more or less compatible the BSM plus SM hypothesis (H_1) is with the data than the SM-only hypothesis (H_0). Then the CL_s [145] method is used to set upper limits on the BSM model. In the following a brief overview over the methodology is given [22].

In order to perform the hypothesis test a test statistic is defined. This test statistic is based on a likelihood ratio, which is the most powerful test at given significance α, according to the Neyman-Pearson lemma [146]. The test statistic [22] is constructed as

$$t_{\vec{\mu}} = -2 \ln \lambda \left(\vec{\mu}\right) = -2 \ln \frac{\text{argmax}_{\vec{\theta}} \mathscr{L}\left(\vec{x} \,|\, \vec{\mu}, \vec{\theta}\right)}{\text{argmax}_{\vec{\theta}} \mathscr{L}\left(\vec{x} \,|\, \vec{\mu}_{SM}, \vec{\theta}\right)} \tag{14.1}$$

using the likelihood function defined in Equation 13.1. Here $\vec{\mu}$ represents the BSM hypothesis and $\vec{\mu}_{SM}$ the SM-only hypothesis. The likelihoods are marginalised over the NPs $\vec{\theta}$.

The confidence level CL gives the probability of the test statistic $t_{\vec{\mu}}$ being higher than what was observed in data ($t_{\vec{\mu},\text{obs}}$) under the assumption that H_1 is true [136]. It is defined as

$$CL\left(\vec{\mu}\right) = \int_{t_{\vec{\mu},\text{obs}}}^{\infty} f\left(t_{\vec{\mu}} \,|\vec{\mu}\right) dt_{\vec{\mu}}. \tag{14.2}$$

The distribution $f\left(t_{\vec{\mu}} \,|\vec{\mu}\right)$ is determined by producing pseudo-experiments (toys) according the statistical and systematic uncertainties in the measurement.

In principle the confidence level can be used to set limits on BSM physics, for example by excluding models for which $CL\left(\vec{\mu}\right) < 0.05$. This would correspond to an exclusion at the 95 % confidence level [136].

However, in cases where the data is inconsistent with H_1, but also with H_0, it is more conservative not to conclude from the data that H_1 is excluded. Furthermore if the data has only little sensitivity to H_1 it would also be more conservative not to exclude H_1 based on

the data [136]. Both these considerations are taken into account in the construction of the CL_s method, where CL_s is defined as

$$CL_s\left(\vec{\mu}\right) = \frac{CL\left(\vec{\mu}\right)}{CL_b}. \tag{14.3}$$

Here CL_b is constructed from the same test statistic under the assumption that the background-only hypothesis (e.g. the SM hypothesis) is true. A small compatibility with H_0 or a weak separation between H_0 and H_1, will lead to larger values of CL_s. Therefore the CL_s method delivers more conservative limits. The BSM hypothesis H_1 is considered excluded, if $CL_s < 0.05$.

In the following the CL_s method is used to set limits on the DMA model. The coupling strength of the mediator to quarks is set to $g_q = 0.25$ and the coupling to the DM particles is set to $g_\chi = 1$. These are the benchmark values recommended by the ATLAS+CMS Dark matter forum and allow for comparability of the limits set by different analyses [57].

For this particular model, the mediator A does not couple to leptons or photons. Therefore the DM signal is only expected to have contributions to the $Z \to \nu\nu$ + jets final state. However the γ + jets final state is also included in the hypothesis test to contribute additional constraining power on the systematic uncertainties. This improves the sensitivity. The γ + jets final state is chosen, as it is measured with the highest statistical and systematic precision of all measured final states. The highest sensitivity is expected in the boson p_T distributions [57] of the monojet and the VBF phase spaces, therefore these distributions are used in the hypothesis test.

The two remaining open parameters of the model, the masses of the mediator m_A and of the dark matter particle m_χ, are used to perform a signal scan. In this signal scan, the CL_s value is calculated for a grid of signal points $\left(m_A, m_\chi\right)$. If $CL_s < 0.05$ for a signal point, that signal point is considered to be excluded.

The signal scan is first performed on pseudo-data, which is determined from the SM prediction to understand the behaviour of the fit and limit setting procedure. Then the signal scan is then performed on the cross sections measured from full Run 2 data.

The results of the signal scan are given in Figure 14.1, which shows the $m_A - m_\chi$ mass plane. The signal points are used to interpolate an exclusion contour. All signal points within the contour are excluded at least at 95 % confidence level. The expected limits are determined from the SM-only pseudo-data and are shown as a dashed line. The $1-\sigma$-band, which contains 68 % of the toys, is indicated in green and the $2-\sigma$-band, which contains 95 % of the toys, is indicated in yellow. The limits observed from the data are shown as a solid black line.

The expected upper limit for the mediator mass is $m_A = 2260\,\mathrm{GeV}$ and the expected upper limit for the DM particle is $m_\chi = 660\,\mathrm{GeV}$. The measured data excludes the mass parameters of the model with $m_A < 2210\,\mathrm{GeV}$ and $m_\chi < 600\,\mathrm{GeV}$ (observed limits). This is an improvement over the previous best ATLAS results of 5 % and 3 % respectively [17].

This result demonstrates the value of precise boson plus jet production cross section measurements also for BSM physics interpretation. Especially the combination of several such measurements in a coherent way helps to additionaly constrain systematic uncertainties and improve the sensitivity.

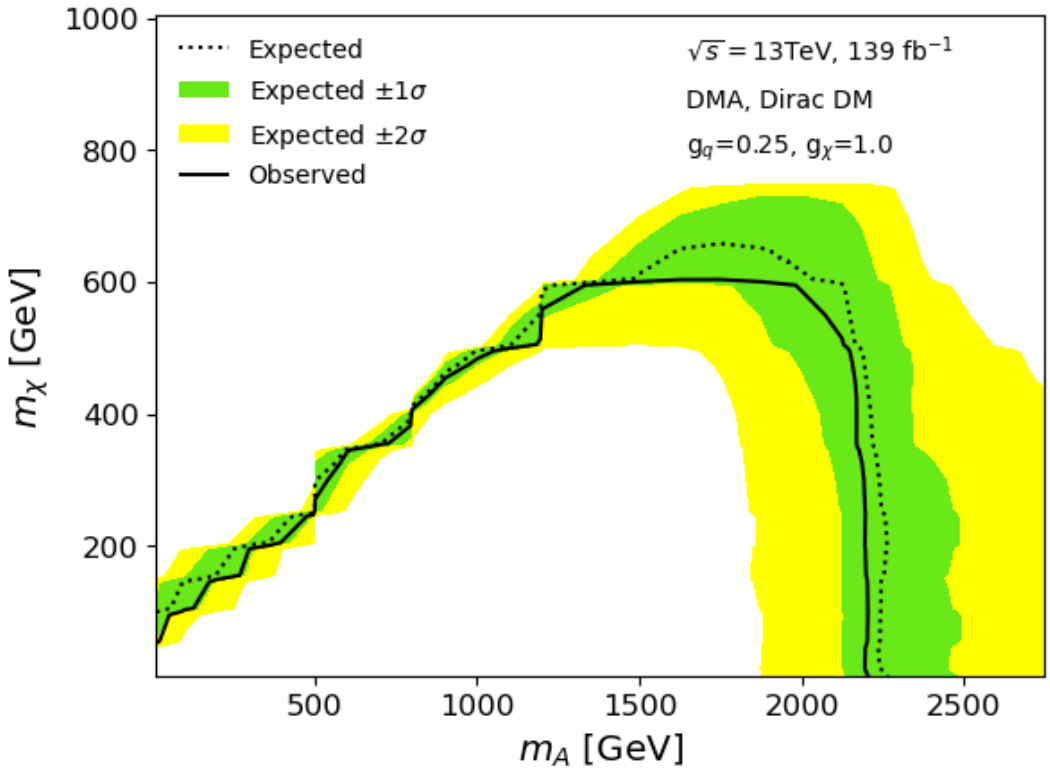

Figure 14.1.: Exclusion limits on the axial vector mediator simplified DM model.

The result also shows the valuable contribution made by the measurement of the γ + jets final state, which was introduced here for the first time for a monojet-like search with ATLAS.

All measured production cross sections are published unfolded to particle level. This means that other models for BSM physics can be easily tested against the measured data. These can include for example other simplified DM models, for example with a different mediator particle [57], or models for vector-like quarks [147]. The latter can benefit from this measurement, as it predicts signal contributions to several of the final states measured here.

15. Summary and Conclusion

Precise tests of the Standard Model are important to advance our knowledge of the fundamental particles and interactions. This includes validating and testing the modelling of differential distributions by state-of-the art Monte Carlo generators. These tests also play an important role in the search for Dark Matter. The existence of this elusive form of matter, that makes up 23 % of the energy content in the universe, has been been confirmed by many astrophysical observations. However the nature of Dark Matter is still unknown.

In the analysis presented here, differential cross sections of six processes including a boson and at least one jet are measured at high boson transverse momentum using the full Run 2 dataset. These are $Z \to \nu\nu$ + jets, $Z \to ee$ + jets, $Z \to \mu\mu$ + jets, $W \to e\nu$ + jets, $W \to \mu\nu$ + jets and γ + jets. These processes allow to test the Standard Model and especially Quantum Chromodynamics at high momentum transfers. Furthermore, measurements of the $Z \to \nu\nu$ + jets final state are used to search for Dark Matter, which would manifest itself as additional signal contributions in this channel. The remaining boson plus jet processes are also important in this context, since they constitute the dominant backgrounds to many searches for beyond the Standard Model physics and their precise measurement will help to improve the background modelling for future searches.

Differential cross sections for each boson plus jet process are measured in two phase space regions that enhance different jet topologies. In the monojet phase space the boson is required to recoil against at least one high energetic jet - this is also the topology expected from Dark Matter production. The differential cross section is measured as a function of the boson p_{T}. In the VBF phase space the electroweak vector boson fusion production channel is enhanced. This channel has for example sensitivity to the invisible decay of the Higgs boson. In the VBF phase space differential cross sections are measured as a function of boson p_{T}, the invariant mass of the two leading jets and the signed azimuthal angle between these jets.

An important part of the measurement is the precise estimation of contributions from background processes. These can be grouped into backgrounds caused by fake objects and backgrounds due to limited detector efficiency and acceptance.

Dedicated data-driven methods are used to provide a robust estimate of the fake background contributions in all regions. The fake $p_{\mathrm{T}}^{\mathrm{miss}}$ estimate with the Jet Smearing method, the fake electron estimate with the matrix method and the fake photon estimate with the 2D-sideband method are discussed in detail.

For the backgrounds due to limited detector efficiency and acceptance a data-driven estimation method is employed, where the shape of the background is estimated using simulation and the normalisation is extracted from control regions in data. The method is also used to constrain systematic uncertainty contributions from the backgrounds to the measured cross section. In the Signal Region, which is the region expected to contain a potential Dark Matter signal, the uncertainty contributions from these backgrounds were reduced sig-

nificantly, thereby making this uncertainty subdominant.

All measured cross sections are corrected for detector-effects using iterative Bayesian unfolding. This greatly facilitates the comparison of the measured cross sections with Standard Model or beyond the Standard Model predictions.

The measured cross sections are used in a goodness-of-fit test to investigate the compatibility with the Standard Model. Very good agreement is found in the fit, with p-values of a combined fit across all regions in a given observable ranging from $p = 0.20$ to $p = 0.74$, depending on the observable.

As no excess over the Standard Model predictions is observed, the measured data is used to constrain a simplified Dark Matter model. CLs limits are set on Dark Matter production with an axial-vector mediator coupling the Dark Matter to Standard Model quarks with respective coupling strengths of $g_\chi = 1.0$ and $g_q = 0.25$. At 95 % confidence level the observed (expected) limits are $m_A = 2210\,\text{GeV}(2260\,\text{GeV})$ for the mass of the mediator and $m_\chi = 600\,\text{GeV}(660\,\text{GeV})$ for the mass of the Dark Matter particle.

A. Additional Information on the Object and Event Selection

A.1. Trigger Items

The trigger system forms the basis of most physics analyses performed with ATLAS. Many trigger items targeting different event topologies exist and a brief overview of the naming scheme relevant to this measurement is given in the following. The triggers names consist of several field separated by an underscore. Consider e.g *HLT_xe110_mht_L1XE50*. The first field signifies that this trigger uses an HLT algorithm. The second field specifies the object, in this case $p_{\mathrm{T}}^{\mathrm{miss}}$ (= xe), and the minimum energy an object needs to have, in this case 110 GeV. The third and following fields specify the specific configuration of this trigger, in this case *mht* signifies that only hadronic jets were used in the calculation of $p_{\mathrm{T}}^{\mathrm{miss}}$. If the last field is prefixed by *L1* it specifically gives the L1 trigger used to seed the event. Other possible values for the different fields are given in Table A.0, if they are relevant for this measurement. More information is given in [148][76][119].

Field	Values	Description
1st (final trigger stage)	HLT	An HLT algorithm is used
2nd (object and threshold)	xeXX	$p_{\mathrm{T}}^{\mathrm{miss}}$ trigger, minimum $p_{\mathrm{T}}^{\mathrm{miss}}$ of XXGeV
	eXX	single electron trigger, minimum p_{T} of XXGeV
	gXX	single photon trigger, minimum p_{T} of XXGeV
	jXX	single jet trigger, minimum p_{T} of XXGeV
3rd and following (configuration)	mht	only jets used in the $p_{\mathrm{T}}^{\mathrm{miss}}$ calculation
	pufit	local pile-up suppression
	nod0	no cut on transverse impact parameter d_0
	lhmedium	likelihood identification, medium working point
	medium	cut-based identification, medium working point
	ivarloose	variable cone isolation, loose working point
	etcut	only cut on the electromagnetic cluster E_{T}
last (L1 seed)	L1XEXX	L1 $p_{\mathrm{T}}^{\mathrm{miss}}$ trigger, minimum $p_{\mathrm{T}}^{\mathrm{miss}}$ of XXGeV
	L1EMXXVH	L1 electromagnetic trigger, minimum p_{T} of XXGeV, varying threshold (V) and hadronic isolation (H)

Table A.0.: Glossary of trigger item name fields. Other working points for the likelihood and cut-based identification include very loose (vloose), loose and tight [148][76][119].

B. Reducible Backgrounds - Additional Studies and Figures

B.1. Multijet Background

B.1.1. Additional Control Region Plots

Figure B.1 shows the comparison between data, MC simulation and the normalised pseudo-data as a function of $p_{\mathrm{T}}^{\mathrm{miss}}$ in the monojet phase space.

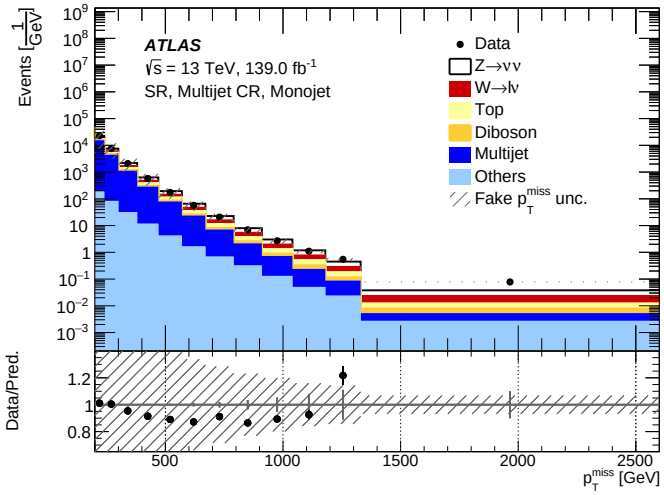

Figure B.1.: $p_{\mathrm{T}}^{\mathrm{miss}}$ distribution in the multijet CR in the monojet phase space in the SR for collision data, MC simulation and normalised pseudo-data in dark blue. The bottom part of the figure shows the ratio of the data and the sum of the various process predictions, with the statistical uncertainty on the data shown in grey and the statistical uncertainty on the predictions shown in black. The systematic uncertainty on the background estimate is shown as a shaded band.

B.1.2. Results of the background estimate - Figures

Figure B.2 shows the results of the fake $p_{\mathrm{T}}^{\mathrm{miss}}$ estimate in the VBF phase space in the SR.

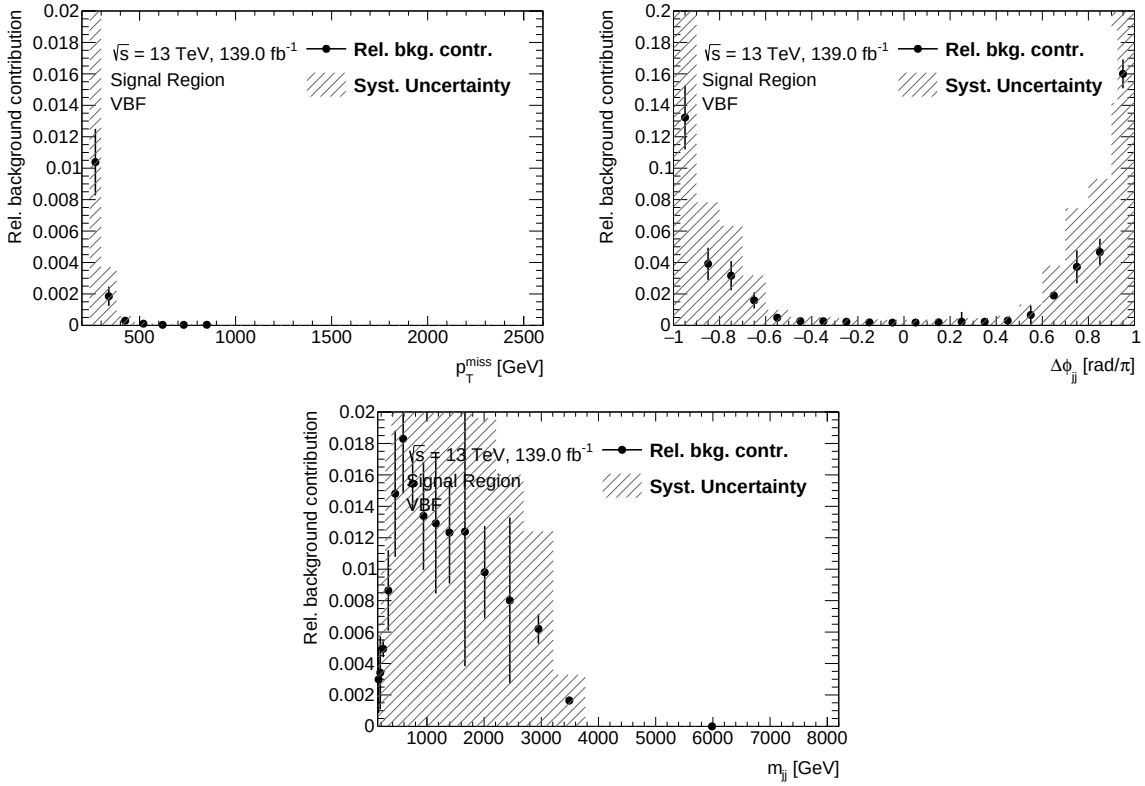

Figure B.2.: Relative contribution of the multijet background to SR as a function of $p_{\mathrm{T}}^{\mathrm{miss}}$ (top left), $\Delta\phi_{jj}$ (top right) and m_{jj} (bottom) in the VBF phase space. The statistical uncertainty is shown as error bars on the points and the systematic uncertainty on the background estimate is shown as a grey hashed band.

B.1.3. Results of the Background Estimate - Tables

Table B.2 and Table B.2 show the result of the fake $p_{\mathrm{T}}^{\mathrm{miss}}$ background estimate in the SR for the monojet and the VBF phase space.

Observable	Background Estimate	
$p_{\mathrm{T}}^{\mathrm{miss}}$ [GeV]	Monojet	VBF
200-240	15960	6902
240-300	3585	1855
300-380	514	134
380-470	74	8
470-570	9	1
>570	<3	<1
Total	20145	8901

Table B.2.: Multijet background estimate in the SR region for $p_{\mathrm{T}}^{\mathrm{miss}}$ for the monojet and VBF phase spaces.

Observable	Background Estimate	Observable	Background Estimate
m_{jj} [GeV]	VBF	$\Delta\phi_{jj}$ [$\frac{rad}{\pi}$]	VBF
200-270	235	[-1.0,-0.9]	841
270-380	2037	[-0.9,-0.8]	1836
380-510	3167	[-0.8,-0.7]	1001
510-660	1614	[-0.7,-0.6]	435
660-840	735	[-0.6,0.]	468
840-1040	517	[0.,0.6]	1023
1040-1270	279	[0.6,0.7]	208
1270-1520	105	[0.7,0.8]	1250
1520-1810	132	[0.8,0.9]	1536
>1810	80	[0.9,1.0]	303
Total	8901		8901

Table B.2.: Multijet estimate in the SR region for m_{jj} and $\Delta\phi_{jj}$ in the VBF.

B.1.4. Additional validation region plots

Figure B.3 shows the comparison between data, MC simulation and the fake $p_{\mathrm{T}}^{\mathrm{miss}}$ estimate for the observables in the VBF phase space.

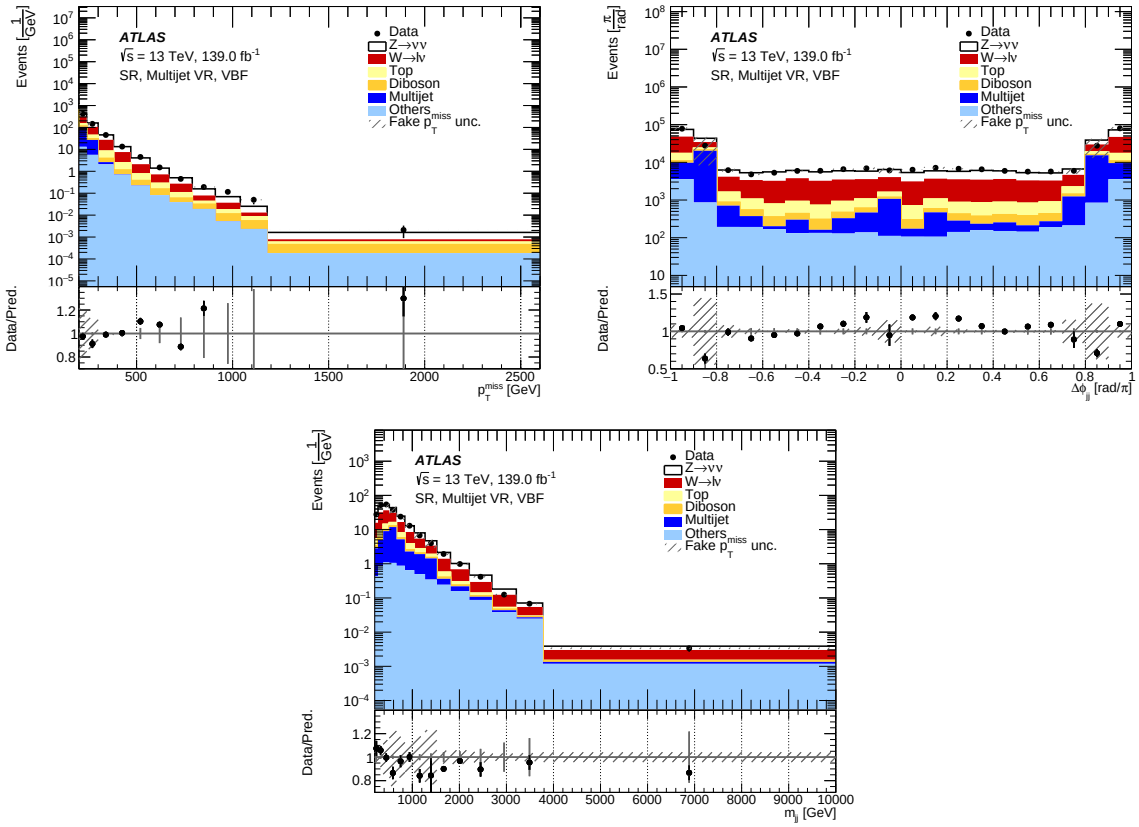

Figure B.3.: Comparison of data and MC in the multijet VR for the SR. Top row: $p_{\mathrm{T}}^{\mathrm{miss}}$ (left panel) and $\Delta\phi_{jj}$ (right panel) distributions in the VBF phase space. Bottom row: m_{jj} distribution in the VBF ps.

B.2. Beam-induced Background

Table B.3 and Table B.3 show the result of the fake BIB background estimate in the SR for the monojet and the VBF phase space.

Observable	Background Estimate	
$p_{\mathrm{T}}^{\mathrm{miss}}$ [GeV]	Monojet	VBF
200-240	5106	1261
240-300	1609	257
300-380	359	40
380-470	61	8
>470	30	15
Total	7165	1581

Table B.3.: BIB estimate for $p_{\mathrm{T}}^{\mathrm{miss}}$ in the monojet and VBF phase spaces.

Observable	Background Estimate	Observable	Background Estimate
m_{jj} [GeV]	VBF	$\Delta\phi_{jj}$ [$\frac{rad}{\pi}$]	VBF
200-270	271	[-1.0,-0.9]	31
270-380	346	[-0.9,-0.8]	44
380-510	234	[-0.8,-0.7]	64
510-660	177	[-0.7,-0.6]	43
660-840	141	[-0.6,0.]	631
840-1040	85	[0.,0.6]	603
1040-1270	56	[0.6,0.7]	42
1270-1520	74	[0.7,0.8]	39
1520-1810	67	[0.8,0.9]	49
>1810	130	[0.9,1.0]	35
Total	1581		1581

Table B.3.: BIB estimate in the SR region for m_{jj} and $\Delta\phi_{jj}$ in the VBF phase space.

B.3. Fake Photon Background

B.3.1. Addition Information on the Shower Shape Identification

Category	Description	Name	Usage
Hadronic leakage	Ratio of E_T in the first layer of the hadronic calorimeter to E_T of the EM cluster (used over the ranges $\|\eta\| < 0.8$ and $\|\eta\| > 1.37$)	R_{had_1}	e/γ
	Ratio of E_T in the hadronic calorimeter to E_T of the EM cluster (used over the range $0.8 < \|\eta\| < 1.37$)	R_{had}	e/γ
EM third layer	Ratio of the energy in the third layer to the total energy in the EM calorimeter	f_3	e
EM second layer	Ratio of the sum of the energies of the cells contained in a 3×7 $\eta \times \phi$ rectangle (measured in cell units) to the sum of the cell energies in a 7×7 rectangle, both centred around the most energetic cell	R_η	e/γ
	Lateral shower width, $\sqrt{(\Sigma E_i \eta_i^2)/(\Sigma E_i) - ((\Sigma E_i \eta_i)/(\Sigma E_i))^2}$, where E_i is the energy and η_i is the pseudorapidity of cell i and the sum is calculated within a window of 3×5 cells	w_{η_2}	e/γ
	Ratio of the sum of the energies of the cells contained in a 3×3 $\eta \times \phi$ rectangle (measured in cell units) to the sum of the cell energies in a 3×7 rectangle, both centred around the most energetic cell	R_ϕ	e/γ
EM first layer	Total lateral shower width, $\sqrt{(\Sigma E_i (i - i_{\text{max}})^2)/(\Sigma E_i)}$, where i runs over all cells in a window of $\Delta\eta \approx 0.0625$ and i_{max} is the index of the highest-energy cell	$w_{s\,\text{tot}}$	e/γ
	Lateral shower width, $\sqrt{(\Sigma E_i (i - i_{\text{max}})^2)/(\Sigma E_i)}$, where i runs over all cells in a window of 3 cells around the highest-energy cell	$w_{s\,3}$	γ
	Energy fraction outside core of three central cells, within seven cells	f_{side}	γ
	Difference between the energy of the cell associated with the second maximum, and the energy reconstructed in the cell with the smallest value found between the first and second maxima	ΔE_s	γ
	Ratio of the energy difference between the maximum energy deposit and the energy deposit in a secondary maximum in the cluster to the sum of these energies	E_{ratio}	e/γ
	Ratio of the energy measured in the first layer of the electromagnetic calorimeter to the total energy of the EM cluster	f_1	e/γ

Table B.3.: Discriminating variables used for electron and photon identification. The usage column indicates if the variables are used for the identification of electrons, photons, or both. Adapted from [79].

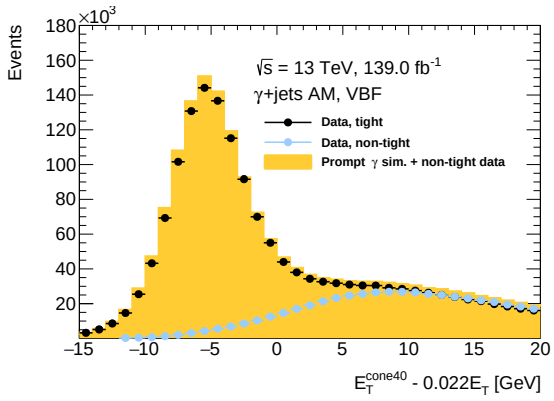

Figure B.4.: Calorimeter isolation energy distribution in γ+jets AM region and the VBF phase space without the calorimeter isolation requirement applied for events in data with tight leading photons (black), non-tight leading photons (blue, normalized to the tight data in $E_T^{cone40} - 0.002E_T > 10$). The sum of the simulation and non-tight data (yellow) adequately describes the tight data.

B.3.2. Additional isolation energy distributions

Figure B.4 shows the data distribution (black) of the calorimeter isolation variable in the γ+jets AM region. Also shown are a template for the fake photons (blue) and the sum (yellow) of the MC simulation used to model the prompt photons and the fake photon template. The fake photon template has been derived by requiring the non-tight identification instead of the tight identification on the signal photon. To allow for a shape comparison, the template is normalised to the data for $E_{\mathrm{T}}^{\mathrm{cone40}} - 0.022E_{\mathrm{T}} > 10$.

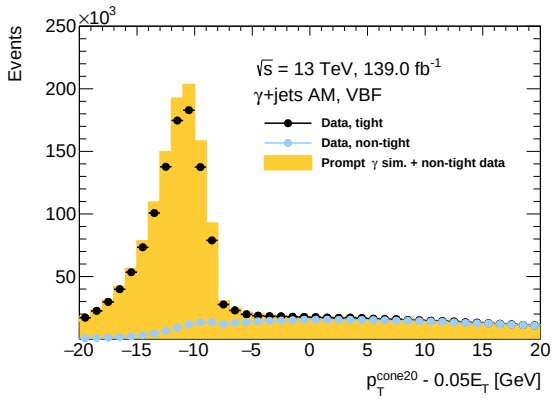

Figure B.5.: Track isolation energy distribution in γ+jets AM region and the VBF phase space without the track isolation requirement applied for events in data with tight leading photons (black), non-tight leading photons (blue, normalized to the tight data in $p_T^{cone20} - 0.05 \times E_T > 10$. The sum of the simulation and non-tight data (yellow) adequately describes the tight data.

Figure B.5 shows the data distribution (black) in the γ+jets AM region without the track

isolation cut applied. The figure also shows a fake template (blue) derived by requiring the non-tight identification instead of the tight identification on the signal photon and the sum of the simulation prediction and the fake template (yellow). To allow for a shape comparison, the fake template is normalized to the tight data for $p_T^{cone20} - 0.05 \times E_T > 10$.

B.3.3. Additional signal leakage distributions

The *leakage fractions* for the distributions in the VBF phase space are shown in Figure B.6

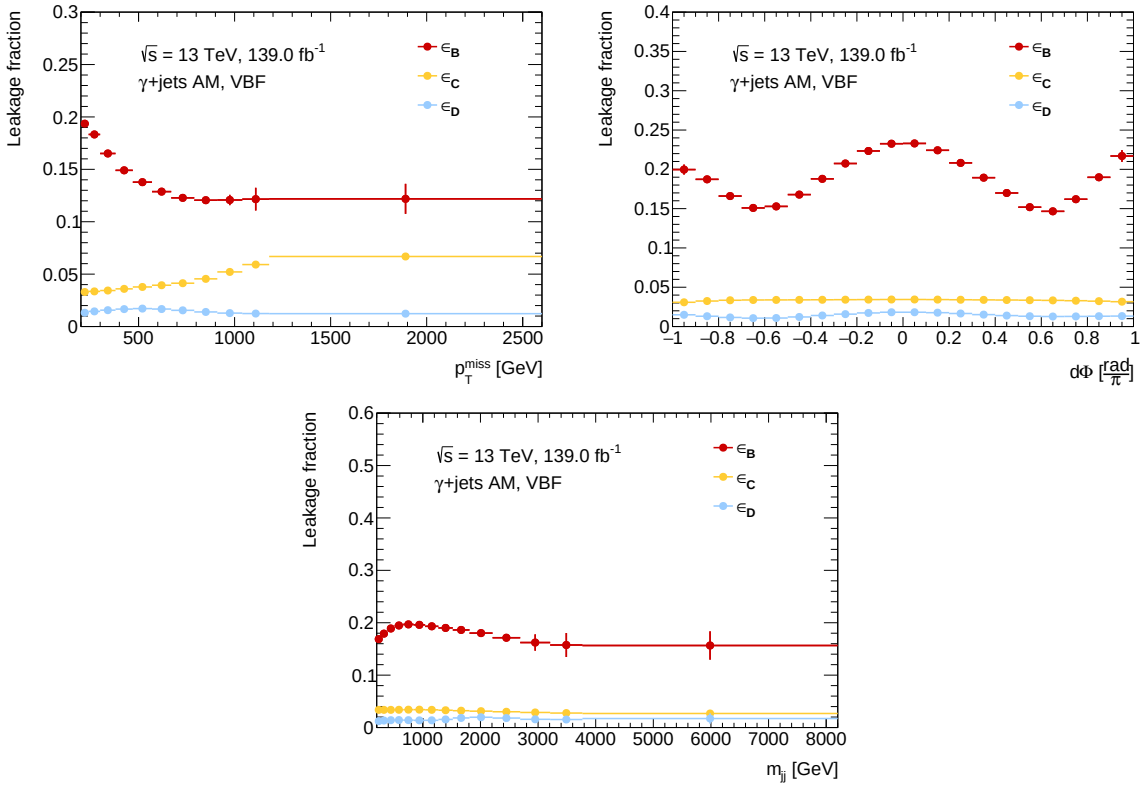

Figure B.6.: Signal leakage for regions B (red), C (yellow) and D in the VBF phase space as function of $p_{\mathrm{T}}^{\mathrm{miss}}$ (top left), $\Delta\phi_{jj}$ (top right) and m_{jj} (bottom).

B.3.4. Additional Purity Distributions

Figure B.7 shows the purity of the γ+jets AM region for the distributions in the VBF phase space.

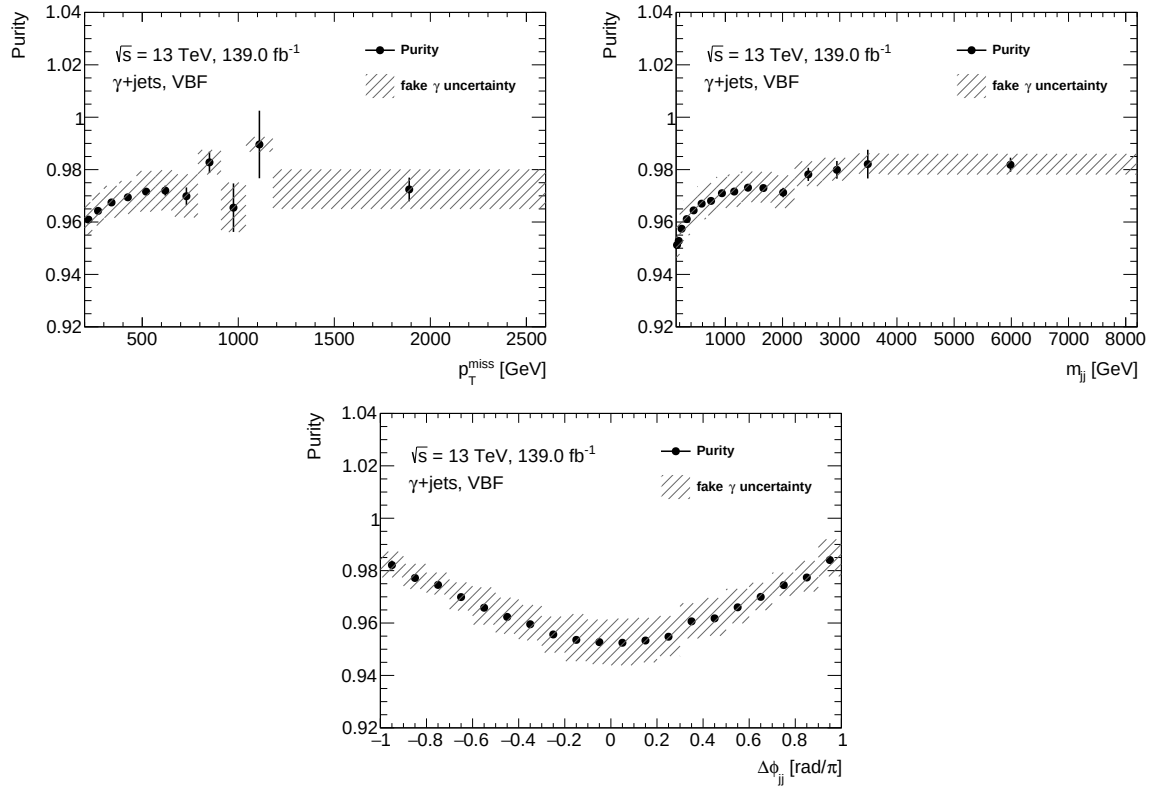

Figure B.7.: Purity as a function of $p_{\mathrm{T}}^{\mathrm{miss}}$ (top left), m_{jj} (top right) and $\Delta\phi_{jj}$ (bottom) in the VBF phase space. The gray bands show the systematic uncertainty on the background estimate.

B.3.5. Additional Uncertainty Distributions

Definition of the non-tight identification

The relative systematic uncertainty on the fake photon estimate in the VBF phase space due to the definition of the loose^{IV} identification is shown in Figure B.10.

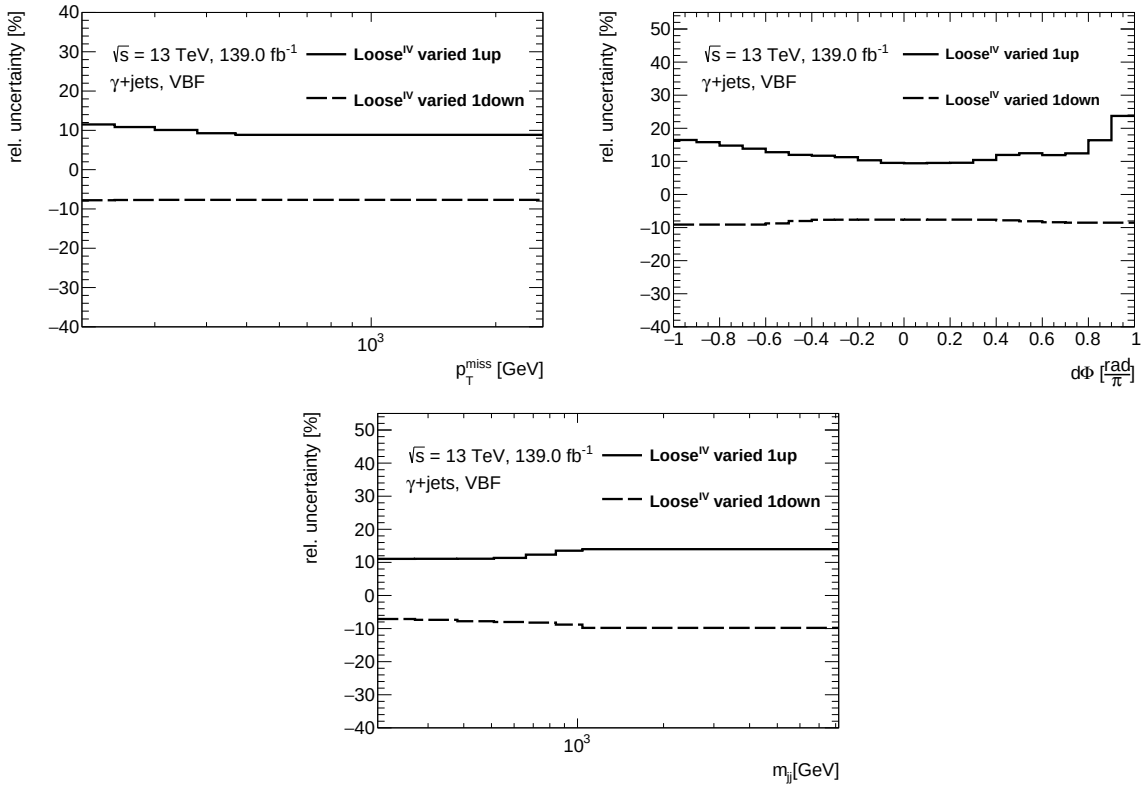

Figure B.8.: Relative uncertainty on the fake photon background due to the choice of the loose^{IV} identification in the VBF phase space as function of $p_{\mathrm{T}}^{\mathrm{miss}}$ (top left), $\Delta\phi_{jj}$ (top right) and m_{jj} (middle left).

Residual Correlations between Isolation and Identification

The leakage fractions used to determine the correlation factor R in the VBF phase space are shown in Figure B.9. The relative systematic uncertainty on the fake photon estimate in the VBF phase space due to the residual correlations between the identification and the isolation is shown in Figure B.10.

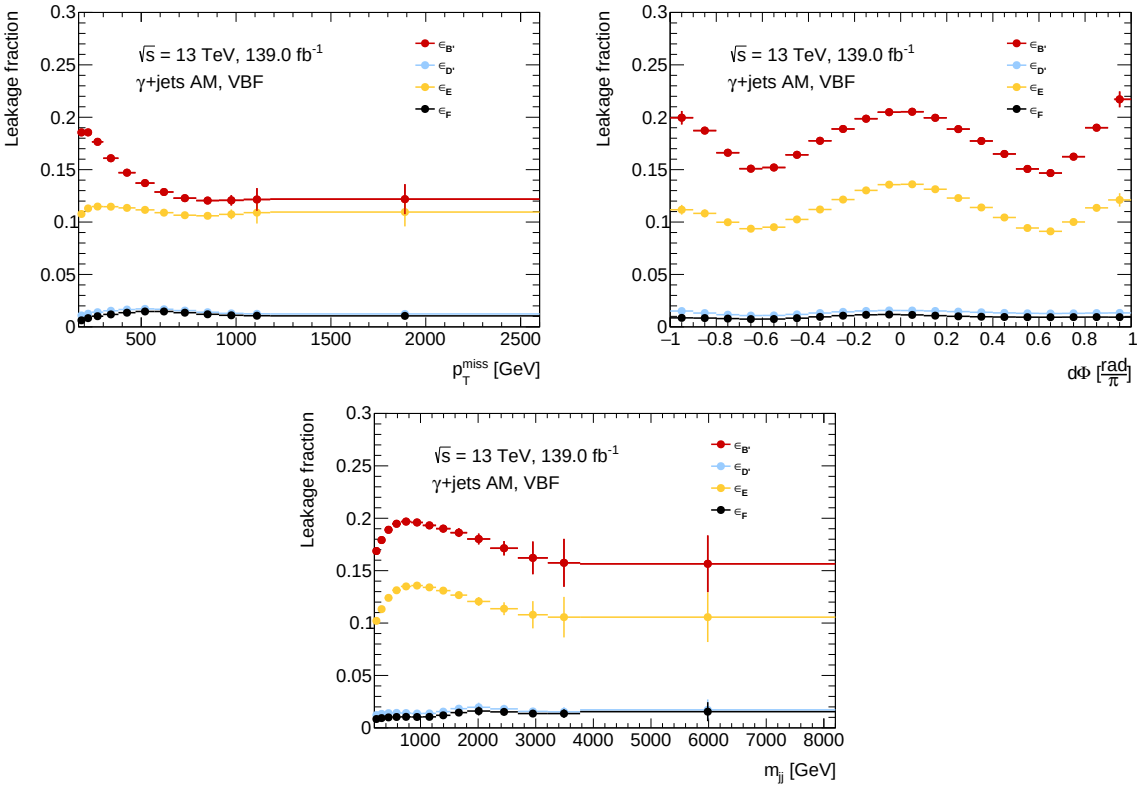

Figure B.9.: Leakage fractions used to determine the correlation factor R in the VBF phase space as function of $p_{\mathrm{T}}^{\mathrm{miss}}$ (top left), $\Delta\phi_{jj}$ (top right) and m_{jj} (middle left).

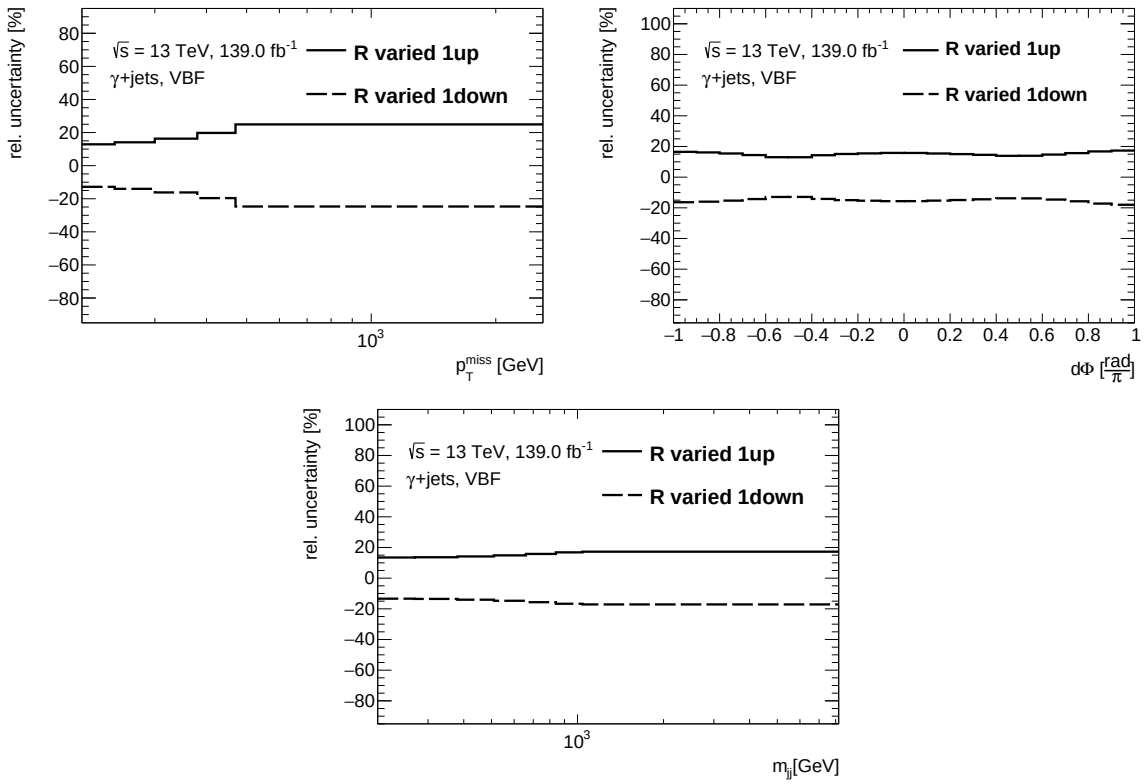

Figure B.10.: Relative uncertainty on the fake photon background due to residual correlations between isolation and identification in the VBF phase space as function of $p_{\mathrm{T}}^{\mathrm{miss}}$ (top left), $\Delta\phi_{jj}$ (top right) and m_{jj} (middle left).

Dependence of the leakage fractions on the MC generator

Figure B.11 shows a comparison of the leakage fractions determined with Sherpa and Pythia in the VBF phase space. The resulting relative uncertainty on the fake photon estimate is shown in Figure B.12.

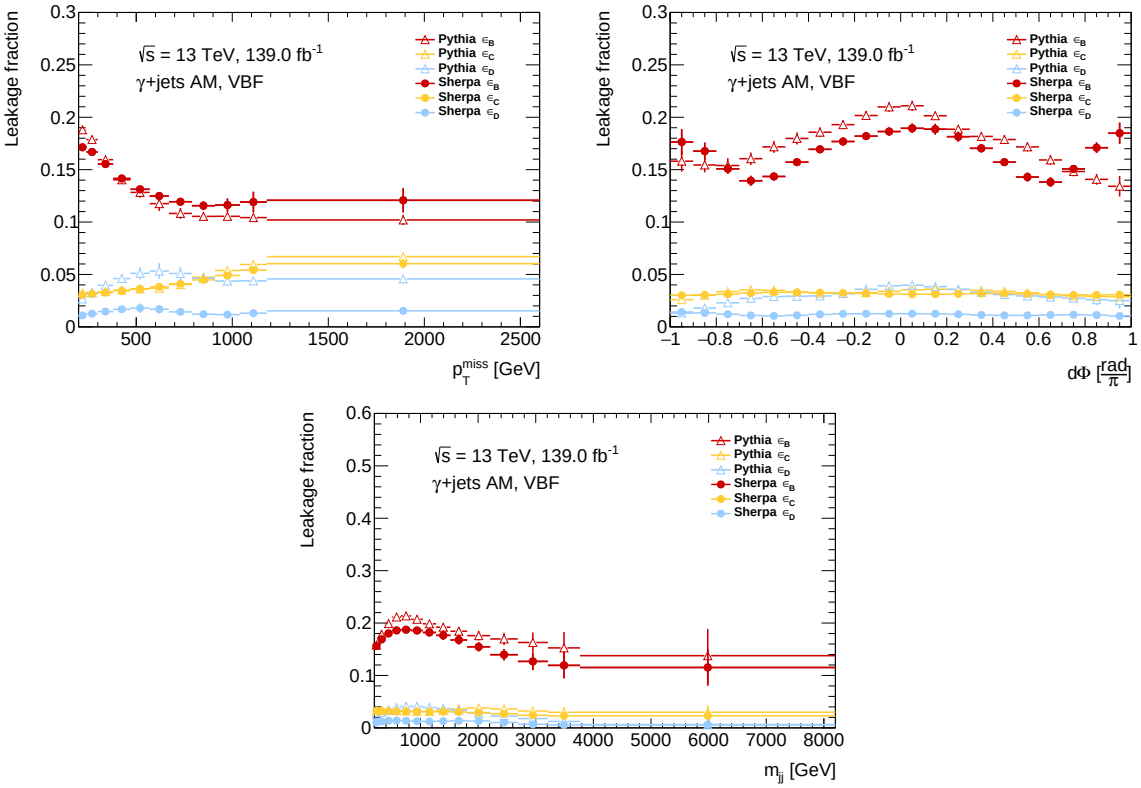

Figure B.11.: Leakage fractions as function of $p_{\mathrm{T}}^{\mathrm{miss}}$ in the VBF phase space as function of $p_{\mathrm{T}}^{\mathrm{miss}}$ (top left), $\Delta\phi_{jj}$ (top right) and m_{jj} (middle left).

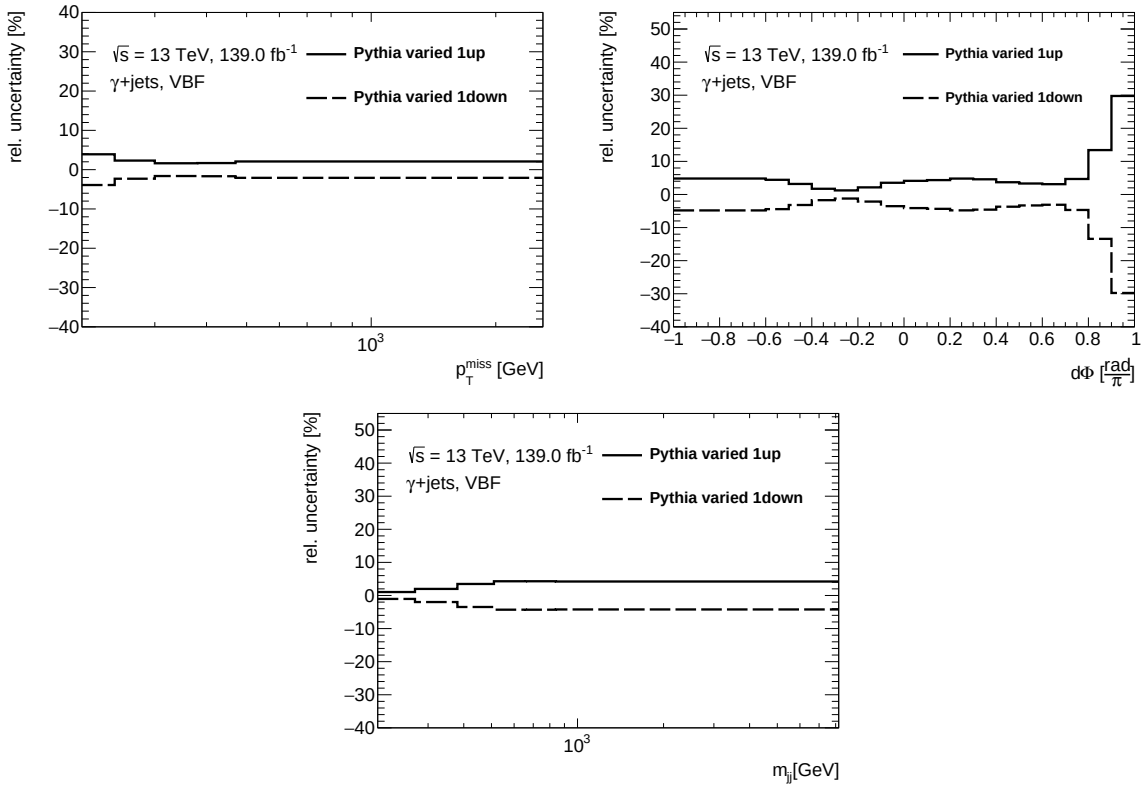

Figure B.12.: Relative uncertainty on the fake photon background due to dependence on the MC generator in the VBF phase space as function of $p_{\mathrm{T}}^{\mathrm{miss}}$ (top left), $\Delta\phi_{jj}$ (top right) and m_{jj} (middle left).

B.4. Fake Electron Background

B.4.1. Additional Real Efficiency Plots

This section shows the real efficiency maps for the 2015/16 (Figure B.13) and 2018 (Figure B.14) data periods.

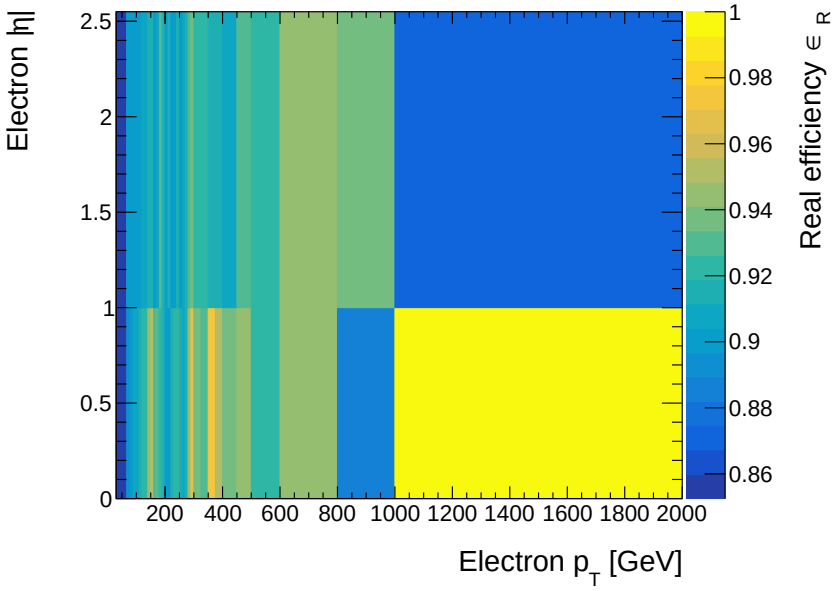

Figure B.13.: Real electron efficiency as a function of p_{T} and η for the 2015/16 data period.

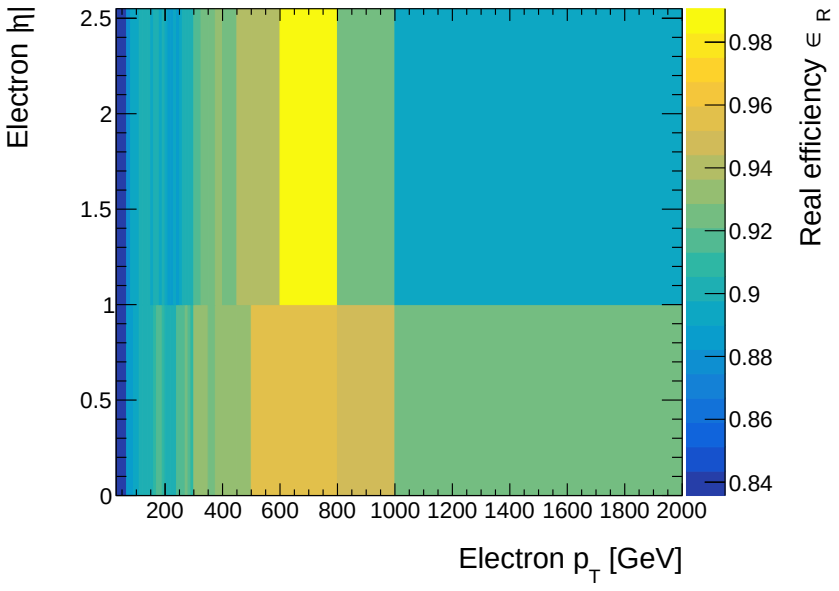

Figure B.14.: Real electron efficiency as a function of p_{T} and η for the 2018 data period.

B.4.2. Smoothness of the Estimate

Figure B.15 shows the p_{T} distribution of fake electrons predicted by the matrix method in the validation region. It is visible that the lepton distribution is smooth, apart from statistical fluctuations when moving from one trigger region the next. This demonstrates that varying baseline definition due to the changing trigger selection does not impact the final result.

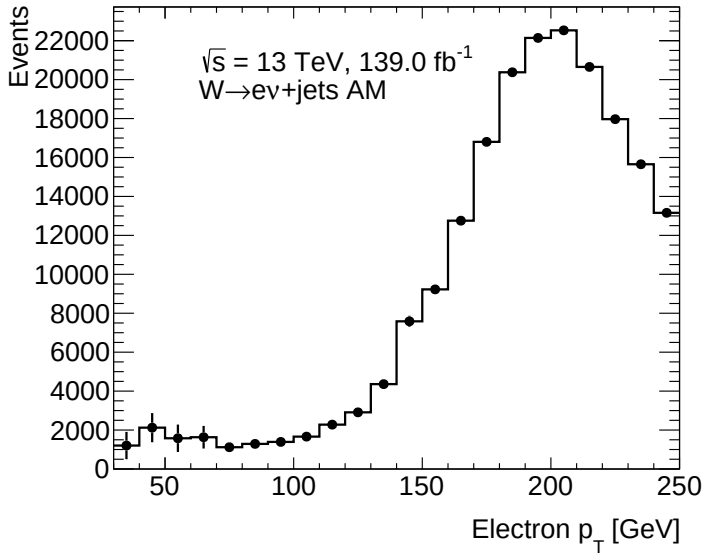

Figure B.15.: p_{T} distribution of fake electrons predicted by the matrix method in the validation region.

B.4.3. Additional Fake Efficiency Plots

This section shows the fake efficiency maps for the 2015/16 (Figure B.16) and 2018 (Figure B.17) data periods.

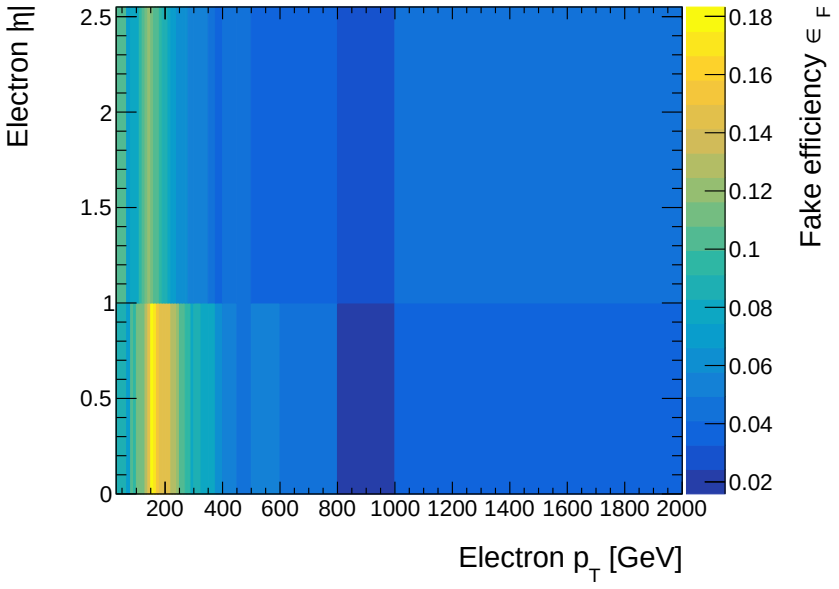

Figure B.16.: Fake electron efficiency as a function of electron p_{T} and η for the 2015/16 data period.

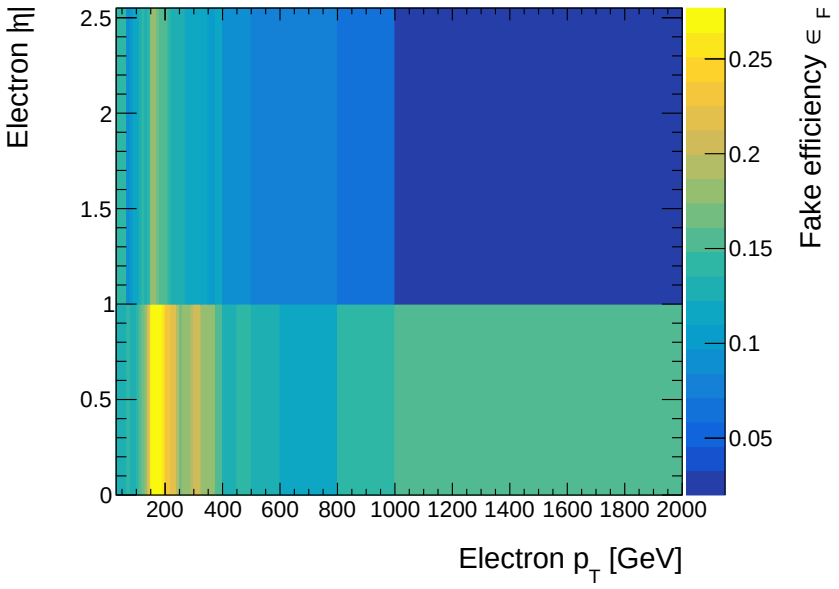

Figure B.17.: Fake electron efficiency as a function of electron p_{T} and η for the 2018 data period.

B.4.4. Additional Fake Background Estimate Results

This section shows the results tables for the fake electron background estimate (Table B.17).

Observable	Background Estimate (±stat. ±syst.)	
$p_{\mathrm{T}}^{\mathrm{miss}}$ [GeV]	Monojet	VBF
200-240	8547 (1.8 %) ±801 ±633	1391 (2.0 %) ±282 ±96
240-300	5958 (1.8 %) ±561 ±441	1028 (2.0 %) ±238 ±80
300-380	2820 (1.8 %) ±349 ±210	467 (1.8 %) ±113 ±36
380-470	2095 (3.6 %) ±257 ±156	486 (5.0 %) ±167 ±38
470-570	775 (3.7 %) ±171 ±58	105 (2.8 %) ±20 ±8
570-670	496 (6.5 %) ±130 ±117	119 (8.4 %) ±63 ±23
670-790	210 (6.1 %) ±89 ±50	12 (1.7 %) ±15 ±2
790-910	87 (7.1 %) ±5 ±21	14 (6.2 %) ±1 ±3
910-1040	45 (8.1 %) ±1 ±11	7 (5.7 %) ±1 ±1
1040-1180	25 (9.6 %) ±1 ±6	3 (5.1 %) ±1 ±1
1180-1330	14 (13.5 %) ±1 ±3	4 (10.6 %) ±1 ±1
1330-2600	14 (21.9 %) ±1 ±3	0 (0.0 %) ±0 ±0
Total	21086	3636

Table B.17.: Fake electron background estimate in the $W \rightarrow ev$ + jets AM region for $p_{\mathrm{T}}^{\mathrm{miss}}$ for the monojet and VBF phase spaces. The relative contribution is given in brackets. The first uncertainty column gives the statistical, the second column the systematic uncertainty.

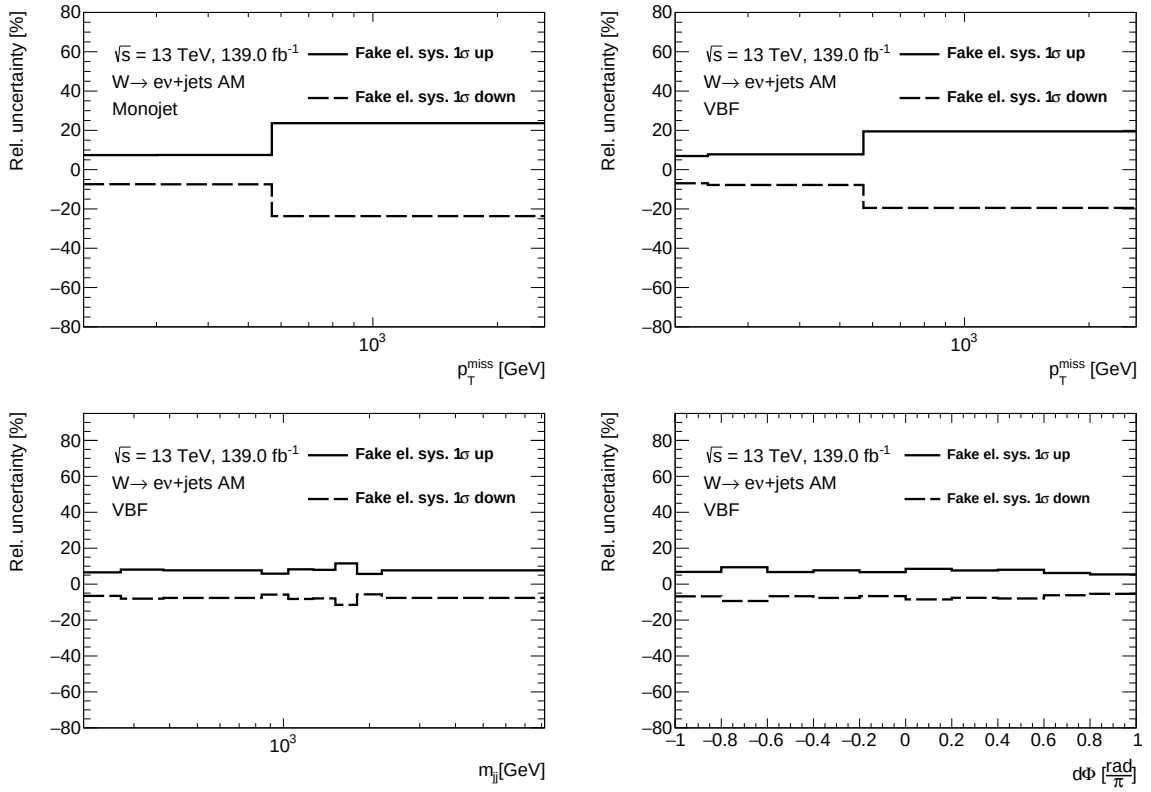

Figure B.18.: Relative uncertainty on the fake electron background estimate due to the fake efficiency as a function of $p_{\mathrm{T}}^{\mathrm{miss}}$ (top left) in the monojet phase space and $p_{\mathrm{T}}^{\mathrm{miss}}$ (top right), m_{jj} (bottom left) and $\Delta\phi_{jj}$ (bottom right) in the VBF phase space.

B.4.5. Additional Relative Systematic Uncertainty Distributions

This section shows additional relative systematic uncertainty distributions (Figure B.18).

C. Background Contributions due to Limited Detector Efficiency and Acceptance - Additional Studies and Figures

C.1. Relative $t\bar{t}$ Contribution

Figure C.1 shows the relative contribution of $t\bar{t}$ events to the total background due to top quark decays as a function of $p_{\mathrm{T}}^{\mathrm{miss}}$ in the monojet phase space in the SR, the $W \to e\nu$ + jets AM region and the $W \to \mu\nu$ + jets AM region.

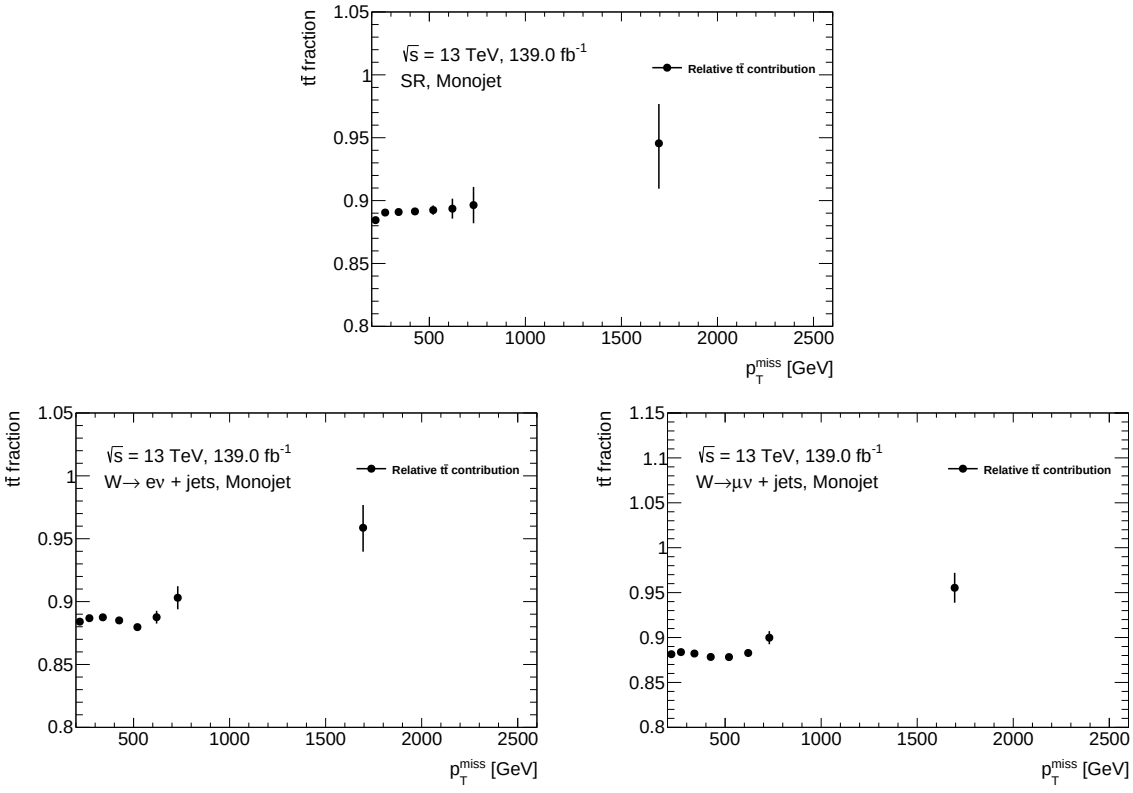

Figure C.1.: Relative contribution of $t\bar{t}$ events to the total *top* background as a function of $p_{\mathrm{T}}^{\mathrm{miss}}$ in the monojet phase space in the SR (top), the $W \to e\nu$ + jets AM region (bottom left) and the $W \to \mu\nu$ + jets AM region (bottom right).

C.2. Signal Region Backgrounds - Additional figures

C.2.1. Pre-fit plots

The comparison of data and MC simulation in the CRs is shown in Figure C.2 as a function of $p_{\mathrm{T}}^{\mathrm{miss,real}}$ in the VBF phase space, in Figure C.3 as a function of m_{jj} in the VBF phase space and in Figure C.4 as a function of $\Delta\phi_{jj}$ in the VBF phase space. The top panel of each plot shows the measured data (black points) and the MC simulation predictions. The bottom panel shows the ratio of data and the total prediction. The shaded bands show the experimental (red) and theoretical (blue) systematic uncertainties on the MC simulation. Good shape agreement and a constant normalisation offset is observed for the $W \to ev$ + jets CR (top left), $W \to \mu\nu$ + jets CR (top right) and $W \to \tau\nu$ + jets CR (bottom left)

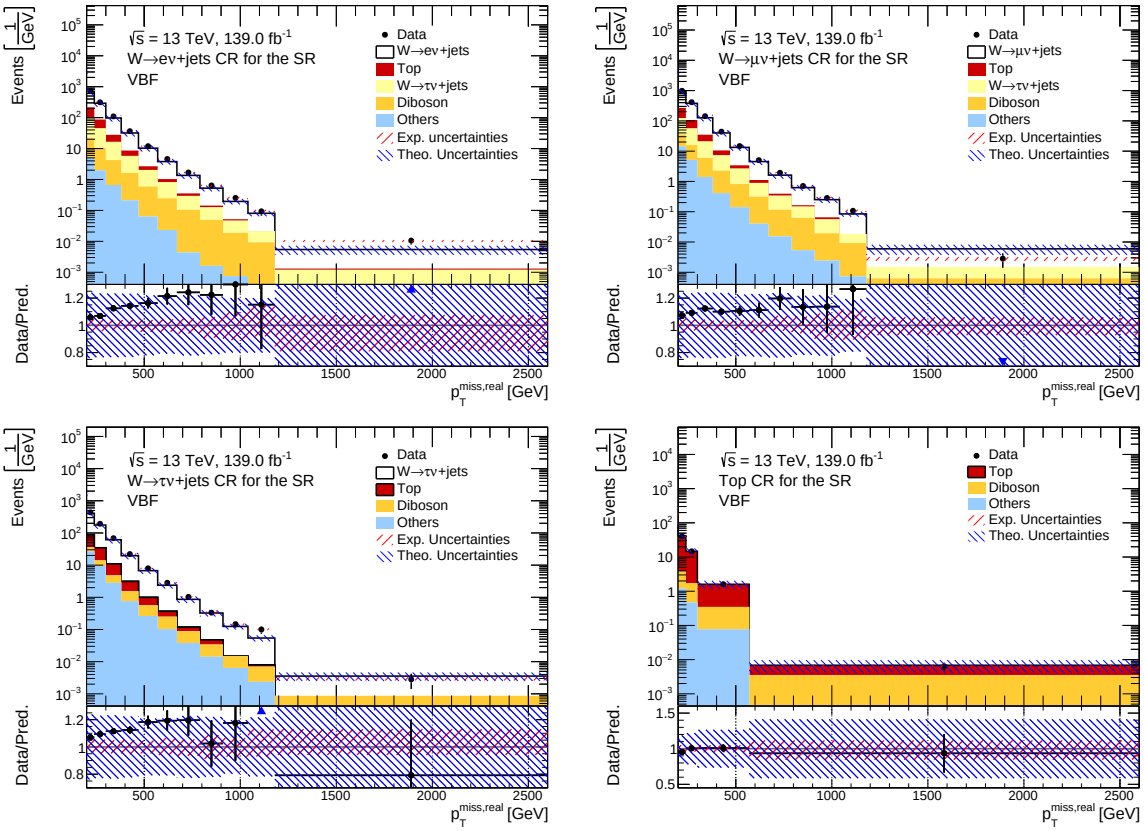

Figure C.2.: Comparison of data and MC simulation in the CRs used to constrain and validate the dominant backgrounds as a function of $p_{\mathrm{T}}^{\mathrm{miss,real}}$ in the SR in the VBF phase space. The bands show the experimental (red) and theoretical (blue) systematic uncertainties. The black error bars show the combined statistical uncertainty on the data and the MC simulation. Top left panel: $W \to ev$ + jets CR, top right panel: $W \to \mu\nu$ + jets CR, bottom left panel: $W \to \tau\nu$ + jets CR, bottom right panel: top CR.

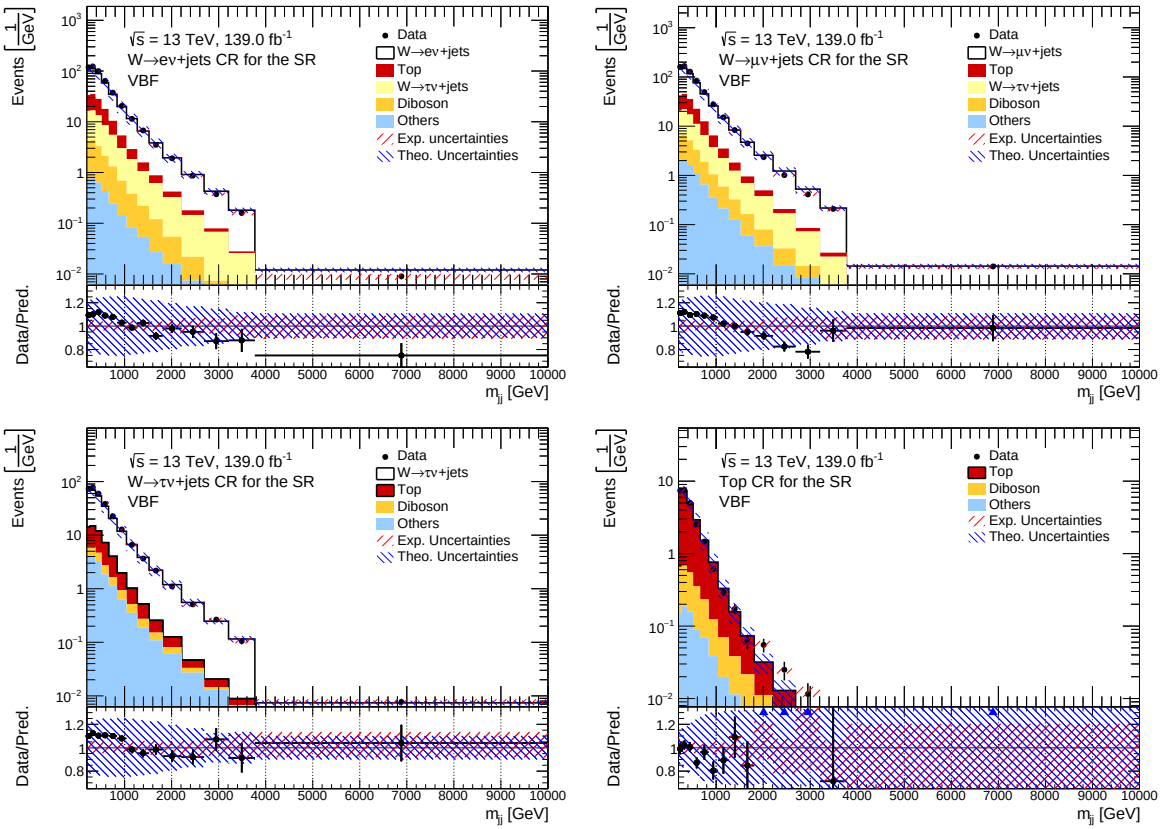

Figure C.3.: Comparison of data and MC simulation in the CRs used to constrain and validate the dominant backgrounds as a function of m_{jj} in the SR in the VBF phase space. The bands show the experimental (red) and theoretical (blue) systematic uncertainties. The black error bars show the combined statistical uncertainty on the data and the MC simulation. Top left panel: $W \to e\nu$ + jets CR, top right panel: $W \to \mu\nu$ + jets CR, bottom left panel: $W \to \tau\nu$ + jets CR, bottom right panel: top CR.

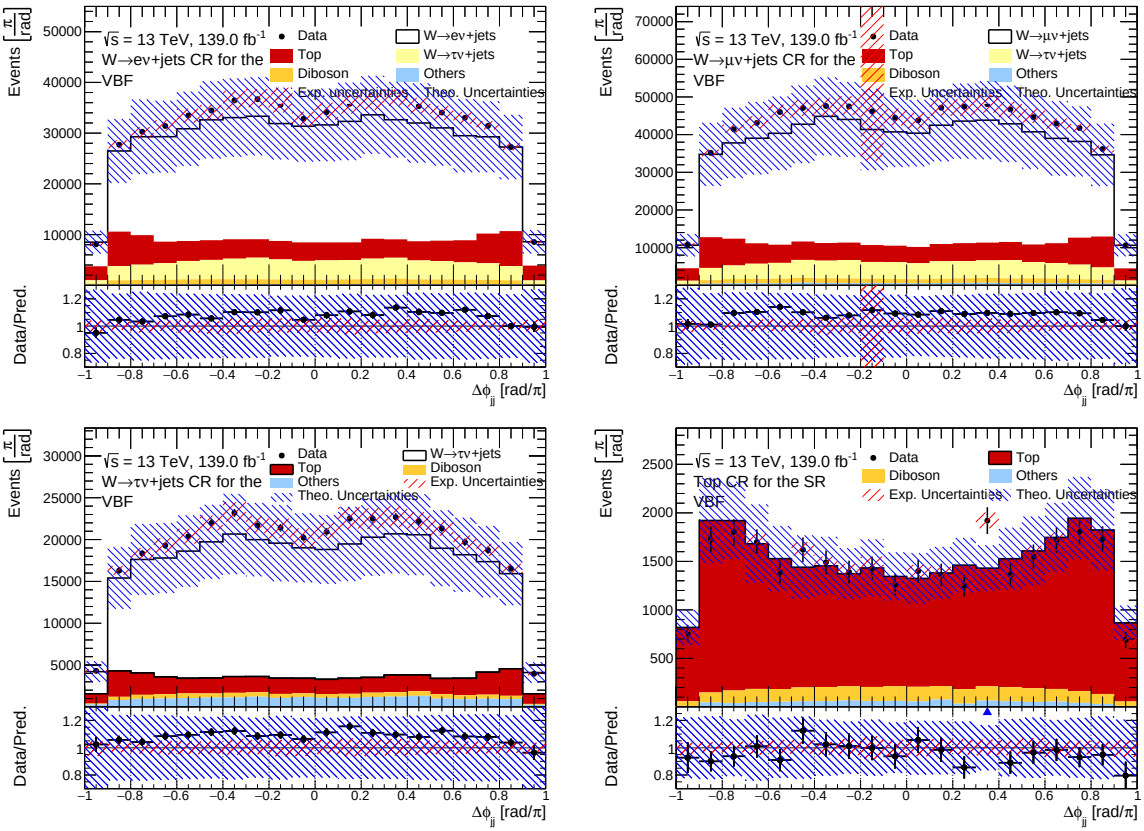

Figure C.4.: Comparison of data and MC simulation in the CRs used to constrain and validate the dominant backgrounds as a function of $\Delta\phi_{jj}$ in the SR in the VBF phase space. The bands show the experimental (red) and theoretical (blue) systematic uncertainties. The black error bars show the combined statistical uncertainty on the data and the MC simulation. Top left panel: $W \rightarrow e\nu$ + jets CR, top right panel: $W \rightarrow \mu\nu$ + jets CR, bottom left panel: $W \rightarrow \tau\nu$ + jets CR, bottom right panel: top CR.

C.2.2. Post-fit figure

The consistency of the normalisation factors k_X for the backgrounds in the VBF phase space is verified by comparing the agreement of data and the normalised MC simulation samples. This is shown in Figure C.5 as a function of $p_{\mathrm{T}}^{\mathrm{miss}}$, in Figure C.6 as a function of m_{jj} and in Figure C.7 as a function of $\Delta\phi_{jj}$ together with the systematic uncertainties.

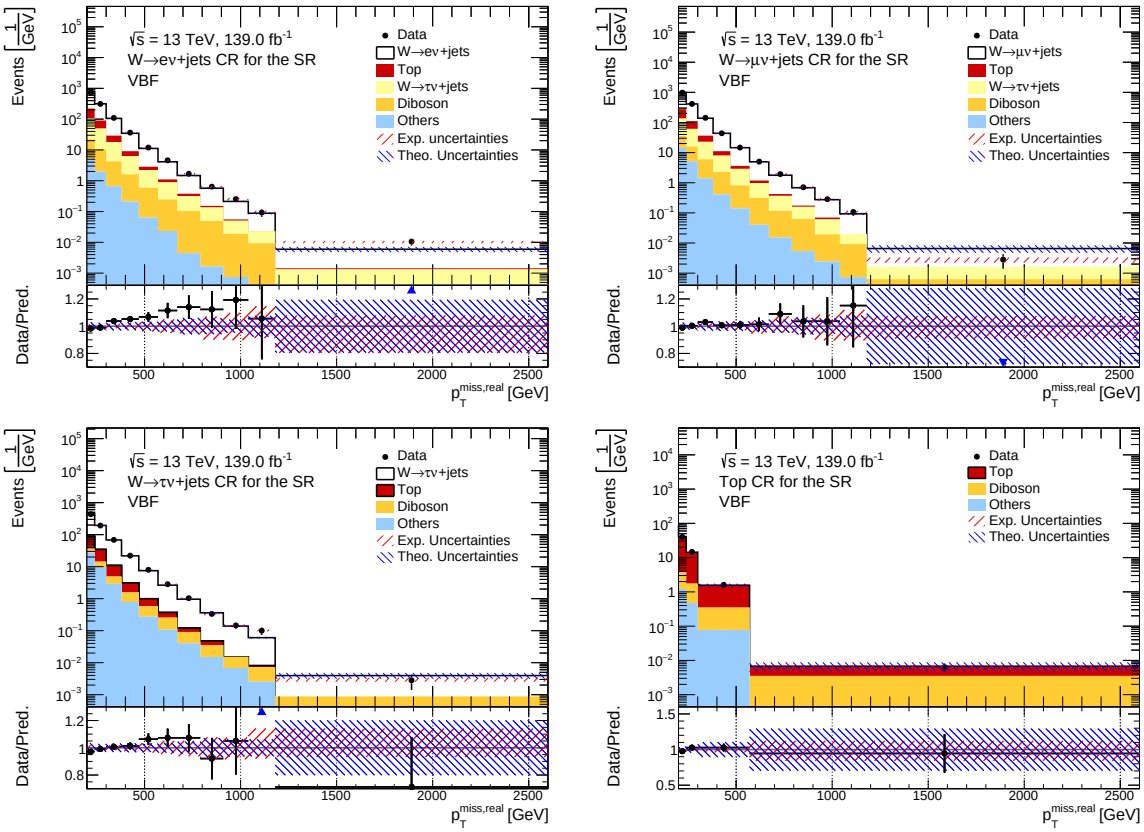

Figure C.5.: Comparison of data and MC simulation in the CRs used to constrain and validate the dominant backgrounds in the $p_{\mathrm{T}}^{\mathrm{miss}}$+jets region in the VBF phase space. The shaded bands show the systematic uncertainties on the theory predictions. Top left panel: $W \rightarrow e\nu$ + jets CR, top right panel: $W \rightarrow \mu\nu$ + jets CR, bottom left panel: $W \rightarrow \tau\nu$ + jets CR, bottom right panel: top CR.

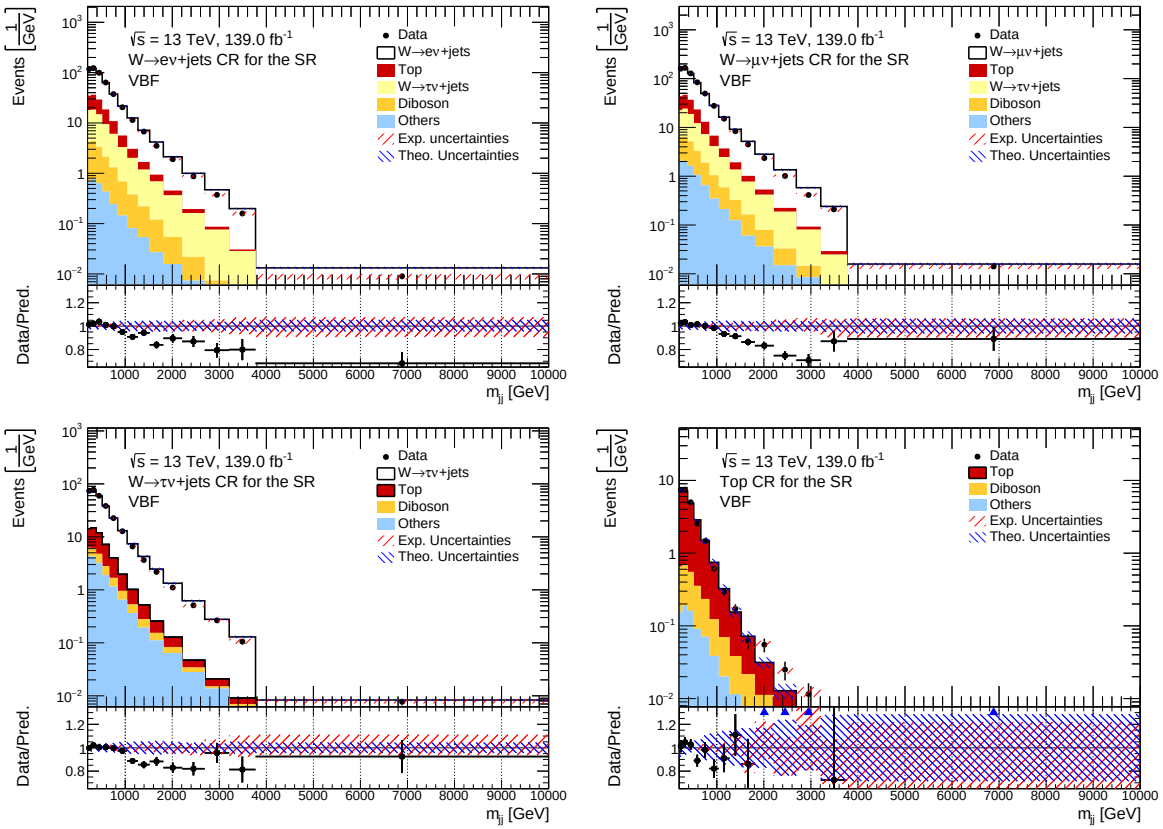

Figure C.6.: Comparison of data and MC simulation in the CRs used to constrain and validate the dominant backgrounds in the m_{jj} region in the VBF phase space. The shaded bands show the systematic uncertainties on the theory predictions. Top left panel: $W \rightarrow e\nu$ + jets CR, top right panel: $W \rightarrow \mu\nu$ + jets CR, bottom left panel: $W \rightarrow \tau\nu$ + jets CR, bottom right panel: top CR.

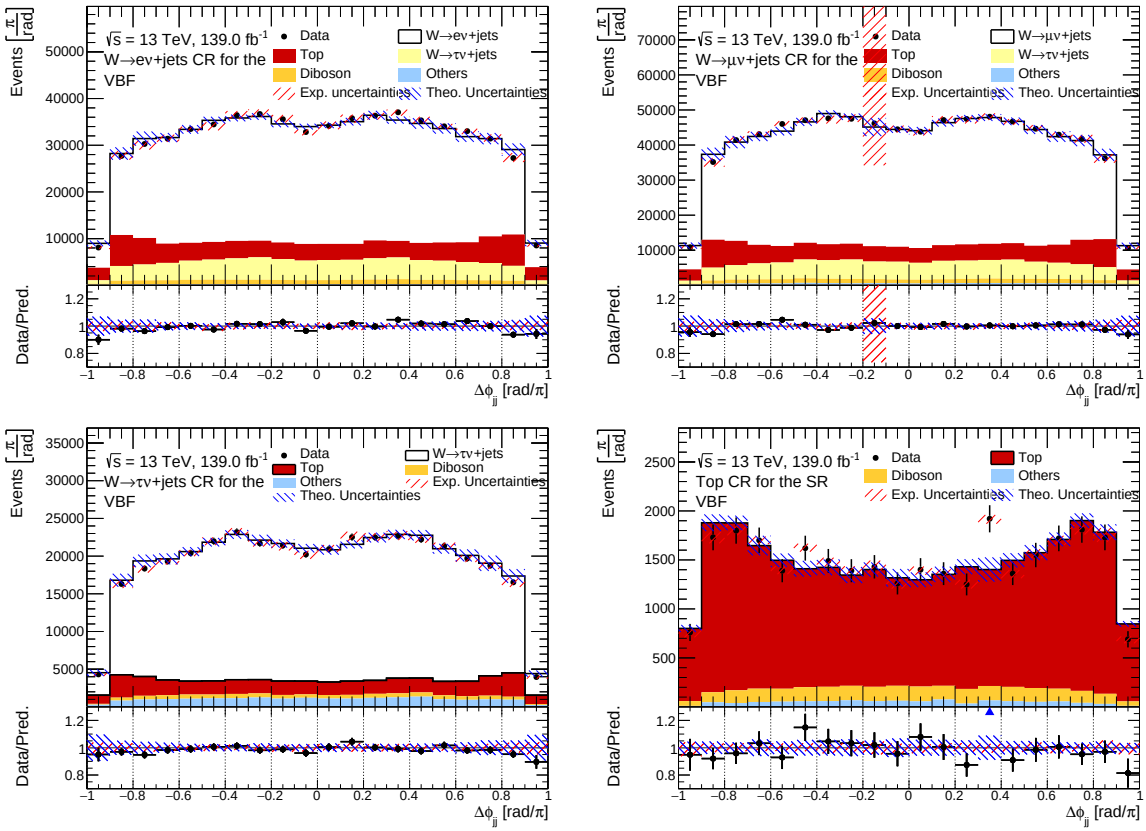

Figure C.7.: Comparison of data and MC simulation in the CRs used to constrain and validate the dominant backgrounds in the $\Delta\phi_{jj}$ region in the VBF phase space. The shaded bands show the systematic uncertainties on the theory predictions. Top left panel: $W \rightarrow e\nu$ + jets CR, top right panel: $W \rightarrow \mu\nu$ + jets CR, bottom left panel: $W \rightarrow \tau\nu$ + jets CR, bottom right panel: top CR.

C.3. Correlations Introduced by the Background Normalisation

The background subtraction procedure introduces correlations between the SR and the $W \to e\nu$ + jets AM and $W \to \mu\nu$ + jets AM regions. This happens because the $W \to e\nu$ + jets CR ($W \to \mu\nu$ + jets CR) and the $W \to e\nu$ + jets AM region ($W \to \mu\nu$ + jets AM region) are not orthogonal, but have overlapping event selections[1] and share events. The size and origin of these correlations is discussed in this section for the $W \to e\nu$ + jets CR as an example, the conclusions also hold for the $W \to \mu\nu$ + jets CR.

The correlation between the $p_{\mathrm{T}}^{\mathrm{miss}}$ distribution in $W \to e\nu$ + jets AM region and the $p_{\mathrm{T}}^{\mathrm{miss,real}}$ distribution in the $W \to e\nu$ + jets CR is calculated using the *bootstrap method* and shown in Figure C.9 for the monojet phase space. It is clearly visible by the shifted diagonal that both distributions are correlated. The shift is explained by the different definition of the observables, where $p_{\mathrm{T}}^{\mathrm{miss}}$ in the $W \to e\nu$ + jets AM region is calculated by adding the electron p_{T} to the $p_{\mathrm{T}}^{\mathrm{miss,real}}$. This typically leads to $p_{\mathrm{T}}^{\mathrm{miss}} > p_{\mathrm{T}}^{\mathrm{miss,real}}$ for a given event.

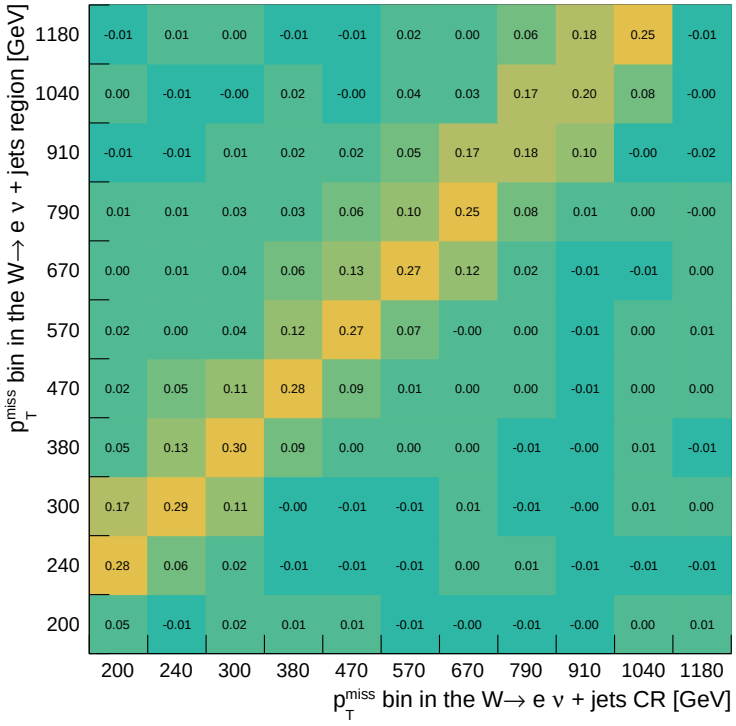

Figure C.8.: Correlation between $p_{\mathrm{T}}^{\mathrm{miss}}$ in the $W \to e\nu$ + jets AM region and $p_{\mathrm{T}}^{\mathrm{miss,real}}$ in the $W \to e\nu$ + jets CR. Lighter colours indication a higher degree of correlation.

[1] See Table 5.3 for the definition of the $W \to e\nu$ + jets AM region and Table 9.2 for the definition of the $W \to e\nu$ + jets CR.

This correlation with the $W \rightarrow e\nu$ + jets AM region also propagates to the background-subtracted data in the SR region via the normalization factors determined from the $W \rightarrow e\nu$ + jets CR. To understand the impact on the SR, the *bootstrap* method is used to determine the correlations between the background-subtracted data in the SR and background-subtracted data in the $W \rightarrow e\nu$ + jets AM region for the case where the backgrounds are not normalized with the k_X and the case where the normalization is applied. The result is shown in Figure C.9 for the $p_{\mathrm{T}}^{\mathrm{miss}}$ distribution in the monojet phase space. The top panel of Figure C.9 shows the correlation for the case of purely MC simulation based subtraction, without application of the normalization factors. As expected, no correlation is observed, since the SR and the $W \rightarrow e\nu$ + jets AM region are defined orthogonal. The bottom panel shows the correlation for the case of background subtraction where the MC samples have been scaled with normalization factors determined above. In this case a small anti-correlation is observed, mostly between $p_{\mathrm{T}}^{\mathrm{miss}}$ of 240 GeV and 470 GeV in the $W \rightarrow e\nu$ + jets AM region and $p_{\mathrm{T}}^{\mathrm{miss}}$ between 200 GeV and 670 GeV in the SR. The anti-correlation is caused by the fact that an increased number of correlated events in the $W \rightarrow e\nu$ + jets AM region, leads to a larger normalization factor. The larger normalization factor leads to the subtraction of more background and hence a reduced number of events in the SR. The localization of the anti-correlation can be understood as well. The value of the normalization factor is mostly determined by the first few bins of the $p_{\mathrm{T}}^{\mathrm{miss,real}}$ distribution in the $W \rightarrow e\nu$ + jets CR, since they have the highest statistics. This means that the normalization factor is correlated to these bins. As shown in Figure C.9, the lowest $p_{\mathrm{T}}^{\mathrm{miss}}$ bins in the $W \rightarrow e\nu$ + jets CR are correlated to the bins between 240 GeV and 470 GeV in $p_{\mathrm{T}}^{\mathrm{miss}}$ in the $W \rightarrow e\nu$ + jets AM region.

The correlation introduced by the background subtraction procedure between SR and the $W \rightarrow e\nu$ + jets AM ($W \rightarrow \mu\nu$ + jets AM) region are relatively small and are localized to a few bins. However they are fully taken into account, thanks to the *bootstrap* method, which is consistently used in all steps of the analysis.

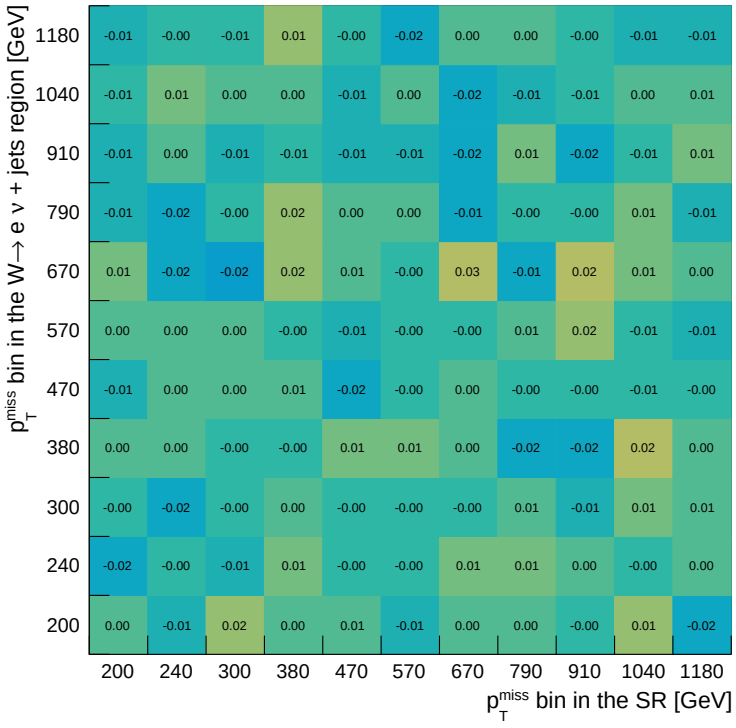

Figure C.9.: Correlation between $p_{\mathrm{T}}^{\mathrm{miss}}$ in the $W \rightarrow e\nu$ + jets AM region and $p_{\mathrm{T}}^{\mathrm{miss}}$ in the SR for background-subtracted data. Top panel: The normalization factors k_X are not applied to the MC simulation before the subtraction. Bottom panel: The normalization factors k_X are applied to the MC simulation before the subtraction.

D. Detector-level Modelling of the Measured Observables - Additional Figures

In this chapter the detector level comparison of the measured data and the different contributions from MC simulation and the background estimates is shown. Figure D.1 shows the $p_{\mathrm{T}}^{\mathrm{miss}}$ distribution in the monojet phase space. Figure D.2, Figure D.3 and Figure D.4 respectively show the $p_{\mathrm{T}}^{\mathrm{miss}}$, $\Delta\phi_{jj}$ and m_{jj} distributions in the VBF phase space.

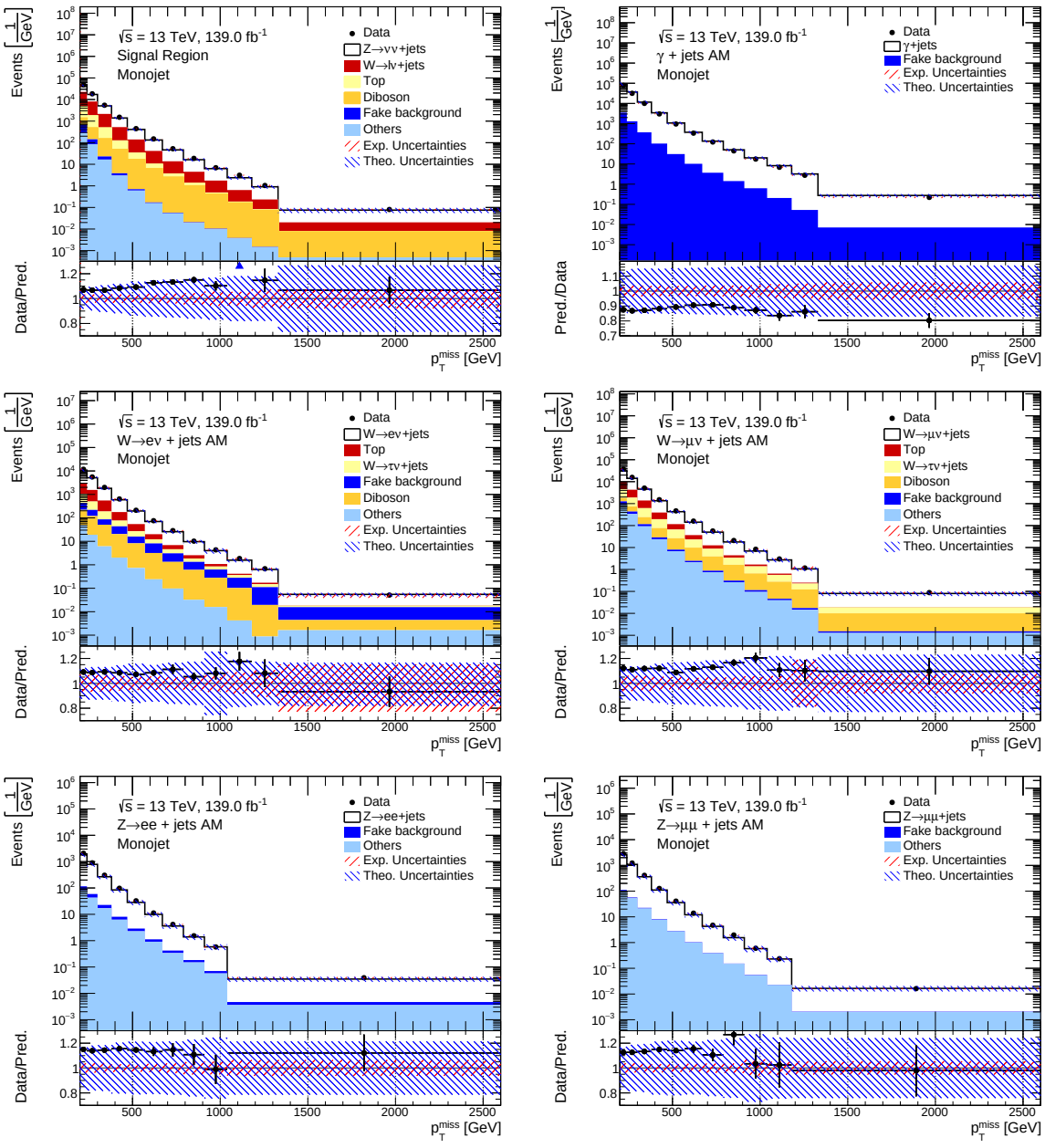

Figure D.1.: Comparison between data, the signal MC simulation, the data-constrained background MC simulation and the fake background estimates as a function of $p_{\mathrm{T}}^{\mathrm{miss}}$ in the monojet phase space in the SR (top left), the γ+jets AM region (top right), the $W \to e\nu$ + jets AM region (middle left), the $W \to \mu\nu$ + jets AM region (middle right), the $Z \to ee$ + jets AM region (bottom left) and the $Z \to \mu\mu$ + jets AM region (bottom right). The error bars include the statistical uncertainty on the data, the MC simulation and the fake background estimates. The experimental (grey) and theoretical (red) systematic uncertainties are shown as hashed bands.

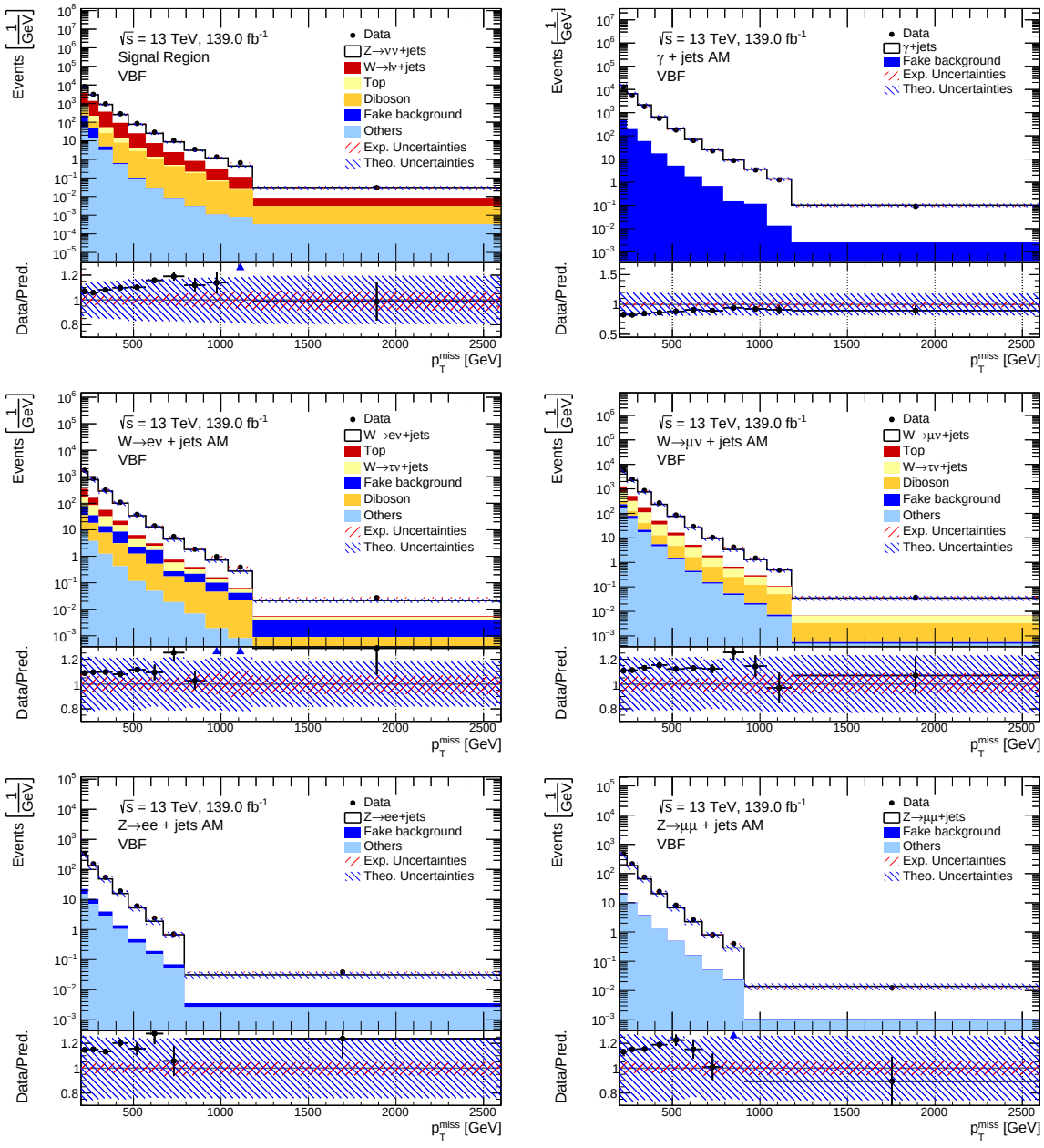

Figure D.2.: Comparison between data, the signal MC simulation, the data-constrained background MC simulation and the fake background estimates as a function of $p_{\mathrm{T}}^{\mathrm{miss}}$ in the VBF phase space in the SR (top left), the γ+jets AM region (top right), the $W \rightarrow e\nu$ + jets AM region (middle left), the $W \rightarrow \mu\nu$ + jets AM region (middle right), the $Z \rightarrow ee$ + jets AM region (bottom left) and the $Z \rightarrow \mu\mu$ + jets AM region (bottom right). The error bars include the statistical uncertainty on the data, the MC simulation and the fake background estimates. The experimental (grey) and theoretical (red) systematic uncertainties are shown as hashed bands.

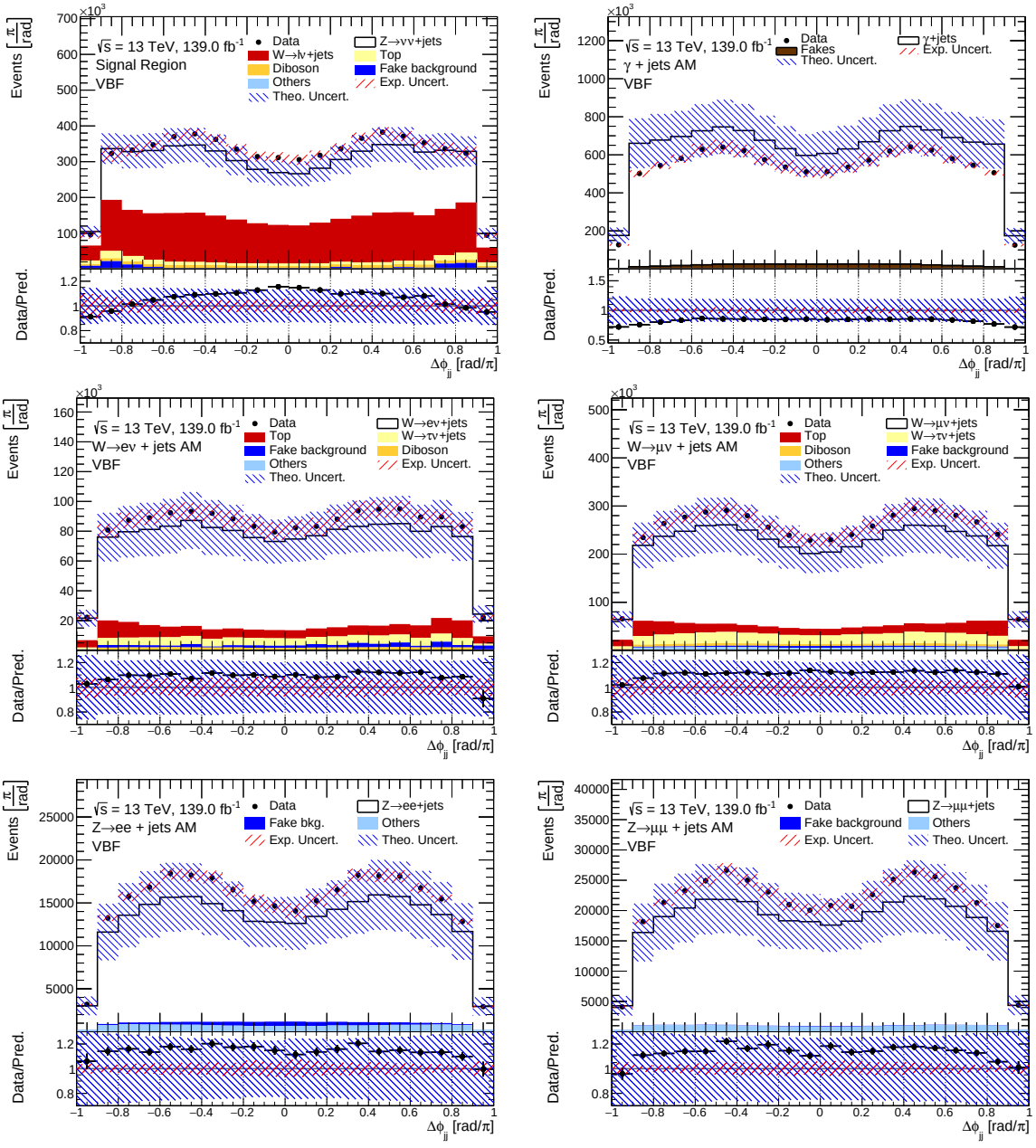

Figure D.3.: Comparison between data, the signal MC simulation, the data-constrained background MC simulation and the fake background estimates as a function of $\Delta\phi_{jj}$ in the VBF phase space in the SR (top left), the γ+jets AM region (top right), the $W \to e\nu$ + jets AM region (middle left), the $W \to \mu\nu$ + jets AM region (middle right), the $Z \to ee$ + jets AM region (bottom left) and the $Z \to \mu\mu$ + jets AM region (bottom right). The error bars include the statistical uncertainty on the data, the MC simulation and the fake background estimates. The experimental (grey) and theoretical (red) systematic uncertainties are shown as hashed bands.

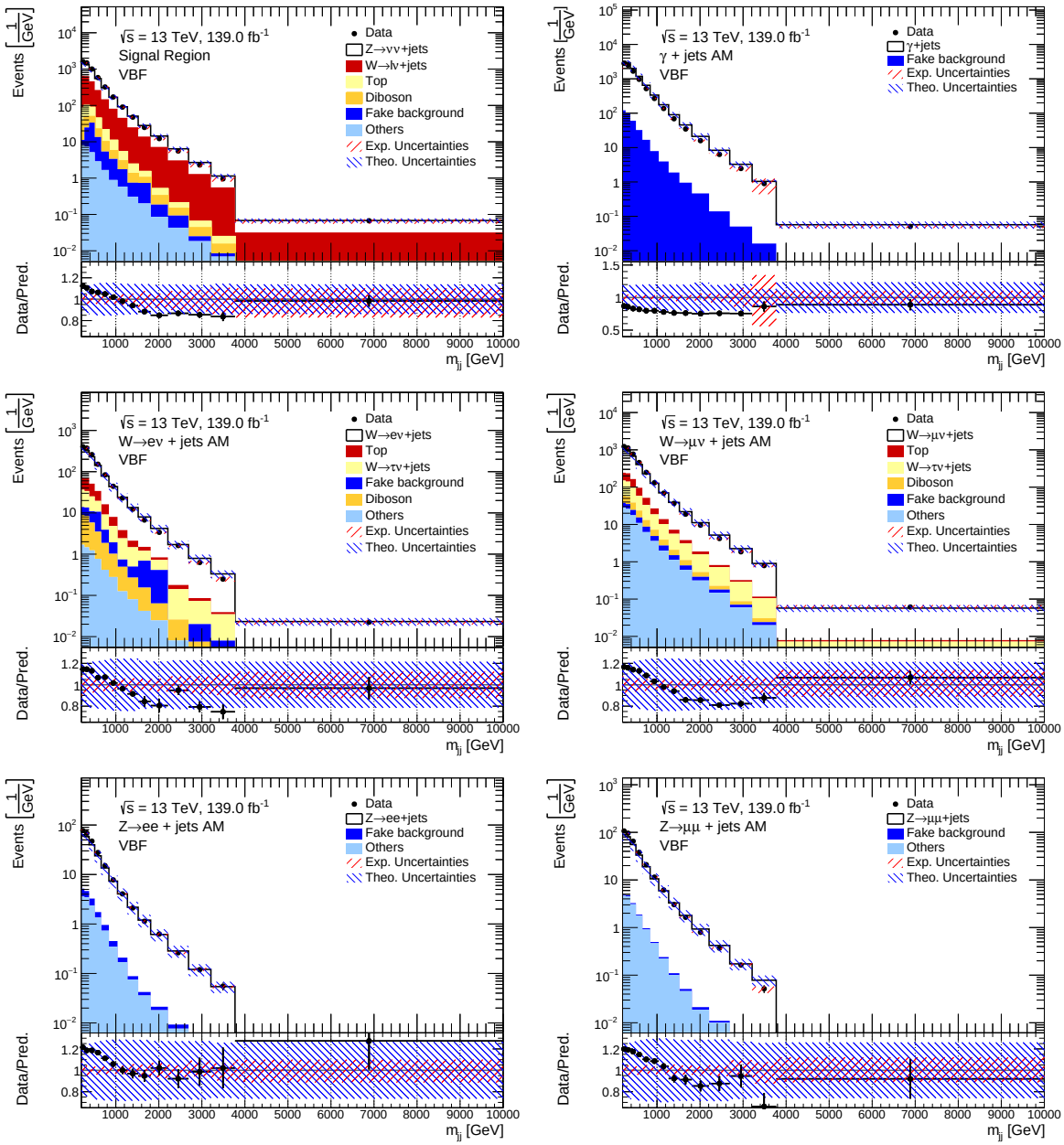

Figure D.4.: Comparison between data, the signal MC simulation, the data-constrained background MC simulation and the fake background estimates as a function of m_{jj} in the VBF phase space in the SR (top left), the γ+jets AM region (top right), the $W \rightarrow e\nu$ + jets AM region (middle left), the $W \rightarrow \mu\nu$ + jets AM region (middle right), the $Z \rightarrow ee$ + jets AM region (bottom left) and the $Z \rightarrow \mu\mu$ + jets AM region (bottom right). The error bars include the statistical uncertainty on the data, the MC simulation and the fake background estimates. The experimental (grey) and theoretical (red) systematic uncertainties are shown as hashed bands.

E. Additional Unfolding Studies

E.1. Detector Response Matrices

Figure E.1 shows example response matrices for the $p_{\mathrm{T}}^{\mathrm{miss}}$, the $\Delta\phi_{jj}$ and the m_{jj} distribution in the VBF phase space.

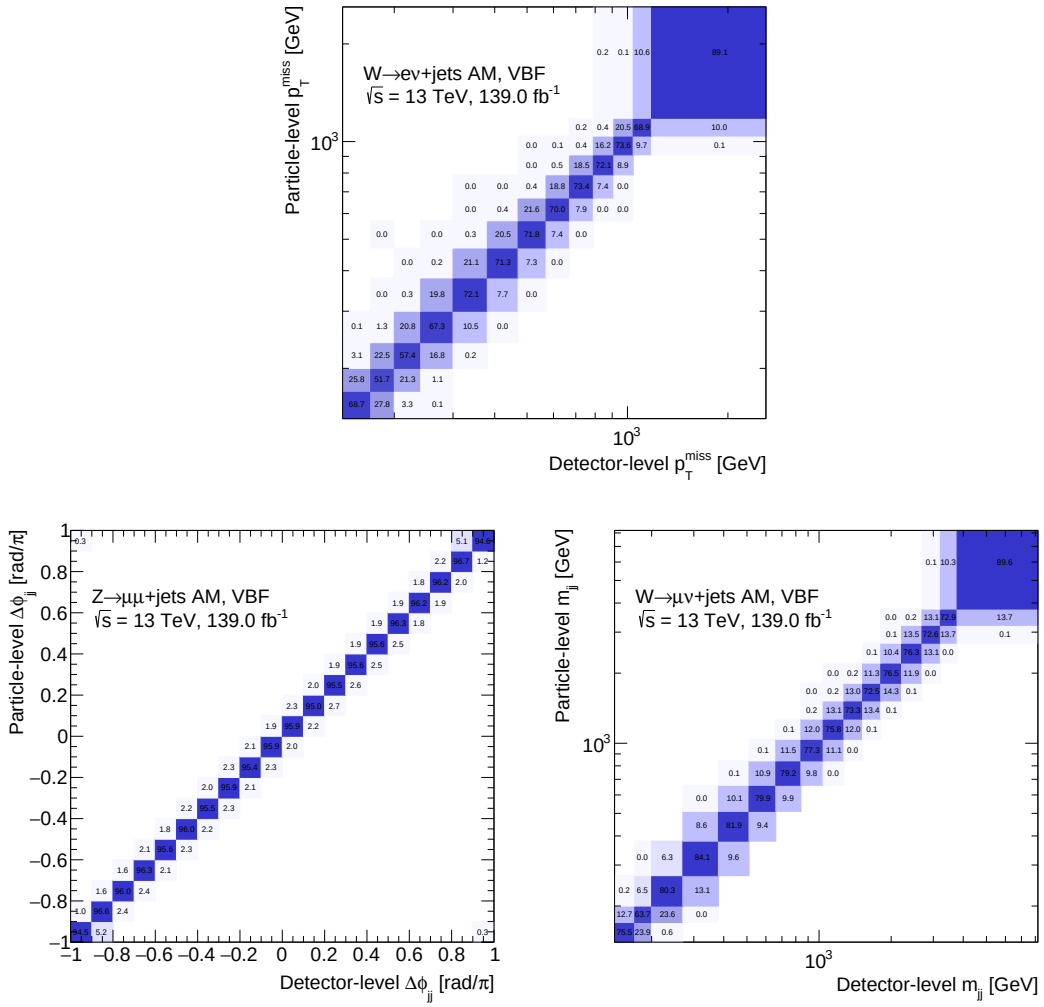

Figure E.1.: Examples for detector response matrices for the $p_{\mathrm{T}}^{\mathrm{miss}}$ distribution (top panel), the $\Delta\phi_{jj}$ distribution and the m_{jj} distribution in the VBF phase space.

E.2. Purity and Stability

Two important quantities of the response matrix $\underline{\underline{A}}$ that help to judge the amount of migrations are the purity and stability of matched events [1]. The purity is defined as the fraction of events in a bin on detector level that are in the same bin on particle level, or

$$\text{purity}_i = \frac{A_{ii}}{\sum_j Aij} \tag{E.1}$$

and allows to judge what fraction of events in a bin on detector level actually stem from the corresponding bin on particle level. $1 - \text{purity}_i$ gives the fraction of events migrating in from a neighbouring particle level bin.

The stability is defined as the fraction of events in a bin on particle level that are in the same bin on detector level

$$\text{stability}_i = \frac{A_{ii}}{\sum_i Aij} \tag{E.2}$$

and allows to judge what fraction of the events remains in a given particle level bin and what fraction migrates out, the latter being given by 1 − stability.

Figure E.2 shows the purity (top panel) and stability (bottom panel) for $p_{\mathrm{T}}^{\mathrm{miss}}$ in the monojet phase space in all regions. In general both the purity and stability are high (above 50 %) with decreasing values towards lower $p_{\mathrm{T}}^{\mathrm{miss}}$, where the binning of the distributions becomes finer, which leads to a slight increase in migrations. In all distributions jumps can be observed in the lowest bin, which are caused by the phase-space boundary. The underflow bins added for the unfolding process ensure that these jumps occur outside of the range of the measurement. Furthermore it is visible that the purities are very similar in all regions of the measurement. The reason for this is that the modelling of the boson p_{T} on particle level is very similar for all processes. The differences observed in the stability for the different processes is a direct consequence of the varying detector resolution for different particles in the final state.

[1] There are several ways to define the diagnostic quantities used to understand the unfolding procedure. The definitions chosen here try to separate the migration effects of the unfolding from the matching efficiency effects (discussed in section Section 11.2.2) to easier understand the impact of the two.

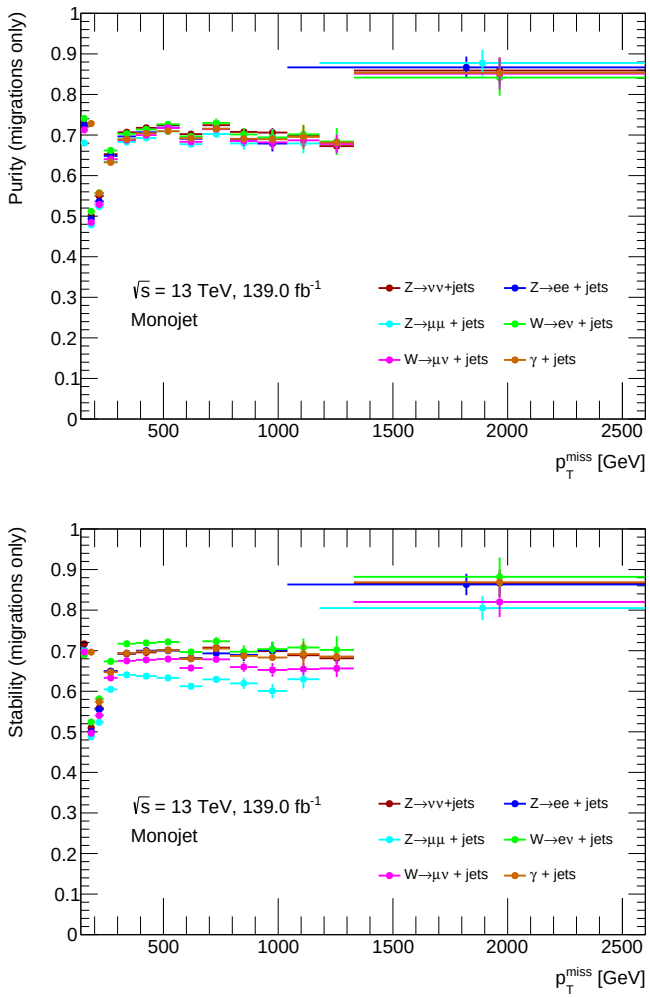

Figure E.2.: Purity (top panel) and stability (bottom panel) for $p_{\mathrm{T}}^{\mathrm{miss}}$ in the monojet phase space for the $Z \to \nu\nu$ + jets (dark red), $Z \to ee$ + jets (dark blue), $Z \to \mu\mu$ + jets (light blue), $W \to e\nu$ + jets (green), $W \to \mu\nu$ + jets (pink) and γ+jets AM (brown) regions.

E.3. Efficiency Distributions

Figure E.3 shows the unfolding efficiencies for all regions and distributions in the monojet and VBF phase spaces.

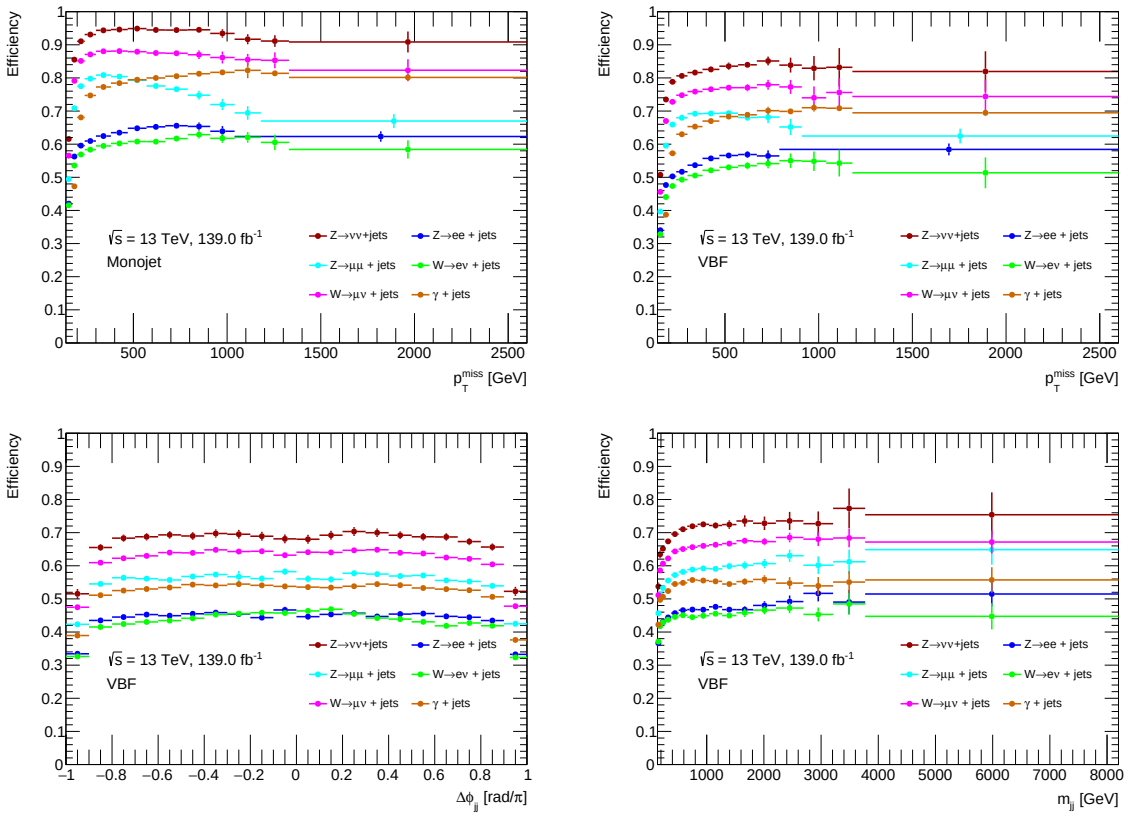

Figure E.3.: Efficiency distributions in all regions for $p_{\mathrm{T}}^{\mathrm{miss}}$ in the monojet phase space (top left), $p_{\mathrm{T}}^{\mathrm{miss}}$ in the VBF phase space (top right), $\Delta\phi_{jj}$ in the VBF phase space (bottom left), m_{jj} in the VBF phase space (bottom right).

E.3.1. Fake Fraction Distributions

Figure E.4 shows the unfolding fake fractions for all regions and distributions in the monojet and VBF phase spaces.

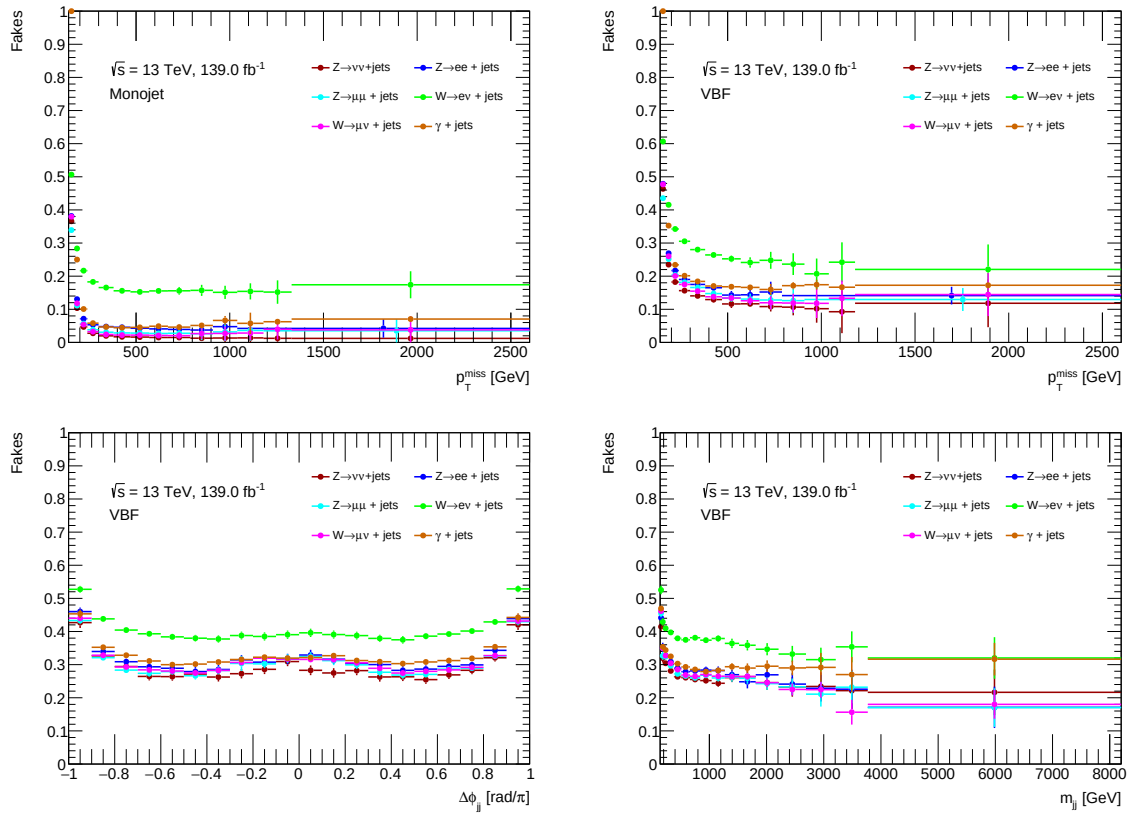

Figure E.4.: Fake fraction distributions in all regions for $p_{\mathrm{T}}^{\mathrm{miss}}$ in the monojet phase space (top left), $p_{\mathrm{T}}^{\mathrm{miss}}$ in the VBF phase space (top right), $\Delta\phi_{jj}$ in the VBF phase space (bottom left), m_{jj} in the VBF phase space (bottom right).

E.3.2. Bias due to Mismodelling of Hidden Observables

The hidden observable test is used to quantify the impact of observables that are not directly used in the unfolding, but could impact the unfolded result indirectly due to poor modelling. Examples for these hidden variables are the p_{T}, η and ϕ of jets and leptons.

The test is performed similar to the data-driven closure test discussed in the previous section. An alternative MC simulation sample is constructed for each hidden variable in each phase space, by reweighting the MC simulation event-by-event such that the agreement between data and MC simulation is close to perfect for the hidden variable. The reweighting functions are determined with the algorithm developed for the data-driven closure test. As an example the jet multiplicity distribution before (left) and after (right) reweighting is shown in Figure E.5. While there is a strong shape discrepancy in the unreweighted case the reweighted MC simulation shows good agreement with the efficiency-corrected data.

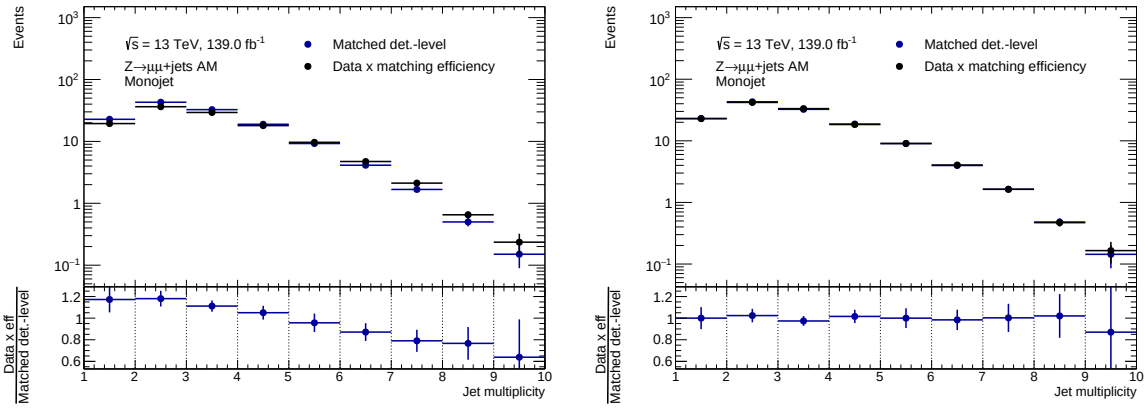

Figure E.5.: Comparisons between *matched* MC simulation and efficiency-corrected data the for jet multiplicity distribution in the monojet phase space in the $Z \to \mu\mu$ + jets AM region. The unreweighted MC simulation is shown in the left panels, the final reweighted MC simulation is shown in the right panels.

The alternative MC simulation sample is treated as pseudo-data and for each observable in the measurement the detector level spectrum determined from the pseudo-data is unfolded with the nominal MC simulation. The unfolded result is then compared to the particle level spectrum of the observable in pseudo-data. The major difference to the data-driven closure test, is that the observables are not directly reweighted, but indirectly via the hidden variables. Any deviations are treated as systematic uncertainties. The final systematic uncertainty for a given observable in a given region and phase space is constructed by symmetrizing the single uncertainties derived for each hidden variable and the summing them quadratically.

E.3.3. Signal injection Ttest

One goal of this measurement is to use the unfolded data to search for BSM physics. Therefore it is important to verify that the unfolding procedure has no major impact on potential signals of BSM physics that might be present in the measured data.

To verify that no bias is introduced on these BSM signals a signal injection test is performed[2]. The test is performed representatively in the SR and two different signals are injected.. For each signal pseudo-data is created by adding the detector spectrum of the BSM signal to the nominal SM signal MC simulation sample ($Z \to \nu\nu$ + jets) in the SR. Figure E.6 shows the nominal SM signal MC simulation sample plus the injected BSM signal (blue) together with the nominal SM signal alone (black) for the $p_{\mathrm{T}}^{\mathrm{miss}}$ distribution in the monojet phase space. The bottom part of each panel shows the ratio of the two. Each test signal exhibits different features. While the pseudo-scalar mediator DM model *DMP* (left panel) is distributed over the bulk of the distribution, the *DMA* model signal (right panel) are more

[2]This is non-trivial, since the BSM signal can not be accounted for when constructing the migration matrix and the efficiency and fake corrections.

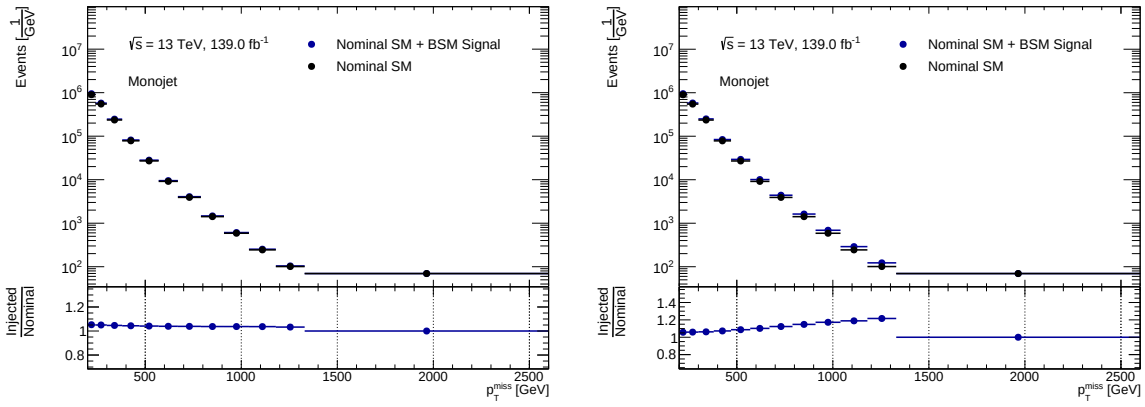

Figure E.6.: Comparison of the detector level distributions of the nominal SM signal plus the BSM signal (blue) and the BSM signal alone (black) in SR in the monojet phase space. Left panel: pseudo-scalar model with $m = 1\,\text{GeV}$ and $m_\text{P} = 50\,\text{GeV}$. Right panel: axial-vector model with $m = 1\,\text{GeV}$ and $m_\text{A} = 700\,\text{GeV}$.

prominent in the tail. The *DMA* model signal point has been chosen such that it has a very large signal contribution as an example for an extreme signal case.

The impact of the injected signals is tested by unfolding the pseudo-data (nominal SM signal + BSM signal) with the nominal signal MC alone. The unfolded distribution is then compared to the particle level distribution of the pseudo-data. The results of the comparison are shown in Figure E.7. For the *DMP* model a negligible bias of $< 0.5\,\%$ is observed, for the extreme signal case of the *DMA* model a slightly larger bias is observed, which still is below $< 2.0\,\%$. However, if a signal of the size of the *DMA* model point chosen here would be observed on detector level in data, the analysis strategy would be modified accordingly to account for the discovery of BSM physics. For a more realistic case like the *DMP* model, the impact of the unfolding on a potential signal is negligible.

E.3.4. Additional reweighted distributions of the data-driven closure test

Figure E.8 shows two more examples of reweighted distributions. The top panels show the agreement between the *matched* MC simulation and the efficiency-corrected data before (left) and after (right) the reweighting for the $\Delta\phi_{jj}$ distribution in the VBF phase space in the $W \to ev$ + jets AM region. The bottom panels show the same for the p_T^miss distribution in the monojet phase space in the $Z \to ee$ + jets AM region. In all cases good agreement is observed after the reweighting. Please note that discrepancies in a few bins are acceptable, since no perfect agreement is necessary to perform the data-driven closure test.

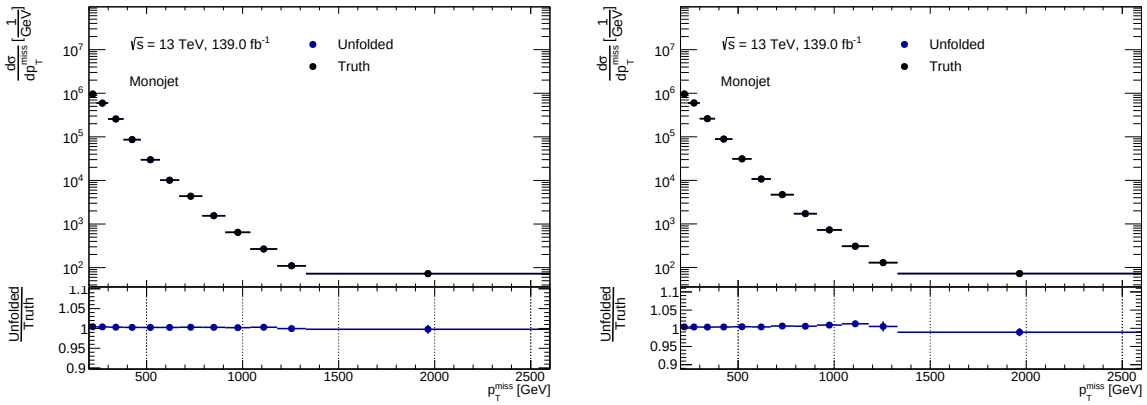

Figure E.7.: Comparison of the unfolded pseudo-data distributions (nominal SM signal plus BSM signal) in blue with the particle level pseudo-data distribution in black. Left panel: pseudo-scalar model with $m_\chi = 1\,\text{GeV}$ and $m_\text{P} = 50\,\text{GeV}$. Right panel: axial-vector model with $m_\chi = 1\,\text{GeV}$ and $m_\text{A} = 700\,\text{GeV}$.

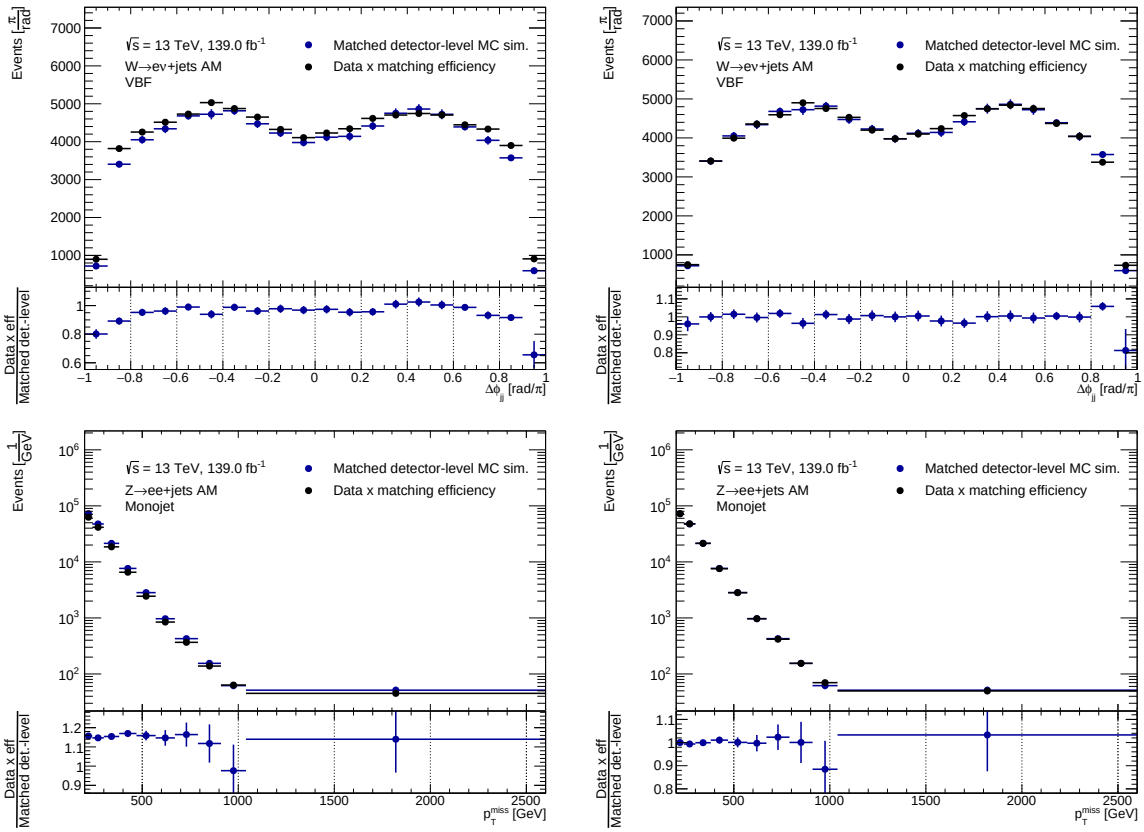

Figure E.8.: Comparisons between *matched* MC simulation and efficiency-corrected data for $\Delta\phi_{jj}$ in the VBF phase space in the $W \to e\nu$ + jets AM region (top panels) and $p_{\mathrm{T}}^{\mathrm{miss}}$ in the monojet phase space in the $Z \to ee$ + jets AM region (bottom panels). The unreweighted MC simulation is shown in the left panels, the final reweighted MC simulation is shown in the right panels.

F. Measured Differential Cross Sections

This chapter shows all measured differential cross sections. Figure F.1 shows the differential cross sections as a function of the boson p_{T} in the monojet phase space. Figure F.2, Figure F.4 and Figure F.3 show the differential cross sections as a function of the boson p_{T}, m_{jj} and $\Delta\phi_{jj}$ in the VBF phase space.

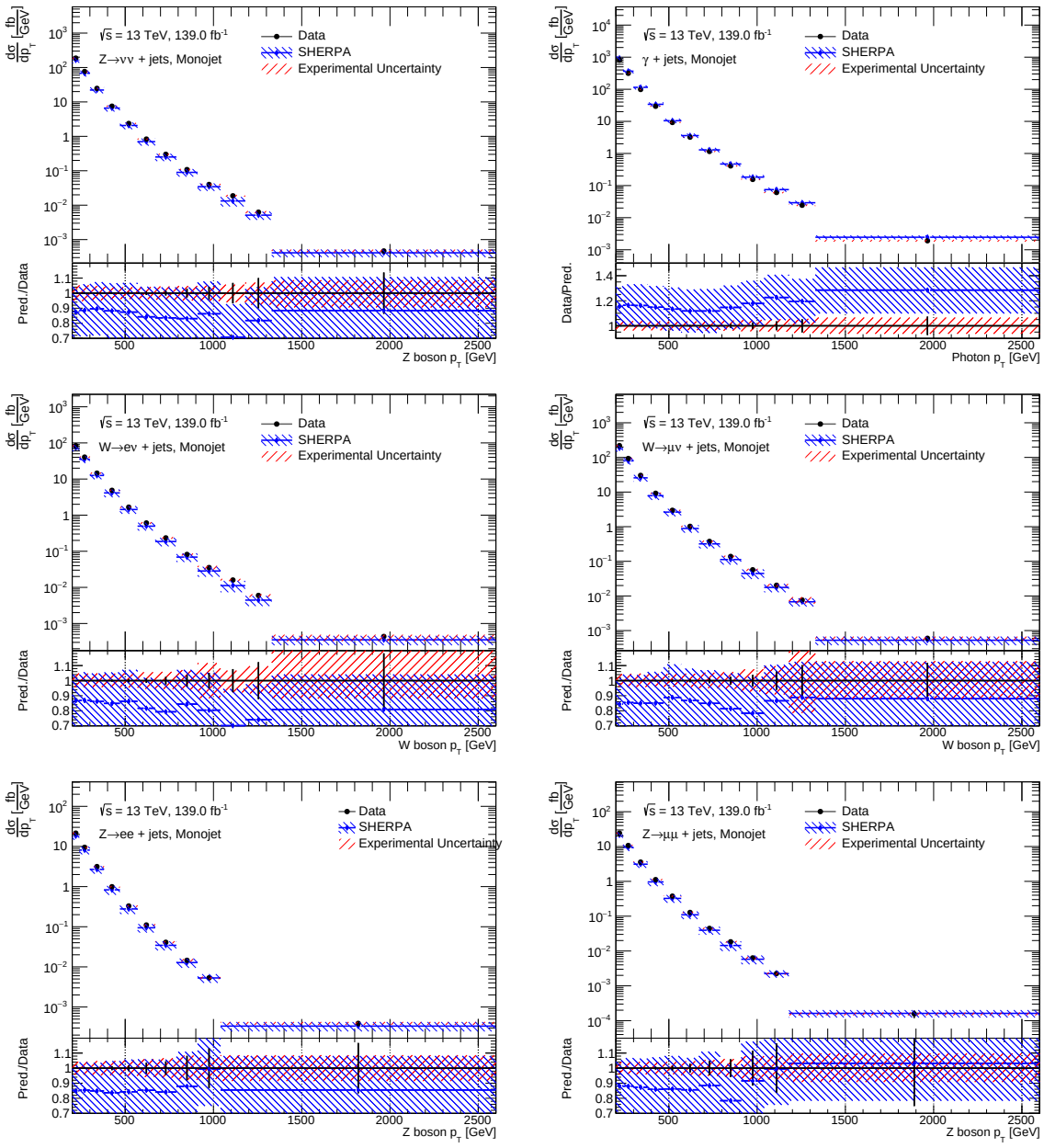

Figure F.1.: Differential cross sections as a function of the boson p_{T} in the monojet phase space for the $Z \to \nu\nu$ + jets (top left), the γ + jets (top right), the $W \to e\nu$ + jets (middle left), the $W \to \mu\nu$ + jets (middle right), the $Z \to ee$ + jets (bottom left) and the $Z \to \mu\mu$ + jets (bottom right) final states. The cross sections predicted by SHERPA are shown in blue. The statistical uncertainty on the cross section (black) and the prediction (blue) is shown as error bars on the respective points. The experimental (red) and theoretical (blue) systematic uncertainties are shown as hashed bands.

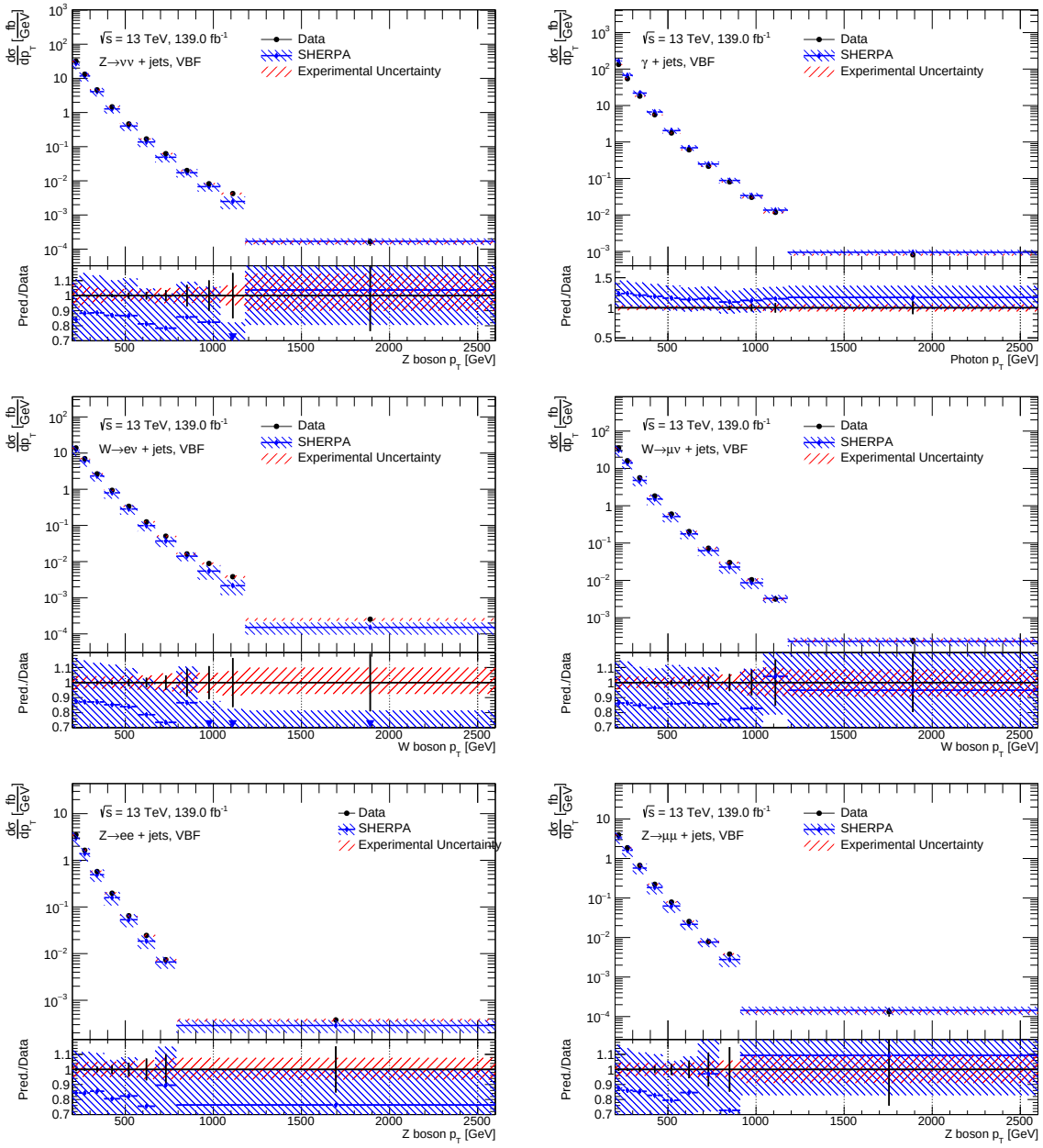

Figure F.2.: Differential cross sections as a function of the boson p_{T} in the VBF phase space for the $Z \to \nu\nu$ + jets (top left), the γ + jets (top right), the $W \to e\nu$ + jets (middle left), the $W \to \mu\nu$ + jets (middle right), the $Z \to ee$ + jets (bottom left) and the $Z \to \mu\mu$ + jets (bottom right) final states. The cross sections predicted by SHERPA are shown in blue. The statistical uncertainty on the cross section (black) and the prediction (blue) is shown as error bars on the respective points. The experimental (red) and theoretical (blue) systematic uncertainties are shown as hashed bands.

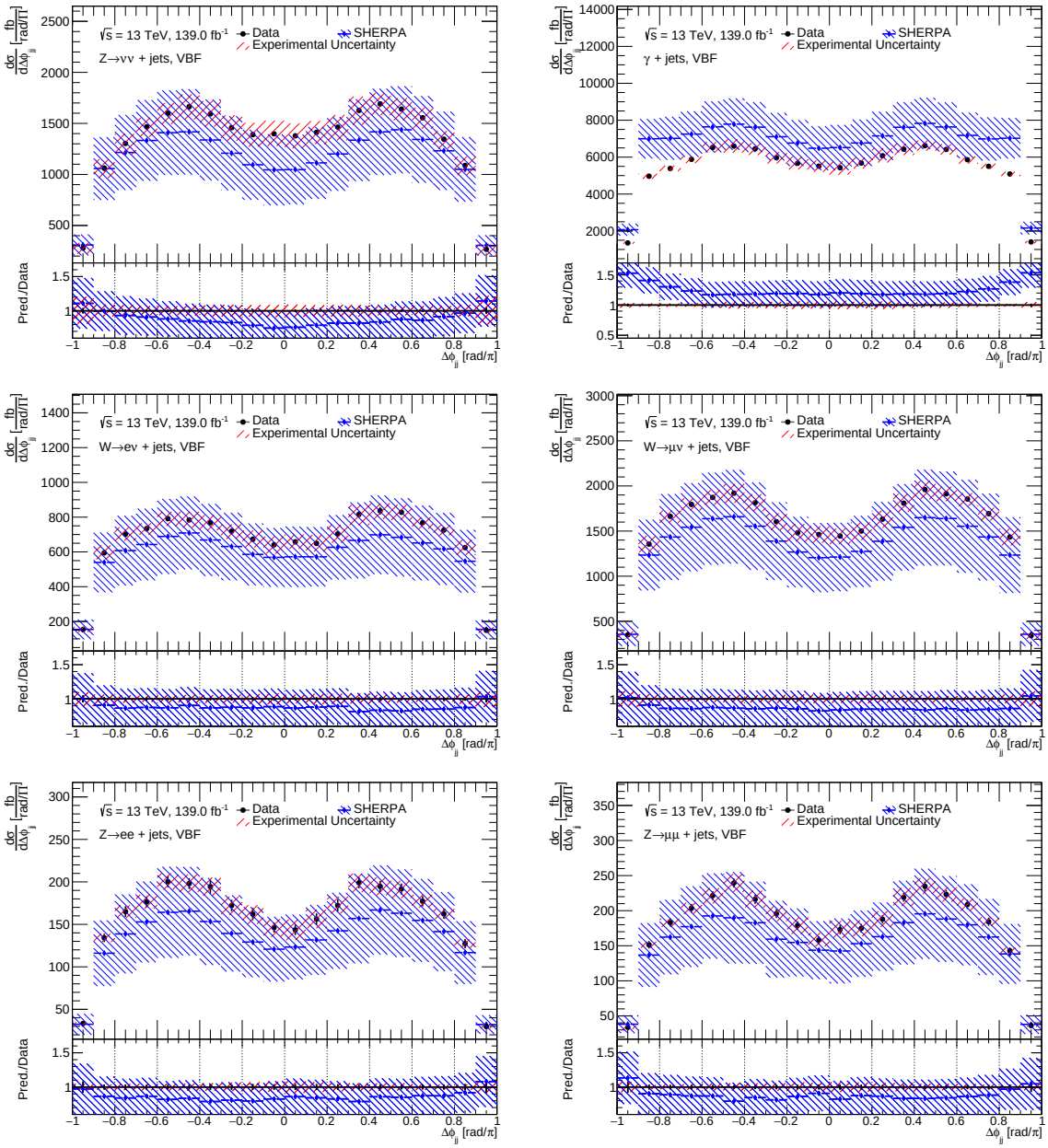

Figure F.3.: Differential cross sections as a function of $\Delta\phi_{jj}$ in the VBF phase space for the $Z \to \nu\nu$ + jets (top left), the γ + jets (top right), the $W \to e\nu$ + jets (middle left), the $W \to \mu\nu$ + jets (middle right), the $Z \to ee$ + jets (bottom left) and the $Z \to \mu\mu$ + jets (bottom right) final states. The cross sections predicted by SHERPA are shown in blue. The statistical uncertainty on the cross section (black) and the prediction (blue) is shown as error bars on the respective points. The experimental (red) and theoretical (blue) systematic uncertainties are shown as hashed bands.

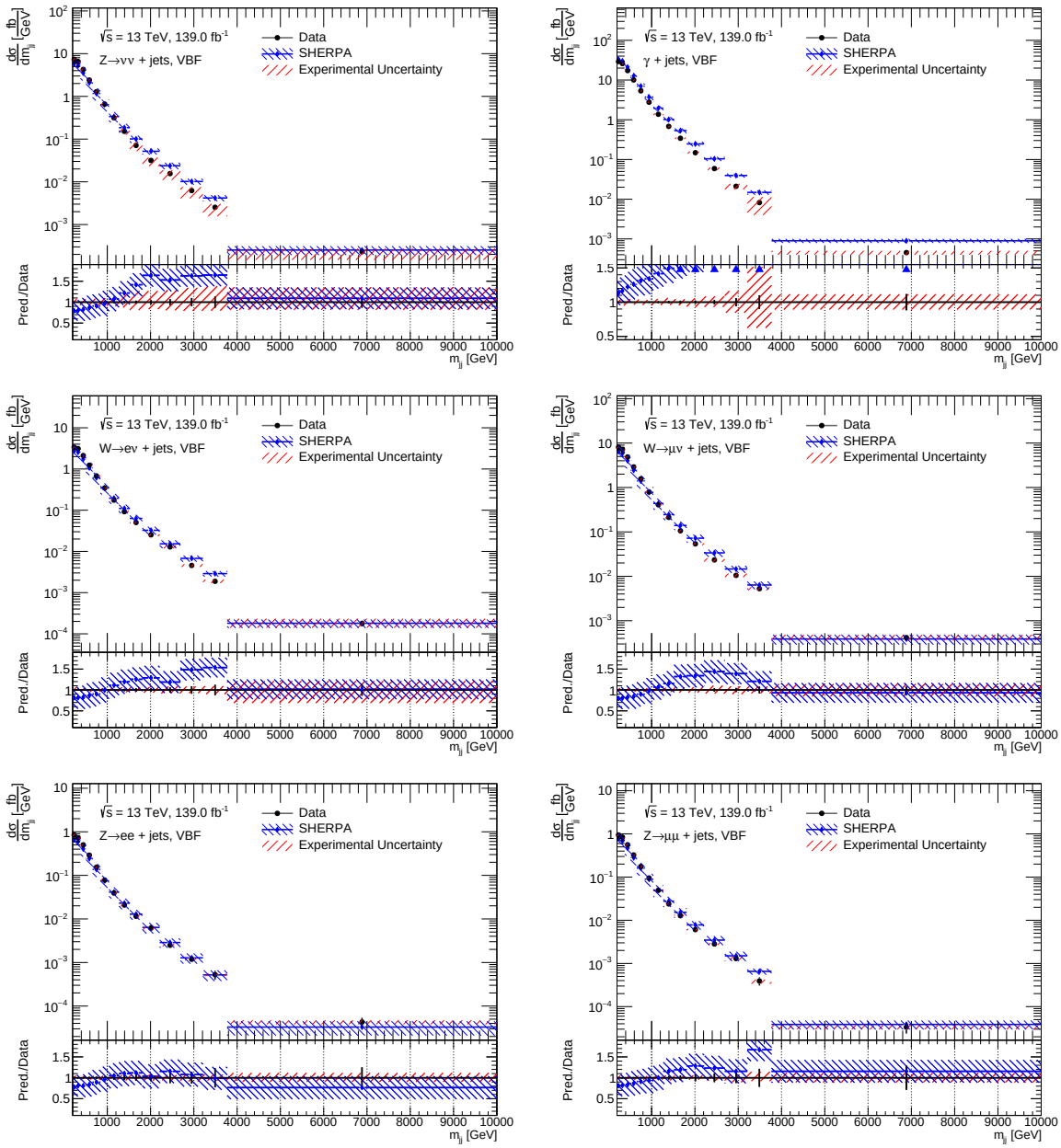

Figure F.4.: Differential cross sections as a function of m_{jj} in the VBF phase space for the $Z \to \nu\nu$ + jets (top left), the γ + jets (top right), the $W \to e\nu$ + jets (middle left), the $W \to \mu\nu$ + jets (middle right), the $Z \to ee$ + jets (bottom left) and the $Z \to \mu\mu$ + jets (bottom right) final states. The cross sections predicted by SHERPA are shown in blue. The statistical uncertainty on the cross section (black) and the prediction (blue) is shown as error bars on the respective points. The experimental (red) and theoretical (blue) systematic uncertainties are shown as hashed bands.

G. The Bootstrap Method

Statistical inference is a central part of this analysis and physics measurements in general. However in the context of a particle physics measurement exact methods are often difficult to employ, since the *probability density function* (PDF) are typically very complex or not known. Examples for this are the correlation between two measurements of the same physics process in different *phase space* regions, the determination of meaningful statistical uncertainties on experimental systematic uncertainties or the determination of statistical uncertainties and correlations between different bins of the measurement after detector-correcting the measured data.

Bootstrapping[149] is a simple and powerful resampling technique that adresses this problem and allows to make inferences directly from the measured data or MC simulation, with large computing power needed as the main cost. It is based on the *empirical distribution function* and the *plug-in principle*. This chapter gives a brief introduction to *bootstrapping* closely following [150] and [136], where more detailed information can be found.

G.1. The Empirical Distribution Function and the Plug-in Principle

Following [150] if the underlying PDF F of a random sample $\underline{x} = (x_1, x_2, \dots, x_n)$ of size n is not known, it can be estimated by the *empirical distribution function* $\hat{F}$.

$\hat{F}$ is defined as the distribution that assigns a probability of $\frac{1}{n}$ to each of the x_i. Thus an "empirical probability" for an x_i to occur is given by

$$P_{\hat{F}}(x_i) = \frac{\#x_i}{n}. \tag{G.1}$$

The *plug-in principle* states that a parameter $\theta = t(F)$ of the underlying PDF F can be estimated using the *empirical distribution function* $\hat{F}$ as

$$\hat{\theta} = t\left(\hat{F}\right). \tag{G.2}$$

Typically the result of Equation G.2 is only useful if it is possible to also determine the standard error $se_{\hat{F}}(\theta)$. While formulas exist for some simple statistics (e.g. the sample mean), their derivation can become very complex for more complicated cases. Calculating the standard error is one very important use-case of *Bootstrapping* [150].

G.2. Estimating the Standard Error using the Bootstrap Method

The first step of the *Bootstrapping* algorithm described in [150] is to resample the original random sample $\underline{x}$ by drawing n times from the *empirical distribution function* $\hat{F}$ function. This creates a *bootstrap replica* [1]

$$\underline{x^*} = \left(x_1^*, x_2^*, \ldots, x_n^*\right). \tag{G.3}$$

Note that this sampling corresponds to *drawing with replacement*, so a given x_i can appear once, several times or not at all in $\underline{x^*}$. This process is repeated to create in total B replica. The second step is to evaluate the parameter $\hat{\theta} = t\left(\hat{F}\right)$ for each bootstrap replica, giving B bootstrapped parameters $\left(\hat{\theta}_1^*, \hat{\theta}_2^*, \ldots, \hat{\theta}_B^*\right)$. In a third step the bootstrap estimate of the standard error $se_{\hat{F}}(\theta)$ is calculated as the sample standard deviation of the $\hat{\theta}_j^*$ determined from the bootstrap replica using the *plug-in principle*

$$se_{\hat{F}}(\theta) = \left\{\sum_{b=1}^{B}\left[\hat{\theta}_b^* - \bar{\hat{\theta}}^*\right]^2 / (B-1)\right\}^{\frac{1}{2}}. \tag{G.4}$$

This means that we have replaced the potentially difficult calculation of $se_{\hat{F}}(\theta)$ using mathematical means, by raw computing power to perform the calculation of $\hat{\theta}*$ many times over the independently fluctuated bootstrap replica and then use the simple calculation of the standard deviation to get an estimate of $se_{\hat{F}}(\theta)$ [150]. This is called the *non-parametric bootstrap*, since only the *empirical distribution function* is used to draw the bootstrap replica. The algorithm is demonstrated for a simple toy example in the following section.

Typically the bootstrap estimate of the standard error has only a small bias and a small standard deviation, given a large enough number of bootstrap replica B [150]. The necessary size of B is problem dependent and needs to be investigated case-by-case. In this measurement, depending on the use-case and the available computation power for the given problem, 100 to 10 000 bootstrap replica are used.

G.2.1. Simple Example: Standard Error of the Mean

A simple example is given in this section to illustrate the estimate of the standard error of the mean using bootstrapping. The sample F with unknown underlying PDF is shown in the top left panel of Figure G.1. The analytically calculated values of the mean and its error (3.66 ± 0.32) are also given.

The associated empirical distribution function $\hat{F}$ is used to create 500 bootstrap replica. One example is shown in the top right panel of Figure G.1, together with the mean calculated for this particular bootstrap replica.

To obtain the error of the mean of F, the mean is calculated for each bootstrap replica. The distribution of means is shown in the bottom panel of Figure G.1. The root-mean-square

[1] The notation deviates from [150] here.

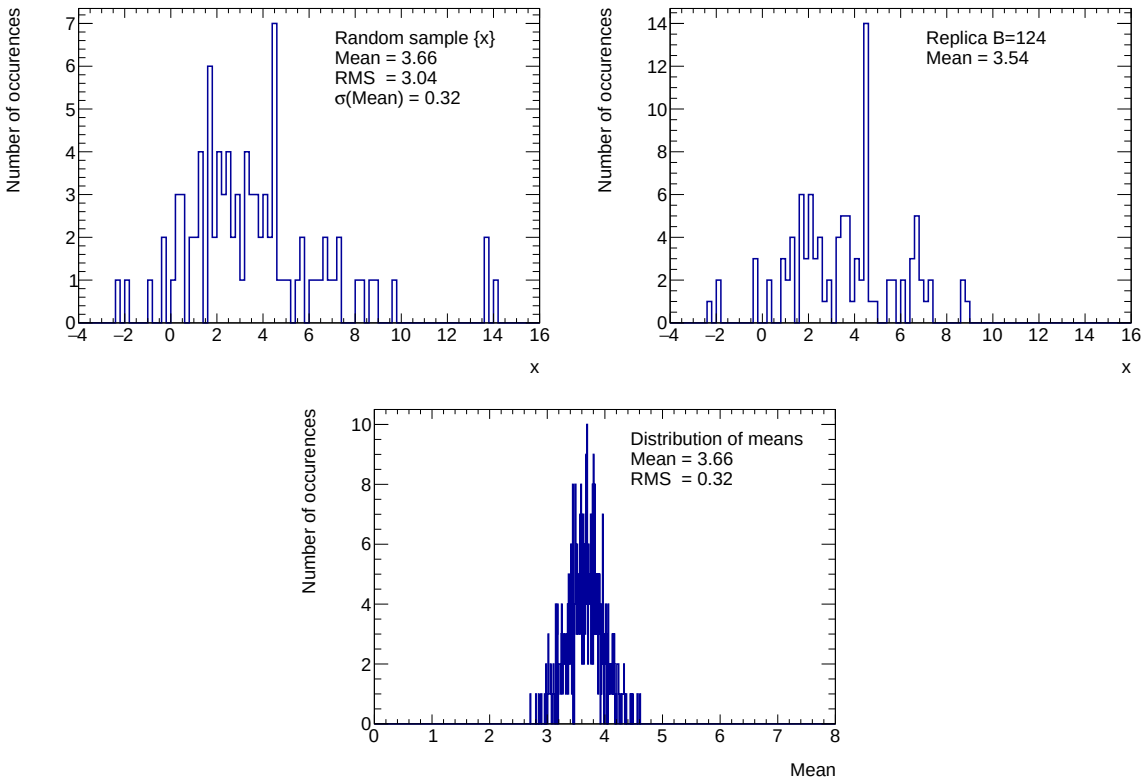

Figure G.1.: Top left: Sample F with unknown underlying PDF. Top right: Bootstrap replica number 124. Bottom: Distribution of the means of all 500 bootstrap replicas.

(RMS) of this distribution is used to estimate the standard error of the mean. The result if the bootstrap estimate (3.66 ± 0.32) agrees with the analytic calculation.

This example, while trivial, demonstrates the power of the bootstrap: The calculation of the error of a quantity is replaced by many calculations of the quantity and the calculation of the RMS.

G.3. Bootstrap Implementation used in this Measurement

While the examples given so far assumed no previous knowledge on the underlying PDF F, for a counting experiment, such as this analysis, it is known that the events in a given bin follow a *Poissonian* distribution. This allows for a refined version of *bootstrapping*, the so-called *parametric* bootstrap, presented in the following.

The idea behind the *parametric* bootstrap is to resample the underlying PDF F instead of the *empirical distribution function* $\hat{F}$ when creating the bootstrap replica. This is achieved by creating B empty replica $(R_1, R_2, \dots, R_B)$ of each *nominal* histogram that is to be bootstrapped. For each event with event weight w that is filled in the *nominal* histogram B bootstrap weights $(wb_1, wb_2, \dots, wb_B)$, one for each bootstrap replica histogram are randomly drawn from a Poissonian

$$P(k, \mu) = \frac{\mu^k}{k!} e^{-\mu} \rightarrow (wb_1, wb_2, \dots, wb_B) \tag{G.5}$$

with mean $\mu = 1$. Then the replica histograms are filled with the nominal event weight w times the bootstrap weight (R_n is filled with $w \times wb_n$ for $n \in (1, \dots, B)$). The mean of $\mu = 1$ ensures that each event is filled once on average. Note that this bootstrapping "on-the-fly" is equivalent to bootstrapping the fully filled nominal histogram, since for a Poissonian $P(k, N)$ (corresponding to a bin with bin content N) it holds [78] that

$$P(k, \mu) \sim \sum_N P(k, 1)\,. \tag{G.6}$$

The "on-the-fly" sampling has the advantage that the random number generator used to draw the wb_n can be re-initialized for each event with the corresponding run and event number (and the unique dataset ID in case of MC simulation). In this way each event is assigned a unique set of Poisson weights that are always used whenever the event is filled into the bootstrap replicas of a given histogram. This is is a powerful tool to correctly evaluate even complex statistical correlations between bootstrapped histograms that share some or all of their events, since the shared events will have the same statistical fluctuations in all bootstrapped histograms. This is accomplished using the bootstrapping code given in [78].

In practice bootstrap histograms are created for every observable measured in any region of the analysis, including all control regions, both in data and MC simulation. Then these bootstraps are propagated through the whole analysis chain, allowing to correctly track all statistical correlations and to properly include all source of statistical uncertainty along the chain.

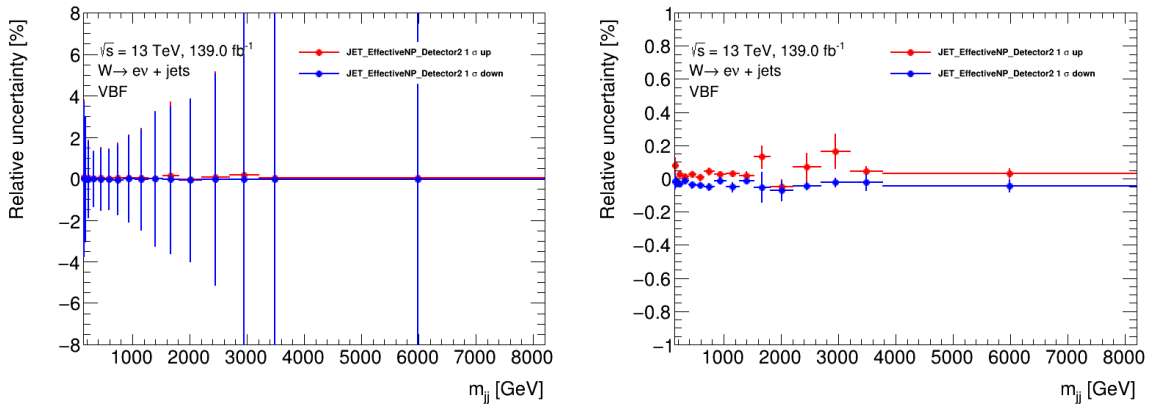

Figure G.2.: Relative systematic uncertainty for m_{jj} in the VBF phase space in the $W \rightarrow e\nu$ + jets AM region. Left panel: No statistical correlations are taken into account. Right panel: Statistical correlations taken into account with the bootstrap method.

An advanced example of this is given in the next section, where it is demonstrated how *bootstrapping* can be used to determine the statistical precision of systematic uncertainties.

G.3.1. Advanced Example: Statistical Errors on Systematic Uncertainties

The propagation of a Gaussian systematic uncertainty, e.g. on the energy scale of jets, to a measured observable, typically consists of shifting the affected quantity, e.g. the jet p_{T}, by $\pm 1\sigma$ and recalculating the observable with the shifted jet p_{T}. This leads to a shifted observable, where some events have migrated into other bins, due to the systematic variation. The shift in the observable is typically quantified by the relative systematic uncertainty, which is calculated by dividing the shifted distribution by the nominal distribution.

For many applications it is necessary to determine the statistical uncertainty on the relative systematic uncertainty, since it is not a priori clear, if the observed shift is due to the systematic variation or due to a statistical fluctuation in the event sample used to determine it. This is however not trivial, since the shifted and the nominal spectrum are statistically correlated and the correlations must be taken into account.

Bootstrapping is used to determine this statistical uncertainty and to properly take the correlations into account. This is achieved by performing the division of the shifted histogram by the nominal histogram replica-by-replica, thereby creating a new bootstrapped ratio histogram. From this the final relative systematic uncertainty is calculated by calculating the average and RMS over all bootstrap replica in each bin and assigning the average as the central value and the RMS as the statistical uncertainty. The result is shown in Figure G.2. The left panel show the relative systematic uncertainty calculated without taking the statistical correlations into account and the right panel show the fully bootstrapped version of the same quantity.

Bibliography

[1] Léo Morel et al. "Determination of the fine-structure constant with an accuracy of 81 parts per trillion". In: *Nature* 588.7836 (2020), pp. 61–65. ISSN: 1476-4687. DOI: 10.1038/s41586-020-2964-7. URL: https://doi.org/10.1038/s41586-020-2964-7.

[2] Philip Sommer. *Probing the Electroweak Sector with Vector-boson Fusion and Vector-boson Scattering Processes at the LHC*. Tech. rep. Geneva: CERN, 2022. URL: https://cds.cern.ch/record/2799207.

[3] Andy Buckley et al. "General-purpose event generators for LHC physics". In: *Physics Reports* 504.5 (July 2011), pp. 145–233. DOI: 10.1016/j.physrep.2011.03.005. URL: https://doi.org/10.1016%2Fj.physrep.2011.03.005.

[4] Giorgio Arcadi, Abdelhak Djouadi, and Martti Raidal. "Dark Matter through the Higgs portal". In: *Physics Reports* 842 (Feb. 2020), pp. 1–180. DOI: 10.1016/j.physrep.2019.11.003. URL: https://doi.org/10.1016%2Fj.physrep.2019.11.003.

[5] Florian U. Bernlochner et al. "Angles on CP-violation in Higgs boson interactions". In: *Physics Letters B* 790 (2019), pp. 372–379. ISSN: 0370-2693. DOI: https://doi.org/10.1016/j.physletb.2019.01.043. URL: https://www.sciencedirect.com/science/article/pii/S0370269319300590.

[6] Enrico Bothmann et al. "Event generation with Sherpa 2.2". In: *SciPost Phys.* 7.3 (2019), p. 034. DOI: 10.21468/SciPostPhys.7.3.034. arXiv: 1905.09127 [hep-ph].

[7] The ATLAS Collaboration. "Cross-section measurements for the production of a Z boson in association with high-transverse-momentum jets in pp collisions at $\sqrt{s} = 13$ TeV with the ATLAS detector". In: (2022). DOI: 10.48550/ARXIV.2205.02597. URL: https://arxiv.org/abs/2205.02597.

[8] Georges Aad et al. "Differential cross-section measurements for the electroweak production of dijets in association with a Z boson in proton–proton collisions at ATLAS". In: *Eur. Phys. J. C* 81.2 (2021), p. 163. DOI: 10.1140/epjc/s10052-020-08734-w. arXiv: 2006.15458 [hep-ex].

[9] Georges Aad et al. "Measurement of the inclusive cross-section for the production of jets in association with a Z boson in proton-proton collisions at 8 TeV using the ATLAS detector". In: *Eur. Phys. J. C* 79.10 (2019), p. 847. DOI: 10.1140/epjc/s10052-019-7321-3. arXiv: 1907.06728 [hep-ex].

[10] Morad Aaboud et al. "Measurement of detector-corrected observables sensitive to the anomalous production of events with jets and large missing transverse momentum in pp collisions at $\sqrt{s} = 13$ TeV using the ATLAS detector". In: *Eur. Phys. J. C* 77.11 (2017), p. 765. DOI: 10.1140/epjc/s10052-017-5315-6. arXiv: 1707.03263 [hep-ex].

[11] M. Aaboud et al. "Measurement of differential cross sections and W+/W− cross-section ratios for W boson production in association with jets at $\sqrt{s}$ = 8TeV with the ATLAS detector". In: *Journal of High Energy Physics* 2018.5 (2018), p. 77. ISSN: 1029-8479. DOI: 10.1007/JHEP05(2018)077. URL: https://doi.org/10.1007/JHEP05(2018)077.

[12] The ATLAS Collaboration. *QCD analysis of ATLAS $W^{\pm}$ boson production data in association with jets*. Tech. rep. Geneva: CERN, 2019. URL: http://cds.cern.ch/record/2670662.

[13] Georges Aad et al. "Measurement of isolated-photon plus two-jet production in pp collisions at $\sqrt{s}$ = 13 TeV with the ATLAS detector". In: *JHEP* 03 (2020), p. 179. DOI: 10.1007/JHEP03(2020)179. arXiv: 1912.09866 [hep-ex].

[14] Morad Aaboud et al. "Measurement of the cross section for isolated-photon plus jet production in pp collisions at $\sqrt{s}$ = 13 TeV using the ATLAS detector". In: *Phys. Lett. B* 780 (2018), pp. 578–602. DOI: 10.1016/j.physletb.2018.03.035. arXiv: 1801.00112 [hep-ex].

[15] Morad Aaboud et al. "High-E_T isolated-photon plus jets production in pp collisions at $\sqrt{s}$ = 8 TeV with the ATLAS detector". In: *Nucl. Phys. B* 918 (2017), pp. 257–316. DOI: 10.1016/j.nuclphysb.2017.03.006. arXiv: 1611.06586 [hep-ex].

[16] Georges Aad et al. "Search for invisible Higgs-boson decays in events with vector-boson fusion signatures using 139 fb^{-1} of proton-proton data recorded by the ATLAS experiment". In: *JHEP* 08 (2022), p. 104. DOI: 10.1007/JHEP08(2022)104. arXiv: 2202.07953 [hep-ex].

[17] Georges Aad et al. "Search for new phenomena in events with an energetic jet and missing transverse momentum in pp collisions at $\sqrt{s}$ =13 TeV with the ATLAS detector". In: *Phys. Rev. D* 103.11 (2021), p. 112006. DOI: 10.1103/PhysRevD.103.112006. arXiv: 2102.10874 [hep-ex].

[18] G. Aad et al. "Search for a heavy charged boson in events with a charged lepton and missing transverse momentum from pp collisions at 13 TeV with the ATLAS detector". In: *Phys. Rev. D* 100 (5 Sept. 2019), p. 052013. DOI: 10.1103/PhysRevD.100.052013. URL: https://link.aps.org/doi/10.1103/PhysRevD.100.052013.

[19] Sebastian Mario Weber on behalf of the ATLAS collaboration. "Operation and Performance of the ATLAS Level-1 Calorimeter and Level-1 Topological Triggers in Run 2 at the LHC". In: *PoS* EPS-HEP2017 (2017), p. 806. DOI: 10.22323/1.314.0806.

[20] G. Aad et al. "ATLAS data quality operations and performance for 2015–2018 data-taking". In: *Journal of Instrumentation* 15.04 (Apr. 2020), P04003. DOI: 10.1088/1748-0221/15/04/P04003. URL: https://dx.doi.org/10.1088/1748-0221/15/04/P04003.

[21] G. Aad et al. "Performance of the upgraded PreProcessor of the ATLAS Level-1 Calorimeter Trigger". In: *Journal of Instrumentation* 15.11 (Nov. 2020), P11016. DOI: 10.1088/1748-0221/15/11/P11016. URL: https://dx.doi.org/10.1088/1748-0221/15/11/P11016.

[22] Emily Nurse et al. *Detector-corrected cross-sections in events with large missing transverse momentum in association with jets*. Tech. rep. Geneva: CERN, Nov. 2019. URL: https://cds.cern.ch/record/2702246.

[23] Andrej B. Arbuzov. "Quantum Field Theory and the Electroweak Standard Model". In: (2018). DOI: 10.48550/ARXIV.1801.05670. URL: https://arxiv.org/abs/1801.05670.

[24] Tilman Plehn. *Lectures on LHC Physics*. Springer Berlin Heidelberg, 2012. DOI: 10.1007/978-3-642-24040-9. URL: https://doi.org/10.1007%2F978-3-642-24040-9.

[25] W. N. Cottingham and D. A. Greenwood. *An Introduction to the Standard Model of Particle Physics*. 2nd ed. Cambridge University Press, 2007. DOI: 10.1017/CBO9780511791\-406.

[26] Mark Thomson. *Modern Particle Physics*. Cambridge University Press, 2013. DOI: 10.1017/CBO9781139525367.

[27] Teresa Marrodá n Undagoitia and Ludwig Rauch. "Dark matter direct-detection experiments". In: *Journal of Physics G: Nuclear and Particle Physics* 43.1 (Dec. 2015), p. 013001. DOI: 10.1088/0954-3899/43/1/013001. URL: https://doi.org/10.1088%2F0954-3899%2F43%2F1%2F013001.

[28] *Standard Model of Elementary Particle Physics*. Sept. 2022. URL: https://upload.wikimedia.org/wikipedia/commons/0/00/Standard_Model_of_Elementary_Particles.svg.

[29] Y. Fukuda et al. "Evidence for Oscillation of Atmospheric Neutrinos". In: *Phys. Rev. Lett.* 81 (8 Aug. 1998), pp. 1562–1567. DOI: 10.1103/PhysRevLett.81.1562. URL: https://link.aps.org/doi/10.1103/PhysRevLett.81.1562.

[30] Q. R. Ahmad et al. "Measurement of the Rate of $\nu_e + d \rightarrow p + p + e^-$ Interactions Produced by ^8B Solar Neutrinos at the Sudbury Neutrino Observatory". In: *Phys. Rev. Lett.* 87 (7 July 2001), p. 071301. DOI: 10.1103/PhysRevLett.87.071301. URL: https://link.aps.org/doi/10.1103/PhysRevLett.87.071301.

[31] G. Aad et al. "Observation of a new particle in the search for the Standard Model Higgs boson with the ATLAS detector at the LHC". In: *Physics Letters B* 716.1 (Sept. 2012), pp. 1–29. DOI: 10.1016/j.physletb.2012.08.020. URL: https://doi.org/10.1016%2Fj.physletb.2012.08.020.

[32] S. Chatrchyan et al. "Observation of a new boson at a mass of 125 GeV with the CMS experiment at the LHC". In: *Physics Letters B* 716.1 (Sept. 2012), pp. 30–61. DOI: 10.1016/j.physletb.2012.08.021. URL: https://doi.org/10.1016%2Fj.physletb.2012.08.021.

[33] Richard D. Ball et al. "Parton distributions for the LHC run II". In: *Journal of High Energy Physics* 2015.4 (Apr. 2015). DOI: 10.1007/jhep04(2015)040. URL: https://doi.org/10.1007%2Fjhep04%282015%29040.

[34] *Standard Model Summary Plots February 2022*. Tech. rep. Geneva: CERN, 2022. URL: http://cds.cern.ch/record/2804061.

[35] F. Zwicky. "Die Rotverschiebung von extragalaktischen Nebeln". In: *Helvetica Physica Acta* 6 (Jan. 1933), pp. 110–127.

[36] V. C. Rubin, Jr. Ford W. K., and N. Thonnard. "Extended rotation curves of high-luminosity spiral galaxies. IV. Systematic dynamical properties, Sa -> Sc." In: *The Astrophysical Journal Letters* 225 (Nov. 1978), pp. L107–L111. DOI: 10.1086/182804.

[37] Douglas Clowe et al. "A Direct Empirical Proof of the Existence of Dark Matter". In: *The Astrophysical Journal* 648.2 (Aug. 2006), pp. L109–L113. DOI: 10.1086/508162. URL: https://doi.org/10.1086/508162.

[38] David Harvey et al. "The nongravitational interactions of dark matter in colliding galaxy clusters". In: *Science* 347.6229 (Mar. 2015), pp. 1462–1465. DOI: 10.1126/science.1261381. URL: https://doi.org/10.1126%2Fscience.1261381.

[39] Volker Springel, Carlos S. Frenk, and Simon D. M. White. "The large-scale structure of the Universe". In: *Nature* 440.7088 (2006), pp. 1137–1144. ISSN: 1476-4687. DOI: 10.1038/nature04805. URL: https://doi.org/10.1038/nature04805.

[40] Edvige Corbelli and Paolo Salucci. "The extended rotation curve and the dark matter halo of M33". In: *Monthly Notices of the Royal Astronomical Society* 311.2 (Jan. 2000), pp. 441–447. ISSN: 0035-8711. DOI: 10.1046/j.1365-8711.2000.03075.x. eprint: https://academic.oup.com/mnras/article-pdf/311/2/441/2881340/311-2-441.pdf. URL: https://doi.org/10.1046/j.1365-8711.2000.03075.x.

[41] C. L. Bennett et al. "Scientific results from the Cosmic Background Explorer (COBE)." eng. In: *Proceedings of the National Academy of Sciences of the United States of America* 90 (11 June 1993), pp. 4766–73.

[42] G. Hinshaw et al. "Nine-year Wilkinson Micorwave Probe Anisotropy Probe WMAP Observations: Cosmological Parameter Results". In: *The Astrophysical Journal Supplement Series* 208.2 (Sept. 2013), p. 19. DOI: 10.1088/0067-0049/208/2/19. URL: https://doi.org/10.1088/0067-0049/208/2/19.

[43] Planck Collaboration et al. "Planck 2018 results - V. CMB power spectra and likelihoods". In: *A&A* 641 (2020), A5. DOI: 10.1051/0004-6361/201936386. URL: https://doi.org/10.1051/0004-6361/201936386.

[44] The Planck Collaboration. "Planck 2018 results". In: *Astronomy & Astrophysics* 641 (Sept. 2020), A6. DOI: 10.1051/0004-6361/201833910. URL: https://doi.org/10.1051%2F0004-6361%2F201833910.

[45] Luca Visinelli and Paolo Gondolo. "Dark matter axions revisited". In: *Phys. Rev. D* 80 (3 Aug. 2009), p. 035024. DOI: 10.1103/PhysRevD.80.035024. URL: https://link.aps.org/doi/10.1103/PhysRevD.80.035024.

[46] A. Ringwald. *Axions and Axion-Like Particles*. 2014. DOI: 10.48550/ARXIV.1407.0546. URL: https://arxiv.org/abs/1407.0546.

[47] Alexey Boyarsky, Oleg Ruchayskiy, and Mikhail Shaposhnikov. "The Role of Sterile Neutrinos in Cosmology and Astrophysics". In: *Annual Review of Nuclear and Particle Science* 59.1 (2009), pp. 191–214. DOI: 10.1146/annurev.nucl.010909.083654. eprint: https://doi.org/10.1146/annurev.nucl.010909.083654. URL: https://doi.org/10.1146/annurev.nucl.010909.083654.

[48] E. Aprile et al. *Search for New Physics in Electronic Recoil Data from XENONnT*. 2022. DOI: 10.48550/ARXIV.2207.11330. URL: https://arxiv.org/abs/2207.11330.

[49] CRESST Collaboration et al. *First results on low-mass dark matter from the CRESST-III experiment*. 2017. DOI: 10.48550/ARXIV.1711.07692. URL: https://arxiv.org/abs/1711.07692.

[50] H. Abdalla et al. "Search for Dark Matter Annihilation Signals in the H.E.S.S. Inner Galaxy Survey". In: *Physical Review Letters* 129.11 (Sept. 2022). DOI: 10.1103/physrevlett.129.111101. URL: https://doi.org/10.1103%2Fphysrevlett.129.111101.

[51] Germán A. Gómez-Vargas et al. "Constraints on WIMP annihilation for contracted dark matter in the inner Galaxy with the Fermi-LAT". In: *Journal of Cosmology and Astroparticle Physics* 2013.10, 029 (Oct. 2013), p. 029. DOI: 10.1088/1475-7516/2013/10/029. arXiv: 1308.3515 [astro-ph.HE].

[52] M. Aaboud et al. "Search for dark matter in events with a hadronically decaying vector boson and missing transverse momentum in pp collisions at sqrt(s)=13 TeV with the ATLAS detector". In: *Journal of High Energy Physics* 2018.10 (2018), p. 180. ISSN: 1029-8479. DOI: 10.1007/JHEP10(2018)180. URL: https://doi.org/10.1007/JHEP10(2018)180.

[53] G. Aad et al. "Search for dark matter produced in association with a Standard Model Higgs boson decaying into b-quarks using the full Run 2 dataset from the ATLAS detector". In: *Journal of High Energy Physics* 2021.11 (2021), p. 209. ISSN: 1029-8479. DOI: 10.1007/JHEP11(2021)209. URL: https://doi.org/10.1007/JHEP11(2021)209.

[54] M. Aaboud et al. "Search for low-mass dijet resonances using trigger-level jets with the ATLAS detector in pp collisions at sqrt(s)=13 TeV". In: *Physical Review Letters* 121.8 (Aug. 2018). DOI: 10.1103/physrevlett.121.081801. URL: https://doi.org/10.1103%2Fphysrevlett.121.081801.

[55] G. Aad et al. "Search for new resonances in mass distributions of jet pairs using 139 fb−1 of pp collisions at sqrt(s)=13 TeV with the ATLAS detector". In: *Journal of High Energy Physics* 2020.3 (2020), p. 145. ISSN: 1029-8479. DOI: 10.1007/JHEP03(2020)145. URL: https://doi.org/10.1007/JHEP03(2020)145.

[56] Jalal Abdallah et al. "Simplified models for dark matter searches at the LHC". In: *Physics of the Dark Universe* 9-10 (Sept. 2015), pp. 8–23. DOI: 10.1016/j.dark.2015.08.001. URL: https://doi.org/10.1016%2Fj.dark.2015.08.001.

[57] Daniel Abercrombie et al. "Dark Matter benchmark models for early LHC Run-2 Searches: Report of the ATLAS/CMS Dark Matter Forum". In: *Physics of the Dark Universe* 27 (Jan. 2020), p. 100371. DOI: 10.1016/j.dark.2019.100371. URL: https://doi.org/10.1016%2Fj.dark.2019.100371.

[58] The ATLAS Collaboration et al. "The ATLAS Experiment at the CERN Large Hadron Collider". In: *Journal of Instrumentation* 3.08 (2008), S08003. URL: http://stacks.iop.org/1748-0221/3/i=08/a=S08003.

[59] Lyndon Evans and Philip Bryant. "LHC Machine". In: *Journal of Instrumentation* 3.08 (2008), S08001. URL: http://stacks.iop.org/1748-0221/3/i=08/a=S08001.

[60] John Jowett. "Colliding Heavy Ions in the LHC". In: (2018), TUXGBD2. 6 p. DOI: 10.18429/JACoW-IPAC2018-TUXGBD2. URL: https://cds.cern.ch/record/2648704.

[61] Christiane Lefèvre. "The CERN accelerator complex." Dec. 2008. URL: https://cds.cern.ch/record/1260465.

[62] L Arnaudon et al. *Linac4 Technical Design Report*. Tech. rep. Geneva: CERN, Dec. 2006. URL: https://cds.cern.ch/record/1004186.

[63] Yan Elie Milo Ihringer and Jacques Herve Fichet. "Energy record of two pilot beams for the restart of LHC". In: (2022). URL: https://cds.cern.ch/record/2807453.

[64] *Luminosity determination in pp collisions at $\sqrt{s} = 13$ TeV using the ATLAS detector at the LHC*. Tech. rep. Geneva: CERN, June 2019. URL: https://cds.cern.ch/record/2677054.

[65] *RLIUP: Review of LHC and Injector Upgrade Plans: Centre de Convention, Archamps, France 29 - 31 Oct 2013. RLIUP: Review of LHC and Injector Upgrade Plans*. CERN. Geneva: CERN, 2014. DOI: 10.5170/CERN-2014-006. URL: https://cds.cern.ch/record/1629486.

[66] The CMS Collaboration et al. "The CMS experiment at the CERN LHC". In: *Journal of Instrumentation* 3.08 (2008), S08004. URL: http://stacks.iop.org/1748-0221/3/i=08/a=S08004.

[67] The LHCb Collaboration et al. "The LHCb Detector at the LHC". In: *Journal of Instrumentation* 3.08 (2008), S08005. URL: http://stacks.iop.org/1748-0221/3/i=08/a=S08005.

[68] K. Aamodt et al. "The ALICE experiment at the CERN LHC". In: *JINST* 3 (2008), S08002. DOI: 10.1088/1748-0221/3/08/S08002.

[69] Georges Aad et al. "The ATLAS Inner Detector commissioning and calibration". In: *Eur. Phys. J. C* 70.arXiv:1004.5293. CERN-PH-EP-2010-043 (June 2010), 787–821. 34 p. URL: https://cds.cern.ch/record/1262789.

[70] Alessandro La Rosa. "The ATLAS Insertable B-Layer: from construction to operation". In: (2016). DOI: 10.48550/ARXIV.1610.01994. URL: https://arxiv.org/abs/1610.01994.

[71] G. Aad et al. "The ATLAS Inner Detector commissioning and calibration". In: *The European Physical Journal C* 70.3 (2010), pp. 787–821. ISSN: 1434-6052. DOI: 10.1140/epjc/s10052-010-1366-7. URL: https://doi.org/10.1140/epjc/s10052-010-1366-7.

[72] Hermann Kolanoski and Norbert Wermes. *Particle Detectors: Fundamentals and Applications*. Oxford University Press, June 2020. ISBN: 9780198858362. DOI: 10.1093/oso/9780198858362.001.0001. URL: https://doi.org/10.1093/oso/9780198858362.001.0001.

[73] A Artamonov et al. "The ATLAS Forward Calorimeter". In: *Journal of Instrumentation* 3.02 (2008), P02010. URL: http://stacks.iop.org/1748-0221/3/i=02/a=P02010.

[74] The ATLAS collaboration. "Operation of the ATLAS trigger system in Run 2". In: *Journal of Instrumentation* 15.10 (Oct. 2020), P10004–P10004. DOI: 10.1088/1748-0221/15/10/p10004. URL: https://doi.org/10.1088/1748-0221/15/10/p10004.

[75] ATLAS. *Internal Communication*.

[76] M. Aaboud et. al. "Electron efficiency measurements with the ATLAS detector using 2012 LHC protonproton collision data". In: *The European Physical Journal C* 77.3 (Mar. 2017). DOI: 10.1140/epjc/s10052-017-4756-2. URL: https://doi.org/10.1140%2Fepjc%2Fs10052-017-4756-2.

[77] *Vertex Reconstruction Performance of the ATLAS Detector at 13 TeV*. Tech. rep. Geneva: CERN, July 2015. URL: http://cds.cern.ch/record/2037717.

[78] *Evaluating statistical uncertainties and correlations using the bootstrap method*. Tech. rep. Geneva: CERN, Apr. 2021. URL: https://cds.cern.ch/record/2759945.

[79] Georges Aad et al. "Electron and photon performance measurements with the ATLAS detector using the 2015-2017 LHC proton-proton collision data". In: *JINST* 14 (Aug. 2019), P12006. 70 p. DOI: 10.1088/1748-0221/14/12/P12006. arXiv: 1908.00005. URL: https://cds.cern.ch/record/2684552.

[80] M. Aaboud et al. "Electron reconstruction and identification in the ATLAS experiment using the 2015 and 2016 LHC proton–proton collision data at sqrt(s) = 13 TeV". In: *The European Physical Journal C* 79.8 (Aug. 2019). ISSN: 1434-6052. DOI: 10.1140/epjc/s10052-019-7140-6. URL: http://dx.doi.org/10.1140/epjc/s10052-019-7140-6.

[81] M. Aaboud et al. "Measurement of the photon identification efficiencies with the ATLAS detector using LHC Run 2 data collected in 2015 and 2016". In: *The European Physical Journal C* 79.3 (Mar. 2019). DOI: 10.1140/epjc/s10052-019-6650-6. URL: https://doi.org/10.1140%2Fepjc%2Fs10052-019-6650-6.

[82] T Cornelissen et al. *Single Track Performance of the Inner Detector New Track Reconstruction (NEWT)*. Tech. rep. Geneva: CERN, Mar. 2008. URL: http://cds.cern.ch/record/1092934.

[83] *ATLAS inner detector: Technical Design Report, 1*. Technical design report. ATLAS. Geneva: CERN, 1997. URL: https://cds.cern.ch/record/331063.

[84] G. Aad et al. "Muon reconstruction performance of the ATLAS detector in proton-proton collision data at sqrt(s)=13 TeV". In: *The European Physical Journal C* 76.5 (2016), p. 292. ISSN: 1434-6052. DOI: 10.1140/epjc/s10052-016-4120-y. URL: https://doi.org/10.1140/epjc/s10052-016-4120-y.

[85] G. Aad et al. "Muon reconstruction and identification efficiency in ATLAS using the full Run 2 pp collision data set at sqrt(s)=13 TeV". In: *The European Physical Journal C* 81.7 (2021), p. 578. ISSN: 1434-6052. DOI: 10.1140/epjc/s10052-021-09233-2. URL: https://doi.org/10.1140/epjc/s10052-021-09233-2.

[86] G. Aad et al. "Identification and energy calibration of hadronically decaying tau leptons with the ATLAS experiment in pp collisions at $\sqrt{s} = 8$TeV". In: *The European Physical Journal C* 75.7 (2015), p. 303. ISSN: 1434-6052. DOI: 10.1140/epjc/s10052-015-3500-z. URL: https://doi.org/10.1140/epjc/s10052-015-3500-z.

[87] Matteo Cacciari, Gavin P Salam, and Gregory Soyez. "The anti-kt jet clustering algorithm". In: *Journal of High Energy Physics* 2008.04 (Apr. 2008), pp. 063–063. DOI: 10.1088/1126-6708/2008/04/063. URL: https://doi.org/10.1088/1126-6708/2008/04/063.

[88] *Reconstruction, Energy Calibration, and Identification of Hadronically Decaying Tau Leptons in the ATLAS Experiment for Run-2 of the LHC*. Tech. rep. Geneva: CERN, Nov. 2015. URL: https://cds.cern.ch/record/2064383.

[89] *Identification of hadronic tau lepton decays using neural networks in the ATLAS experiment*. Tech. rep. Geneva: CERN, Aug. 2019. URL: https://cds.cern.ch/record/2688062.

[90] M. Aaboud et al. "Jet reconstruction and performance using particle flow with the ATLAS Detector". In: *The European Physical Journal C* 77.7 (July 2017). DOI: 10.1140/epjc/s10052-017-5031-2. URL: https://doi.org/10.1140%2Fepjc%2Fs10052-017-5031-2.

[91] Georges Aad et al. "Jet energy scale and resolution measured in proton–proton collisions at $\sqrt{s} = 13$ TeV with the ATLAS detector". In: *Eur. Phys. J. C* 81.8 (2021), p. 689. DOI: 10.1140/epjc/s10052-021-09402-3. arXiv: 2007.02645 [hep-ex].

[92] G. Aad et al. "Performance of pile-up mitigation techniques for jets in p p collisions at 8 TeV using the ATLAS detector". In: *The European Physical Journal C* 76.11 (Oct. 2016). DOI: 10.1140/epjc/s10052-016-4395-z. URL: https://doi.org/10.1140%2Fepjc%2Fs10052-016-4395-z.

[93] M. Aaboud et al. "Identification and rejection of pile-up jets at high pseudorapidity with the ATLAS detector". In: *The European Physical Journal C* 77.9 (2017), p. 580. ISSN: 1434-6052. DOI: 10.1140/epjc/s10052-017-5081-5. URL: https://doi.org/10.1140/epjc/s10052-017-5081-5.

[94] D Adams et al. *Recommendations of the Physics Objects and Analysis Harmonisation Study Groups 2014*. Tech. rep. Geneva: CERN, 2014. URL: https://cds.cern.ch/record/1743654.

[95] *E_T^{miss} performance in the ATLAS detector using 2015-2016 LHC p-p collisions*. Tech. rep. Geneva: CERN, June 2018. URL: http://cds.cern.ch/record/2625233.

[96] M. Aaboud et al. "Performance of missing transverse momentum reconstruction with the ATLAS detector using proton–proton collisions at sqrt(s)=13 TeV". In: *The European Physical Journal C* 78.11 (Nov. 2018). ISSN: 1434-6052. DOI: 10.1140/epjc/s10052-018-6288-9. URL: http://dx.doi.org/10.1140/epjc/s10052-018-6288-9.

[97] The ATLAS collaboration. "Performance of the ATLAS trigger system in 2015". In: *The European Physical Journal C* 77.5 (May 2017). DOI: 10.1140/epjc/s10052-017-4852-3. URL: https://doi.org/10.1140%2Fepjc%2Fs10052-017-4852-3.

[98] Martin Klassen. *Private Communication*.

[99] D.R Yennie, S.C Frautschi, and H Suura. "The infrared divergence phenomena and high-energy processes". In: *Annals of Physics* 13.3 (1961), pp. 379–452. ISSN: 0003-4916. DOI: https://doi.org/10.1016/0003-4916(61)90151-8. URL: https://www.sciencedirect.com/science/article/pii/0003491661901518.

[100] S. Agostinelli et al. "Geant4—a simulation toolkit". In: *Nuclear Instruments and Methods in Physics Research Section A: Accelerators, Spectrometers, Detectors and Associated Equipment* 506.3 (2003), pp. 250–303. ISSN: 0168-9002. DOI: https://doi.org/10.1016/S0168-9002(03)01368-8. URL: https://www.sciencedirect.com/science/article/pii/S0168900203013688.

[101] and G. Aad et al. "Modelling and computational improvements to the simulation of single vector-boson plus jet processes for the ATLAS experiment". In: *Journal of High Energy Physics* 2022.8 (Aug. 2022). DOI: 10.1007/jhep08(2022)089. URL: https://doi.org/10.1007%2Fjhep08%282022%29089.

[102] Georges Aad et al. "AtlFast3: the next generation of fast simulation in ATLAS". In: *Comput. Softw. Big Sci.* 6 (2022), p. 7. DOI: 10.1007/s41781-021-00079-7. arXiv: 2109.02551 [hep-ex].

[103] J. M. Lindert et al. "Precise predictions for V+jets dark matter backgrounds". In: *The European Physical Journal C* 77.12 (2017), p. 829. ISSN: 1434-6052. DOI: 10.1140/epjc/s10052-017-5389-1. URL: https://doi.org/10.1140/epjc/s10052-017-5389-1.

[104] Torbjörn Sjöstrand et al. "An Introduction to PYTHIA 8.2". In: *Comput. Phys. Commun.* 191 (2015), pp. 159–177. DOI: 10.1016/j.cpc.2015.01.024. arXiv: 1410.3012 [hep-ph].

[105] Richard D. Ball et al. "Parton distributions with LHC data". In: *Nuclear Physics B* 867.2 (Feb. 2013), pp. 244–289. DOI: 10.1016/j.nuclphysb.2012.10.003. URL: https://doi.org/10.1016%2Fj.nuclphysb.2012.10.003.

[106] *The Pythia 8 A3 tune description of ATLAS minimum bias and inelastic measurements incorporating the Donnachie-Landshoff diffractive model*. Tech. rep. Geneva: CERN, 2016. URL: https://cds.cern.ch/record/2206965.

[107] T. Gleisberg et al. "Event generation with SHERPA 1.1". In: *JHEP* 02 (2009), p. 007. DOI: 10.1088/1126-6708/2009/02/007. arXiv: 0811.4622 [hep-ph].

[108] ATLAS Collaboration. *ATLAS simulation of boson plus jets processes in Run 2*. ATL-PHYS-PUB-2017-006. 2017. URL: https://cds.cern.ch/record/2261937.

[109] T. Sjostrand, S. Mrenna, and P. Skands. "A brief introduction to PYTHIA 8.1". In: *Comput. Phys. Commun.* 178 (2008), pp. 852–867. DOI: 10.1016/j.cpc.2008.01.036. arXiv: 0710.3820 [hep-ph].

[110] ATLAS Collaboration. *Multi-Boson Simulation for* 13 *TeV ATLAS Analyses*. ATL-PHYS-PUB-2017-005. 2017. URL: https://cds.cern.ch/record/2261933.

[111] S. Frixione et al. "A positive-weight next-to-leading-order Monte Carlo for heavy flavour hadroproduction". In: *JHEP* 09 (2007), p. 126. DOI: 10.1088/1126-6708/2007/09/126. arXiv: 0707.3088 [hep-ph].

[112] Paolo Nason. "A New method for combining NLO QCD with shower Monte Carlo algorithms". In: *JHEP* 0411 (2004), p. 040. DOI: 10.1088/1126-6708/2004/11/040. arXiv: hep-ph/0409146.

[113] Stefano Frixione, Paolo Nason, and Carlo Oleari. "Matching NLO QCD computations with Parton Shower simulations: the POWHEG method". In: *JHEP* 11 (2007), p. 070. DOI: 10.1088/1126-6708/2007/11/070. arXiv: 0709.2092 [hep-ph].

[114] Simone Alioli et al. "A general framework for implementing NLO calculations in shower Monte Carlo programs: the POWHEG BOX". In: *JHEP* 1006 (2010), p. 043. DOI: 10.1007/JHEP06(2010)043. arXiv: 1002.2581 [hep-ph].

[115] Emanuele Re. "Single-top Wt-channel production matched with parton showers using the POWHEG method". In: *Eur. Phys. J. C* 71 (2011), p. 1547. DOI: 10.1140/epjc/s10052-011-1547-z. arXiv: 1009.2450 [hep-ph].

[116] Rikkert Frederix, Emanuele Re, and Paolo Torrielli. "Single-top t-channel hadroproduction in the four-flavour scheme with POWHEG and aMC@NLO". In: *JHEP* 09 (2012), p. 130. DOI: 10.1007/JHEP09(2012)130. arXiv: 1207.5391 [hep-ph].

[117] Simone Alioli et al. "NLO single-top production matched with shower in POWHEG: s- and t-channel contributions". In: *JHEP* 09 (2009), p. 111. DOI: 10.1007/JHEP02(2010)011,10.1088/1126-6708/2009/09/111. arXiv: 0907.4076 [hep-ph].

[118] *ATLAS Pythia 8 tunes to 7 TeV data*. Tech. rep. Geneva: CERN, 2014. URL: https://cds.cern.ch/record/1966419.

[119] G. Aad et al. "Performance of electron and photon triggers in ATLAS during LHC Run 2". In: *The European Physical Journal C* 80.1 (2020), p. 47. ISSN: 1434-6052. DOI: 10.1140/epjc/s10052-019-7500-2. URL: https://doi.org/10.1140/epjc/s10052-019-7500-2.

[120] William Buttinger. *Using Event Weights to account for differences in Instantaneous Luminosity and Trigger Prescale in Monte Carlo and Data*. Tech. rep. Geneva: CERN, May 2015. URL: https://cds.cern.ch/record/2014726.

[121] *Measurement of the tau lepton reconstruction and identification performance in the ATLAS experiment using pp collisions at $\sqrt{s}$ = 13 TeV*. Tech. rep. Geneva: CERN, 2017. URL: https://cds.cern.ch/record/2261772.

[122] Jon Butterworth et al. "PDF4LHC recommendations for LHC Run II". In: *Journal of Physics G: Nuclear and Particle Physics* 43.2 (Jan. 2016), p. 023001. DOI: 10.1088/0954-3899/43/2/023001. URL: https://doi.org/10.1088%2F0954-3899%2F43%2F2%2F023001.

[123] S Owen. *Data-driven estimation of the QCD multijet background to SUSY searches with jets and missing transverse momentum at ATLAS using jet smearing*. Tech. rep. Geneva: CERN, Feb. 2012. URL: https://cds.cern.ch/record/1423310.

[124] G. Aad et al. "Beam-induced and cosmic-ray backgrounds observed in the ATLAS detector during the LHC 2012 proton-proton running period". In: *Journal of Instrumentation* 11.05 (May 2016), P05013–P05013. DOI: 10.1088/1748-0221/11/05/p05013. URL: https://doi.org/10.1088/1748-0221/11/05/p05013.

[125] "Characterisation and mitigation of beam-induced backgrounds observed in the ATLAS detector during the 2011 proton-proton run". In: *Journal of Instrumentation* 8.07 (July 2013), P07004–P07004. DOI: 10.1088/1748-0221/8/07/p07004. URL: https://doi.org/10.1088/1748-0221/8/07/p07004.

[126] R W Assmann et al. "The final collimation system for the LHC". In: (July 2006), 4 p. URL: http://cds.cern.ch/record/972336.

[127] R Bruce et al. "Sources of machine-induced background in the ATLAS and CMS detectors at the CERN Large Hadron Collider". In: *Nucl. Instrum. Methods Phys. Res., A* 729 (Jan. 2014), 825–840. 22 p. DOI: 10.1016/j.nima.2013.03.058. URL: https://cds.cern.ch/record/1646958.

[128] M. Aaboud et al. "Comparison between simulated and observed LHC beam backgrounds in the ATLAS experiment at E_{beam}=4 TeV". In: *Journal of Instrumentation* 13.12 (Dec. 2018), P12006–P12006. DOI: 10.1088/1748-0221/13/12/p12006. URL: https://doi.org/10.1088/1748-0221/13/12/p12006.

[129] *Selection of jets produced in 13TeV proton-proton collisions with the ATLAS detector*. Tech. rep. Geneva: CERN, July 2015. URL: https://cds.cern.ch/record/2037702.

[130] M. Aaboud et al. "Electron and photon energy calibration with the ATLAS detector using 2015–2016 LHC proton-proton collision data". In: *Journal of Instrumentation* 14.03 (Mar. 2019), P03017–P03017. DOI: 10.1088/1748-0221/14/03/p03017. URL: https://doi.org/10.1088%2F1748-0221%2F14%2F03%2Fp03017.

[131] *Photon/PI0 Event Display*. ATLAS Collaboration, Sept. 2022. URL: https://atlas.web.cern.ch/Atlas/GROUPS/PHYSICS/EGAMMA/PublicPlots/20100721/display-photons/index.html.

[132] Aaron Meurer et al. "SymPy: symbolic computing in Python". In: *PeerJ Computer Science* 3 (Jan. 2017), e103. ISSN: 2376-5992. DOI: 10.7717/peerj-cs.103. URL: https://doi.org/10.7717/peerj-cs.103.

[133] Enrico Bothmann et al. "Event generation with Sherpa 2.2". In: *SciPost Physics* 7.3 (Sept. 2019). ISSN: 2542-4653. DOI: 10.21468/scipostphys.7.3.034. URL: http://dx.doi.org/10.21468/SciPostPhys.7.3.034.

[134] M. Aaboud et al. "Measurement of the cross section for isolated-photon plus jet production in pp collisions at s=13 TeV using the ATLAS detector". In: *Physics Letters B* 780 (2018), pp. 578–602. ISSN: 0370-2693. DOI: https://doi.org/10.1016/j.physletb.2018.03.035. URL: https://www.sciencedirect.com/science/article/pii/S0370269318302247.

[135] Fabio Cardillo et al. *Tools for estimating fake/non-prompt lepton backgrounds in ATLAS*. Tech. rep. Geneva: CERN, July 2022. URL: https://cds.cern.ch/record/2686919.

[136] Olaf Behnke et al., eds. *Data analysis in high energy physics: A practical guide to statistical methods*. Weinheim, Germany: Wiley-VCH, 2013. ISBN: 978-3-527-41058-3, 978-3-527-65344-7, 978-3-527-65343-0.

[137] Andreas Höcker and Vakhtang Kartvelishvili. "SVD approach to data unfolding". In: *Nuclear Instruments and Methods in Physics Research Section A: Accelerators, Spectrometers, Detectors and Associated Equipment* 372.3 (Apr. 1996), pp. 469–481. DOI: 10.1016/0168-9002(95)01478-0. URL: https://doi.org/10.1016%2F0168-9002%2895%2901478-0.

[138] G. D'Agostini. "A multidimensional unfolding method based on Bayes' theorem". In: *Nuclear Instruments and Methods in Physics Research Section A: Accelerators, Spectrometers, Detectors and Associated Equipment* 362.2 (1995), pp. 487–498. ISSN: 0168-9002. DOI: https://doi.org/10.1016/0168-9002(95)00274-X. URL: https://www.sciencedirect.com/science/article/pii/016890029500274X.

[139] J. de Favereau et al. "DELPHES 3: a modular framework for fast simulation of a generic collider experiment". In: *Journal of High Energy Physics* 2014.2 (2014), p. 57. ISSN: 1029-8479. DOI: 10.1007/JHEP02(2014)057. URL: https://doi.org/10.1007/JHEP02(2014)057.

[140] I.P. Nedelkov. "Improper problems in computational physics". In: *Computer Physics Communications* 4.2 (1972), pp. 157–164. ISSN: 0010-4655. DOI: https://doi.org/10.1016/0010-4655(72)90002-1. URL: https://www.sciencedirect.com/science/article/pii/0010465572900021.

[141] G. D'Agostini. *Improved iterative Bayesian unfolding*. 2010. DOI: 10.48550/ARXIV.1010.0632. URL: https://arxiv.org/abs/1010.0632.

[142] Tim Adye. "Unfolding algorithms and tests using RooUnfold". In: (2011). DOI: 10.48550/ARXIV.1105.1160. URL: https://arxiv.org/abs/1105.1160.

[143] *Proceedings of the 1974 CERN School of Computing: Godøysund, Norway 11 - 24 Aug 1974. 3rd CERN School of Computing*. CERN. Geneva: CERN, 1974. DOI: 10.5170/CERN-1974-023. URL: https://cds.cern.ch/record/186223.

[144] Stefano Frixione. "Isolated photons in perturbative QCD". In: *Phys. Lett. B* 429 (1998), pp. 369–374. DOI: 10.1016/S0370-2693(98)00454-7. arXiv: hep-ph/9801442.

[145] A L Read. "Presentation of search results: the CLs technique". In: *Journal of Physics G: Nuclear and Particle Physics* 28.10 (Sept. 2002), pp. 2693–2704. DOI: 10.1088/0954-3899/28/10/313. URL: https://doi.org/10.1088/0954-3899/28/10/313.

[146] J. Neyman and E. S. Pearson. "On the problem of the most efficient tests of statistical hypotheses". In: *Philosophical Transactions of the Royal Society (A)* 231 (1933), pp. 289–337.

[147] Mathieu Buchkremer et al. "Model-independent framework for searches of top partners". In: *Nuclear Physics B* 876.2 (Nov. 2013), pp. 376–417. DOI: 10.1016/j.nuclphysb.2013.08.010. URL: https://doi.org/10.1016%2Fj.nuclphysb.2013.08.010.

[148] G. Aad et al. "Performance of the missing transverse momentum triggers for the ATLAS detector during Run-2 data taking". In: *Journal of High Energy Physics* 2020.8 (2020), p. 80. ISSN: 1029-8479. DOI: 10.1007/JHEP08(2020)080. URL: https://doi.org/10.1007/JHEP08(2020)080.

[149] B. Efron. "Bootstrap Methods: Another Look at the Jackknife". In: *The Annals of Statistics* 7.1 (1979), pp. 1–26. ISSN: 00905364. URL: http://www.jstor.org/stable/2958830 (visited on 07/06/2022).

[150] Bradley Efron and Robert J. Tibshirani. *An Introduction to the Bootstrap*. Monographs on Statistics and Applied Probability 57. Boca Raton, Florida, USA: Chapman & Hall/CRC, 1994.

Acknowledgments

This thesis would not have been possible without the support of a great number of people.

First and foremost I want to thank my supervisor Prof. Dr. Hans-Christian Schultz-Coulon for giving me the possibility to do my thesis in his group. He supported me generously and provided insightful scientific discussion, as well as great advice, which furthered me in my personal development. His cheerful, motivating and encouraging nature reliably helped me through the occasional rough patch. He really helps however he can - even if this includes writing last-minute reference letters on short notice on a Sunday afternoon. For all this, I will ever be grateful.

Furthermore I want to thank Prof. Dr. Stephanie Hansmann-Menzemer for being my second referee. She also supported me in my doctoral studies, especially in the activities organised by the Research Training Group, like Pizza-Seminars, Student Lectures and Physics Teams.

I also want thank Rainer Stamen, who always had an open door and open ear for all problems and questions that arise during a PhD.

My special thanks goes to Pavel Starovoitov and Monica Dunford who provided feedback, ideas and discussion on this measurement and many other scientific (and non-scientific[2]) topics. In these discussions I learned a lot about physics and also how to properly present it. They taught me what it means to be precise, but also when to be pragmatic.

A great thank you goes to the combined F8 & F11 groups for the great atmosphere - not only during work, coffee breaks and meetings, but also outside during numerous joint activities. Special thanks goes to my diligent proof-readers: Falk, Fer, Lisa, Martin, Philipp, Thomas and Varsiha.

For shared adventures I want to thank my fellow farm admins and friends Falk and Martin. We worked together for long but fun hours to keep the cluster running and growing - sometimes even rushing to the university in the middle of the night, to prevent disaster from yet another cooling failure. We also have our love for board games and good food[3] in common, which we often enjoyed together with Hannah, Ralf, Iris and Philipp.

Immeasurable thanks goes to my best friends Michi and Nils, who have supported me since we were children and keep reminding me, that there is life outside of physics.

To my parents, Christine and Günter and my sister Ines thank you for the years of support and encouragement that has carried me this far.

[2] For example how to properly make Pelmeni and the necessary tools, or where to find the perfect turkey recipe.

[3] Although they both are a bit more on the veggie side of things.